A Parametric Framework for Modelling the Influence of Semi-Rigid Connections on Unbraced Timber Gridshell Behaviour

K.M. Hasenaar

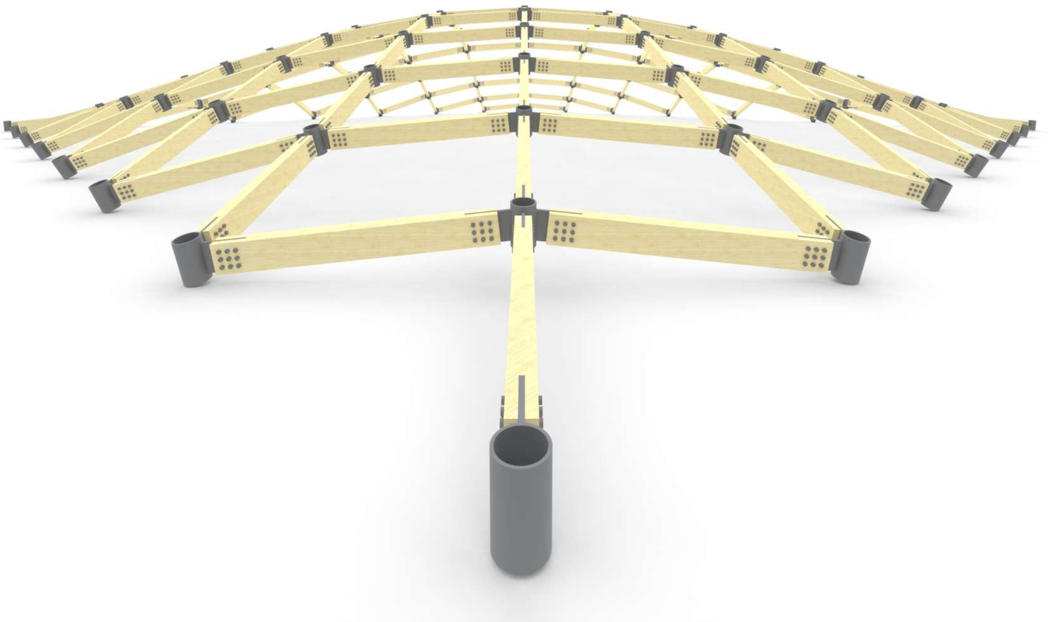

Graduation supervising committee:

Ir. A.P.H.W. Habraken

Ir. J.P. Janssen

Ir. R.H.G. Roijakkers

02/07/2026

Architecture, Building, and Planning; Structural Engineering and Design, 45 ECTS

This Master's thesis has been carried out in accordance with the rules of the TU/e Code of Scientific Integrity.

Abstract

Unbraced timber gridshells provide a lightweight and materially efficient structural solution, but their structural response is highly sensitive to the rotational stiffness of their connections. In current engineering practice, timber connections are commonly idealised as either pinned or rigid, despite exhibiting semi-rigid behaviour resulting from dowel bending, timber embedment deformation, and connection slip. Although Eurocode 5 provides practical stiffness formulations for dowel-type connections, several geometric and mechanical parameters that influence rotational stiffness are not explicitly accounted for.

This research develops a multi-scale analytical, numerical, and parametric framework that links the rotational stiffness of semi-rigid steel–timber knife-plate connections to the global behaviour of unbraced timber gridshells. A global parametric gridshell model is first used to establish the stiffness requirements associated with different grid configurations. Subsequently, beam-on-elastic-foundation formulations are developed to investigate the influence of geometric and material parameters on the linear elastic rotational stiffness of individual dowels and multi-dowel connection groups. The analytical formulations are validated using finite element simulations in MSC Nastran/Femap before being applied to the design of a practical connection through a full case study.

The results demonstrate that dowel diameter, embedment length, timber density, and bolt-group geometry all significantly influence rotational stiffness. Dowel diameter was found to produce the largest increase in stiffness. In contrast, embedment length exhibited the most complex behaviour, characterised by multiple plateau regions associated with changes in the dowel–timber contact mechanism. Comparison with Eurocode 5 indicates that the empirical slip-modulus formulation provides a practical design-oriented approximation but does not explicitly capture the additional stiffness resulting from finite embedment length and distributed dowel–timber interaction. Following calibration, the analytical formulation predicted the finite element results with an accuracy of approximately 5%.

At the global scale, the analyses demonstrate that the diagonal gridshell is governed predominantly by the out-of-plane rotational stiffness. In contrast, the orthogonal configuration exhibits a coupled dependence on both the in-plane and out-of-plane stiffness. The practical case study further demonstrates that the required global rotational stiffness can be translated directly into a feasible steel–timber connection satisfying both stiffness and strength requirements.

Overall, the proposed methodology establishes a direct relationship between local connection mechanics and global structural behaviour. By treating connection stiffness as a design variable rather than an assumed modelling parameter, the research provides a practical framework for stiffness-informed analysis and design of timber gridshells. It demonstrates the value of integrating analytical modelling, finite element analysis, and parametric design within a unified computational workflow.

Table of Contents

1. Introduction

The environmental impact of the construction sector has become a central concern within contemporary structural engineering. The built environment accounts for approximately 37% of global carbon dioxide emissions, while demand for construction materials is expected to continue to increase in the coming decades (OECD, 2019; UNEP, 2023). Consequently, the development of structurally efficient systems that reduce material consumption and embodied carbon remains an important research objective.

Timber has emerged as a promising structural material due to its renewable nature, favourable strength-to-weight ratio, and increasing availability of engineered timber products. Advances in manufacturing and design have enabled timber to be applied in increasingly ambitious structural systems, including long-span roofs, free-form structures, and lightweight shell geometries. Among these systems, timber gridshells are of particular interest because they combine material efficiency with geometric stiffness, enabling large spans with relatively slender structural members.

Gridshells are spatial lattice structures in which an initially planar grid is shaped into a doubly curved surface to introduce structural depth over large spans while minimising material consumption. Unlike conventional beam-and-column structures, gridshells derive a significant portion of their load-carrying capacity from their geometry. Through membrane action and geometric stiffening, loads can be transferred predominantly as axial forces rather than as bending moments, resulting in highly efficient structural forms.

In an idealised gridshell with an optimised geometry, the majority of the applied loading is resisted through membrane action. In practice, however, fabrication tolerances, construction imperfections, asymmetric loading, and architectural constraints inevitably introduce bending moments and second-order effects(Adriaenssens *et al.*, 2014). These effects become increasingly significant when the shell geometry deviates from its structurally optimal form or when the connections provide only limited restraint against in-plane deformation. Consequently, the relative stiffness of the members and their semi-rigid connections directly influence the redistribution of internal forces, the development of bending moments, the sensitivity to second-order effects, and the overall stability of the structure.

The increasing use of computational design and digital fabrication has enabled architects and engineers to realise increasingly complex free-form gridshell geometries. While these tools provide greater architectural freedom, they also produce structures whose geometry is often governed by architectural intent, construction constraints, fabrication limitations, or site-specific requirements rather than by purely structural optimisation. As these practical constraints reduce the effectiveness of membrane action, the influence of connection stiffness becomes increasingly important, making an accurate representation of semi-rigid connection behaviour essential for predicting structural response and ensuring efficient, reliable designs.

The influence of connection behaviour is particularly relevant in timber structures. While numerical models commonly idealise joints as either pinned or rigid, timber connections generally exhibit semi-rigid behaviour resulting from local embedment deformation, fastener bending, slip, and time-dependent effects. These mechanisms contribute residual stiffness that can influence both local force transfer and global structural behaviour. Although considerable research has focused on the strength and failure mechanisms of timber connections, particularly through experimental testing, comparatively less attention has been given to their influence on structural stiffness and the behaviour of the structural system as a whole.

Current design approaches evaluate connection stiffness using simplified empirical formulations. Eurocode 5, for example, provides the slip modulus K_{ser} for practical structural design. However, these formulations are primarily calibrated for design purposes and do not explicitly account for several geometric and mechanical parameters known to influence dowel-type connections, such as finite embedment length, distributed dowel–timber interaction, and the rotational behaviour of multi-fastener groups. Consequently, discrepancies may arise between the simplified stiffness assumptions used in design and the rotational stiffness developed through the underlying connection mechanics.

At the same time, advances in analytical and numerical modelling have enabled greater detail in the investigation of connection behaviour. Beam-on-elastic-foundation formulations and finite element methods allow local deformation mechanisms to be represented explicitly, providing insight into how geometric and material parameters influence rotational stiffness. Despite these developments, existing research largely treats local connection behaviour and global structural behaviour independently. A systematic design framework that links analytical connection mechanics to the global behaviour of timber gridshells, therefore, remains largely absent from the current literature.

Previous research on gridshell stiffness has predominantly focused on steel structures(Dyvik, Manum and Rønnquist, 2021). Isufi and Spengler demonstrated the influence of nodal stiffness on global behaviour and stress redistribution(Isufi F., 2021; Spengler van F., 2024). Fan et al. developed classifications for rigid and semi-rigid joints based on stiffness and strength criteria(Fan *et al.*, 2011). Within timber gridshell research, Larsson and Nakajima investigated several connection systems using analytical, numerical, and experimental approaches(Larsson, 2018; Nakajima, Terazawa, et al., 2019; Nakajima, Yamazaki, et al., 2019). Despite these contributions, the relationship between connection stiffness, geometry and global stability remains insufficiently understood in timber gridshells.

This research addresses this gap through a multi-scale investigation that links global structural requirements to local connection mechanics. A parametric gridshell model is first used to establish the rotational stiffness required to achieve the desired structural behaviour. Subsequently, analytical and numerical models are employed to investigate how this stiffness can be realised through the geometric and material parameters of semi-rigid steel–timber knife plate dowel connections. Finally, the developed methodology is demonstrated through a practical case study in which the required global stiffness is translated into a feasible connection design. The broader objective is to support stiffness-informed analysis and design of timber gridshell structures by providing a practical framework for incorporating semi-rigid connection behaviour into computational design workflows. This objective is addressed through the following main research question:

How do material and geometric parameters influence the rotational stiffness of semi-rigid steel–timber knife-plate connections, and how does this stiffness influence the global structural behaviour of unbraced timber gridshells?

To answer this question, the research is divided into four interconnected sub-questions:

1. How can parametric workflows support the efficient analysis and design of semi-rigid steel–timber connections and timber gridshell structures?
2. How can the rotational stiffness of steel–timber dowel connections be determined from geometric and material parameters using analytical modelling approaches?
3. To what extent can finite element modelling reproduce the rotational stiffness behaviour predicted by the analytical formulation?
4. How does semi-rigid in and out-of-plane connection behaviour influence the stability, stiffness response, and design space of unbraced timber gridshell structures?

2. Theory and Background

2.1. Gridshell Structures

By introducing double curvature into an initially planar grid, the structure develops geometric stiffness, enabling efficient load transfer through membrane action while maintaining a relatively low self-weight. By introducing double curvature into an initially planar grid, the structure develops geometric stiffness that enables efficient load transfer through membrane action while maintaining a relatively low self-weight. Consequently, gridshells are capable of spanning large distances using comparatively slender structural members, making them attractive from both an architectural and a sustainability perspective (Block *et al.*, 2017).

2.1.1. Structural Behaviour

Although a gridshell behaves similarly to a continuous shell, it consists of a discretised lattice of interconnected beam elements. As a result, its structural behaviour differs from that of a continuous shell and depends strongly on the interaction between member stiffness, connection behaviour and overall geometry.

The efficiency of shell structures originates primarily from membrane action, whereby external loads are transferred predominantly through axial forces rather than bending moments. For an ideal gridshell geometry subjected to its design loading, this mechanism enables highly efficient use of material while limiting member bending. Classic examples include Hooke's catenary for self-weight loading and the parabolic arch for uniformly distributed loading.

In practice, however, fabrication tolerances, construction imperfections, asymmetric loading and architectural constraints inevitably introduce bending moments and second-order effects (Adriaenssens *et al.*, 2014). These effects become increasingly significant when the geometry deviates from its structurally optimal form or when the connections provide only limited restraint. Since gridshell members typically carry relatively large axial forces, even small deformations generate additional bending moments through second-order effects, making the accurate prediction of the structural response increasingly challenging (Williams, 2017). Consequently, inaccurate assumptions about nodal stiffness can lead to discrepancies between predicted and actual structural performance(Yuan *et al.*, 2019; Li *et al.*, 2025).

To prevent excessive in-plane deformation, quadrilateral gridshells require an additional stabilisation mechanism to resist in-plane shear deformation. This can be achieved through geometric triangulation, diagonal bracing, or sufficient in-plane rotational stiffness in the connections. Although these approaches differ fundamentally in their load-transfer mechanisms, they all increase the structure's in-plane stability.

2.1.2. Stiffness Influence

The stiffness of the connections plays an important role in determining how efficiently forces are transferred throughout a gridshell. Rather than acting as perfectly pinned or rigid joints, timber connections generally exhibit semi-rigid behaviour due to dowel bending, timber embedment deformation and local slip. Consequently, the rotational stiffness of the connections directly influences the redistribution of internal forces, the development of bending moments and the global stability of the structure.

Larsson demonstrated that the effectiveness of a connection cannot be evaluated independently of the structural members to which it is connected. Instead, the influence of the connection depends on its stiffness relative to the stiffness of the surrounding members(Figure 1). To express this relationship, Larsson proposed a dimensionless fixity parameter that relates the rotational stiffness of the connection to the bending stiffness of the connected members. This approach provides a consistent basis for comparing different gridshell configurations independently of their absolute dimensions.

(a) The spring is weak in comparison to beam

(b) The spring is strong in comparison to beam

Figure 1: Illustration of how the stiffness of a rotational spring relative to the connected beam governs the boundary behaviour, ranging from pinned to nearly fixed conditions(Larsson, 2018)

The interpretation of the fixity parameter differs throughout the literature. Eurocode 3 and Fan et al. propose stiffness ranges that distinguish between nominally pinned, semi-rigid and rigid connections. These classifications provide practical guidance for structural design but do not imply that perfectly rigid behaviour can be achieved in practice. Since every physical connection exhibits some degree of flexibility, the present research considers the fixity parameter as a continuous measure of rotational restraint rather than assigning discrete categories to specific stiffness ranges.

A further distinction must be made between rotational stiffness and rotational capacity. Fan et al. showed that these two properties govern different aspects of structural behaviour. The rotational stiffness determines the deformation of the connection within the linear-elastic range and therefore influences the global stiffness and stability of the gridshell. The rotational capacity, on the other hand, defines the maximum moment that can be transmitted before yielding or failure occurs(Figure 2). Increasing the rotational stiffness without a corresponding increase in rotational capacity may therefore lead to premature connection failure, whereas increasing the rotational capacity without increasing the rotational stiffness may result in a significant portion of the available connection capacity remaining unutilised.

An efficient connection design, therefore, requires that rotational stiffness and rotational capacity be developed in proportion to one another, ensuring that neither stiffness nor available strength governs prematurely.

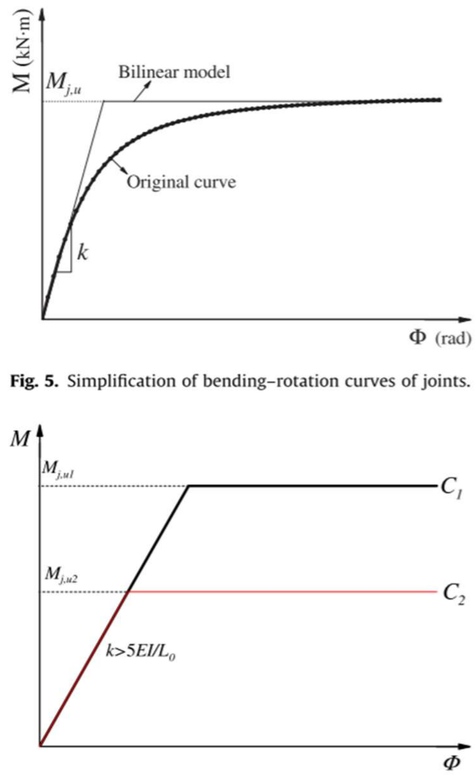

Figure 2: Nonlinear moment–rotation behaviour of semi-rigid connections and its bilinear approximation used to distinguish between rotational stiffness and rotational capacity(Fan et al., 2011).

2.2. Timber Gridshells

Historically, timber gridshells have been used to demonstrate the structural and architectural potential of timber construction. Well-known examples include the Mannheim Multihalle, the Downland Gridshell and, more recently, the Portcullis House Gridshell and Chiddingstone Orangery Gridshell. These projects illustrate how geometric form can be utilised to create lightweight structures with high structural efficiency while maintaining considerable architectural freedom.

Figure 3: Examples of contemporary timber gridshell structures: (left) Downland Gridshell, (centre) Portcullis House Gridshell and (right) Chiddingstone Orangery Gridshell(Pictures by Eward Culling Architects, Nathaniel Noir and Peter Hulbert Chartered Architect).

2.2.1. Orthotropy

Timber is an orthotropic material whose mechanical properties differ in the longitudinal, radial and tangential directions of the wood. This directional behaviour originates from the cellular structure of timber, in which the cellulose fibres aligned with the grain provide the majority of the stiffness and strength. At the same time, the surrounding lignin matrix primarily governs the behaviour perpendicular

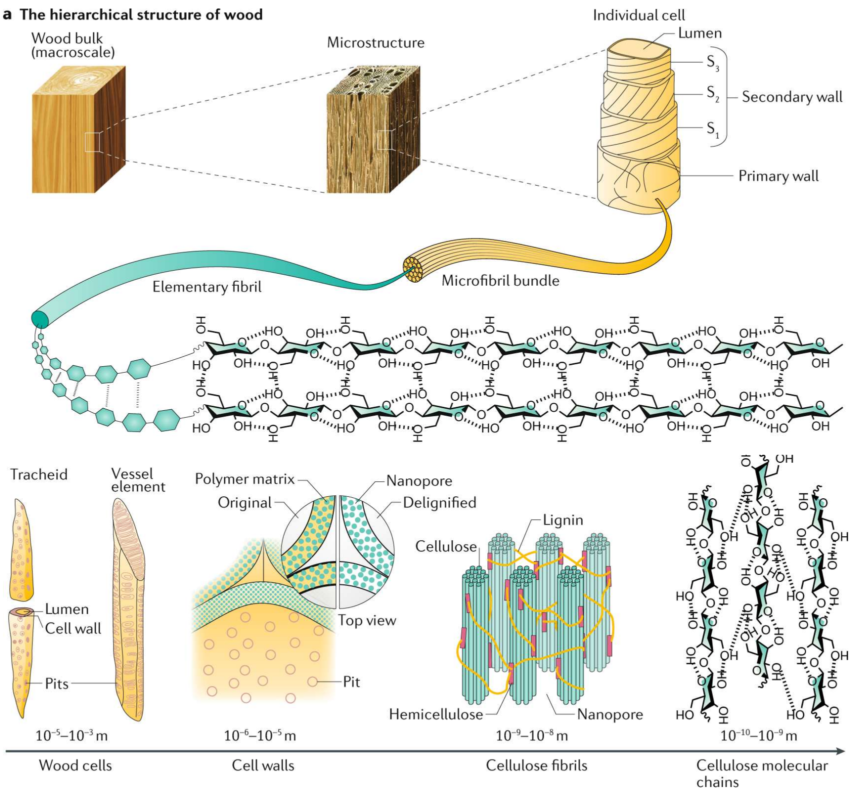

Figure 4: Hierarchical composition of timber across multiple length scales, illustrating the fibre structure responsible for the orthotropic stiffness and strength of wood(Chen et al., 2020)

to the grain (Chen et al., 2020). Consequently, both the stiffness and the strength of timber depend strongly on the orientation of the applied load relative to the grain direction.

Loading parallel to the grain mobilises the cellulose fibres, resulting in comparatively high stiffness and strength. In contrast, loading perpendicular to the grain is resisted primarily by the lignin matrix, leading to substantially lower stiffness, lower bearing strength and brittle tensile failure. This directional dependence is particularly important for dowel-type connections, where the force transferred by each dowel is generally oriented at a different angle relative to the timber grain. The load-to-grain angle, therefore, directly influences both the stiffness of the timber foundation and the embedment capacity of the connection.

Unlike steel, timber exhibits markedly different yielding behaviour in tension and compression. Tensile loading parallel to the grain results in an almost linear elastic response followed by relatively brittle fracture, providing only a limited opportunity for stress redistribution. Compression parallel to the grain, however, exhibits progressive crushing of the cellular structure after the elastic limit has been reached. This gradual collapse allows local stress redistribution and results in a nonlinear stress–strain response that a bilinear constitutive model approximates.

The bilinear approximation assumes an initial linear-elastic branch with stiffness equal to the elastic modulus, followed by a second branch with reduced tangent stiffness after the compressive yield stress is exceeded. Although the actual compressive response is nonlinear and depends on timber species, density and moisture content, the bi-linear approximation captures the dominant behaviour while remaining computationally efficient(Figure 5). Consequently, it is widely adopted in structural analyses where redistribution of compressive stresses is of interest.

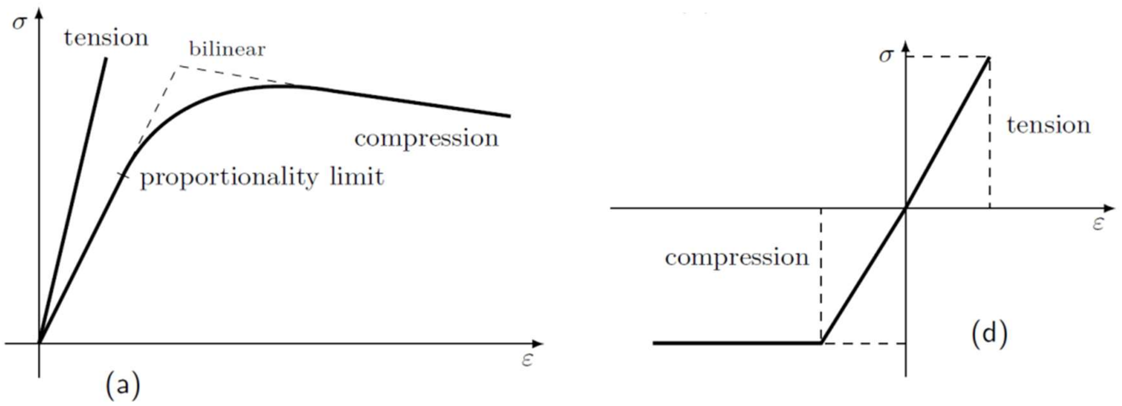

Figure 5: Stress–strain behaviour of timber loaded parallel to the grain in tension and compression, together with the bilinear approximation commonly adopted in structural analysis. The material exhibits limited plasticity in compression, whereas tensile failure remains predominantly brittle(Saad and Lengyel, 2022).

For the analytical formulation developed in this research, only the initial linear elastic range is considered, as the objective is to determine the rotational stiffness of the connection prior to the onset of material yielding. The bi-linear material response is therefore introduced only when discussing the transition from stiffness-controlled behaviour to capacity-controlled behaviour in the later stress-development analyses.

2.2.2. Density

Since timber is a natural material, considerable variability exists both between species and within individual species. Structural timber is therefore classified into strength classes based on its mechanical properties, which are strongly correlated with the mean density. In general, increasing timber density results in higher stiffness, greater bearing strength and increased compressive capacity. Higher densities may be achieved either by selecting naturally denser species or by artificial densification processes.

For dowel-type timber connections, density plays a particularly important role because it governs the stiffness of the surrounding timber supporting the fastener. Within beam-on-elastic-foundation models, this support is represented through the stiffness of the elastic foundation. Experimental work by Gikonyo, Schweigler and Bader demonstrated that the foundation stiffness may be expressed as a function of the mean timber density,

$$k_{\mathrm{el},0} = 0.1374\,\rho_m - 12.9 \tag{1}$$

$$k_{\mathrm{el},90} = 0.0922\,\rho_m - 18.2 \tag{2}$$

where $k_{\mathrm{el},0}$ and $k_{\mathrm{el},90}$ represent the elastic foundation stiffness parallel and perpendicular to the grain, respectively.

These relationships demonstrate the orthotropic nature of timber, as the increase in foundation stiffness with density differs between the longitudinal and transverse grain directions. Consequently, timber density governs not only the global stiffness of timber members but also the local stiffness of the embedment zone surrounding the dowel. For this reason, density is adopted throughout this research as the primary material parameter governing both the elastic foundation stiffness and the bearing resistance of the connection. Using density rather than discrete strength classes also enables the influence of the material properties to be investigated continuously, making it particularly suitable for parametric analyses.

2.2.3. Creep and Moisture

Timber exhibits pronounced time-dependent behaviour resulting from sustained loading and moisture content variations. Under constant loading, the material continues to deform over time due to creep, while changes in the surrounding humidity cause repeated swelling and shrinkage of the cellular structure. Both mechanisms reduce the effective stiffness of timber and increase long-term deformations.

For conventional timber structures, creep is primarily associated with serviceability considerations such as floor deflections and roof sagging. For slender shell structures and gridshells, however, creep may also affect the structure's global stability. Since gridshells rely on geometric stiffness and membrane action, the increase in deformation caused by creep can amplify second-order effects, reduce the stability margin and, in extreme cases, contribute to creep buckling(Stahl and Rosenkranz, 2024).

In structural design, these long-term effects are generally incorporated through creep factors or reduced elastic moduli rather than by explicitly modelling the time-dependent material behaviour. In the present research, creep is therefore considered only at the global structural level, by distinguishing among serviceability, ultimate, and characteristic stiffness. At the same time, the local analytical and numerical connection models represent the short-term linear-elastic response.

2.2.4. Structural Timber Products

The inherent variability of natural timber has led to the development of engineered timber products with improved mechanical performance and more consistent material properties. By laminating, grading, or reconstituting timber elements, defects such as knots, fibre deviation, and local imperfections are distributed more uniformly throughout the cross-section, resulting in higher characteristic strengths, improved dimensional stability, and reduced variability between individual members.

Among the most widely used engineered timber products are glued laminated timber (glulam) and laminated veneer lumber (LVL). Glulam consists of multiple timber laminations bonded together with the grain aligned in the longitudinal direction, allowing large structural members to be manufactured with relatively consistent mechanical properties. LVL is manufactured from thin veneers and generally provides even greater stiffness and strength due to its increased material homogeneity.

Particularly relevant to dowel-type connections are developments in densified timber products. Since the embedment stiffness and bearing resistance of timber increase with density, increasing material density directly improves both the rotational stiffness and the load-carrying capacity of dowel-type connections. Consequently, densified timber offers considerable potential for applications requiring high connection stiffness or compact connection geometries.

The increased consistency of engineered timber products reduces the influence of local material imperfections and enables more reliable prediction of structural behaviour. Consequently, engineered timber products are particularly well suited to applications in which stiffness, dimensional stability and predictable connection behaviour are of primary importance, including long-span timber gridshells.

2.3. Dowel-Type Timber Connections

2.3.1. Mechanics

Dowel-type timber connections transfer load through the interaction between dowel bending and timber embedment. When an external force is applied, the dowel bears against the surrounding timber while simultaneously deforming in bending. The resulting stiffness is therefore governed by the combined behaviour of the steel dowel and the timber embedment zone rather than by either component individually.

In bolted connections, an additional contribution may arise from rope effect, whereby axial tension within the fastener is mobilised through the bearing action of the bolt head and washer. For tightly fitted smooth dowels, however, this contribution is generally negligible, and the connection behaviour is governed primarily by the interaction between timber embedment and dowel bending.

2.3.2. Previous Research

Research on dowel-type timber connections has predominantly focused on ultimate capacity and failure mechanisms. Consequently, most experimental programmes investigate the bearing resistance and slip behaviour of individual dowels or bolt groups subjected to monotonic tensile loading. Rotational stiffness is therefore commonly evaluated only as a secondary outcome of these investigations.

Rahim et al. investigated the determination of the slip modulus from experimental and numerical analyses, demonstrating considerable discrepancies between the experimentally determined stiffness and the values prescribed by Eurocode 5 (Rahim, Raftery and Quenneville, 2018). Wang et al.

extended this work through analytical and experimental investigations of rotational timber-to-timber connections, demonstrating good agreement between analytical predictions and full-scale testing (Wang *et al.*, 2021). Tao et al. subsequently investigated knife-plate connections using detailed numerical models and likewise reported stiffnesses exceeding those predicted by Eurocode 5 (Tao *et al.*, 2021). However, these studies primarily considered single-fastener behaviour and therefore provide only limited insight into the influence of embedment length, bolt-group geometry and distributed load transfer on the rotational stiffness of multi-dowel knife-plate connections.

Chen et al. investigated rotational timber connections between beam elements (Chen *et al.*, 2022). Although their work provides valuable insight into rotational connection behaviour, the governing deformation mechanism differs from that of knife-plate connections, as the observed rotation is dominated by rocking and timber crushing rather than by distributed dowel embedment.

2.3.3. Eurocode 5 Stiffness Formulation

Within structural design, the rotational stiffness of dowel-type connections is commonly represented through the slip modulus K_{ser}, which forms the basis of the Eurocode 5 stiffness formulation. Current engineering practice generally represents connection stiffness using the Eurocode 5 slip modulus K_{ser},

$$K_{ser} = \frac{\rho_m^{1.5} d}{23} \tag{3}$$

which relates the slip stiffness to the mean timber density and fastener diameter. The expression is empirically calibrated from experimental testing and is intended to provide a practical design-oriented estimate of connection stiffness.

The experimental determination of K_{ser}prescribed by the European Committee for Standardisation is based on the secant stiffness measured between 10% and 40% of the ultimate load obtained from monotonic loading tests(Figure 6). Consequently, the slip modulus represents only the initial linear-elastic behaviour of the connection rather than its complete nonlinear load–displacement response.

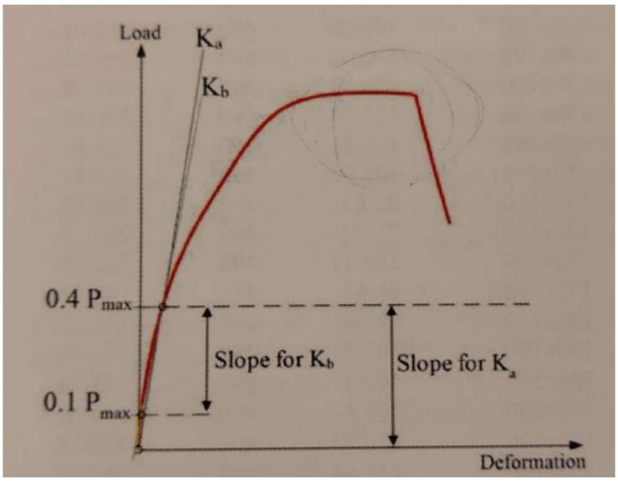

Figure 6: Typical load–deformation response of a dowel-type timber connection under monotonic loading. The serviceability slip modulus $K_b$is determined from the secant stiffness between 10% and 40% of the maximum load, while $K_a$represents the initial tangent stiffness(Rahim, Raftery and Quenneville, 2018).

Although Eurocode 5 provides a practical and widely accepted engineering formulation, several parameters known to influence the rotational stiffness of dowel-type connections are not explicitly represented. In particular, embedment length, distributed embedment behaviour, plate stiffness and bolt-group geometry are absent from the empirical expression. Consequently, the formulation is well-suited for routine structural design but offers only limited insight into how individual material and geometric parameters affect the rotational stiffness of the connection. These limitations motivate the analytical and numerical modelling approaches discussed in the following chapter.

Unlike the connection capacity, which governs the maximum transferable load, the slip modulus represents only the initial stiffness of the connection and therefore primarily influences the serviceability behaviour and the global structural response.

2.4. Modelling of Timber Connections

The semi-rigid behaviour of dowel-type timber connections cannot be represented adequately using simple empirical stiffness expressions or physical tests alone. Consequently, a range of analytical and numerical modelling approaches has been developed to capture the interactions among dowel bending, timber embedment, and local deformation mechanisms. Sandhaas et al. provide a comprehensive overview of the currently available modelling strategies, ranging from simplified beam models to fully nonlinear three-dimensional contact analyses (Sandhaas, Munch-Andersen and Dietsch, 2018). Each approach represents a trade-off between physical accuracy, computational effort and analytical transparency.

2.4.1. Analytical Modelling

Analytical modelling provides an efficient means of investigating the influence of individual material and geometric parameters on the behaviour of dowel-type timber connections. Compared with detailed numerical simulations, analytical formulations offer greater physical insight into the governing deformation mechanisms while requiring only limited computational effort. Consequently, they are particularly well-suited to parametric studies in which large numbers of connection configurations must be evaluated.

The derivation of rotational spring stiffness is commonly based on classical beam theory. Euler–Bernoulli beam theory provides analytical relationships among the applied loading, member deformation, and rotational restraint, making it well-suited to deriving equivalent rotational spring stiffnesses for beam connections and supports.

One of the most widely adopted analytical approaches is the beam-on-elastic-foundation (BOEF) model, in which the dowel is represented as a beam supported by a continuous elastic foundation representing the surrounding timber. The governing differential equation describes the interaction between dowel bending and timber embedment.

$$EI\frac{d^4u}{dx^4} + k_y u = p(x) \tag{4}$$

where EI is the bending stiffness of the dowel, k_y is the embedment stiffness of the surrounding timber and $p(x)$ is the applied distributed load.

The governing differential equation underpins many analytical formulations of dowel-type timber connections, as it directly couples the fastener's bending stiffness to the embedment stiffness of the surrounding timber.

The beam-on-elastic-foundation formulation is based on Winkler foundation theory, in which the surrounding timber is represented by a continuous distribution of independent linear elastic springs. One of the classical references for solving beams resting on elastic foundations is the work of Hetényi, who presents analytical solutions for a wide range of loading and boundary conditions (Hetényi, 1946).

More recent developments have extended the classical BOEF formulation to represent timber connections better. Sandhaas et al. (2018) provide a comprehensive overview of beam-on-elastic-foundation models and demonstrate their suitability for modelling dowel-type connections. Gikonyo, Schweigler and Bader (2025) developed experimentally calibrated relationships for the embedment stiffness parallel and perpendicular to the grain, allowing the orthotropic behaviour of timber to be incorporated directly into beam-on-elastic-foundation models. Tao et al. (2021) similarly employed beam-on-elastic-foundation formulations to investigate the influence of geometric parameters on the stiffness of steel–timber knife-plate connections.

Collectively, these studies demonstrate that beam-on-elastic-foundation models provide an effective compromise between physical realism and analytical simplicity. By explicitly representing dowel bending and timber embedment, they enable investigation of the influence of individual geometric and material parameters on the rotational stiffness of timber connections using exact analytical solutions to the governing differential equations.

2.4.2. Numerical Modelling

Advances in finite element analysis have enabled increasingly detailed numerical representations of timber connections. Compared with analytical formulations, numerical models permit more realistic representations of complex geometries, orthotropic material behaviour and local stress concentrations. However, this increased accuracy is accompanied by substantially greater computational effort and increased model complexity.

Sandhaas et al. classify timber connection models according to their level of detail, ranging from simplified beam-element representations to fully three-dimensional solid models incorporating nonlinear contact behaviour. The available modelling approaches differ primarily in how the timber embedment behaviour around the dowel is represented and in the extent to which geometric and material nonlinearities are included.

A common challenge in modelling dowel-type timber connections is accurately representing the local embedment behaviour around the dowel. Using only the bulk orthotropic material properties of timber does not adequately reproduce the local deformation mechanisms that develop within the embedment zone. Consequently, various modelling approaches have been proposed to represent this local behaviour better. Kekeliak et al. introduced a reduced-stiffness embedment zone surrounding the dowel hole, thereby concentrating the local deformation within the timber immediately adjacent to the fastener (Kekeliak, An and Gocál, 2013). Sandhaas and Van de Kuilen proposed comparable approaches in which local nonlinear material behaviour is introduced around the dowel, while the remaining timber volume remains linear elastic (Sandhaas and Van De Kuilen, 2013)Other simplifications go so far as to model the remaining beam as isotropic.

An alternative strategy was proposed by Fu et al., who instead modified the stiffness distribution within a timber dowel itself, rather than the surrounding timber (Fu *et al.*, 2024). Although these different modelling strategies alter the representation of the local embedment behaviour, they all seek to reproduce the experimentally observed interaction between dowel bending and timber deformation while maintaining computational efficiency.

An alternative approach is the use of three-dimensional solid models with nonlinear contact. Skotny and Hidalgo explain that nonlinear contact elements provide a more realistic representation of the bearing interaction between the dowel and the surrounding timber, particularly for rotationally loaded connections (Skotny and Hidalgo, 2018). As a result, the transfer of forces across the shear interface can be modelled more accurately than with simplified connection models, albeit with a substantially higher computational cost.

A further consideration concerns the constitutive material models adopted for timber. Many detailed numerical studies employ nonlinear orthotropic material models, often based on yield criteria such as the Hill criterion, to reproduce the nonlinear embedment behaviour observed experimentally. However, these constitutive models are not available in all finite element software packages and require extensive material calibration. Consequently, an important research question remains whether simplified linear-elastic orthotropic models can reproduce the stiffness behaviour of dowel-type timber connections with sufficient accuracy for engineering design applications.

2.5. Definitions and Limitations

2.5.1. Scope of the Research

The research question defines the overall objective of this study, but also contains several terms whose interpretation influences the scope of the investigation. To clearly establish the boundaries of the research, the principal concepts and assumptions are defined below.

How do material and geometric parameters influence the rotational stiffness of semi-rigid steel–timber knife-plate connections, and how does this stiffness influence the global structural behaviour of unbraced timber gridshells?

Leaves some potential for misinterpretation of what is covered and what is not. For that reason, the most important terms are explained as follows:

Within this research, the "material parameters" comprise the timber embedment stiffness, timber density and dowel bending stiffness. The investigated "geometric parameters" include the dowel diameter, embedment length, bolt-group geometry and the dimensions of the timber member that define the feasible connection layout. Together, these parameters govern the rotational stiffness developed by the semi-rigid connection.

The term "rotational stiffness of knife-plate connections" refers specifically to steel plates inserted into the end of a timber member and connected using dowels or bolts. The rotational stiffness represents the relationship between the applied moment and the resulting rotation within the linear-elastic range. The combined effects of dowel bending, timber embedment, and connection geometry govern it.

Within this research, "global structural behaviour" refers to the influence of connection stiffness on the deformation, internal force distribution and stability of the gridshell under both serviceability and ultimate loading conditions.

The focus on "unbraced timber gridshells" is deliberate. In engineering, insufficient in-plane stiffness is commonly compensated for by introducing diagonal bracing or triangulating the grid. Although these measures improve structural stability, they also reduce the direct influence of the connection stiffness on the global structural response. By considering unbraced quadrilateral gridshells, the influence of the semi-rigid knife-plate connections can therefore be isolated and evaluated more clearly.

2.5.2. Research Boundaries

To ensure a focused investigation, the following assumptions and exclusions apply:

- Triangular gridshells are not considered because their inherently higher in-plane stiffness results in fundamentally different structural behaviour compared with quadrilateral gridshells (Isufi F., 2021).
- Axial spring stiffness is excluded following the findings of Larsson (2018), which demonstrated a negligible influence on the investigated structural behaviour.
- Moisture variation is assumed to remain constant under typical indoor service conditions (Holzer, Loferski and Dillard, 1988; NEN 1995, 2014).
- Clamped support conditions are excluded because the rotational restraint at the supports generates additional boundary moments that alter the internal force distribution within the structure.
- Experimental validation falls outside the scope of this research.
- The analytical and numerical formulations are limited to the linear-elastic material response. Consequently, nonlinear connection behaviour, including progressive embedment yielding, damage development and failure progression, is not modelled.

3. Global Structural Behaviour

3.1. Global Modelling Methodology

The objective of the global analysis is to establish the relationship between connection stiffness and the structural behaviour of timber gridshells. To achieve this, a dimensionless stiffness formulation is first derived and subsequently implemented within a parametric numerical model. This approach allows the influence of semi-rigid connection behaviour to be evaluated independently of the absolute member dimensions.

The global analytical model is used to define stiffness parameters that can be implemented consistently within the numerical gridshell model. Since the structural response of a beam or gridshell member depends not only on the absolute spring stiffness but also on the relative stiffness and length of the connected members, the spring stiffness is expressed in dimensionless form and scaled relative to the maximum rotational stiffness of the member. This allows pinned, semi-rigid, and rigid connection conditions to be evaluated within a unified parametric framework.

The global behaviour is governed by two primary stiffness components, as can be seen in Figure 1:

1. The in- and out-of-plane rotational stiffness of the connections.
2. The bending stiffness of the connected members.

Boundary stiffness is not considered further in this research because it is not an independent property of the connection. Instead, it is governed by the combined stiffness of the supporting members, shell geometry, and support configuration. Consequently, changes in boundary stiffness cannot be directly related to the design of the steel–timber connection, which forms the primary focus of this study.

Similarly, axial connection stiffness is not introduced as a separate parameter. Although an equivalent dimensionless axial stiffness could be defined relative to the member stiffness EA/L, the investigated steel–timber connections remain comparatively stiff in the axial direction. Consequently, axial shortening has only a limited influence on the global structural response compared with rotational flexibility. Furthermore, reducing the axial stiffness to zero would result in a physically disconnected structure rather than a meaningful semi-rigid connection.

The rotational stiffness parameter is derived from the response of a beam with rotational springs at its ends.

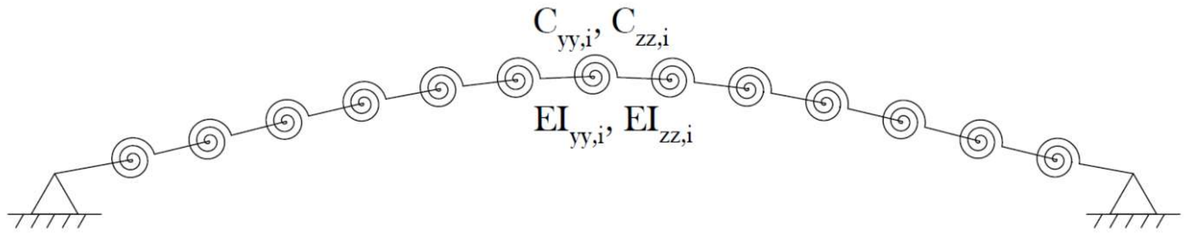

Figure 7: Simplified visualisation of the global analysis model

The global numerical model is generated using a Grasshopper script and analysed in RFEM6. The gridshell geometry is defined as a two-way spanning parabolic surface. The primary geometric parameters are the span, base dimensions, rise, grid density, and grid orientation. This parametric setup allows different gridshell configurations to be evaluated using a consistent modelling procedure.

Two grid orientations are considered: orthogonal and diagonal, seen in Figure 9. Both grid layouts are projected onto the same parabolic reference surface to ensure that differences in structural response are attributable to grid orientation and stiffness conditions rather than to differences in global form.

The gridshell surface is discretised by subdividing the grid cells. This subdivision improves the planarization of load surfaces and provides greater control over the spatial distribution of applied loads. The resulting model is used both for the parametric analysis and for the later case study.

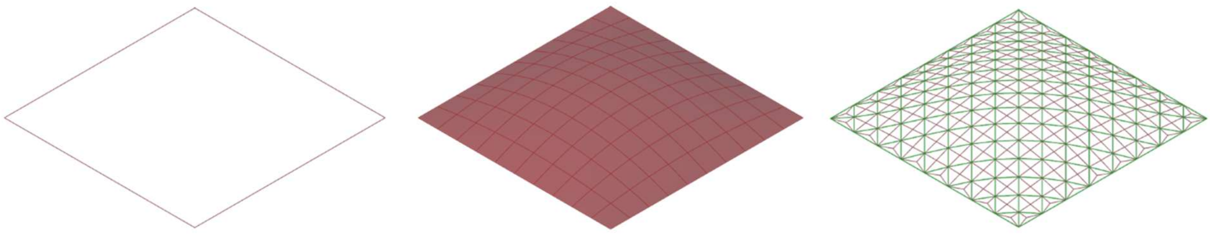

Figure 8: Parametric geometry generation for RFEM6 export. From left to right: 10 × 10 m base geometry, parabolic reference surface, and discretised surface with grid members and planar load surfaces.

The reference gridshell geometry used in the analysis has plan dimensions of 10 × 10 m and a grid spacing of 0.643 × 0.643 m diagonally and 0.625 × 0.625 orthogonally. All members were modelled as C24 timber beams with a cross-section of 100 × 50 mm, rotated to match the surface normal at midspan. A rise of 1200mm is consistent for both grids.

3.1.1. Structural Idealisation and Boundary Conditions

The gridshell members are modelled as beam elements possessing both bending and axial stiffness. Member intersections are represented by a central node connected to the adjacent beam elements through rotational springs, depending on the stiffness condition being evaluated. The central node is idealised as an infinitely stiff region of zero length, as shown in Figure 10. This allows the rotational stiffness of the connection to be controlled explicitly without introducing additional member length or unintended local flexibility.

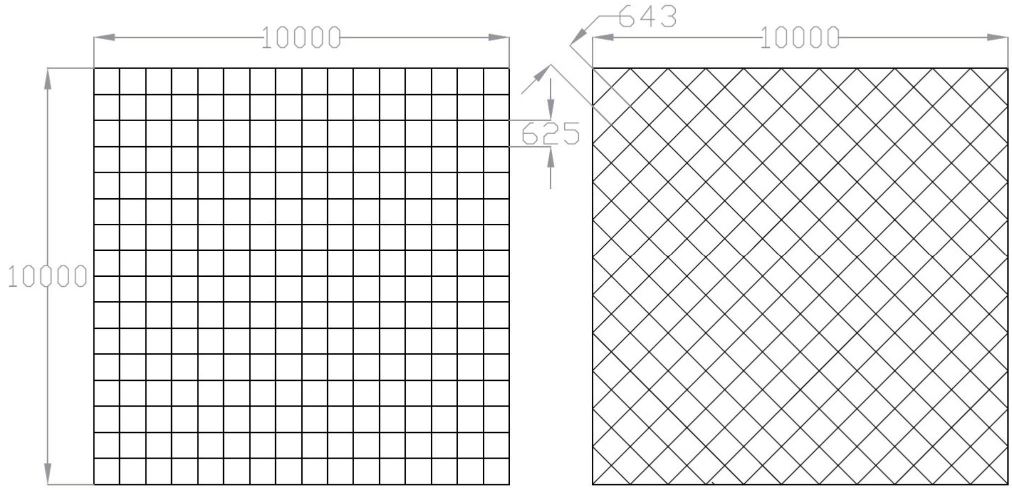

Figure 9: Orthogonal and Diagonal grid configurations

All support nodes are fully restrained against translation, thereby removing the influence of support flexibility from the analysis and allowing the structural response to be attributed solely to the investigated rotational connection stiffness. The connection between the support points and the timber members is modelled as hinged to avoid unintended moment transfer to the foundation.

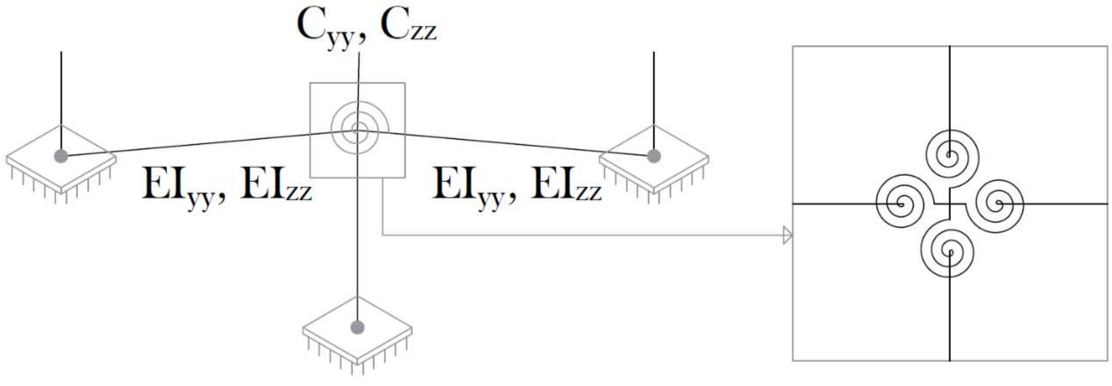

Figure 10: RFEM6 implementation of the global stiffness model, showing the discretisation of nodal in- and out-of-plane rotational stiffness and boundary restraint.

To prevent the development of artificial torsional restraint within the structural model, the member end releases are defined such that torsional moments cannot be transferred between adjacent elements. Consequently, the global response remains governed by the prescribed in- and out-of-plane rotational spring stiffnesses rather than by unintended torsional stiffness within the member network.

This modelling approach ensures that the observed structural behaviour can be attributed directly to the investigated connection and boundary stiffness parameters.

3.1.2. Load Assumptions

The structure is treated as an inaccessible roof. The applied loads, therefore, consist of self-weight, roof finishing loads, snow loads, and wind loads. The structural self-weight is updated parametrically according to the member dimensions used in each model.

Since the final roof build-up is not defined at this stage, an additional permanent surface load of 1.0 kN/m² is applied to represent the non-structural roof build-up.

Seven load patterns are defined based on Eurocode 1 and can be seen in Figure 11. These include wind-pressure and suction zones, uniformly distributed snow, and asymmetric snow-accumulation patterns. The snow pile cases are represented by spatially varying load distributions, with peak values at the centre of the accumulation zone.

The characteristic surface loads used in the model are summarised below in Table 1.

Load	Zone	Factor	Force (kN/m²)
Wind	A	0.19	0.13
	B	-0.71	0.49
	C	-0.4	0.27
Snow	$\mu_{0,8}$	0.8	0.56
	$0.5\mu_4$	0.69	0.48
	μ_4	1.38	0.97
Permanent load	-	-	1

Table 1: Load zones, factors, and characteristic loads used in the global analysis.

The load cases are combined in accordance with Eurocode 0. For the ultimate limit state, the following simplified combination is used:

$$1.35 \cdot G_k + 1.5 \cdot Q_k \tag{5}$$

For serviceability evaluation, creep effects due to permanent loading are included using:

$$\left(1 + k_{def}\right) \cdot G_k + 1 \cdot Q_k \tag{6}$$

Creep is therefore introduced through the load combination rather than by modifying the Young's modulus. This approach simplifies the transfer of results between Grasshopper, RFEM6, and the analytical post-processing workflow.

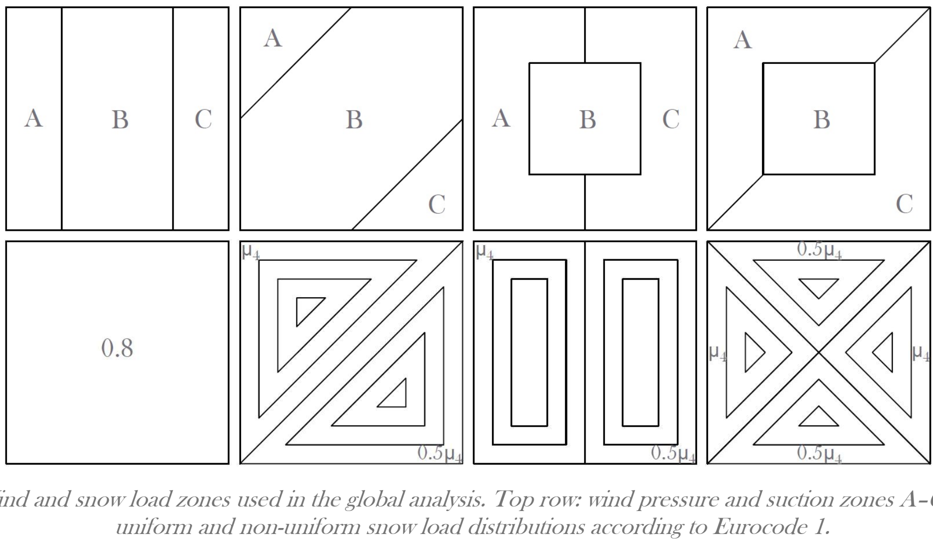

Figure 11: Wind and snow load zones used in the global analysis. Top row: wind pressure and suction zones A–C. Bottom row: uniform and non-uniform snow load distributions according to Eurocode 1.

3.2. Parametric Stiffness Formulation

The equivalent rotational spring stiffness used in the global model is derived using Euler–Bernoulli beam theory rather than the formulation proposed by Larsson. Although both approaches aim to represent the same physical behaviour, the beam deflection expression presented by Larsson does not satisfy the governing boundary conditions used in the present research. A complete derivation based on classical beam theory is therefore adopted.

3.2.1. Beam Equation and Displacement Function

The rotational stiffness parameter is derived using an Euler-Bernoulli beam subjected to a uniformly distributed transverse load. The governing differential equation is:

$$\frac{d^2}{dx^2}\left(EI\frac{d^2w(x)}{dx^2}\right) = q_z \tag{7}$$

where E is the Young's modulus, I is the second moment of area, $w(x)$ is the transverse displacement, and q_z is the uniformly distributed load.

Assuming constant flexural rigidity along the beam length, the equation simplifies to:

$$\frac{d^4w(x)}{dx^4} = \hat{q}_z, \qquad \hat{q}_z = \frac{q_z}{EI} \tag{8}$$

Integrating four times yields the general displacement function:

$$w(x) = \frac{\hat{q}_z x^4}{24} + \frac{C_1x^3}{6} + \frac{C_2x^2}{2} + C_3x + C_4$$

For notational clarity, the integration constants are rewritten as:

$$A_1 = \frac{C_1}{6}, \qquad A_2 = \frac{C_2}{2}, \qquad A_3 = C_3, \qquad A_4 = C_4$$

Giving:

$$w(x) = \frac{\hat{q}_z x^4}{24} + A_1x^3 + A_2x^2 + A_3x + A_4$$

The first and second derivatives describe beam rotation and curvature, respectively:

$$\frac{dw(x)}{dx} = \frac{\hat{q}_z x^3}{6} + 3A_1x^2 + 2A_2x + A_3$$

$$\frac{d^2w(x)}{dx^2} = \frac{\hat{q}_z x^2}{2} + 6A_1x + 2A_2$$

These expressions form the basis of the pinned, semi-rigid, and fixed boundary-condition formulations. The boundary conditions associated with these modes can be seen below in Figure 12.

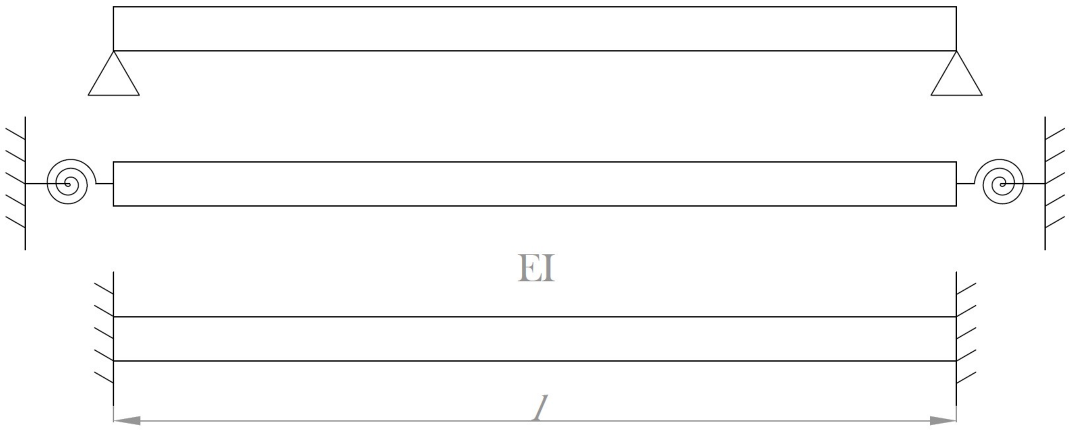

Figure 12: Idealised hinged, semi-rigid and fixed beam systems

3.2.2. Pinned Beam Formulation

The pinned beam case represents the lower-bound stiffness condition. In this case, vertical displacement and bending moment are zero at both supports. The boundary conditions are:

$$w_h(0) = 0$$

$$\frac{d^2 w_h(0)}{dx^2} = 0$$

$$w_h(l) = 0$$

$$\frac{d^2 w_h(l)}{dx^2} = 0$$

Solving the integration constants gives the displacement function:

$$w_h(x) = \frac{\hat{q}_z}{24} x^4 - \frac{\hat{q}_z l}{12} x^3 + \frac{\hat{q}_z l^3}{24} x \tag{9}$$

This expression represents the behaviour of a beam with no rotational restraint at the supports.

3.2.3. Semi-rigid Beam Formulation

The semi-rigid case represents the beam ends using rotational springs with stiffness C_r. The end moment is therefore related to the end rotation through the rotational spring. The boundary conditions are:

$$w_s(0) = 0$$

$$-EI \frac{d^2 w_s(0)}{dx^2} + C_r \frac{dw_s(0)}{dx} = 0$$

$$w_s(l) = 0$$

$$EI \frac{d^2 w_s(l)}{dx^2} + C_r \frac{dw_s(l)}{dx} = 0$$

Solving the integration constants with these boundary conditions yields:

$$w_s(x) = \frac{\hat{q}_z x^4}{24} - \frac{\hat{q}_z l}{12} x^3 + \frac{\hat{q}_z l^2 C_r l}{24(C_r l + 2EI)} x^2 + \frac{\hat{q}_z l^3 EI}{12(C_r l + 2EI)} x \tag{10}$$

The dimensionless fixity parameter is introduced as:

$$\alpha = \frac{C_r l}{C_r l + 2EI} \tag{11}$$

Or equivalently:

$$\alpha = \frac{1}{1+\gamma}, \qquad \gamma = \frac{2EI}{C_r l} \tag{12}$$

Substituting this parameter into the displacement expression gives:

$$w_s(x) = \frac{\hat{q}_z}{24} x^4 - \frac{\hat{q}_z l}{12} x^3 + \alpha \cdot \frac{\hat{q}_z l^2}{24} x^2 + \alpha\gamma \cdot \frac{\hat{q}_z l^3}{24} x \tag{13}$$

The parameter α, therefore, describes the degree of rotational restraint relative to the flexural stiffness of the beam. A value of $\alpha = 0$ represents a pinned support, while $\alpha = 1$ corresponds to a fully fixed support.

3.2.4. Fixed Beam Formulation

The fixed beam case is included as the upper-bound stiffness condition. The vertical displacement and rotation are zero at both supports:

$$w_r(0) = 0$$

$$\frac{dw_r(0)}{dx} = 0$$

$$w_r(l) = 0$$

$$\frac{dw_r(l)}{dx} = 0$$

The corresponding displacement function is:

$$w_r(x) = \frac{\hat{q}_z}{24} x^4 - \frac{\hat{q}_z l}{12} x^3 + \frac{\hat{q}_z l^2}{24} x^2 \tag{14}$$

This function is recovered from the semi-rigid formulation when $\alpha = 1$. The pinned and fixed cases, therefore, provide limiting checks for the semi-rigid expression.

3.2.5. Rotational Spring Stiffness as a Function of Fixity

Because the rotational stiffness required for a connection depends on the stiffness of the connected members, expressing the spring stiffness directly in units of kNm/rad is not sufficient for a general parametric study. Instead, the stiffness is normalised with respect to the flexural stiffness of the member, resulting in the dimensionless fixity parameter α. This enables the same connection condition to be represented consistently for members of different dimensions and stiffness.

The fixity parameter can be rearranged to determine the rotational spring stiffness required to obtain a prescribed degree of fixity. For a fixity of 0 (a hinge), the rotational stiffness of the beam is multiplied by 0, creating a hinge. Moreover, for alpha, the boundary stiffness is much greater than that of the beam, creating a hinge. The resulting rotational spring stiffness is proportional to the flexural stiffness of the connected member. Consequently, the fixity parameter represents the degree of rotational restraint relative to the stiffness of the beam rather than an absolute spring stiffness. Figure 13:

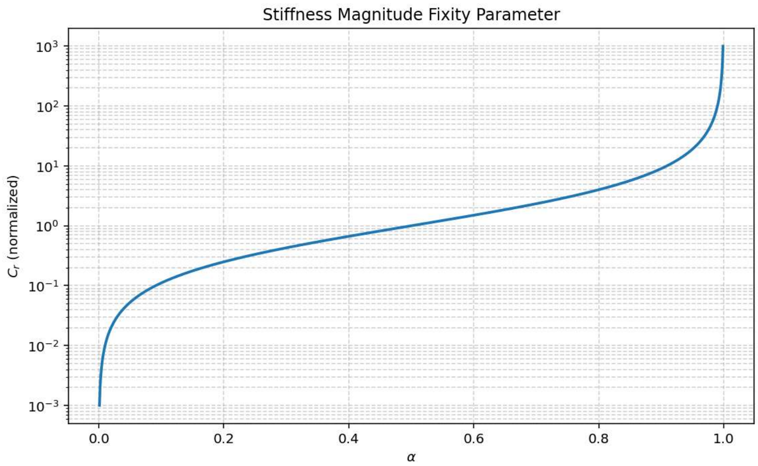

Figure 13: Amplification factor as a function of the fixity parameter α

$$C_r = \frac{\alpha}{1-\alpha} \cdot \frac{2EI}{l} \tag{15}$$

This expression is used to assign rotational spring stiffnesses in the global numerical model. It ensures that the stiffness of the connection is scaled relative to the bending stiffness and length of the beam element to which it is connected.

The moment expressions at the beam ends further clarify the interpretation of α. For the fixed case, the end moment is:

$$M_r(0) = M_r(l) = \frac{\hat{q}_z l^2}{12}$$

For the semi-rigid case, the end moment is:

$$M_s(0) = M_s(l) = \alpha \frac{\hat{q}_z l^2}{12}$$

The semi-rigid end moment is therefore a scaled version of the fixed-end moment:

$$M_s = \alpha M_r$$

This confirms that α can be interpreted as a moment fixity ratio. The formulation follows the approach proposed by Larsson for evaluating node-stiffness effects in gridshells (Larsson, 2018). In the present derivation, the rotational spring contribution is explicitly included in the beam boundary conditions to ensure consistency between the displacement field, end moment, and stiffness parameter.

For reference, the three displacement functions are collected below w_h for hinged, w_s for semi-rigid and w_r for rigid:

$$w_h(x) = \frac{\hat{q}_z}{24}x^4 - \frac{\hat{q}_z l}{12}x^3 + \frac{\hat{q}_z l^3}{24}x \tag{9}$$

$$w_s(x) = \frac{\hat{q}_z}{24}x^4 - \frac{\hat{q}_z l}{12}x^3 + \alpha \cdot \frac{\hat{q}_z l^2}{24}x^2 + \alpha\gamma \cdot \frac{\hat{q}_z l^3}{24}x \tag{13}$$

$$w_r(x) = \frac{\hat{q}_z}{24}x^4 - \frac{\hat{q}_z l}{12}x^3 + \frac{\hat{q}_z l^2}{24}x^2 \tag{14}$$

3.3. Global Behaviour and Stiffness Requirements

3.3.1. Diagonal Grid

The parametric analyses contain isolated duplicate datasets resulting from numerical non-convergence, in which the solver retains the previously converged solution. These duplicate results were identified through sequential comparison and removed from the dataset before post-processing. The resulting gaps were subsequently filled using linear interpolation to preserve the continuity of the contour plots. Converged solutions are indicated by the plotted data points, whereas unconverged regions remain unpopulated.

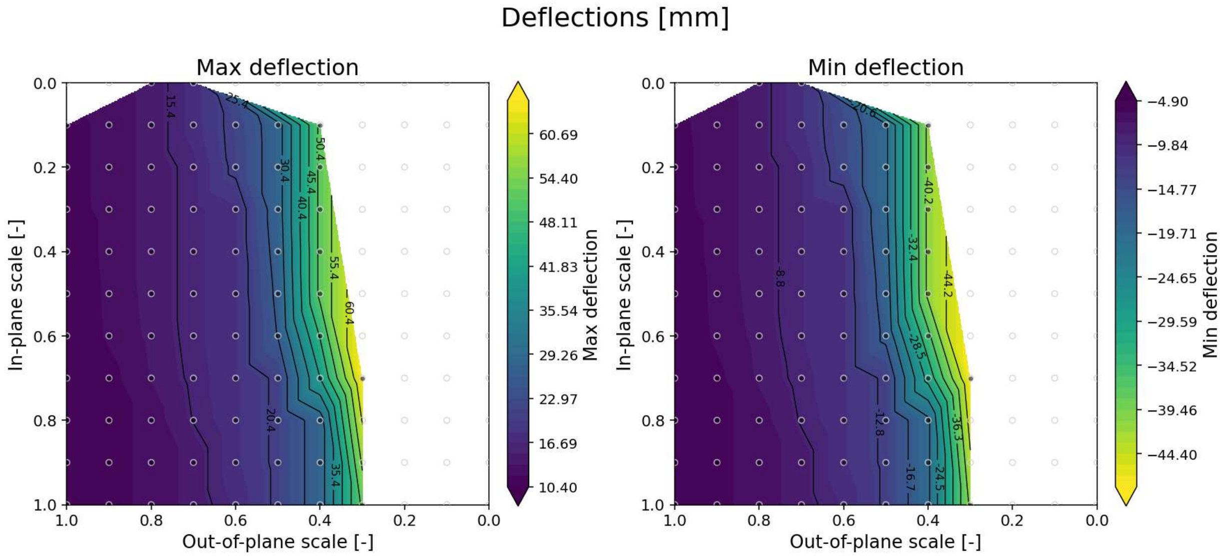

Figure 14: Maximum and minimum deflections of the diagonal gridshell as a function of the in-plane and out-of-plane fixity parameters. The predominantly vertical contour lines indicate that the global deflection is governed primarily by the out-of-plane rotational stiffness.

The deflection response, seen in Figure 14, it demonstrates a pronounced sensitivity to reductions in the out-of-plane rotational stiffness. As the out-of-plane fixity decreases, both the maximum and minimum deflections increase rapidly, indicating a substantial reduction in the gridshell's global stiffness. In contrast, the influence of the in-plane rotational stiffness remains comparatively limited throughout most of the investigated parameter range. Only when the in-plane stiffness approaches a fully hinged condition does the structural response become increasingly sensitive, thereby reducing the converged solution space.

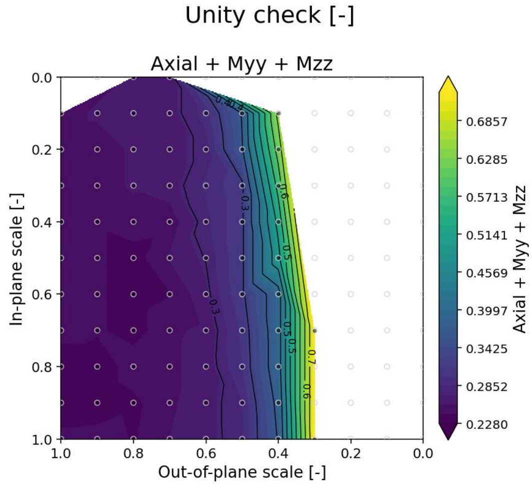

Figure 15: Governing member utilisation resulting from the combined axial force and in- and out-of-plane bending moments as a function of the in-plane and out-of-plane fixity parameters for the diagonal grid variant.

The governing member utilisation(Figure 15) is controlled by the combined action of the axial force and the in- and out-of-plane bending moments. The resulting unity checks follow trends comparable to those observed for the displacement response. Decreasing the out-of-plane rotational stiffness results in a rapid increase in member utilisation as second-order effects produce progressively larger bending moments. Although the influence of the in-plane rotational stiffness is less pronounced, removing the in-plane restraint further reduces the available stability margin and increases the likelihood of numerical non-convergence.

Interestingly, introducing a limited degree of in-plane flexibility increases the region of converged solutions compared with a fully hinged in-plane connection. This suggests that a small amount of rotational restraint is sufficient to stabilise the global response. In contrast, complete release of the in-plane rotational stiffness rapidly reduces the available stability margin.

The development of the internal forces seen in Figure 16 confirms these observations. The axial force remains relatively constant over the investigated stiffness range, whereas the bending moments and shear forces increase significantly as the out-of-plane rotational stiffness decreases. The largest changes occur in the out-of-plane bending moment, indicating that reductions in rotational restraint primarily influence the global response by increasing bending rather than by significant redistribution of axial forces. Torsional moments remain comparatively small throughout the investigated parameter range.

The limited influence of the in-plane rotational stiffness suggests that the investigated diagonal gridshell derives most of its stability from its resistance against out-of-plane bending. Consequently, reducing the out-of-plane rotational restraint directly diminishes the shell's ability to maintain its curved geometry, leading to increased second-order effects and larger bending moments.

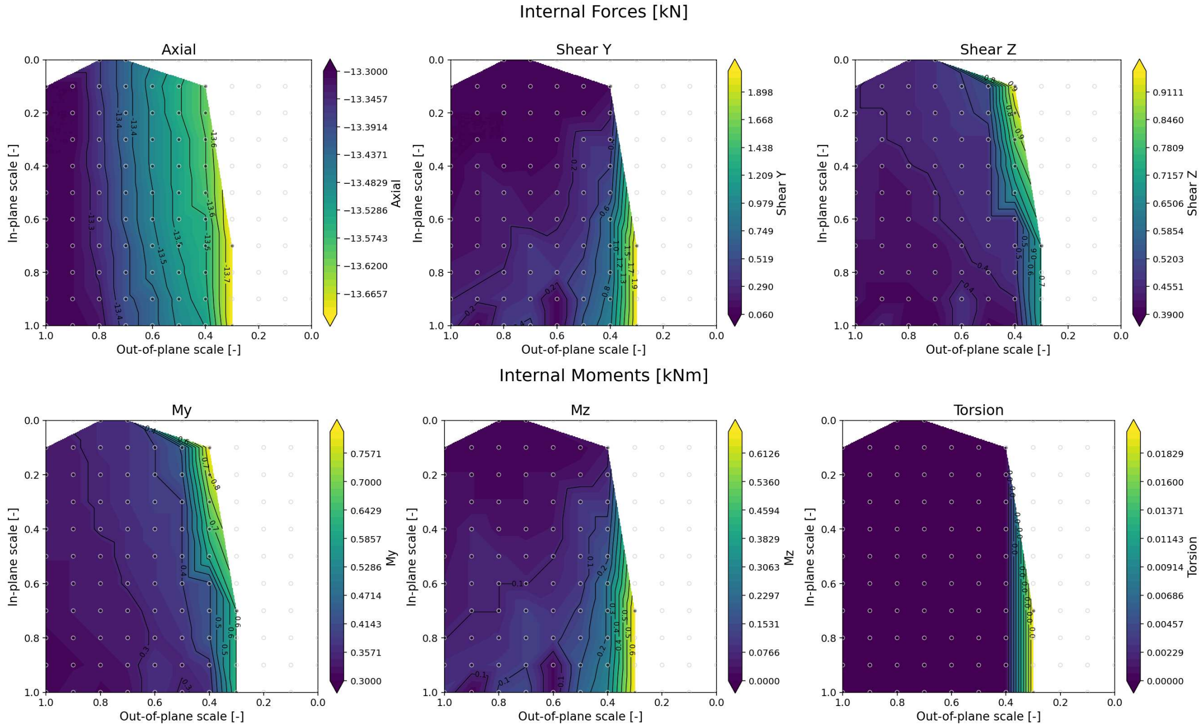

Figure 16: Development of the governing internal forces and moments of the diagonal gridshell over the investigated in-plane and out-of-plane stiffness range. Most response quantities are governed primarily by the out-of-plane rotational stiffness, whereas the influence of the in-plane stiffness remains comparatively small.

3.3.2. Orthogonal Grid

The orthogonal gridshell exhibits a substantially different response from the diagonal configuration. The converged solution space is bounded by a pronounced diagonal transition, seen in Figure 17, indicating that stable behaviour depends on a combination of the in-plane and out-of-plane rotational stiffness. Compared with the diagonal gridshell, which is governed predominantly by the out-of-plane stiffness, the orthogonal configuration shows a much stronger dependence on the in-plane rotational restraint.

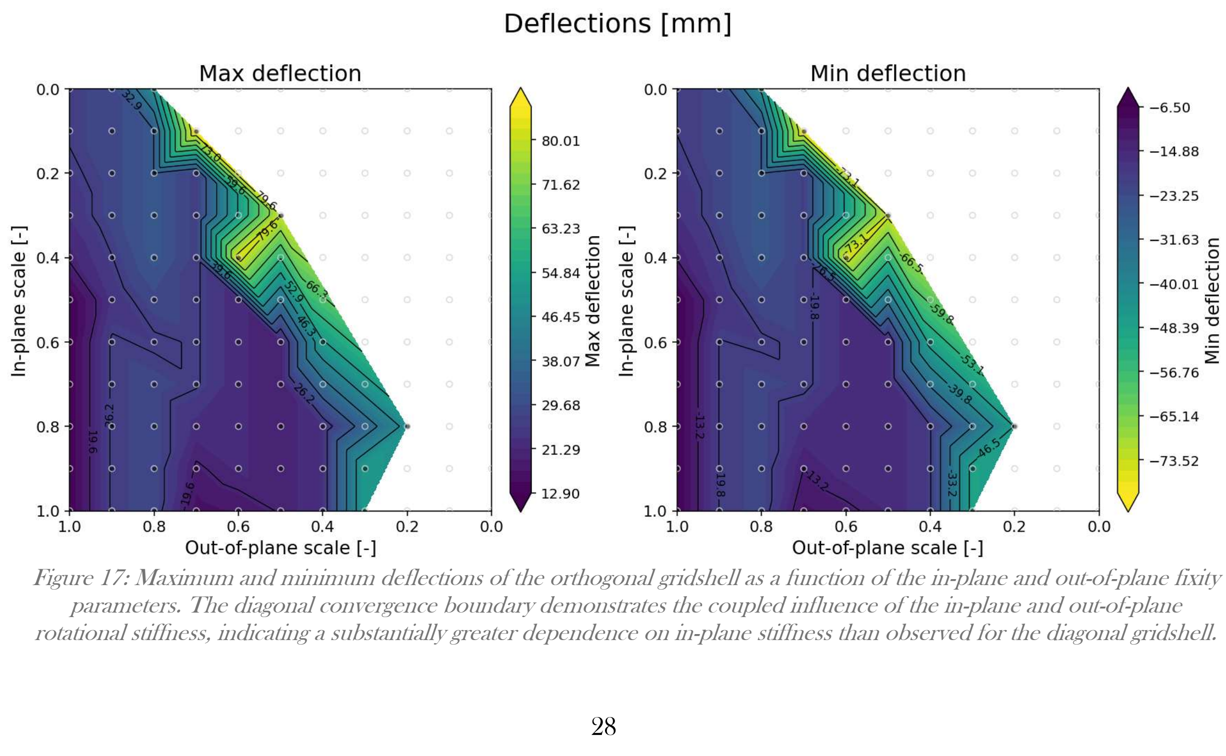

Figure 17: Maximum and minimum deflections of the orthogonal gridshell as a function of the in-plane and out-of-plane fixity parameters. The diagonal convergence boundary demonstrates the coupled influence of the in-plane and out-of-plane rotational stiffness, indicating a substantially greater dependence on in-plane stiffness than observed for the diagonal gridshell.

The governing member utilisation follows a similar trend to the displacement response. The larger plateau regions visible in Figure 18 These are primarily due to interpolation between converged solutions, although the overall development remains consistent with the reduction in structural stiffness. Unlike the displacement plots, which represent only the vertical response, the governing unity check accounts for the effects of axial force and in- and out-of-plane bending moments, resulting in a broader region of elevated utilisation.

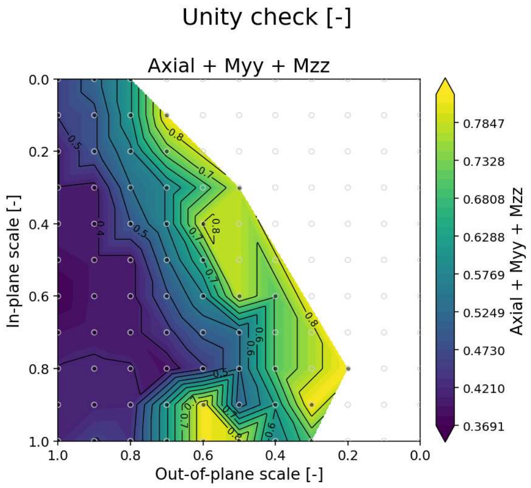

Figure 18: Governing member utilisation resulting from the combined axial force and in- and out-of-plane bending moments as a function of the in-plane and out-of-plane fixity parameters for the orthogonal grid variant.

The development of the internal forces further illustrates the coupled behaviour of the orthogonal gridshell. Pronounced local maxima occur in several response quantities near the convergence boundary, particularly in the out-of-plane bending moment(Figure 19). These local peaks coincide with reductions in the corresponding in-plane bending moments, indicating a redistribution of bending between the two principal directions as the available rotational stiffness decreases. This behaviour is

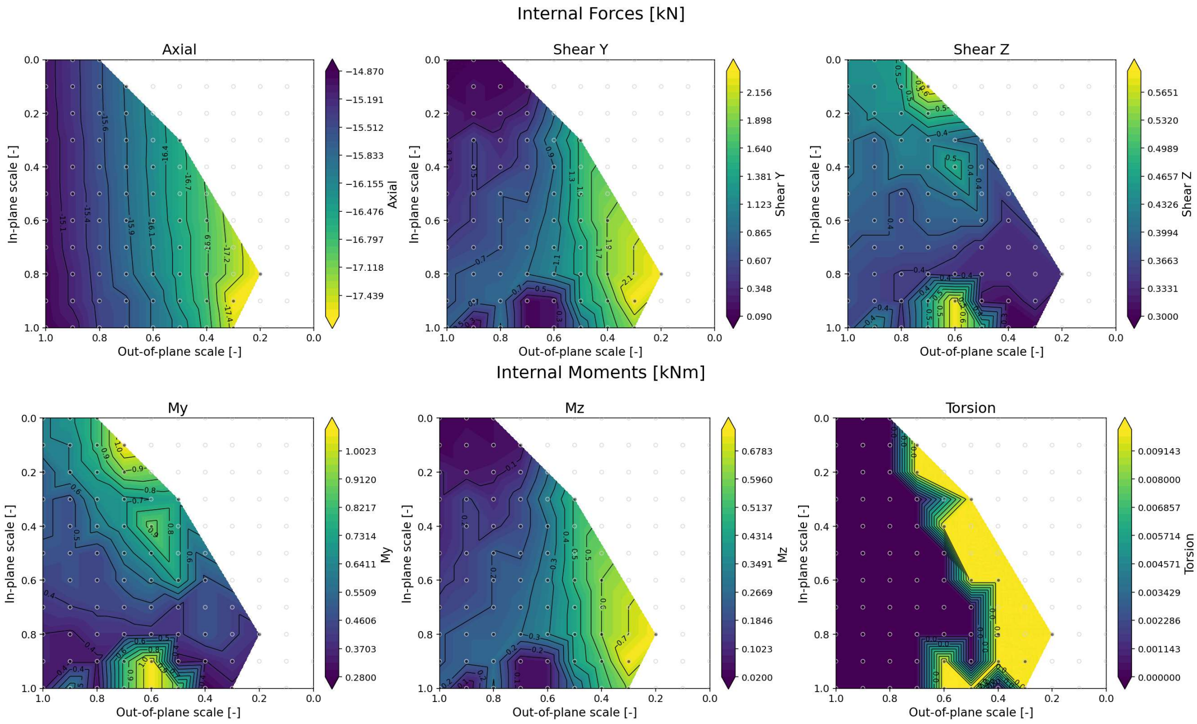

Figure 19: Development of the governing internal forces and moments of the orthogonal gridshell over the investigated in-plane and out-of-plane stiffness range. The local maxima occurring near the convergence boundary indicate a strong coupled dependence on both stiffness parameters as the structure approaches instability.

considerably less pronounced in the diagonal gridshell, suggesting that the orthogonal configuration is more sensitive to the interaction between in-plane and out-of-plane stiffness.

Overall, the orthogonal gridshell exhibits a coupled stiffness response, in which both the in-plane and out-of-plane rotational stiffness govern the structural behaviour. This contrasts with the diagonal gridshell, where the response is controlled primarily by the out-of-plane rotational stiffness.

3.4. Discussion

The contour plots exhibit limited numerical noise due to the relatively coarse parameter discretisation and the use of a single nonlinear analysis for each stiffness combination. Since the analyses include second-order effects, small differences in the converged equilibrium configuration can produce local irregularities in the calculated response. These irregularities are particularly visible near the convergence boundary, where the structural response becomes increasingly sensitive to small changes in stiffness. Nevertheless, the overall trends remain consistent across the investigated parameter space.

Although torsional releases were assigned at the member ends, small torsional moments are still observed within the global model. These arise primarily from the nodal idealisation used to connect the beam elements and the rotational springs. Their magnitude remains negligible compared with the governing bending moments and therefore has only a limited influence on the evaluated structural response. Even if these torsional effects were entirely transferred to the out-of-plane bending moment, the resulting deviation would remain within approximately 2.5% of the maximum measured value.

The present study further considers only a single gridshell density. The influence of the grid discretisation on the global behaviour was therefore not investigated explicitly. Nevertheless, a coarser structural grid is expected to reduce the available membrane action, resulting in larger bending moments and a smaller stable solution space. Consequently, the stiffness requirements identified in this chapter should be interpreted as specific to the investigated reference configuration.

Despite these limitations, the analyses demonstrate clear and consistent trends. Both the diagonal and orthogonal gridshells exhibit rapidly increasing deflections and member utilisation as the out-of-plane rotational stiffness decreases, confirming that the rotational restraint provided by the connections plays a fundamental role in maintaining the structure's global stiffness.

The comparison between the two grid topologies further demonstrates that the influence of the in-plane rotational stiffness depends strongly on the structural layout. The diagonal gridshell remains governed predominantly by the out-of-plane rotational stiffness, whereas the orthogonal configuration exhibits a coupled dependence on both stiffness directions. The pronounced local maxima observed in the orthogonal configuration indicate a redistribution of bending between the principal directions as the available rotational restraint decreases, suggesting that the orthogonal gridshell is considerably more sensitive to reductions in connection stiffness.

For both grid configurations, a pronounced transition occurs when the out-of-plane fixity approaches approximately 0.3. Below this value, no stable solutions satisfying the applied loading could be obtained for the investigated model. Rather than representing a classical bifurcation buckling load, this transition reflects the progressive increase in second-order deformations and the associated bending moments as the rotational stiffness decreases. The results, therefore, indicate a practical lower bound on the rotational stiffness required to maintain a stable structural response for the investigated gridshell configuration.

3.5. Conclusions

The global parametric analyses demonstrate that the rotational stiffness of the connections significantly influences the structural behaviour of timber gridshells. For both investigated grid configurations, reducing the out-of-plane rotational stiffness increases deflections, member utilisation, and bending moments due to second-order effects. The analyses further indicate the existence of a practical lower stiffness limit, below which stable solutions could no longer be obtained for the investigated loading conditions, beam sizes, geometry and dimensions.

The influence of the in-plane rotational stiffness was found to depend strongly on the grid topology. The diagonal gridshell remained governed primarily by the out-of-plane rotational stiffness. In contrast, the orthogonal configuration exhibited a coupled dependence on both the in-plane and out-of-plane stiffness. Consequently, the required connection stiffness cannot be considered independently of the structural configuration in which it is applied.

Although the numerical results exhibit minor irregularities due to nonlinear convergence and discretisation of the parameter space, the overall trends remain consistent. The analyses demonstrate that the global structural response is governed predominantly by the rotational restraint available at the connections rather than by the member stiffness alone.

The global parameter study demonstrates that the diagonal gridshell provides the most appropriate reference configuration for the subsequent connection analyses. Its behaviour is governed primarily by the out-of-plane rotational stiffness. In contrast, the influence of the limited in-plane stiffness associated with the investigated knife-plate connection remains comparatively small. In contrast, the orthogonal configuration exhibits a strong coupled dependence on both stiffness directions and pronounced local force redistributions. The diagonal configuration, therefore, provides a more robust basis for relating the rotational stiffness of the developed connection detail to the global structural behaviour of the gridshell.

4. Single Dowel Behaviour

4.1. Analytical Formulation

4.1.1. Purpose of the Local Stiffness Model

The local analytical model is used to estimate the rotational stiffness of the steel–timber connection from its material and geometric parameters. The model is developed based on the mechanisms in Figure 20 to provide a physically interpretable stiffness value that can be implemented in the global gridshell model as a rotational spring.

The local model accounts for dowel bending, timber embedment deformation, dowel-group geometry, and steel-plate flexibility. The stiffness contributions are combined using series and parallel stiffness relationships, depending on whether the deformation mechanisms act through the same degree of freedom or through separate deformation paths.

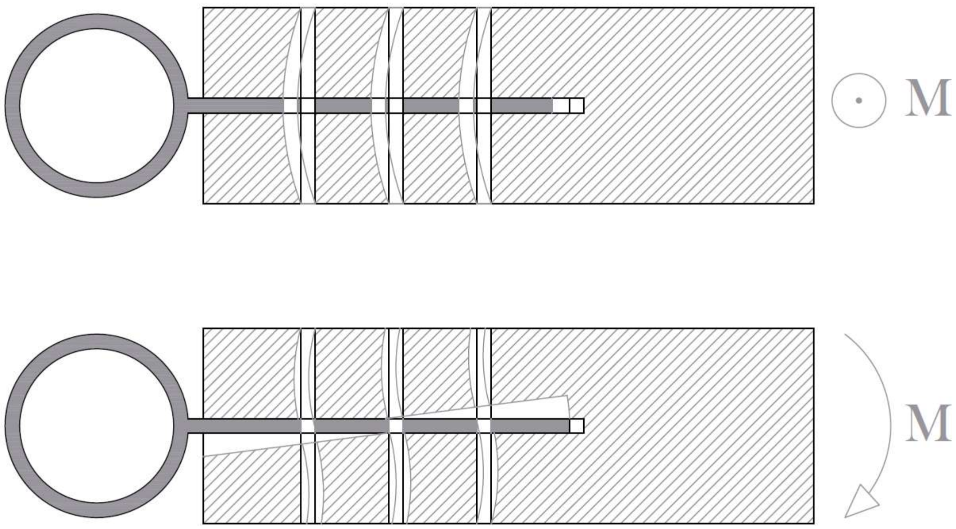

Figure 20: Top view of the connection illustrating the assumed bearing behaviour for out-of-plane and in-plane rotational loading.

Both in-plane and out-of-plane rotational stiffness components are evaluated because the global response of the gridshell depends on the directional stiffness of the connection. Neglecting either component could lead to an underestimation or overestimation of the joint restraint in the structural model. The analytical model is also used as a reference for the local finite element model. This allows the numerical model to be checked against a simplified mechanical formulation before the connection stiffness is used in the global structural analysis.

The local stiffness model includes both material and geometric parameters. The main parameters considered in the analytical study are listed below in Table 2.

Parameter	Symbol	Baseline Value	Range
Dowel diameter	d	10 mm	6-20 mm
Timber density	ρ_m	420 kg/m^3	300-600 kg/m^3
Embedment stiffness	k	-	-
Embedment length	l_0	100	20-250 mm
Load-to-grain angle	ϑ	-	0-90°
Youngs modulus steel	E	210000 N/mm^2	-

Table 2: Parameters used in the rotational stiffness analysis of the steel–timber knife connection.

The dowel diameter affects both the bending stiffness of the dowel and the embedment response of the timber. Timber density is included because it influences the local embedment stiffness of the timber around the fastener. The load-to-grain angle is included to account for the orthotropic behaviour of timber. The embedment length determines the effective interaction length between the dowel and timber.

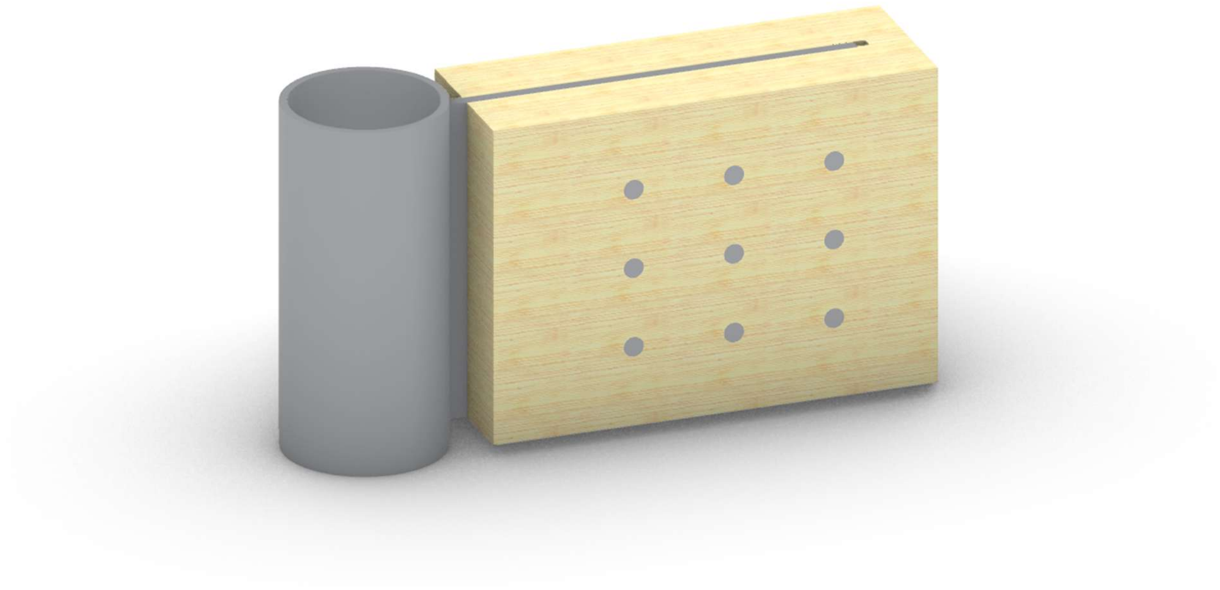

Figure 21: Three-dimensional representation of the proposed steel–timber knife plate connection.

4.1.2. Embedment Stiffness

An elastic foundation represents the interaction between the dowel and the surrounding timber. The embedment stiffness is defined as a function of timber density and load-to-grain angle, expressed in N/mm^3. The stiffness values parallel and perpendicular to the grain are taken from Gikonyo et al. (Gikonyo, Schweigler and Bader, 2025):

$$k_{el,0} = 0.1374\rho_m - 12.9 \tag{1}$$

$$k_{el,90} = 0.0922\rho_m - 18.2 \tag{2}$$

where ρ_m is the mean timber density. The effective embedment stiffness for an arbitrary load-to-grain angle ϑ is then obtained by combining the parallel and perpendicular components:

$$k_{eff} = k_{el,0}\cos^2(\vartheta) + k_{el,90}\sin^2(\vartheta) \tag{16}$$

This effective embedment stiffness is used in beam-on-elastic-foundation models to include the orthotropic embedment behaviour of timber without requiring separate models for each grain direction.

4.1.3. Beam-On-Elastic-Foundation Modelling

The dowel–timber interaction is modelled using a beam-on-elastic-foundation approach based on Hetényi's formulation (Hetényi, 1946). This model is appropriate because the dowel transfers load to the timber through distributed embedment stresses along its length, while the dowel itself deforms in bending. The formulation, therefore, captures the combined influence of dowel bending stiffness and local timber embedment stiffness.

The governing equation is:

$$EI\frac{d^4u(x)}{dx^4} + k_{eff}u(x) = p(x) \tag{4}$$

Where $u(x)$ is the dowel displacement, EI is the bending stiffness of the dowel, k_{eff} is the embedment stiffness, and $p(x)$ is the external load distribution. Introducing:

$$\lambda = \sqrt[4]{\frac{k_{eff}}{4EI}}, \qquad \check{p}(x) = \frac{p(x)}{EI}$$

The equation can be written as:

$$\frac{d^4u(x)}{dx^4} + 4\lambda^4 u(x) = \check{p}(x)$$

Since the loads are applied as boundary forces and moments in the evaluated models, the particular solution is omitted, and only the homogeneous solution is required. The displacement function is written as:

$$u_0(x) = e^{\lambda x}[C_1 \cos(\lambda x) + C_2 \sin(\lambda x)] + e^{-\lambda x}[C_3 \cos(\lambda x) + C_4 \sin(\lambda x)]$$

Which can be rewritten in a more functional form as:

$$u_0(x) = A_1 \cos(\lambda x) \cosh(\lambda x) + A_2 \cos(\lambda x) \sinh(\lambda x) + A_3 \sin(\lambda x) \cosh(\lambda x) + A_4 \sin(\lambda x) \sinh(\lambda x) \quad (17)$$

The constants A_1 to A_4 are determined from the boundary conditions of each connection idealisation. The required stiffness is then obtained by relating the applied force or moment to the resulting displacement or rotation.

4.1.4. Out-of-Plane Dowel Model

The out-of-plane model describes the symmetric deformation of a dowel subjected to shear transfer between the steel plate and the timber member. Due to symmetry, only half of the system is modelled. The plane of symmetry is represented by a zero-rotation condition at the mirrored face. The boundary conditions for the half-model can be seen in Figure 22 and are:

$$-EI \frac{d^2u_{d,0}(0)}{dx^2} = 0$$

$$-EI \frac{d^3u_{d,0}(0)}{dx^3} = 0$$

$$\frac{du_{d,0}(l)}{dx} = 0$$

$$\frac{d^3u_{d,0}(l)}{dx^3} = \frac{F}{EI}$$

where F is the force transferred through one shear plane. Substitution of these boundary conditions into the BOEF shape function gives the displacement along the dowel:

$$u_{d,0}(x) = -\frac{F}{EI\lambda^3(\sinh(2\lambda l) + \sin(2\lambda l))}\Big[\cos(\lambda l)\cosh(\lambda l)\cos(\lambda x)\cosh(\lambda x) + \frac{1}{2}(\sin(\lambda l)\cosh(\lambda l) - \cos(\lambda l)\sinh(\lambda l))(\cos(\lambda x)\sinh(\lambda x) + \sin(\lambda x)\cosh(\lambda x))\Big]$$

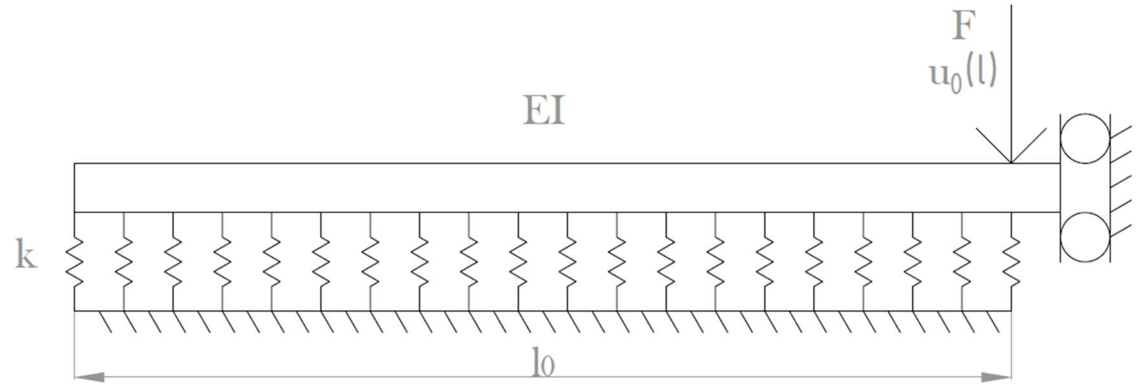

Figure 22: Beam-on-elastic-foundation representation of dowel bearing with a clamped symmetry condition at the shear plane.

The maximum displacement is assumed to occur at the timber-steel interface, where $x = l$. The expression can therefore be reduced to

$$u_{d,0}(l) = -F\frac{\cos^2(\lambda l) + \cosh^2(\lambda l)}{2EI\lambda^3(\sinh(2\lambda l) + \sin(2\lambda l))} \tag{18}$$

The flexibility of the dowel in the out-of-plane direction is obtained from the ratio between displacement and force:

$$c_{d,0} = \frac{u_{d,0}(l)}{F}, \qquad or\ k_{d,0} = \frac{1}{c_{d,0}} \tag{19}$$

This stiffness describes the local force-displacement response of a single dowel for the out-of-plane mechanism.

4.1.5. In-Plane Dowel Model

The in-plane model describes the rotational deformation of the connection about the plate axis. In this mechanism, the dowel exhibits a diagonal bearing response under the applied bending moment. The model is formulated by applying a moment at the interface rather than a shear force, which allows the resulting rotation to be related directly to rotational stiffness.

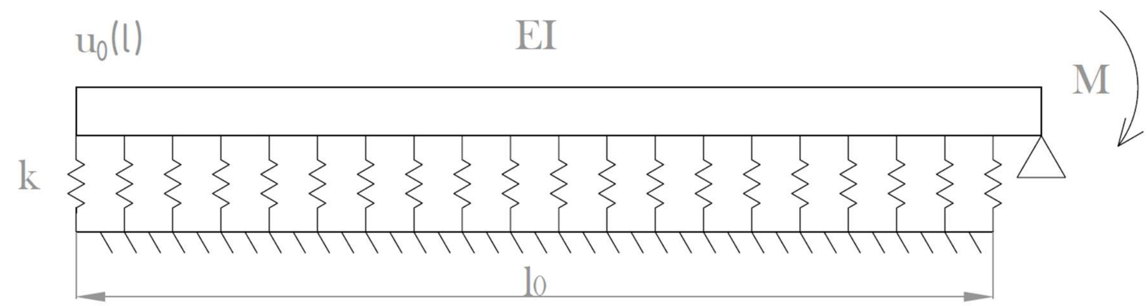

Figure 23: Beam-on-elastic-foundation model of a dowel subjected to a rotational moment.

The boundary conditions can be seen in Figure 23 and are

$$-EI\frac{d^2u_{d,1}(0)}{dx^2} = 0$$

$$-EI\frac{d^3u_{d,1}(0)}{dx^3}=0$$

$$-EI\frac{d^2u_{d,1}(l)}{dx^2}=M$$

$$u_{d,1}(l)=0$$

where M is the applied moment. The resulting displacement function is

$$u_{d,1}(x)=\frac{M}{2\lambda^2EI(\sinh(\lambda l)\cosh(\lambda l)-\cos(\lambda l)\sin(\lambda l))}[(\cos(\lambda l)\sinh(\lambda l)+\sin(\lambda l)\cosh(\lambda l))\cos(\lambda x)\cosh(\lambda x)-\cos(\lambda l)\cosh(\lambda l)\,(\cos(\lambda x)\sinh(\lambda x)+\sin(\lambda x)\cosh(\lambda x))]$$

The rotation at the interface is obtained by differentiating the displacement function and evaluating it at $x=l$.

$$u'_{d,1}(l)=\frac{M}{2\lambda EI}\cdot\frac{\cosh^2(\lambda l)+\cos^2(\lambda l)}{\sinh(\lambda l)\cosh(\lambda l)-\sin(\lambda l)\cos(\lambda l)} \tag{20}$$

The corresponding rotational stiffness contribution of a single dowel is

$$C_{zz,1,i}=\frac{M}{u_{d,1}{}'(l)} \tag{21}$$

This formulation directly links the moment applied at the interface to the rotation generated by local dowel bending and timber embedment.

4.2. Results

4.2.1. In- and Out-of-Plane Dowel Behaviour

The analytical formulation developed in the previous section describes both the in-plane and out-of-plane behaviour of the dowel. Since the influence of the governing parameters is consistent for both loading directions, the following discussion focuses primarily on the out-of-plane formulation. This loading condition is more readily interpreted because it is represented by a concentrated force at the shear plane rather than an applied bending moment.

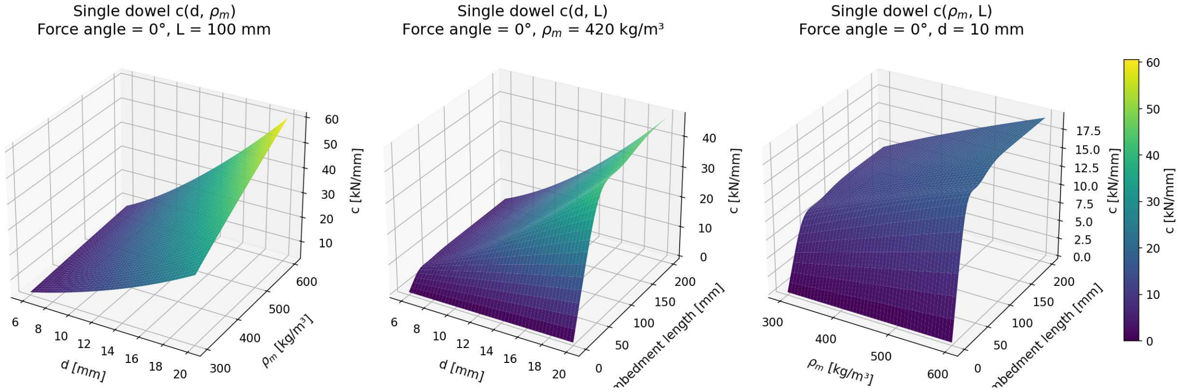

Figure 24: Parametric study of stiffness of the BOEF model loaded parallel to the grain, the as a function of dowel diameter, embedment length, and timber density, with one parameter fixed in each analysis.

The analytical stiffness formulation is governed primarily by three parameters: dowel diameter, embedment length, and timber density. The timber density controls the elastic embedment stiffness within the beam-on-elastic-foundation model. At the same time, the embedment length defines the active contact region between the dowel and the timber.

To evaluate the influence of these parameters, the analytical stiffness response is visualised using a series of three-dimensional parameter studies in which one parameter is held constant while the remaining two vary, see Figure 24.

To facilitate interpretation, one parameter is subsequently fixed so that the influence of the remaining variables can be examined individually. Here, the effects of the different parameters are clearly observable. The results in Figure 25 show that dowel diameter and timber density yield a strong, approximately monotonic increase in stiffness. In contrast, the influence of embedment length exhibits a distinct nonlinear development.

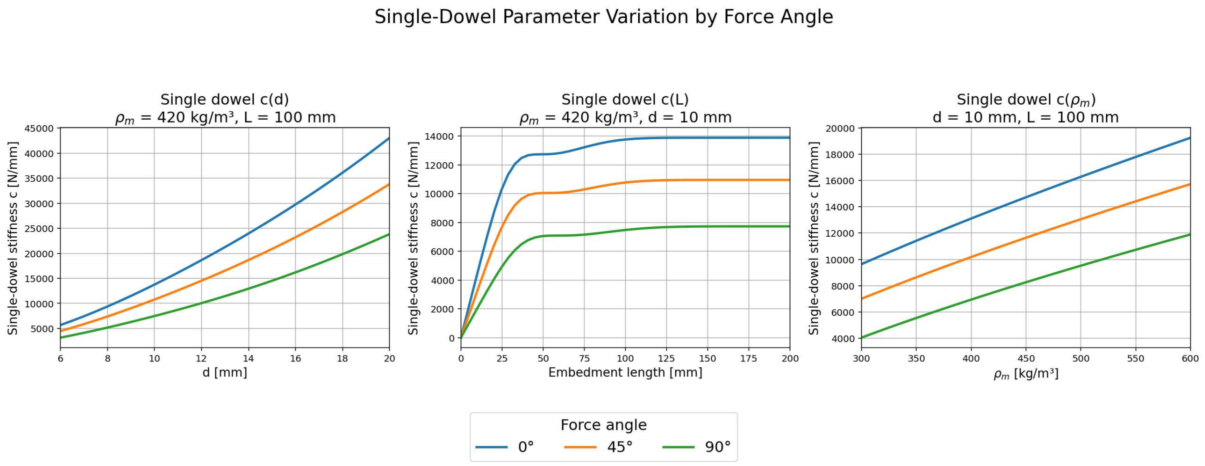

Figure 25: Influence of dowel diameter, embedment length, and timber density on the out-of-plane rotational stiffness of a single dowel for loading parallel, inclined, and perpendicular to the grain.

Unlike the diameter and density parameters, the embedment-length response is distinctly nonlinear and can be divided into four characteristic regions (Figure 26):

1. **Initial linear region (I)**
   Stiffness increases rapidly with embedment length as the dowel-bearing interaction develops.

2. **Initial plateau region (II)**
   The increase in stiffness diminishes as the elastic embedment stiffness behaviour becomes dominant.

3. **Secondary increase region (III)**
   A secondary increase in stiffness likely occurs upon switching contact surfaces, leading to additional bearing interaction due to dowel deformation within the hole.

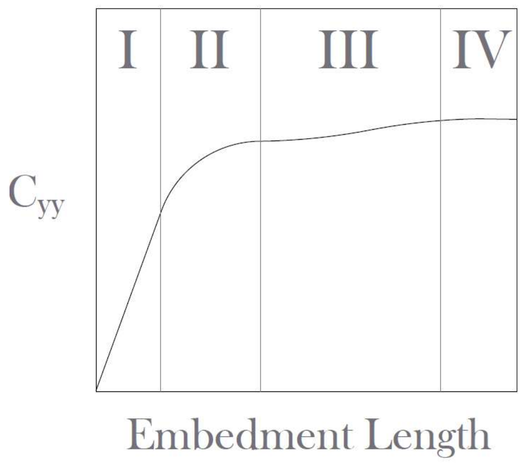

Figure 26: Conceptual stiffness development and behavioural phases associated with embedment length.

4. **Final plateau region (IV)**
   The stiffness response gradually stabilises as the embedment stiffness effects dominate the behaviour.

The embedment-length parameter, therefore, exhibits significantly greater complexity than the density and dowel-diameter parameters. To better understand the origin of the embedment-length response, the deformed shapes of dowels with varying embedment lengths were evaluated in Figure 27 assuming full contact between the dowel and the surrounding timber. These deformation profiles illustrate how the force-transfer mechanism changes as the embedment length increases.

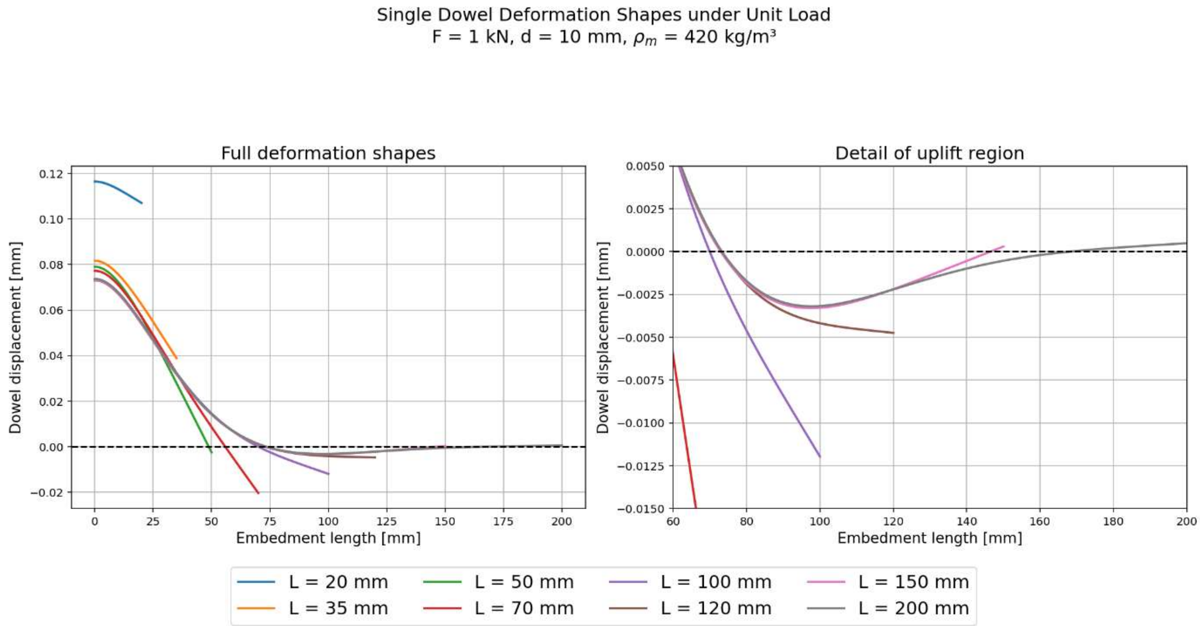

Figure 27: Deformation profiles of dowels with varying embedment lengths under unit loading. The detailed view illustrates the progressive restraint provided by the elastic timber embedment, reducing dowel rotation and uplift as the embedment length increases.

For short embedment lengths, the expected yield response is governed primarily by the formation of a plastic hinge near the shear plane at the maximum moment seen in Figure 28. As the embedment length increases, the restraint provided by the surrounding timber progressively clamps the dowel,

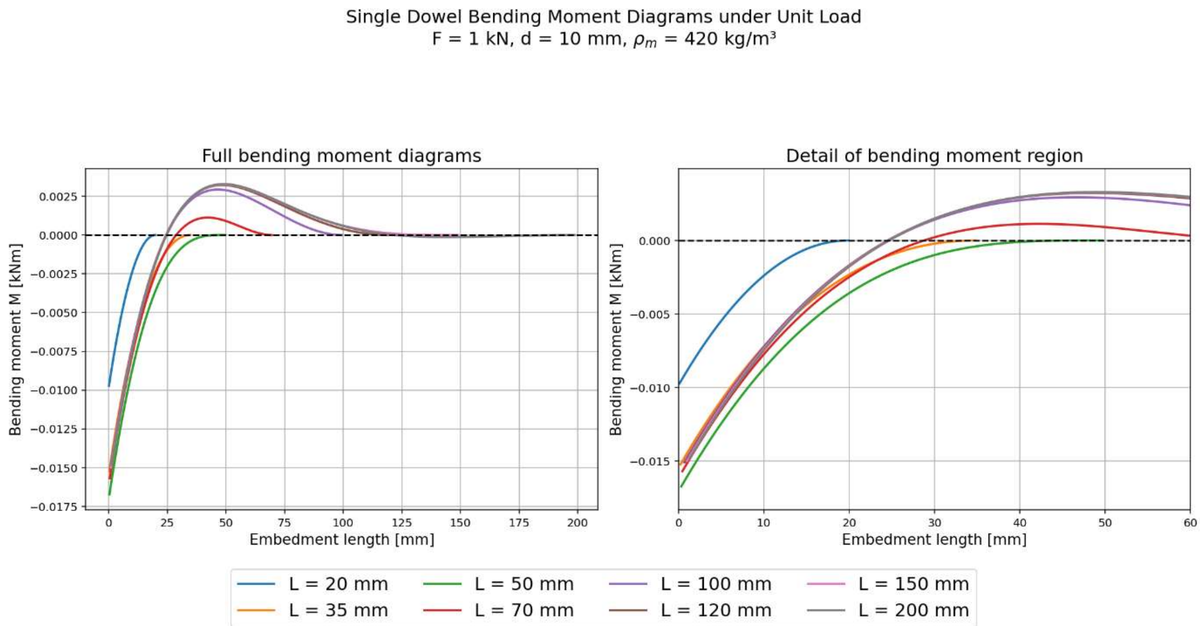

Figure 28: Bending moment distributions for dowels with varying embedment lengths under unit loading. A primary bending moment develops at the shear plane, while increasing embedment length introduces a secondary bending region through the restraint provided by the elastic timber embedment.

introducing a secondary bending region further along the embedded length. Following the yielding of the first plastic hinge, this second bending region is expected to develop into an additional plastic hinge, resulting in the two-stage behaviour observed in the stiffness curves.

To relate the predicted stiffness development to the onset of yielding, an indicative yielding assessment was performed for both the dowel and the timber embedment zone. The objective of this assessment is not to predict the ultimate connection capacity, but rather to identify the regions where yielding is expected to initiate as embedment length increases.

For the dowel, the yield stress is taken as 360 **MPa**, corresponding to the lowest-strength steel grade (4.6) commonly used for connections. The bending stresses are obtained by dividing the analytical bending moments by the dowel section modulus. This allows the embedment-length response to be related directly to the onset of yielding, resulting in an illustrative bilinear representation of the dowel behaviour.

A similar approach is adopted for the timber embedment zone. Here, yielding is assumed to occur at the characteristic bearing strength defined by Eurocode 5, where:

$$f_{h,1,k} = \frac{f_{h,0,k}}{k_{90}\sin^2\alpha + \cos^2\alpha} \tag{22}$$

$$f_{h,0,k} = 0.082(1 - 0.01d)p_k \tag{23}$$

This formulation directly accounts for the influence of the load-to-grain angle, enabling consistent comparison of the yielding behaviour of both the dowel and the surrounding timber. The reduction in bearing strength with increasing load angles relative to the grain, seen in Figure 29is reflected in an earlier onset of embedment yielding, while simultaneously allowing larger local deformations to develop before the connection reaches its ultimate capacity.

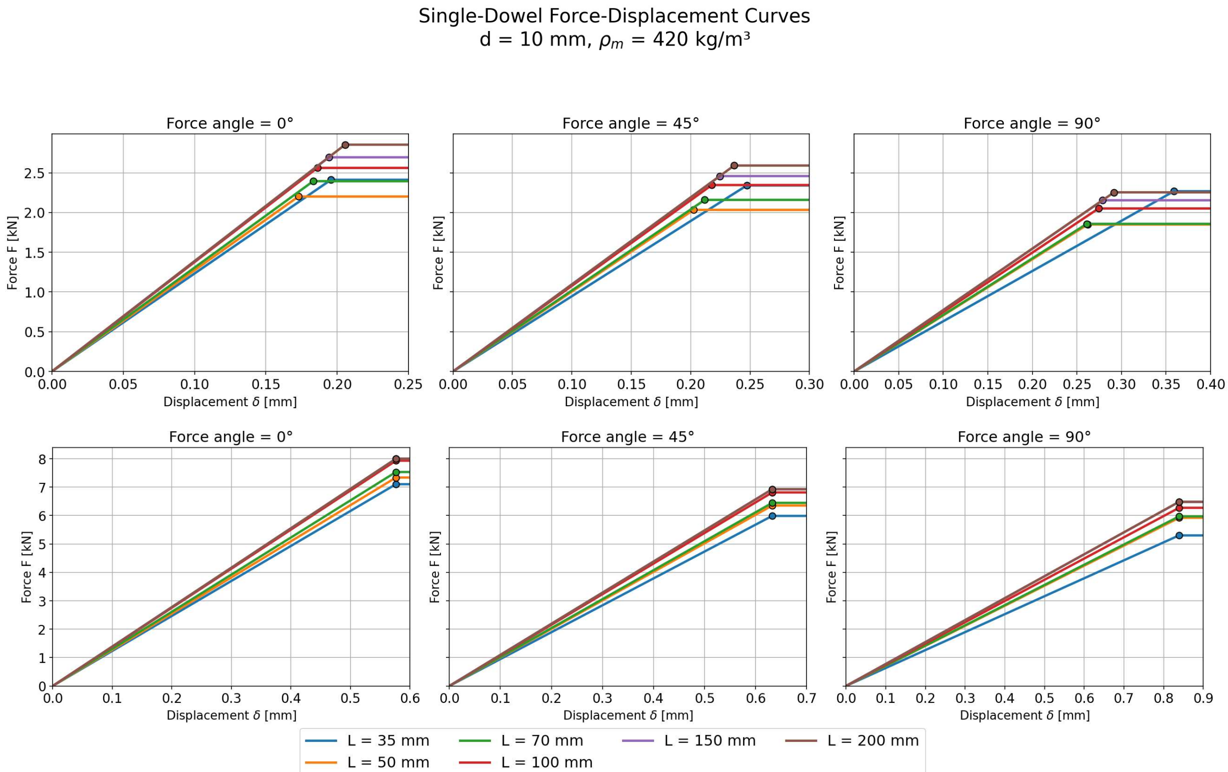

Figure 29: Illustrative bilinear force–displacement relationships for dowel yielding (top) and timber embedment yielding (bottom) for varying embedment lengths and load-to-grain orientations.

4.2.2. Sensitivity Analysis

The relative influence of the investigated parameters on the stiffness of a single dowel is evaluated by comparing the stiffness increase produced by each parameter range relative to a common baseline configuration. Owing to the interaction between embedment length, embedment stiffness, and dowel stiffness within the analytical formulation, the effectiveness of each parameter varies considerably with the load-to-grain orientation.

For loading parallel to the grain, the results shown in Figure 30 indicate that the dowel diameter has the largest influence on stiffness, producing an increase exceeding 270% over the investigated parameter range. Timber density has the second-largest influence, increasing the stiffness by approximately 57%, while embedment length contributes a smaller but still significant increase of approximately 25% within the selected practical range.

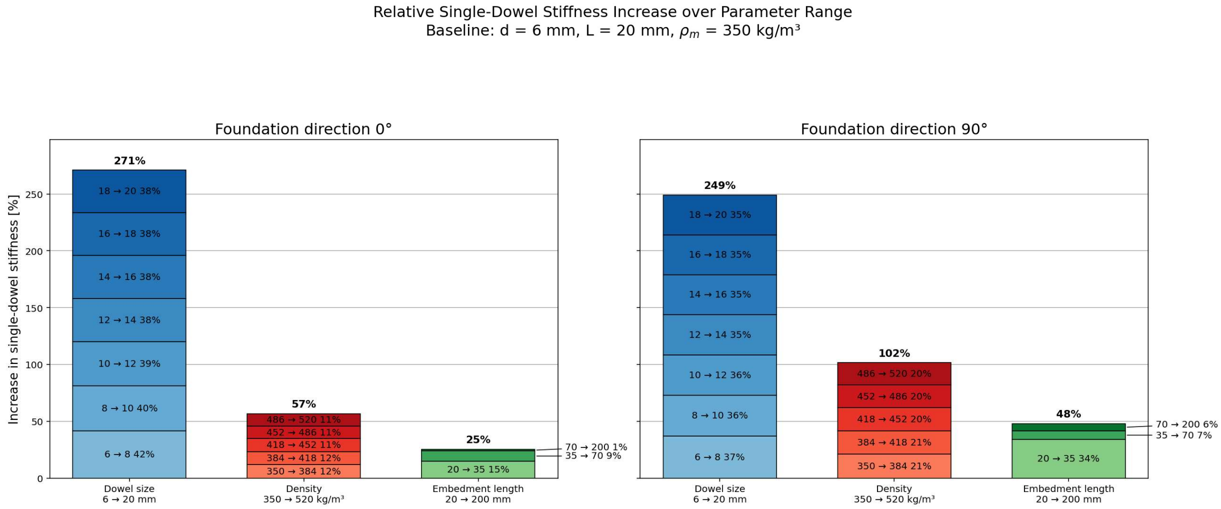

Figure 30: Relative increase in rotational stiffness obtained by varying each parameter across its investigated range, relative to the baseline configuration.

For loading perpendicular to the grain, the influence of dowel diameter is slightly reduced, increasing by just below 250%. In contrast, the influence of both timber density and embedment length becomes considerably more pronounced, with their relative contribution to the stiffness response increasing substantially compared to the parallel-to-grain case. This behaviour suggests that density- and embedment-related effects become increasingly important for loading perpendicular to the grain, where the lower embedment stiffness causes the response to become increasingly governed by the timber embedment.

Connection geometry is not included in the present comparison. Unlike the material and dowel parameters, its influence depends strongly on the selected reference pattern, force orientation, and distribution of the rotational load among the fasteners. As a result, a direct comparison would be highly dependent on the chosen baseline configuration and would not provide a meaningful measure of parameter sensitivity.

Overall, the results indicate that dowel diameter remains the dominant parameter governing stiffness, while timber density provides the second most significant contribution. The influence of embedment length is comparatively smaller, although its importance increases substantially for loading perpendicular to the grain.

4.2.3. **Bolt vs Dowel**

Although the primary focus of this research is on dowel-type connections, an adapted analytical formulation was also developed to estimate the influence of bolt clamping on connection stiffness. The derivation follows the same beam-on-elastic-foundation approach as the dowel formulation. Still, it replaces the free-end boundary condition with a clamped boundary to represent the restraint provided by the bolt head and washer. The complete derivation is presented in Appendix 4.

The objective of this comparison is not to establish a complete analytical model for bolted connections, but rather to evaluate whether the additional restraint provided by the bolt significantly alters the stiffness relative to the dowel formulation. Since the analytical model does not explicitly account for axial fastener action (rope effects), only the local rotational restraint introduced by the bolt head and washer is represented. Consequently, the analytical bolt formulation should be regarded as an approximation of the physical behaviour.

The comparison indicates that the influence of bolt clamping is relatively modest and is confined primarily to intermediate embedment lengths. For the investigated stiffness ratio of

$$EI: k = 2 \times 10^7 : 1$$

The bolt formulation increases the predicted stiffness by a maximum of approximately 19% at an embedment length of around 100 mm, as shown in Figure 31. For short embedment lengths, the local embedment behaviour dominates the response, resulting in only minor differences between bolts and dowels. At larger embedment lengths, the timber embedment increasingly restrains dowel rotation, reducing the additional stiffness provided by the bolt head and washer. Consequently, the differences

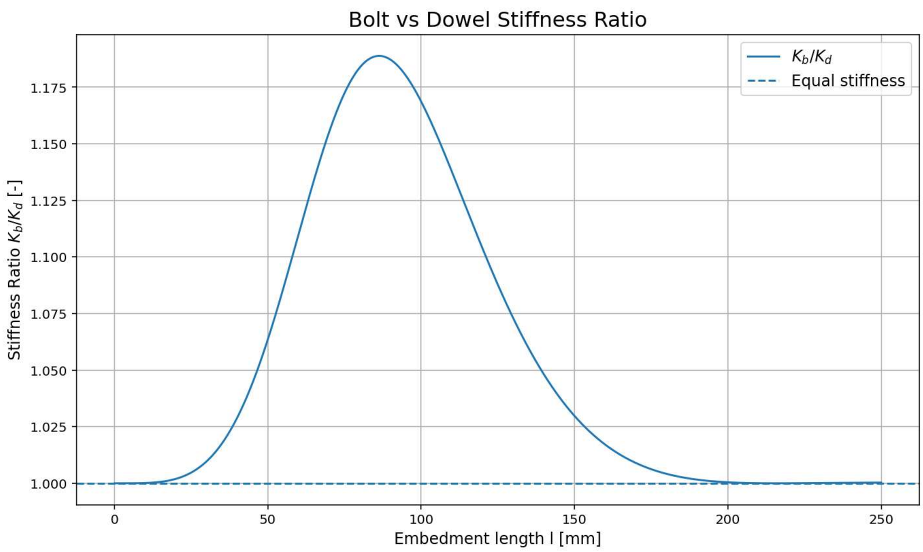

Figure 31: Ratio of bolt to dowel stiffness as a function of embedment length.

between the two formulations diminish as the embedment length increases.

These results suggest that neglecting bolt clamping in the main analytical formulation introduces only a limited error for the investigated parameter range. The dowel formulation, therefore, provides an appropriate basis for subsequent parameter studies while avoiding the additional complexity of modelling bolt-specific restraint mechanisms.

4.3. Discussion

4.3.1. Influence of Evaluated Parameters

The analytical parameter studies demonstrate that embedment length produces significantly more complex behaviour than either timber density or dowel diameter. Whereas density and dowel diameter yield approximately monotonic increases in stiffness, the embedment-length response exhibits multiple plateaus and nonlinear transitions.

The observed response can be divided into several behavioural phases. Initially, the stiffness increases rapidly as the dowel-bearing interaction develops within the elastic embedment. This is followed by a plateau region in which further increases in embedment length contribute only marginally to the connection's stiffness.

A secondary increase in stiffness is subsequently observed. This behaviour appears to be associated with a change in the contact mechanism between the dowel and the surrounding timber. At shorter embedment lengths, the rotational response is governed primarily by an almost diagonal action of the dowel. As the embedment length increases and dowel deformation progresses along the embedded region, contact begins to form on the opposite side of the hole. This additional contact interaction increases the rotational resistance of the connection and results in a renewed increase in stiffness.

Within the analytical beam-on-elastic-foundation formulation, this mechanism appears as a transition between compressive and tensile foundation reactions. Physically, however, timber cannot sustain tensile contact stresses as represented by the foundation model. Instead, the load transfer would occur through additional bearing interaction between the dowel and the opposite side of the hole. The apparent tensile foundation response should therefore be interpreted as an idealised representation of this secondary contact mechanism rather than a direct physical phenomenon.

As the embedment length increases further, the contribution of this additional contact interaction gradually diminishes, and the embedment behaviour once again becomes dominant. Consequently, the stiffness response approaches a second plateau region, indicating that further increases in embedment length yield very limited additional stiffness. The development of an apparent uplift region with increasing embedment length supports the interpretation of a secondary contact mechanism and the associated changes in stiffness development.

These observations suggest that embedment behaviour cannot be represented adequately using purely local bearing assumptions. Rather, the stiffness depends on the interaction between dowel bending deformation, the distributed embedment response of the timber, and the evolution of the contact zone along the embedded length. This behaviour explains why embedment length exhibits a fundamentally different stiffness development compared with timber density and dowel diameter.

Since the development of the secondary contact zone depends on the initial contact conditions between the dowel and the surrounding timber, manufacturing tolerances and hole clearances may significantly influence the stiffness obtained in practice. Small variations in hole geometry could therefore alter both the development of stiffness and the onset of yielding, particularly for intermediate embedment lengths, where the transition between the two contact mechanisms occurs.

It should be noted that the preceding interpretation considers primarily the rotational response of the connection. In practical applications, the connection will generally be subjected to a combination of axial force, shear force, and moment. Although the presence of additional loading may significantly increase the stresses, reaction forces, and load angles within the connection, it does not fundamentally alter the deformation mechanism described above. Instead, the characteristic deformation shape of the dowel remains similar, while the magnitude of the dowel deformation and the associated bearing stresses increase. Consequently, the embedment-length behaviour discussed in this section is expected to remain relevant under combined loading conditions, provided the connection response remains within the linear-elastic range.

Although embedment length governs the characteristic nonlinear stiffness development, the location of the plateau regions depends on both the dowel stiffness and the stiffness of the surrounding timber embedment. Increasing the timber density increases the stiffness of the elastic embedment, allowing the rotational restraint to develop more rapidly. Consequently, the plateau stiffness is reached at slightly shorter embedment lengths, as shown in Figure 32. Over the investigated density range, the embedment length required to reach approximately 99% of the plateau stiffness decreases by around 15 mm.

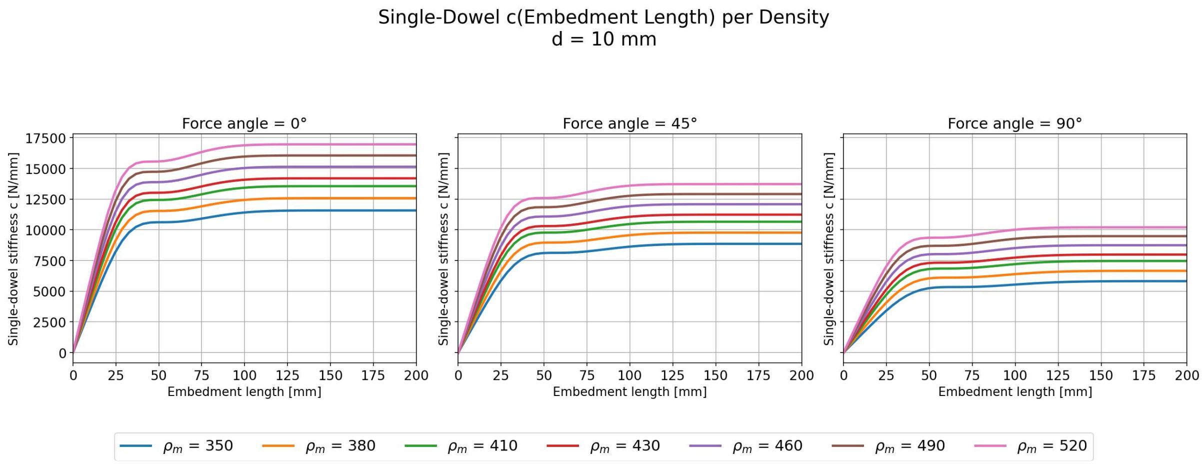

Figure 32: Influence of timber density on the embedment-length response. Increasing embedment stiffness slightly advances the onset of the stiffness plateaus while preserving the characteristic nonlinear behaviour.

The influence of dowel diameter is considerably more pronounced. Increasing the dowel diameter substantially increases the dowel's bending stiffness, requiring a larger embedment length before the timber embedment can provide sufficient rotational restraint. As a result, both the transition between the characteristic stiffness regions and the final plateau shift towards larger embedment lengths, as illustrated in Figure 33. Across the investigated diameter range, the embedment length required to reach approximately 99% of the plateau stiffness increases by approximately 110 mm. This demonstrates that larger dowels require substantially greater embedment lengths before their full stiffness can be mobilised.

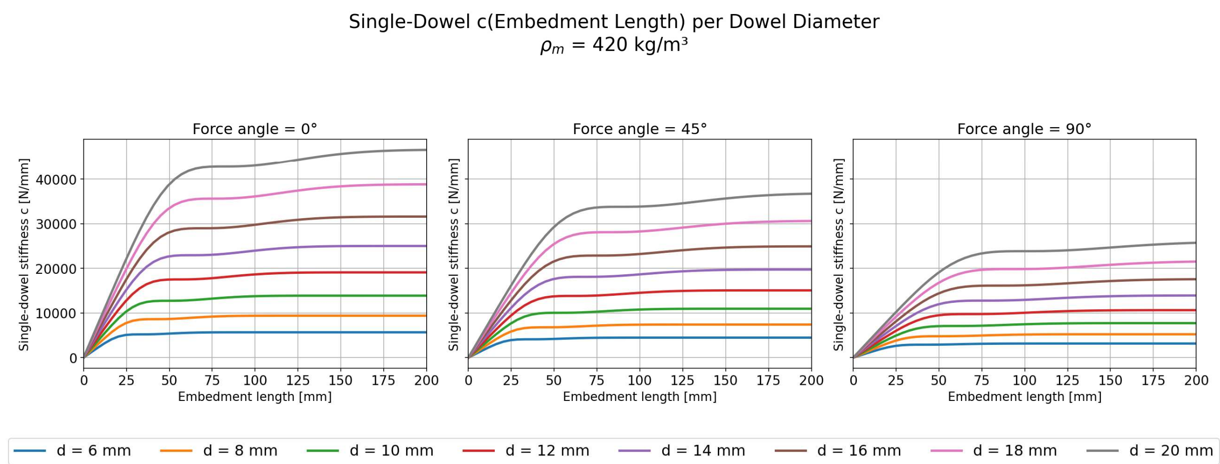

Figure 33: Influence of dowel diameter on the embedment-length response, illustrating the progressive shift of the stiffness plateaus towards larger embedment lengths as the dowel bending stiffness increases.

4.3.2. **Yield Behaviour**

To better understand the relationship between stiffness development and the onset of yielding, the analytical stress distributions of both the dowel and the timber embedment zone were evaluated over the investigated embedment lengths, as seen in Figure 34. Rather than considering only the stiffness, this analysis provides insight into the governing deformation mechanisms that ultimately limit the connection capacity.

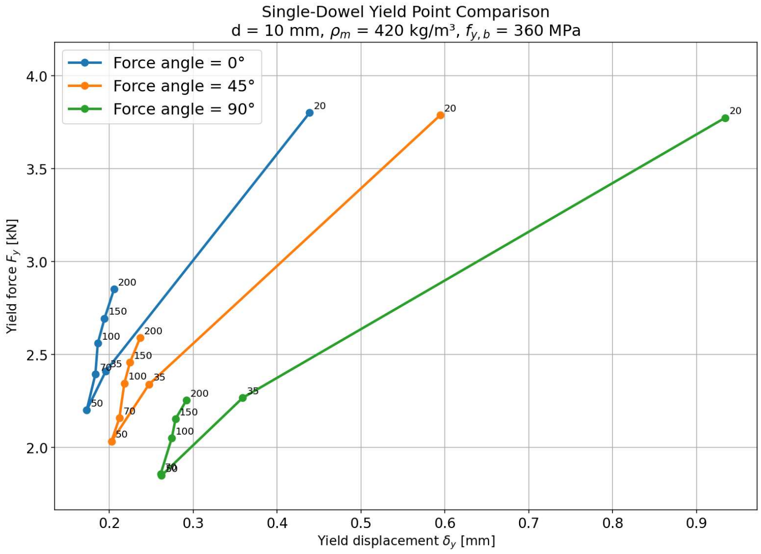

Figure 34: Yield force and corresponding yield displacement of a single dowel for increasing embedment lengths and different load-to-grain orientations.

The predicted yield force of the dowel is not constant as embedment length increases and can be divided into three characteristic behavioural regions. For very short embedment lengths, relatively large external forces are required to initiate yielding. However, these higher forces are accompanied by considerably larger yield displacements. This behaviour can be explained by the limited lever arm available for bending, causing the response to be governed primarily by local bearing deformation adjacent to the shear plane. Although the dowel can sustain a relatively high load before yielding, this is achieved at the expense of larger deformations.

As the embedment length increases to intermediate values, the effective lever arm between the applied load and the timber reaction also increases. For a given external force, this produces larger internal bending moments within the dowel, causing the steel yield stress to be reached at lower applied forces. Consequently, the predicted yield force decreases, while the increasing restraint provided by the surrounding timber reduces the displacement required to initiate yielding. This transition corresponds to the first plateau region identified in the stiffness response.

With further increases in embedment length, the behaviour changes fundamentally. The development of the secondary contact mechanism discussed previously allows the surrounding timber to restrain dowel rotation more effectively, distributing the bending stresses over a larger portion of the dowel and introducing a second bending region further along the embedded length. Although the embedment length continues to increase, the peak bending stress near the shear plane is reduced, and progressively larger external forces are therefore required before yielding is initiated. Unlike the high yield forces observed for very short embedment lengths, however, this increase is accompanied by only a modest increase in yield displacement. The additional embedment therefore improves the load-carrying capacity more effectively than it increases the deformation at first yield, corresponding to the second plateau region in the stiffness response.

The timber embedment zone exhibits a markedly different response. Unlike the dowel, the predicted onset of embedment yielding develops almost linearly with embedment length. This behaviour reflects the increasing contact area available for force transfer, allowing the bearing stresses to be distributed over a larger volume of timber. When the dowel and embedment yield limits are considered simultaneously, they are visible in Figure 35. Overall, the comparison indicates that first yield is generally controlled by the dowel. Embedment yielding only governs for the smallest investigated embedment lengths, as indicated by the black crosses. These points form a localised group of outliers associated with the 20 mm embedment length, where the limited contact region causes the timber embedment limit to be reached before dowel yielding. The apparent intersection in the plot therefore reflects this local short-embedment behaviour rather than a broader shift in the governing yielding mechanism.

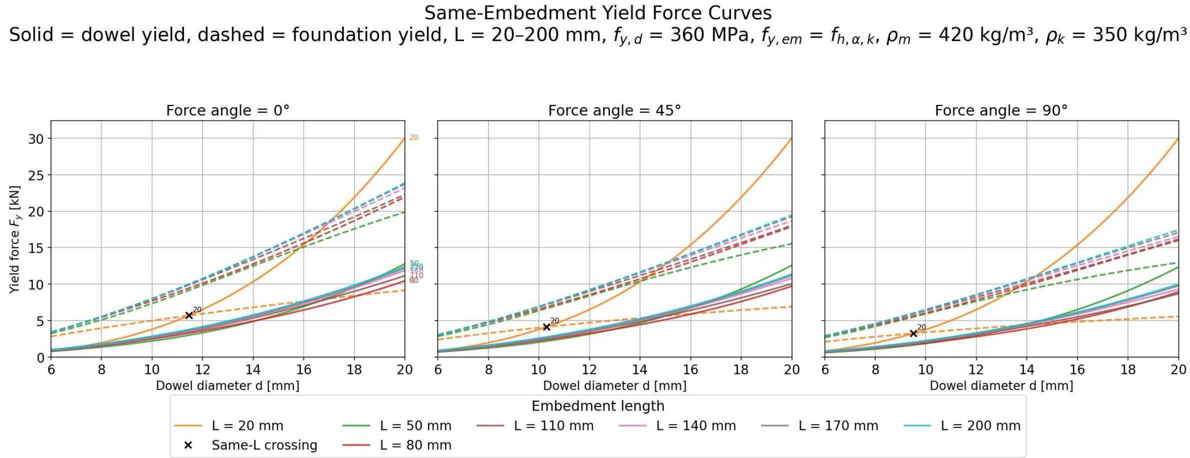

Figure 35: Comparison of the predicted dowel and timber embedment yield forces for varying dowel diameters, illustrating the transition from steel-controlled to timber-controlled behaviour.

It should be recognised that the present analytical formulation does not account for local stress concentrations around the dowel. In practice, these stress concentrations are expected to accelerate the onset of timber yielding, particularly near the shear plane where the bearing stresses are greatest. Consequently, the analytical formulation is likely to overestimate the load at which embedment yielding first occurs. Nevertheless, the observed transition from dowel-controlled to timber-controlled behaviour provides valuable insight into the governing mechanisms influencing the stiffness and yielding behaviour of dowel-type connections.

4.3.3. **Eurocode 5 Comparison**

The transition from steel-controlled to timber-controlled behaviour provides a possible explanation for the differences observed between the analytical formulation and the Eurocode 5 slip modulus. Whereas the analytical model explicitly represents the interaction among dowel bending, distributed timber support, and the evolution of the contact zone, the Eurocode 5 formulation is based on an empirical relationship intended to provide a practical stiffness estimate for design purposes. Consequently, differences between the two approaches are expected, particularly for larger embedment lengths where the interaction between the dowel and the timber embedment becomes increasingly important. The analytical mean stiffness lies relatively high within the predicted range because the embedment-length response is highly nonlinear. Following the rapid initial increase in stiffness, the response reaches two plateau regions over which relatively little additional stiffness is gained despite further increases in embedment length. Since a substantial proportion of the investigated embedment lengths lies within these plateau regions, the corresponding high stiffness values dominate the calculated mean.

As shown in Figure 36, the discrepancy between the analytical formulation and the Eurocode slip modulus increases markedly for loading parallel to the grain. In contrast, considerably closer agreement is obtained for loading perpendicular to the grain. In contrast, the agreement is substantially closer for loading perpendicular to the grain. This behaviour is consistent with the mechanics captured by the analytical model, in which the timber embedment stiffness varies with the load-to-grain orientation.

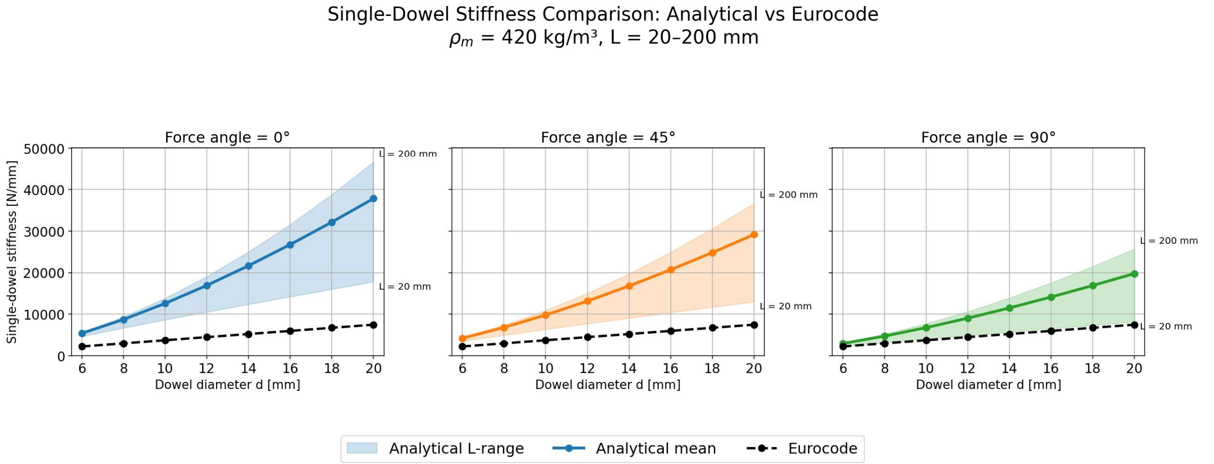

Figure 36: Comparison of the analytical single-dowel stiffness range and mean stiffness with the Eurocode 5 slip modulus for varying dowel diameters and load-to-grain orientations.

Since the Eurocode 5 formulation does not distinguish between loading parallel and perpendicular to the grain in the definition of K_{ser}, it cannot reproduce this directional dependence.

Additional differences are expected because the present analytical model assumes idealised elastic embedment and does not account for local stress concentrations, plastic embedment behaviour, or other nonlinear deformation mechanisms that are implicitly incorporated within the empirical Eurocode formulation. Consequently, the analytical model is better suited to investigating the influence of individual geometric and material parameters. In contrast, the Eurocode expression provides a conservative design-oriented estimate of the connection stiffness.

4.4. Conclusions

The analytical beam-on-elastic-foundation formulation provides valuable insight into the fundamental mechanics governing the stiffness of a single dowel. Among the investigated parameters, embedment length exhibits the most complex behaviour. Unlike timber density and dowel diameter, which produce approximately monotonic increases in stiffness, embedment length results in multiple stiffness plateaus associated with changes in the contact mechanism between the dowel and the surrounding timber. This demonstrates that the stiffness cannot be adequately represented using local bearing assumptions alone but depends on the interaction among dowel bending, distributed timber support, and the evolution of the contact zone.

The stress analyses further show that the governing yielding mechanism evolves as the embedment length and dowel diameter increase. For short embedment lengths, the connection behaviour is governed primarily by concentrated bending near the shear plane, whereas increasing embedment promotes the development of a secondary contact region that redistributes the bending stresses along the dowel. Consequently, the predicted yield force initially decreases due to the increasing bending lever arm before increasing again as the additional timber restraint becomes dominant. Comparison of the dowel and embedment yield limits indicates a gradual transition from steel-controlled behaviour for smaller dowel diameters towards timber-controlled behaviour for larger diameters.

Comparison with the Eurocode 5 slip modulus highlights the limitations of simplified empirical stiffness formulations. While the Eurocode expression provides a practical and generally conservative estimate for design, it does not explicitly account for finite embedment length, distributed dowel–timber interaction, or the influence of load-to-grain orientation. As a result, the analytical formulation predicts significantly higher stiffness for loading parallel to the grain, whereas substantially closer agreement is obtained for loading perpendicular to the grain.

Overall, the results demonstrate that the stiffness of a single dowel is governed by a combination of dowel bending, embedment behaviour, and the evolution of the contact mechanism within the timber. These findings establish the mechanical basis for extending the analytical formulation to multi-dowel groups, in which the behaviour of individual dowels is combined to predict the stiffness of complete steel–timber connections.

5. Dowel Group Behaviour

Unlike the previous chapter, which considered the behaviour of an individual dowel, this chapter investigates how multiple dowels interact to form the rotational stiffness of a complete connection. In addition to the stiffness of the individual fasteners, the connection behaviour is governed by the spatial distribution of the dowels, their lever arms, and the distribution of forces within the dowel group.

5.1. Group Stiffness Formulation

5.1.1. Out-of-Plane Rotational Stiffness of the Dowel Group

The out-of-plane rotational stiffness of the connection is obtained by assembling the translational stiffnesses of the individual fasteners. When the connection rotates, each fastener translates by an amount proportional to its distance from the centre of rotation:

$$u_i(x) = r_i\theta$$

The translational displacement of each fastener is also related to its flexibility or stiffness:

$$u_i(x) = F_i c_i$$

$$F_i = \frac{r_i\theta}{c_i}$$

Or since

$$k_i = \frac{1}{c_i}, \qquad F_i = k_i r_i \theta$$

The moment contribution of each fastener is obtained by multiplying the fastener force by its lever arm. For a double-shear connection, the total moment is

$$M = 2\sum_i F_i r_i$$

Substitution gives

$$M = 2\sum_i \frac{r_i^2\theta}{c_i}$$

and therefore the rotational stiffness of the fastener group is

$$C_{yy,0} = \frac{M}{\theta} = 2\sum_i r_i^2 k_i \tag{24}$$

This expression shows that fasteners located farther from the centre of rotation contribute disproportionately to the rotational stiffness of the connection. The fastener pattern is therefore an important parameter in addition to the stiffness of the individual fasteners.

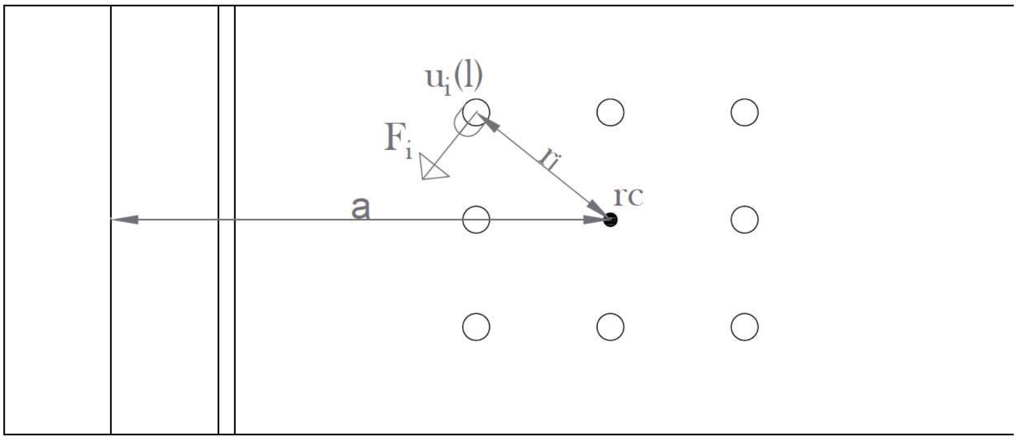

Figure 37: Geometric definition of the rotational centre, bolt lever arm, and force-displacement relationship used in the rotational stiffness formulation.

After the rotational stiffness has been implemented in the global model, the moment attracted by the connection can be used to recover the force in each fastener:

$$F_i = \frac{k_i r_i}{2\sum_i r_i^2 k_i} M \tag{25}$$

Because the centre of the fastener group is offset from the idealised node in the global model, as seen in Figure 38, the eccentricity between the connection and the node must also be considered. The stiffness of the steel plate between the fastener group and the node is represented as

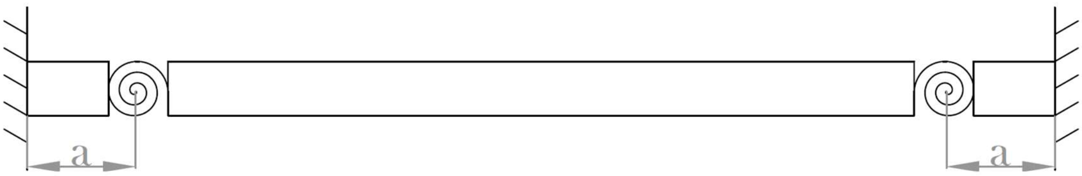

Figure 38: Spring-ended beam model illustrating the eccentricity between the rotational spring and the support.

$$C_{yy,1} = \frac{EI_{yy}}{a} \tag{26}$$

where a is the eccentricity length. The out-of-plane plate stiffness and fastener group stiffness are combined in series:

$$\frac{1}{C_{yy,1}} + \frac{1}{C_{yy,2}} = \frac{1}{C_{yy,tot}} \tag{27}$$

This ensures that the final connection stiffness is not overestimated when plate flexibility contributes to the total rotation. The reciprocal sum ensures that the most flexible component governs the overall connection stiffness, while the remaining components contribute according to their relative flexibility. Consequently, increasing the stiffness of an already stiff component provides only limited improvement when another component remains significantly more flexible.

5.1.2. **Combined In-plane Rotational Stiffness**

The complete in-plane rotational stiffness is obtained by combining the stiffness contributions of the:

1. Dowels and timber bearing stiffness
2. The in-plane steel plate bending stiffness
3. The bearing interaction between the plate and timber.

Deformation mechanisms that act through the same rotational degree of freedom are combined in parallel, while mechanisms that occur sequentially along the load path are combined in series.

The combined stiffness is expressed as

$$\frac{1}{\frac{1}{\sum_i C_{zz,1,i} + C_{zz,3}} + \frac{1}{C_{zz,2}}} = C_{zz} \tag{28}$$

where $C_{zz,1,i}$ is the rotational stiffness contribution of the fastener i, $C_{zz,2}$ is the lateral stiffness contribution of the steel plate, and $C_{zz,3}$ represents the plate–timber bearing contribution. This formulation prevents the total stiffness from exceeding the stiffness of the weakest deformation mechanism in the load path.

5.2. Pattern Studies

5.2.1. **In-Plane Connection Behaviour**

The in-plane behaviour of the connection is governed by the same beam-on-elastic-foundation formulation as the out-of-plane configuration. The principal difference lies in the deformation mechanism. Rotation of the steel plate produces a comparatively large bearing area between the plate and the surrounding timber, resulting in a very high rotational stiffness of both the dowels and the timber bearing zone. When these stiffness contributions are combined using the reciprocal stiffness formulation, the lateral bending stiffness of the steel plate becomes the governing deformation mechanism over the investigated parameter range, even for relatively thick plates.

Consequently, the combined rotational stiffness is controlled almost entirely by the plate bending stiffness, while the influence of the dowels and the timber bearing stiffness becomes negligible. Further refinement of the dowel or bearing formulations, therefore, provides little improvement in the prediction of the global in-plane stiffness. For practical applications, the in-plane behaviour can be adequately represented using the plate's lateral bending stiffness alone, or, where appropriate, by idealising the connection as a hinge.

5.2.2. **Out-of-Plane Connection Behaviour**

To evaluate the influence of connection geometry, multiple dowel patterns are analysed. A constant beam height of 320 mm is adopted to ensure adequate dowel spacing for the larger dowel diameters. The selected dowel patterns in Figure 39 represent both commonly used configurations and geometries that are expected to produce distinct structural behaviour. In particular, the spacing differences between the 2x2 and 3x2 configurations are introduced to evaluate the effects of increased spacing and force transfer parallel to the timber grain.

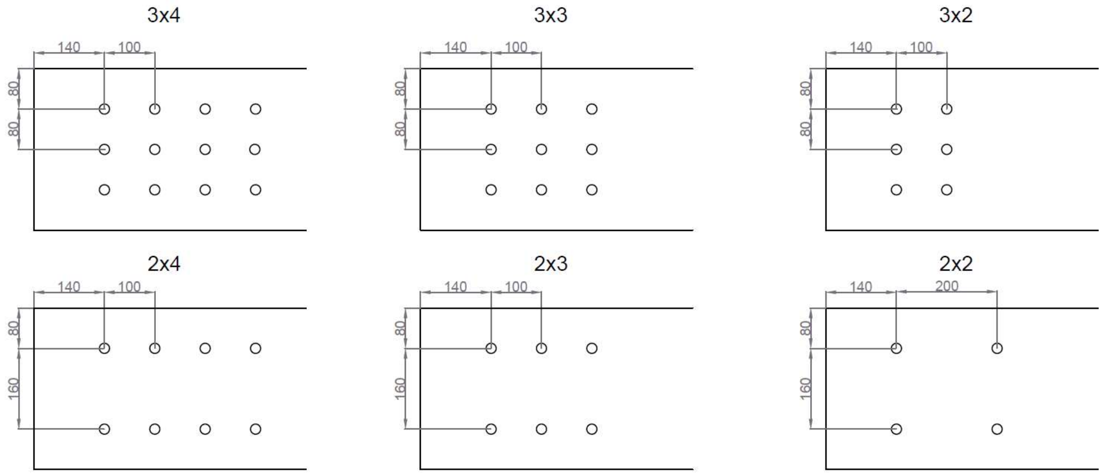

Figure 39: Dowel-group layouts used in the analytical study. Spacing and edge distances were selected to accommodate dowel diameters up to 20 mm while providing different force-to-grain distributions.

The parameter studies show that timber density and dowel diameter produce an approximately linear increase in rotational stiffness across all investigated dowel patterns, as shown in Figure 40. Although the absolute stiffness differs considerably between the connection geometries, the relative influence of both parameters remains remarkably consistent. Increasing timber density increases the stiffness of every individual dowel through the embedment stiffness, whereas increasing the dowel diameter primarily increases the bending stiffness of the fastener. Consequently, the stiffness ranking of the investigated dowel patterns remains largely unchanged over the examined parameter range.

In contrast, the embedment-length response remains strongly nonlinear and varies considerably between dowel patterns and dowel diameters. This indicates that connection geometry not only

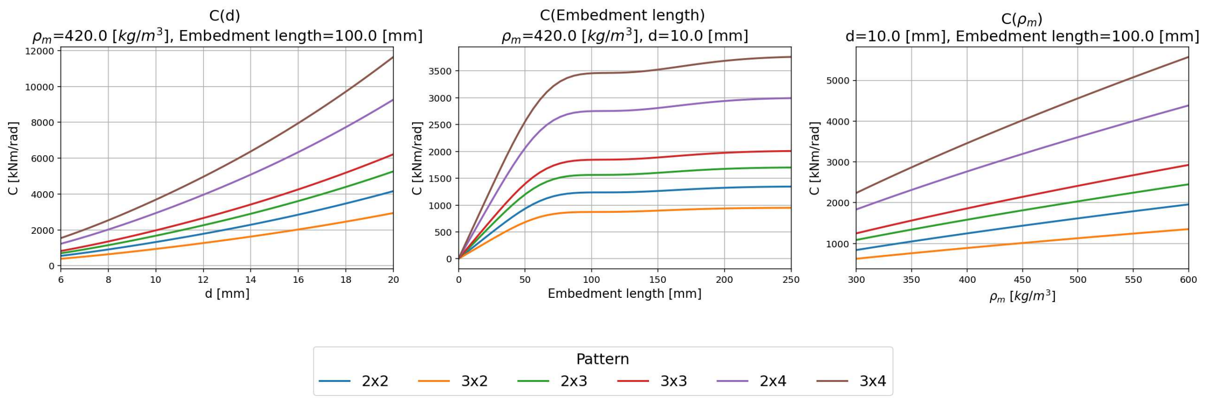

Figure 40: Influence of dowel diameter, embedment length, and timber density on rotational stiffness for the investigated dowel-group patterns. In each analysis, two parameters are held constant.

determines the magnitude of the rotational stiffness but also influences how efficiently additional embedment length can be mobilised.

5.2.3. Eurocode 5 Comparison

Using the previously established embedment-length range, the analytical stiffness formulation is compared with the Eurocode 5 slip modulus according to:

$$n \sum_i K_{ser} \cdot \frac{r_i^3}{r_{max}} = C_{yy}\,, \qquad K_{ser} = 2\,\frac{\rho_m^{1.5} d}{23} \tag{29}$$

The Eurocode 5 formulation depends primarily on timber density, dowel diameter and the local dowel-group geometry. In contrast to the analytical formulation, embedment length is not included explicitly as a governing parameter.

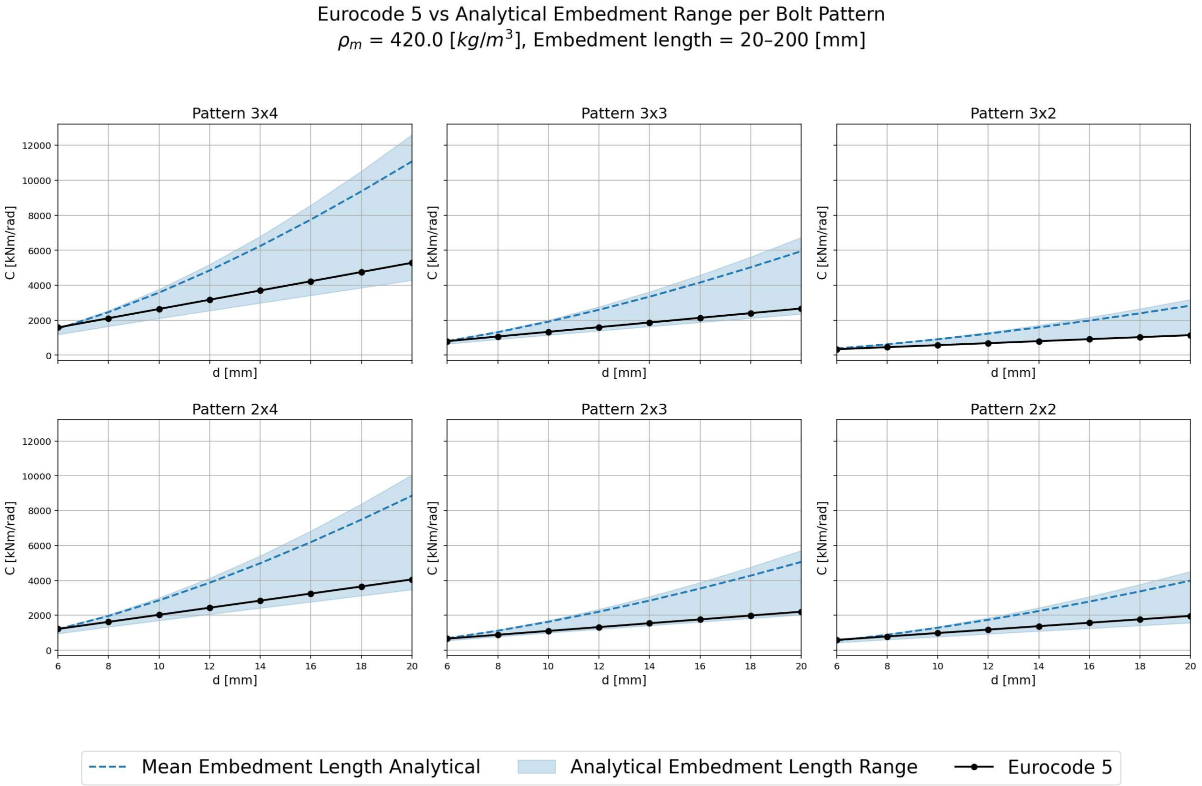

Figure 41: Comparison between the analytical stiffness formulation and the Eurocode 5 stiffness prediction for varying dowel diameters. The shaded region represents the analytical stiffness range obtained for embedment lengths between 20 and 200 mm.

Figure 41 compares the analytical stiffness predictions over the investigated embedment-length range with the corresponding Eurocode 5 values. The Eurocode 5 formulation corresponds approximately to the lower bound of the analytical stiffness range, which is associated with embedment lengths of approximately 25 mm. As the embedment length increases, the analytical formulation predicts progressively higher rotational stiffnesses, resulting in a widening gap between the two approaches.

The mean analytical stiffness lies closer to the upper bound of the investigated range than to its midpoint. Furthermore, the difference between the mean analytical stiffness and the Eurocode 5 prediction increases with dowel diameter, indicating that the two formulations exhibit different stiffness developments over the investigated parameter range.

5.3. Discussion

5.3.1. **Force Distribution**

Although the rotational stiffness of the connection can be determined directly from the contributions of the individual dowels, verification of the connection also requires the corresponding forces acting on each fastener. The same stiffness-based formulation used to derive the rotational stiffness can therefore be employed to distribute the applied hinge actions over the dowel group.

The force carried by the dowel due to an applied moment is determined from Formula 25, where $k_i$is the rotational stiffness contribution of the individual dowel and $r_i$is its distance from the centroid of the connection. The force is subsequently projected onto the unit vector perpendicular to the dowel radius,

$$\hat{F}_{M,i} = F_i \hat{v}_{r,i} \tag{30}$$

which defines the local loading direction acting on each dowel.

Figure 42/Table 3 illustrates the resulting force distribution for a representative dowel group for a unit moment. As expected, the outer corner dowels carry the largest proportion of the applied moment owing to their larger lever arms. In contrast, the inner dowels contribute primarily to the overall rotational stiffness of the connection.

Dowel	Load-to-grain angle [∘]	Force per shear plane 1 kNm [N]
1	61.93	622
2	90	460
3	61.93	622
4	32.01	460
5	90	153
6	32.01	460
7	32.01	460
8	90	153
9	32.01	460
10	61.93	622
11	90	460
12	61.93	622

Table 3: Force distribution per shear plane and corresponding load-to-grain angle for each dowel in the 3 × 4 dowel group under a unit bending moment of 1 kNm.

The resulting force distribution demonstrates that the applied moment is resisted through forces proportional to both the rotational stiffness and the radial distance of each dowel from the connection centroid. Consequently, increasing the spacing of the outer fasteners is generally more effective than simply increasing the total number of dowels, since the resisting moment increases with both the applied force and the corresponding lever arm. Connection geometry, therefore, influences not only the magnitude of the rotational stiffness but also the distribution of forces within the connection.

In addition to the rotational loading, axial and shear forces are assumed to be distributed uniformly over the dowel group,

$$\hat{F}_{N,i} = \frac{N}{2n} \hat{v}_x \tag{31}$$

$$\hat{F}_{V,i} = \frac{V_z}{2n} \hat{v}_z \tag{32}$$

The three loading components are subsequently combined vectorially for every dowel,

$$\hat{F}_{d,i} = \hat{F}_{M,i} + \hat{F}_{N,i} + \hat{F}_{V,i} \tag{33}$$

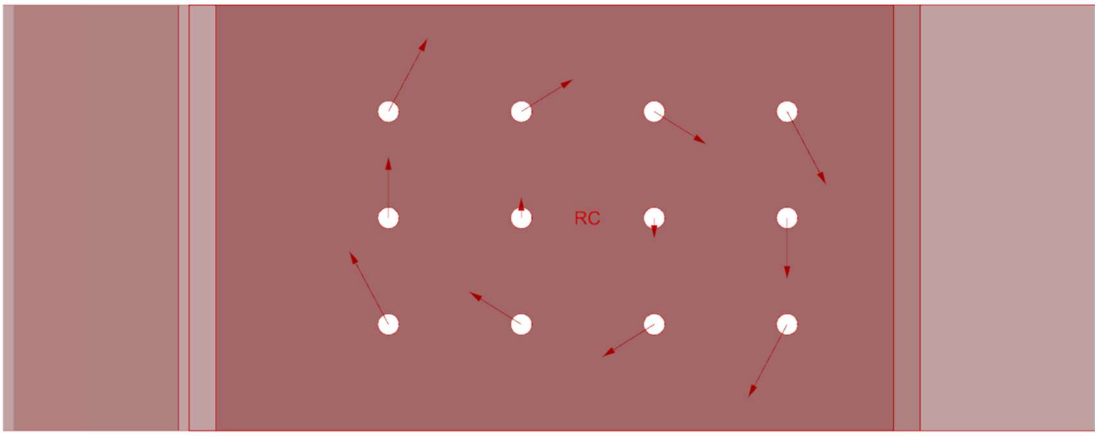

Figure 42: Force vectors generated by a unit bending moment acting on the 3 × 4 dowel group. The vector magnitude is proportional to the rotational stiffness contribution and lever arm of each dowel and is shown scaled by a factor of 0.1 for clarity.

Representing the loading as vectors allows the resultant force magnitude and direction to be determined individually for every dowel. Consequently, the angle between the applied force and the timber grain is evaluated from the actual resultant loading rather than from the individual load components. This becomes particularly important for bearing verification, since the bearing strength of timber depends directly on the load-to-grain orientation. Under combined loading, the governing axial force generally rotates the resultant force towards the grain direction, resulting in higher bearing resistance than would be obtained by evaluating the individual load components.

5.3.2. **Selection of Embedment-Length Range**

Since embedment length exhibits the greatest variation in stiffness behaviour, an appropriate range of investigation must first be established. Rather than selecting this range arbitrarily, the embedment length corresponding to approximately 99% of the attainable rotational stiffness is adopted as an indicator of stiffness plateauing. Figure 42Figure 43 shows the resulting embedment-length development for all investigated dowel patterns.

Based on this criterion, an embedment length range of 20–200 mm was selected for subsequent analyses. The lower limit represents a practical minimum timber thickness for the investigated connection typologies. In contrast, the upper limit corresponds to the point beyond which further increases in embedment length provide only marginal improvements in rotational stiffness.

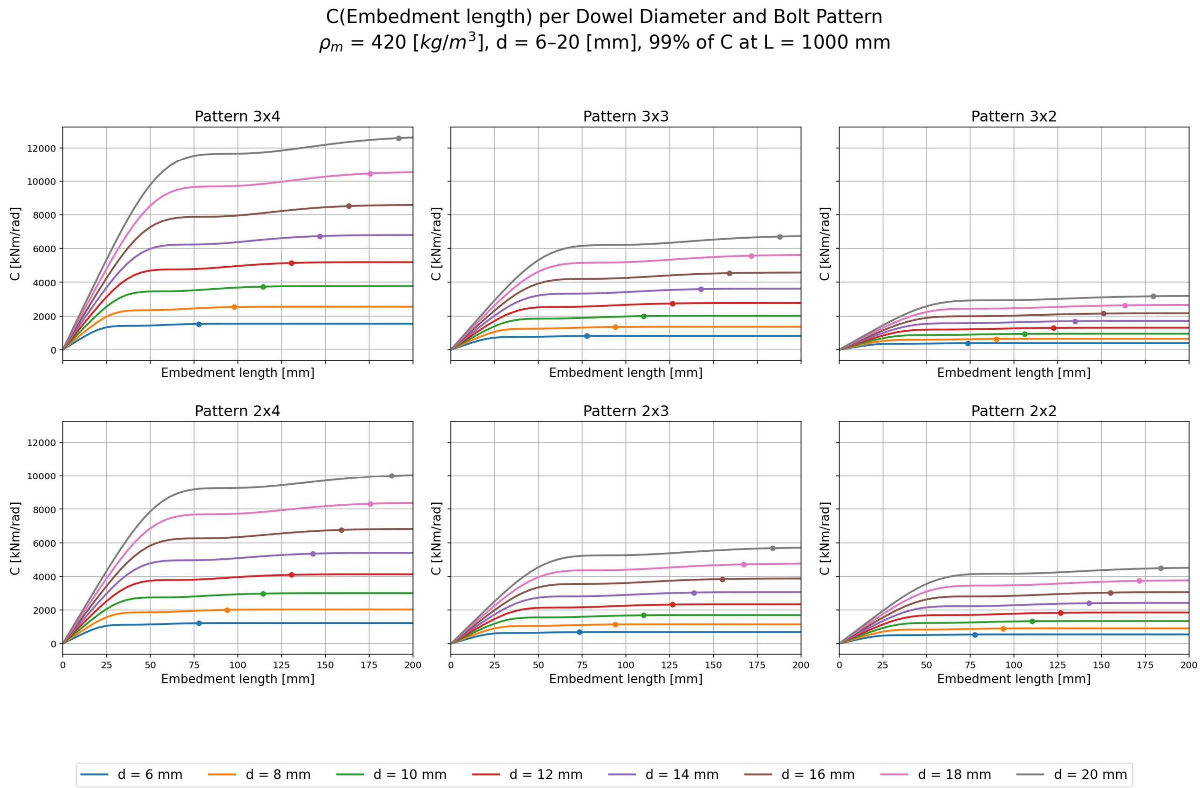

Figure 43: Identification of the stabilisation embedment-length limit using a 1% stiffness-development criterion. The shaded region represents the stiffness range associated with dowel diameters between 6 and 20 mm.

5.3.3. **Eurocode 5 Comparison**

The comparison between the analytical formulation and the Eurocode 5 slip modulus reveals systematic differences in the predicted rotational stiffness of multi-dowel connections. Since the Eurocode 5 formulation does not explicitly account for embedment length, its stiffness predictions depend primarily on timber density, dowel diameter and the local connection geometry. In contrast, the analytical formulation predicts additional stiffness development as embedment length increases due to the distributed interaction between the dowel and the surrounding timber. Consequently, the analytical model predicts progressively greater rotational stiffnesses as embedment length increases, with the difference becoming increasingly pronounced for larger dowel diameters.

It should be noted that the analytical formulation remains based on linear-elastic assumptions and does not account for local crushing, damage accumulation, or nonlinear embedment behaviour. The increased stiffness predicted by the analytical model should therefore be interpreted primarily within the context of serviceability behaviour rather than ultimate capacity.

When the analytical results are compared with the Eurocode 5 predictions for an embedment length of 25 mm in Figure 44, the discrepancies initially appear irregular. However, when the individual dowel patterns are evaluated with respect to the directional distribution of forces within the connection (Figure 45), a potential trend emerges.

Connections that transfer a relatively large proportion of their forces parallel to the grain, such as the 3×3, 3×2 and 2×3 configurations, consistently exhibit higher analytical stiffnesses than predicted by Eurocode 5. Conversely, more elongated dowel patterns, including the 2×2 and 3×4 configurations,

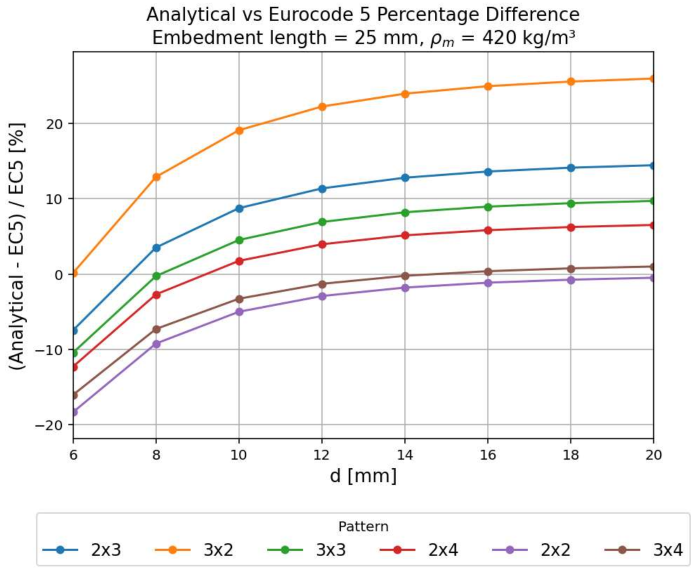

Figure 44: Percentage difference between the analytical rotational stiffness formulation and the Eurocode 5 stiffness prediction for varying dowel diameters and patterns.

transfer a larger proportion of their forces perpendicular to the grain and therefore produce analytical stiffnesses that lie closer to the Eurocode predictions.

These observations indicate that part of the discrepancy originates from the directional distribution of forces within the connection. Since the analytical formulation explicitly accounts for the anisotropic stiffness of the timber embedment, differences in dowel-group geometry directly affect the predicted rotational stiffness.

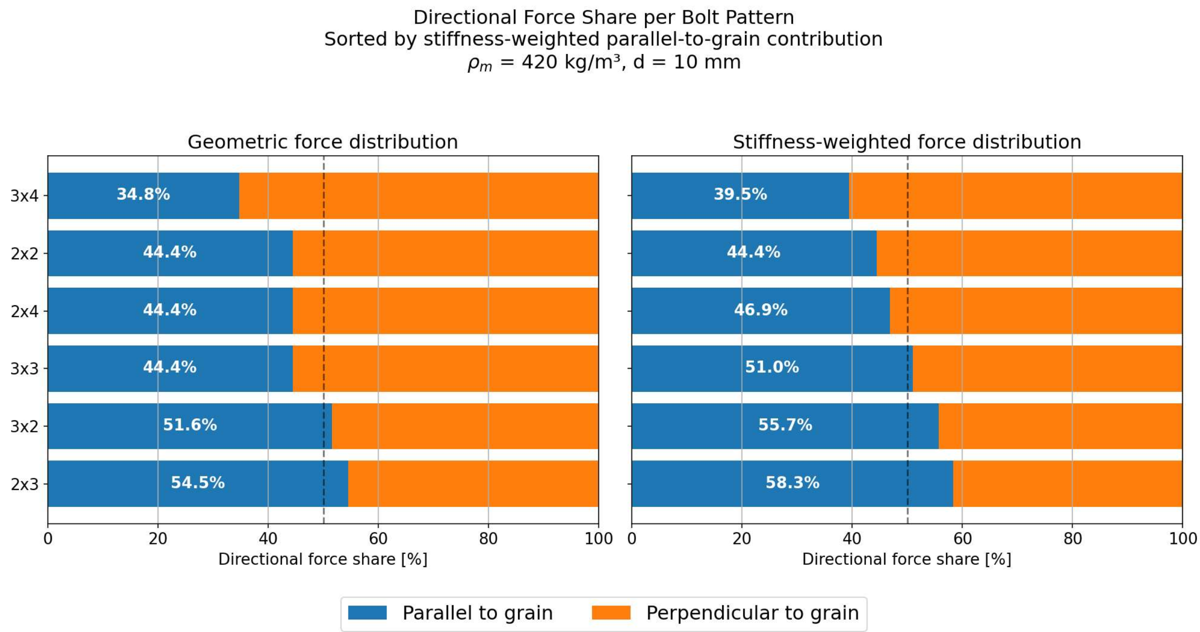

Figure 45: Parallel- and perpendicular-to-grain force shares for the investigated dowel patterns based on geometric and stiffness-weighted force distributions.

Although the directional force distribution explains part of the observed variation, it does not fully account for the systematic offset between the analytical formulation and Eurocode 5. Additional differences arise from how the governing parameters influence the stiffness response.

The analytical formulation predicts monotonic but nonlinear relationships with both dowel diameter and timber density, whereas the Eurocode 5 slip modulus is based on simplified empirical expressions. The influence of timber density is further complicated by the different stiffness development observed for loading parallel and perpendicular to the grain (Figure 46). Nevertheless, the analytical and Eurocode density ranges continue to overlap for most dowel diameters, indicating that timber density alone cannot explain the observed divergence.

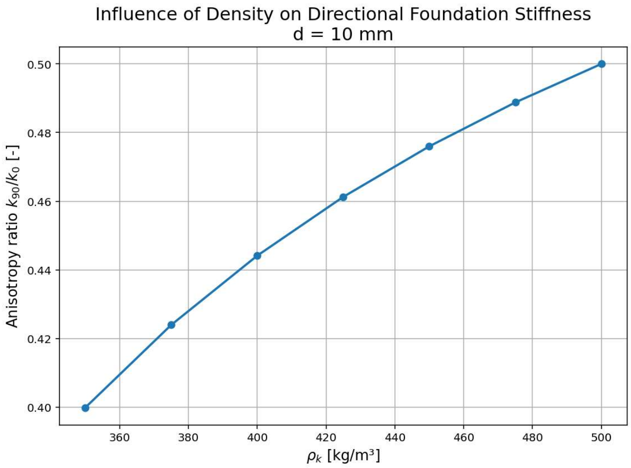

Figure 46: The difference in development of stiffness in the different grain directions for increasing densities.

The remaining difference appears to be governed primarily by dowel diameter. The analytical formulation predicts an increasingly steep stiffness development for larger diameters owing to the interaction between dowel bending, distributed timber support and finite embedment length. This nonlinear development is not represented to the same extent within the Eurocode 5 formulation, resulting in progressively larger differences for larger fasteners.

The comparison demonstrates that the discrepancies between the two approaches cannot be attributed to a single parameter. Instead, they result from the combined influence of connection geometry, force orientation and the different parameter sensitivities inherent to the two formulations.

More fundamentally, however, the analytical formulation and the Eurocode 5 slip modulus do not represent equivalent mechanical models. Eurocode 5 provides an empirically calibrated engineering expression intended to produce practical and robust stiffness estimates over a wide range of applications. The analytical formulation, by contrast, explicitly represents dowel bending, finite embedment length, and distributed timber-embedment interaction, while neglecting nonlinear material behaviour. Consequently, the two approaches should not be expected to produce identical stiffness predictions, even for identical geometric configurations.

The comparison, therefore, suggests that Eurocode 5 should be interpreted primarily as a conservative, design-oriented stiffness approximation rather than as a direct mechanical representation of dowel-bearing behaviour. Conversely, the analytical formulation provides greater insight into how individual geometric and material parameters affect rotational stiffness, making it particularly suitable for investigating connection behaviour and for supporting stiffness-informed design.

5.4. Conclusions

The rotational stiffness of multi-dowel connections is governed not only by the stiffness of the individual dowels but also by the spatial distribution of the fasteners within the connection. The analytical formulation demonstrates that the connection geometry directly influences both the rotational stiffness and the resulting force distribution, with dowels farther from the connection centroid contributing disproportionately due to their larger lever arms. Consequently, increasing the spacing of the outer fasteners is generally more effective for increasing rotational stiffness than simply increasing the total number of dowels.

The developed force-distribution formulation provides a direct relationship between the global hinge actions and the forces acting on the individual dowels. By combining the moment, axial and shear components into a resultant force for each fastener, the load-to-grain angle can be evaluated directly, allowing the connection capacity to be assessed consistently using the Eurocode 5 bearing formulation.

Comparison with Eurocode 5 shows that the analytical formulation predicts systematically higher rotational stiffnesses, particularly for larger embedment lengths and dowel diameters. These differences arise from the explicit representation of distributed dowel–timber interaction, finite embedment length, and anisotropic embedment behaviour, which are not explicitly represented in the empirical Eurocode slip modulus. Consequently, the analytical formulation is well-suited to investigating the influence of individual design parameters, whereas the Eurocode 5 formulation remains an efficient and conservative, design-oriented stiffness approximation.

Overall, the results demonstrate that the rotational behaviour of multi-dowel connections cannot be described adequately by considering individual dowels in isolation. Instead, the interaction between individual dowel behaviour, connection geometry and force distribution governs both the rotational stiffness and the verification of the connection. These findings provide the analytical basis for the numerical validation presented in the following chapter.

6. Finite Element Validation

6.1. Numerical Model

6.1.1. Purpose and Modelling Approach

A local finite element model is developed in Nastran/Femap to verify the analytical stiffness formulation. The numerical model is not intended to reproduce the complete connection geometry in full detail. Instead, it is designed to evaluate whether the analytical assumptions regarding dowel–timber interaction, local embedment deformation, and rotational stiffness are mechanically plausible.

To reduce computational cost, the model is simplified by exploiting symmetry, dividing the connection along the XZ symmetry plane(Figure 47). The steel plate is omitted from the numerical model to enable direct comparison of the timber–fastener interaction with the analytical beam-on-elastic-foundation formulation. Plate flexibility is included separately in the analytical stiffness model through the series stiffness relationship.

To prevent dowel spin, rotational degrees of freedom about the global y-axis are restrained at both ends of the fastener. This axis corresponds to the dowel's local x-axis. On the shear-plane side, the fastener is fully fixed to represent the symmetry and support conditions of the complete connection system.

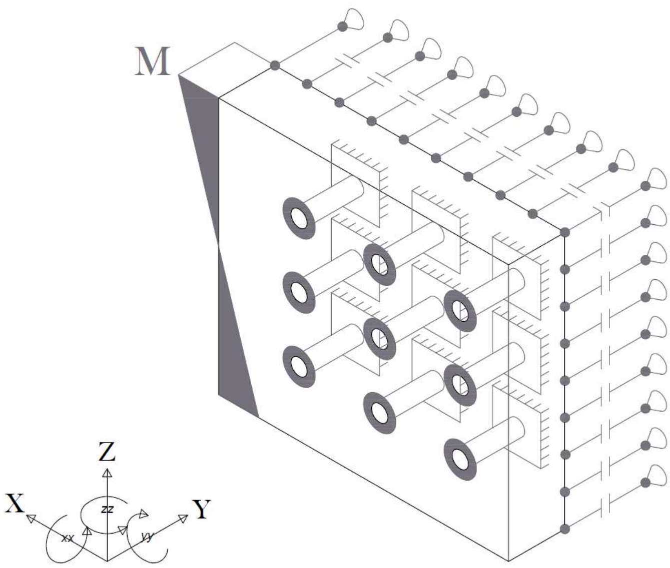

Figure 47: Finite element model and boundary conditions used for the local connection analysis. Compression-only gap elements represent the steel plate, symmetry is imposed through restrained dowels, and the connection is loaded by an applied moment.

In addition, the timber member is restrained from global translation in the y-direction at the right section interface, where the external load is applied. This constraint prevents rigid-body slip of the timber member relative to the dowels. The restraint is applied at the interface rather than at the beam end so that local deformation of the timber end remains unconstrained and so that plane sections remain plane, since the moment formulation is based on this assumption. The boundary condition, therefore, represents the symmetry and continuity of the remaining beam section that is not explicitly included in the model.

The finite element model is solved using the SOL106 nonlinear static solver in Nastran Femap 2406. The analysis is performed using 50 load increments. The stiffness update method is defined as ITER, in which the stiffness matrix is updated at each iteration to improve convergence during contact activation (Skotny and Hidalgo, 2018). Although the large-displacement formulation (LGDISP) was enabled following the recommended modelling procedure for nonlinear contact analyses, additional analyses indicated that its influence on the predicted rotational stiffness was negligible. The response is therefore governed primarily by the nonlinear activation of the compression-only gap elements rather than by geometric nonlinearity.

6.1.2. Timber and Fastener Discretisation

The timber member is modelled as an orthotropic solid using a structured hexahedral mesh with an element size of 5 mm. Hexahedral elements are selected because they provide a consistent mesh topology for the rectangular timber geometry while maintaining a suitable balance between accuracy and computational efficiency. Although higher-order tetrahedral elements may also provide accurate results, the hexahedral mesh offers greater consistency across the parameter variations considered in this study.

A finer mesh was evaluated, but resulted in only limited changes in the predicted stiffness response, while significantly increasing computational cost, as seen in Table 4Table 4: Influence of mesh refinement on the rotational stiffness obtained from the local finite element model.. The validation of a 2.5 mm mesh resulted in a maximum of 1.88% decrease in rotational stiffness for a 7600% increase in computation time.

	5 mm mesh		2.5 mm mesh	
[kNm/rad]	Front	Back	Front	Back
Rotational stiffness X	2094.3614	1842.1316	2060.0106	1838.9268
Rotational stiffness Z	2738.6310	2510.0992	2688.0230	2474.0189
Average	2296		2265	
Difference	1.37%			

Table 4: Influence of mesh refinement on the rotational stiffness obtained from the local finite element model.

The fastener is represented using beam elements rather than a full solid discretisation. The beam elements are connected to the timber hole through compression-only gap elements, which represent the contact interaction between the fastener and the surrounding timber and allow local bearing behaviour to develop. The fastener is fixed at the shear-plane interface to reproduce the support conditions imposed by the steel plate in the analytical model.

Compression-only gap elements are also applied at the timber–plate interface on the shear-plane side of the timber member. These elements prevent inward displacement of the timber towards the plate upon contact, thereby enforcing the intended bearing behaviour of the connection. By providing additional compressive restraint at the interface, the gap elements increase the local support stiffness and consequently the predicted rotational stiffness of the connection.

The penalty stiffness assigned to the gap elements must be sufficiently large to minimise numerical penetration while avoiding excessive numerical ill-conditioning. A commonly adopted guideline is to select a penalty stiffness three orders of magnitude larger than the representative material stiffness. A sensitivity study showed negligible differences between the stiffness values of 10^6 and $2.1 \cdot 10^8$, the latter corresponding to the Young's modulus of steel multiplied by a factor of 1000. Since the penalty value primarily serves numerical stabilisation purposes, further increases provide limited mechanical benefit while increasing computational expense. Consequently, rounded representative stiffness values are adopted for the gap elements, which can be seen in Table 5.

Element	Compression stiffness	Tension stiffness
C-Gap Dowel	$1 \cdot 10^8$	1
C-Gap Timber-Plate	$1 \cdot 10^7$	1

Table 5: Stiffness properties of the compression-only gap elements used in the local finite element model.

6.1.3. Local Material Stiffness Reduction Around Fastener Hole

Initial simulations using a standard orthotropic timber stiffness matrix overestimated the linear elastic bearing stiffness around the fastener hole. To account for local embedment softening, a reduced orthotropic stiffness matrix is assigned to a 10-mm-radius zone around the hole. This approach is adapted from the material model proposed by Kekeliak et al. (Kekeliak, An and Gocál, 2013).

A similar modelling strategy is presented by Fu et al. However, rather than reducing the stiffness of the local bearing zone, their approach directly modifies the dowel stiffness. (Fu *et al.*, 2024). Since the dowel is represented using beam elements rather than a full solid discretisation in the present study, the local stiffness reduction approach proposed by Kekeliak et al. is considered more appropriate.

The local stiffness reduction improves the agreement among the analytical, numerical, and Eurocode-calculated stiffnesses by accounting for the reduced embedment stiffness of timber in the immediate vicinity of the fastener.

The material properties used for the reduced embedment zone and the surrounding C24 timber are summarised below in Table 6.

Property	Embedment Zone (MPa)	C24 Beam (MPa)
$E_L(E_1)$	1170	11000
$E_T = E_R; E_{R(T)}(E_2; E_3)$	304	370
$G_{LT} = G_{RL};\ G_{LT(RL)}(G_{12}; G_{13})$	150	690
$G_{RT}; G_{LT}(G_{23})$	50	50
$Possions\ Ratio(12; 23; 13)$	0.4 ; 0.104 ; 0.4	0.4 ; 0.013 ; 0.4

Table 6: Orthotropic elastic material properties assigned to the C24 timber and reduced embedment zone.

To ensure consistent interaction between the beam and the local bearing zone, the number of nodes surrounding the hole is maintained across all dowel diameters. For the 8 mm dowel configuration, the surrounding solid elements are additionally subdivided to maintain the recommended hexahedral element aspect ratio limit of 1:5, since larger aspect ratios are more prone to numerical instability.

6.1.4. Application of Bending Moment

Since solid elements lack rotational degrees of freedom, the bending moment is represented by an equivalent force couple. The force couple is distributed over the loaded cross-section of the timber member via a Python script that connects to Nastran/Femap using the PyFemap library(Codex,-).

The script identifies the nodes on the loaded cross-section, sorts them by coordinate, and assigns nodal forces proportional to their distance from the neutral axis. Edge and corner nodes are assigned reduced weighting factors to account for their smaller tributary areas.

The nodal force distribution is derived from the classical elastic bending stress relation:

$$\sigma_x = \frac{M_y}{I_y}(z - z_0)$$

The second moment of area is approximated using discrete nodal weighting:

$$I_y \approx \sum_j w_j\,(z_j - z_0)^2$$

The nodal force applied at the node i is then calculated as:

$$F_{x,i} = \frac{M}{\sum_j w_j\,(z_j - z_0)^2}\, w_i(z_i - z_0) \tag{34}$$

with:

$$A_i = w_i$$

This procedure applies the bending moment while avoiding artificial stress concentrations at individual nodes.

6.1.5. Extraction of Rotational Stiffness

The rotational stiffness is obtained from the applied moment and the equivalent rotation extracted from the deformation field surrounding the dowel holes. By evaluating only the nodal displacements within the local contact region, the method isolates the bearing deformation associated with dowel embedment behaviour. This allows direct comparison with the rotational response predicted by the analytical dowel-bearing formulation.

Including nodes farther from the dowel holes would introduce additional deformation mechanisms into the stiffness evaluation, such as shear deformation of the timber member, deformation of the reduced embedment zone, and global member flexibility. These mechanisms are generally represented separately in analytical line-model approaches and are therefore not considered part of the localised rotational stiffness associated with dowel embedment behaviour.

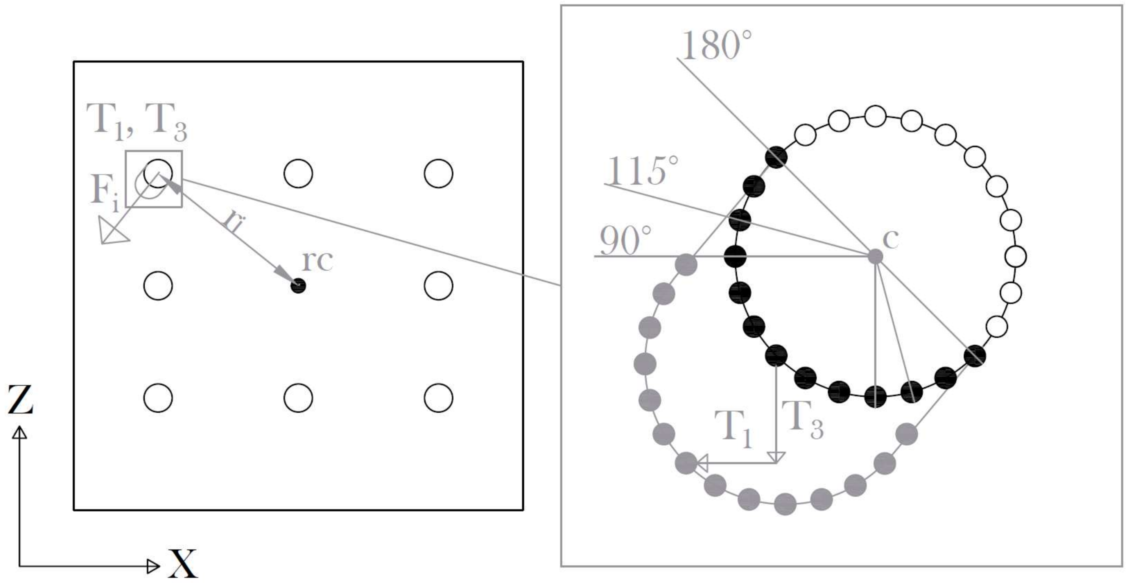

Figure 48: Definition of the bearing zones and displacement extraction points used for the rotational stiffness evaluation. Black nodes are included in the displacement extraction because they lie within the assumed contact angle, whereas white nodes are excluded as they do not experience compressive bearing.

Furthermore, nodes located outside the compressive contact region typically experience smaller deformations. Including these nodes in the rotational fitting procedure would therefore artificially increase the apparent rotational stiffness of the connection. For this reason, only nodes located within the compressive contact region of each dowel hole are considered. Multiple angular sectors are evaluated to investigate the sensitivity of the extracted stiffness to the assumed contact zone.

The investigated sectors, as seen in Figure 48 are defined as follows:

- The $180°$ The sector represents the full compressive half of the dowel hole and assumes that the entire half-perimeter contributes to bearing resistance.
- The $115°$ The sector represents the projected dowel-bearing surface commonly assumed in analytical bearing formulations and design approaches.
- The $90°$ The sector represents a more localised contact region and therefore provides a conservative approximation of the active bearing zone.

Although fewer nodes are included in the smaller sectors, these nodes experience the largest deformations and therefore still provide a representative estimate of the rotational response.

The projected bearing area is defined as:

$$A_b = dt$$

The projected bearing area is defined below, where d is the dowel diameter and t is the member thickness.

The out-of-plane rotational stiffness calculation assumes that the connection undergoes an equivalent rigid-body rotation about the geometric centre of the dowel group. The nodal displacement field obtained from the finite element model is projected onto this rigid-body rotational mode using a least-squares regression approach.

For an infinitesimal rotation about the global y-axis:

$$u_x = \theta_y z_r$$
$$u_z = -\theta_y x_r$$

where:

$$x_r = x - x_c$$
$$z_r = z - z_c$$

and (x_c, z_c) represents the global centre of rotation.

Since the finite element model does not behave as a perfectly rigid body due to orthotropic timber behaviour, gap-element contact response, and embedment-zone flexibility, the displacement field deviates from ideal rigid-body kinematics. The equivalent rotation is therefore obtained using a weighted least-squares formulation in which nodes located further from the centre contribute more strongly to the rotational fit. This weighting procedure is analogous to the polar second-moment formulation commonly used in connection mechanics.

The equivalent rotation is calculated as:

$$\theta_y = \frac{\sum(z_r T_1) - \sum(x_r T_3)}{\sum(z_r^2 + x_r^2)}$$

which gives:

$$C_{yy} = M \frac{\sum(z_r^2 + x_r^2)}{\sum(z_r T_1) - \sum(x_r T_3)} \tag{35}$$

This formulation provides an equivalent out-of-plane rotational stiffness for the localised dowel-hole bearing deformation, extracted directly from the finite element deformation field.

6.2. Results

Multiple finite element models are constructed to evaluate the effects of dowel diameter, dowel pattern, and embedment length on out-of-plane rotational stiffness; the extracted stiffnesses can be seen in Figure 49.

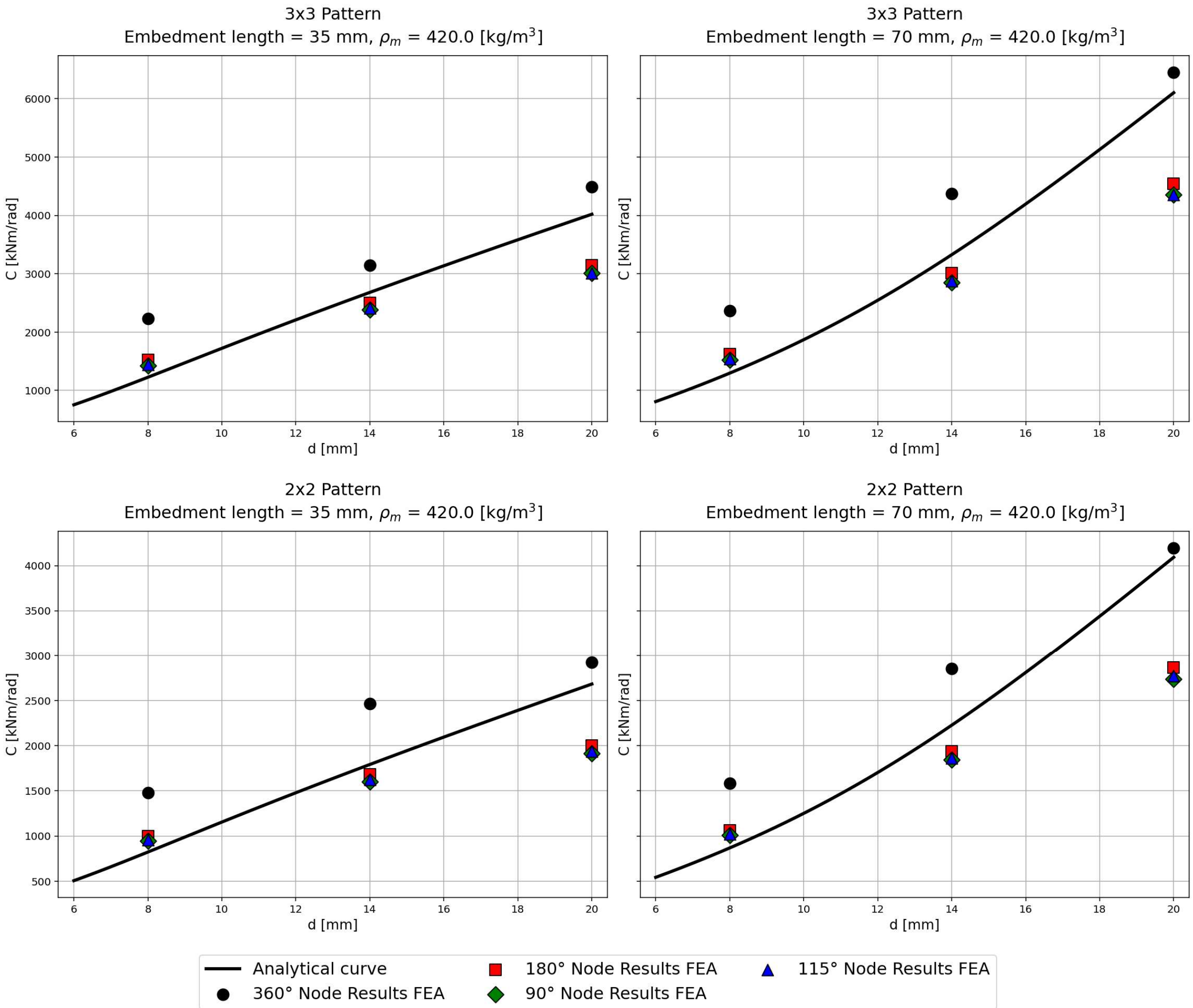

Figure 49: Comparison of analytical and finite element out-of-plane rotational stiffness predictions for varying dowel diameters and embedment lengths. Different bearing-zone definitions are used for the finite element stiffness extraction.

The out-of-plane rotational stiffness is extracted by evaluating nodal displacements surrounding the dowel holes. Different angular sectors are compared to evaluate the sensitivity of the extracted stiffness to the assumed contact region.

The results show that using the full 180° contact region produces significantly larger stiffness values because nodes outside the active compressive region experience substantially smaller deformations. Reducing the evaluated region to 115° and 90° produces more consistent stiffness values.

The relatively small difference between the 115° and 90° sectors indicate that the selected 115° contact region provides a reasonable approximation of the active dowel-bearing zone.

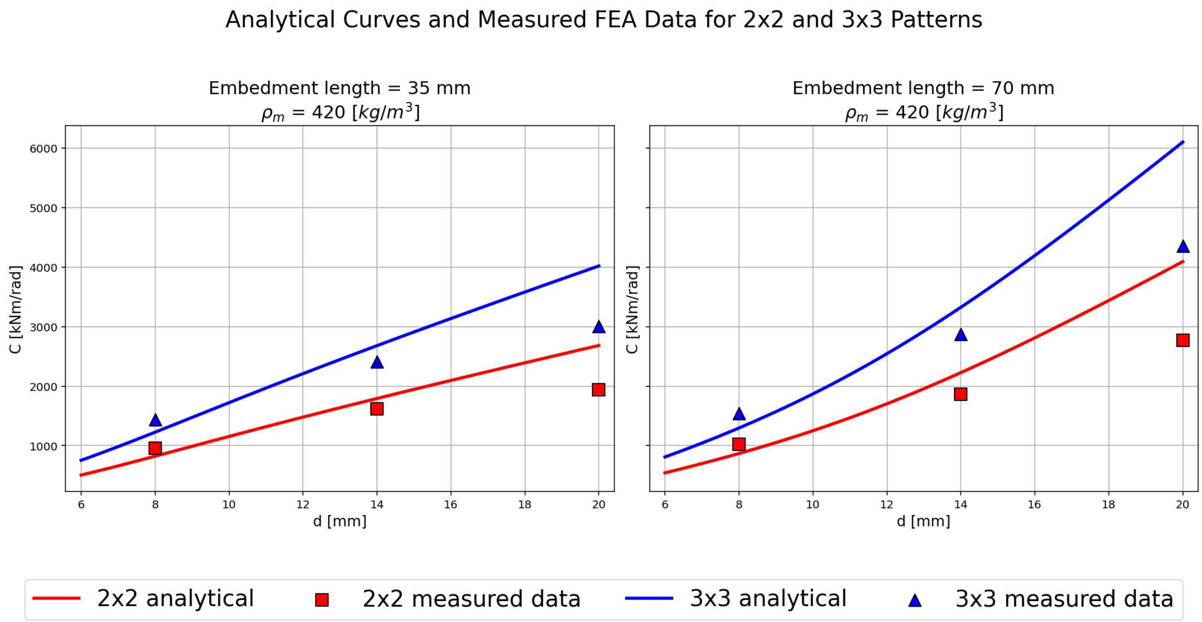

Figure 50: Influence of embedment length on the analytical and finite element out-of-plane rotational stiffness predictions for the 2×2 and 3×3 dowel patterns.

The comparison between the finite element results and the analytical stiffness curves shows generally consistent trends in the influence of dowel diameter and embedment length, as seen in Figure 50. Both approaches predict increasing out-of-plane rotational stiffness for increasing dowel diameter and embedment length.

However, the finite element results exhibit a less pronounced nonlinear increase than the analytical formulation. The analytical curves display stronger curvature for larger dowel diameters, whereas the finite element results remain closer to linear behaviour.

When comparing the finite element results with the Eurocode 5 formulation, as shown in Figure 51, a similar, approximately linear stiffness development as dowel diameter increases is observed. However, the finite element model also exhibits a clear increase in stiffness as embedment length increases. Since this parameter is not explicitly accounted for in the Eurocode 5 stiffness expression, the discrepancy between the two approaches increases with larger embedment lengths.

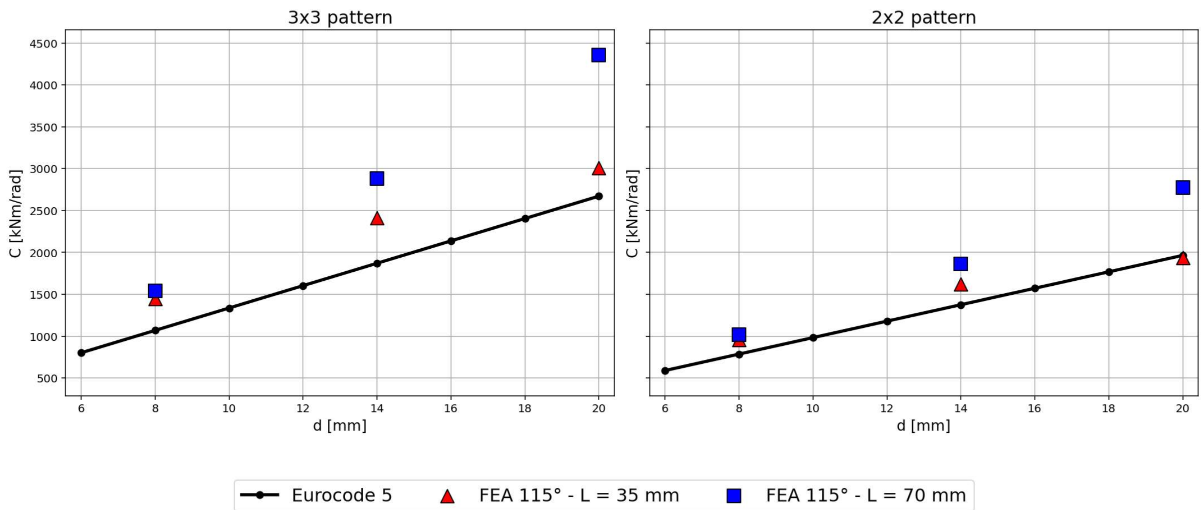

Figure 51: Comparison between Eurocode 5 stiffness predictions and finite element results for varying dowel diameters and embedment lengths.

6.3. Discussion

The finite element validation demonstrates generally consistent trends with the analytical formulation regarding the influence of dowel diameter and embedment length. Both approaches predict that out-of-plane rotational stiffness increases with increasing dowel diameter and embedment length, indicating that the beam-on-elastic-foundation formulation captures the principal deformation mechanisms governing the connection response.

The extraction procedure further demonstrates that the selected contact region significantly influences the evaluated out-of-plane rotational stiffness. Including the full 180° sector surrounding the dowel hole consistently produces higher stiffness values because nodes outside the active compressive contact zone experience relatively small displacements. In contrast, the difference between the 115° and 90° sectors remains comparatively small, suggesting that the adopted 115° sector provides a reasonable representation of the active bearing region while remaining consistent with the projected bearing surface assumed in the analytical formulation.

Although both approaches exhibit similar global trends, the analytical formulation predicts a more pronounced nonlinear increase in out-of-plane rotational stiffness than the finite element model. The analytical curves show a stronger increase in stiffness with increasing embedment length and dowel diameter, whereas the finite element results display a damped response. Consequently, the agreement varies across the investigated parameter range, with differences ranging from approximately 20% overestimation to 30% underestimation (Figure 52).

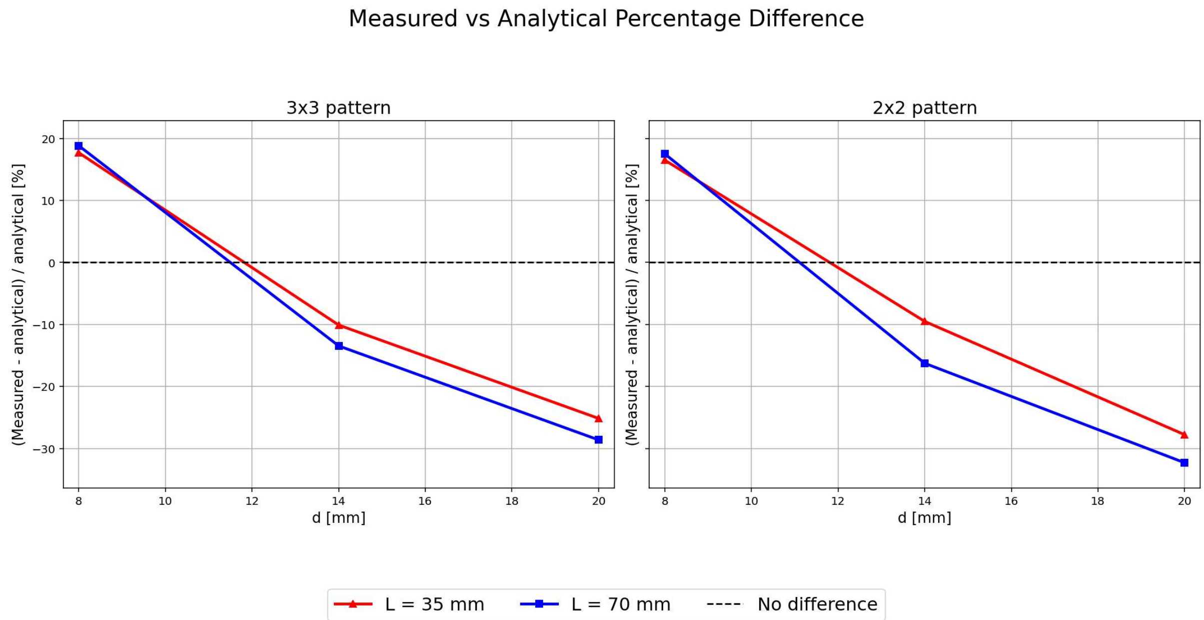

Figure 52: Percentage difference between the finite element and analytical stiffness predictions for the 2×2 and 3×3 patterns at embedment lengths of 35 mm and 70 mm.

Several modelling assumptions may contribute to these discrepancies. The first concerns the representation of the reduced embedment zone surrounding the dowel hole. Since the analytical formulation derives its stiffness directly from the assumed embedment behaviour, any over- or underestimation of the local embedment stiffness directly influences both the magnitude of the predicted out-of-plane rotational stiffness and the onset of the characteristic plateau regions. The finite element model represents this behaviour through a reduced orthotropic material zone, the dimensions and stiffness of which remain approximate.

A second source of discrepancy may be the assumed extent of the reduced embedment zone. Throughout the present study, a constant radius of 10 mm was used for all dowel diameters. In reality, however, the stress field around a dowel scales with fastener size(Todd, 2026), suggesting that both the extent of the softened material region and the mesh density around the hole should vary with dowel diameter. A diameter-dependent embedment zone may therefore improve the consistency of the numerical predictions.

Additional differences originate from the fundamentally different representation of the local contact behaviour. The analytical beam-on-elastic-foundation model assumes a continuously distributed elastic support along the embedded length. In contrast, the finite element model explicitly captures local contact interactions and stress concentrations around the dowel. These local effects increase the deformation of the surrounding timber and are therefore expected to reduce the apparent stiffness relative to the idealised analytical formulation.

The influence of the assumed embedment stiffness is further illustrated by the embedment-length study presented in Chapter 4. Increasing the embedment stiffness systematically reduces the embedment length required to reach the stabilisation plateau. Consequently, relatively small changes in the assumed local stiffness may significantly alter both the onset and the extent of the plateau behaviour observed in the analytical formulation.

Comparison with the Eurocode 5 formulation provides additional insight into the observed behaviour. For the shorter embedment length, the finite element predictions remain relatively close to the Eurocode stiffness, whereas the difference increases noticeably for the larger embedment length. This observation supports the analytical prediction that embedment length contributes additional out-of-plane rotational stiffness that is not explicitly represented in the Eurocode slip-modulus formulation. At the same time, the finite element analyses indicate that this additional stiffness develops more gradually than the current analytical model predicts.

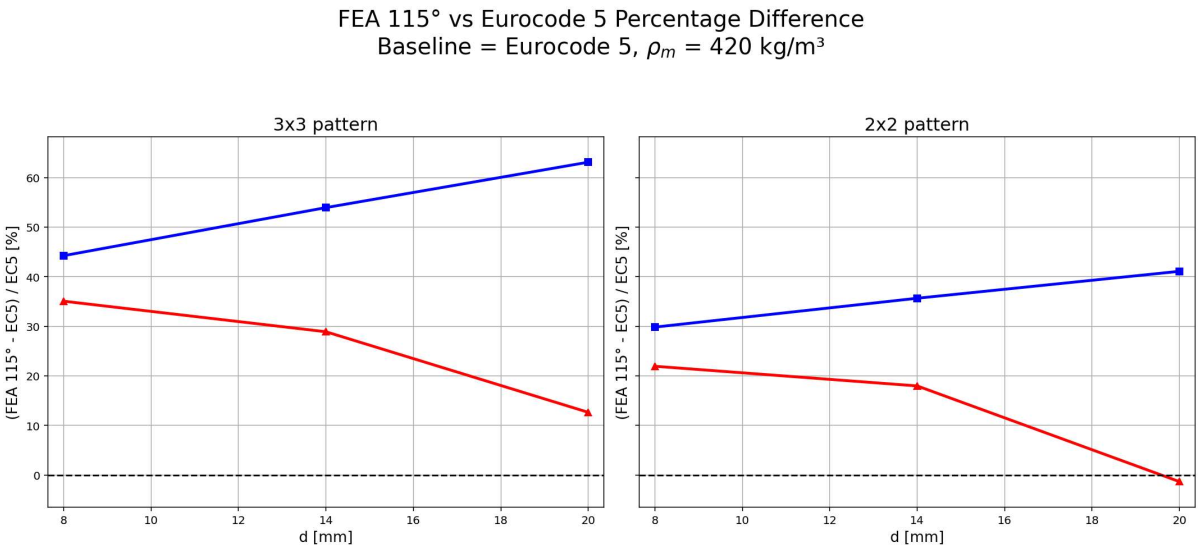

Figure 53: Percentage difference between the finite element stiffness and the Eurocode 5 stiffness prediction for varying dowel diameters and embedment lengths.

Overall, the finite element analyses support the principal trends predicted by the analytical formulation while highlighting several assumptions that influence the quantitative agreement. In particular, the representation of the local embedment stiffness, the extent of the reduced material zone and the idealised treatment of distributed bearing interaction appear to govern much of the remaining discrepancy between the analytical and numerical approaches. These observations provide the basis for calibrating the analytical formulation presented in the following section.

6.4. Calibration of the Analytical Formulation

The comparison between the analytical beam-on-elastic-foundation formulation and the finite element results revealed a consistent discrepancy in the predicted stiffness development. While both approaches show similar global trends, the analytical formulation predicts a stronger increase in out-of-plane rotational stiffness for larger dowel diameters and embedment lengths than observed in the numerical model. Consequently, it is useful to investigate which assumptions within the analytical formulation may contribute to this behaviour.

The characteristic parameter governs the embedment response:

$$\lambda = \sqrt[4]{\frac{kd}{4EI}}$$

which combines the embedment stiffness, dowel stiffness and dowel diameter into a single expression. Since the embedment stiffness formulation is adopted directly from Gikonyo et al., modifying it would imply disagreement with the underlying experimental calibration. Therefore, the present investigation focuses on the assumptions relating to dowel diameter and the effective bearing contact width.

The analytical formulation assumes that the effective bearing contact width is directly proportional to the dowel diameter. To investigate whether this assumption contributes to the observed discrepancies, a modified diameter relationship of the form:

$$ad^b$$

was introduced. The constants a and b were calibrated against the finite element results. The objective was not only to minimise the differences between the analytical and numerical results, but also to maintain a conservative analytical prediction wherever possible. Particular emphasis was placed on improving stiffness development with increasing embedment length, as this behaviour appeared strongly influenced by dowel diameter.

The calibration indicates that the analytical formulation tends to overestimate the effectiveness of increasing dowel diameter. Reducing the effective diameter used within the formulation results in a significantly improved agreement between the analytical and numerical results. The resulting variance between analytical and finite element stiffnesses decreases from approximately 50% to approximately 18%, while the analytical formulation remains predominantly conservative.

A second hypothesis concerns the dowel's own contribution to stiffness. Evaluation of the embedment-length response showed that the development of stiffness with increasing embedment length remained approximately linear with increasing dowel diameter. This behaviour suggested that the analytical formulation may overestimate the contribution of dowel bending stiffness for larger diameters.

To investigate this effect, a correction factor c was applied to the dowel radius used in the moment of inertia term:

$$E(cr)^4$$

Applying a radius reduction factor of $c = 0.9$ produced a substantially closer agreement between the finite element and analytical results. Under these assumptions, the maximum discrepancy seen in Figure 54 between the two approaches was reduced to below 5%, while the total variation between measured points remained of similar magnitude.

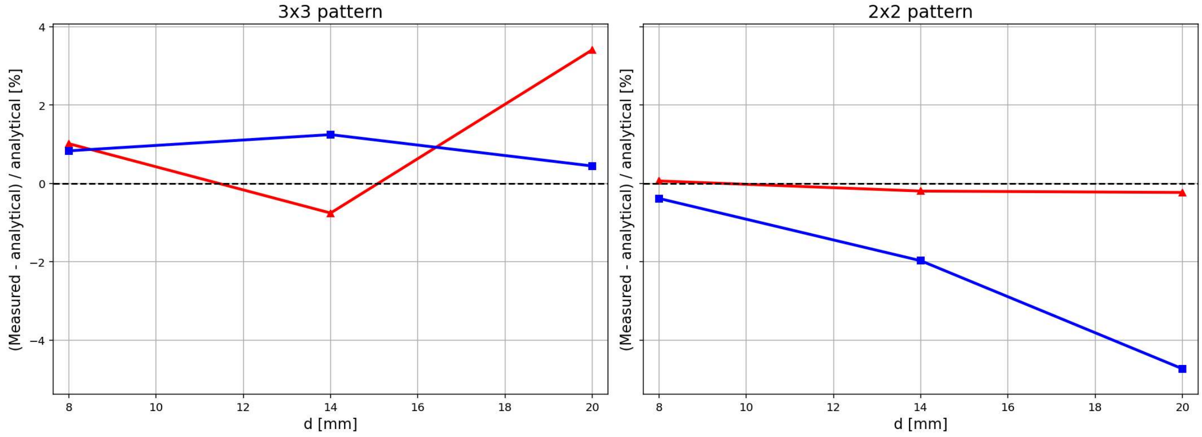

Figure 54: Percentage difference between the calibrated analytical formulation and the finite element results for the 2×2 and 3×3 dowel patterns.

The improvement observed with this modification suggests that the analytical formulation overestimates the effectiveness of increasing the dowel diameter. Whether the assumed contact width causes this, the representation of dowel bending behaviour, or other modelling assumptions cannot be determined conclusively from the present study.

A third observation concerns the treatment of grain-direction effects. The finite element results indicated that the majority of the load transfer occurred parallel to the grain. Consequently, assuming equal embedment stiffnesses in both principal timber directions produced a noticeably improved agreement between the analytical and numerical models without requiring further corrections.

This observation suggests that the influence of perpendicular-to-grain embedment behaviour may be overrepresented in the current analytical formulation. However, this conclusion remains tentative, since the material parameters adopted from Kekeliak et al. were derived primarily from tests performed in the principal grain directions. The behaviour at intermediate grain angles was not investigated explicitly and therefore remains a source of uncertainty.

After applying the diameter-related corrections, the influence of the grain-direction assumption became comparatively small. In fact, including the directional stiffness variation resulted in a slightly poorer agreement with the finite element results. This suggests that the diameter-related assumptions dominate the observed discrepancy, while the influence of grain-direction effects is secondary for the investigated connection configurations.

Combining the preceding adjustments yields the following empirically calibrated formulation:

$$k_{d,0}(l) = EI\,\frac{1.3 \cdot \lambda^3(\sinh(2\lambda l) + \sin(2\lambda l))}{\cos^2(\lambda l) + \cosh^2(\lambda l)} \tag{36}$$

$$with, \qquad \lambda = \sqrt[4]{\frac{9 \cdot k_{eff} d^{0.3}}{EI}}$$

The calibrated formulation provides substantially improved agreement with the finite element results and remains conservative throughout the investigated parameter range, as seen in Figure 55.

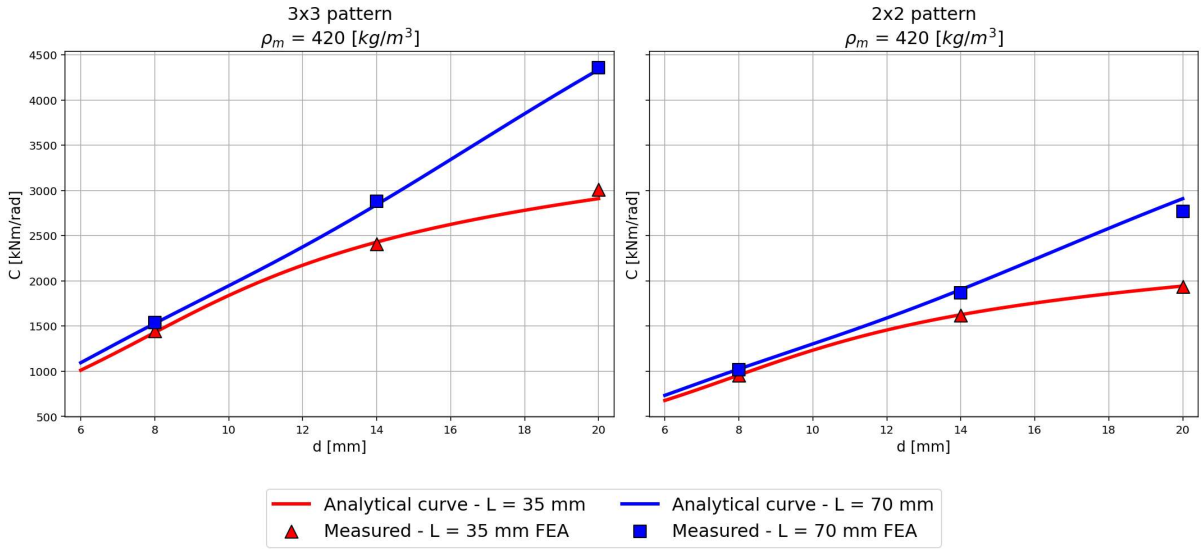

Figure 55: Calibrated analytical stiffness curves and corresponding finite element results for the 2×2 and 3×3 dowel patterns.

Although the modified formulation provides a substantially improved fit to the numerical results, its physical interpretation remains uncertain. When the implied contact widths are evaluated, the resulting contact areas for smaller dowel diameters become unrealistically large. For a 6 mm dowel, the required contact area exceeds half the dowel's circumference, which is unlikely in practice.

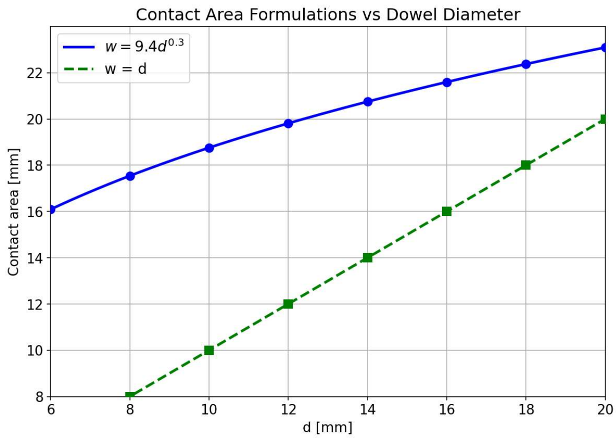

Figure 56: Effective contact width implied by the calibrated analytical formulation compared with the original diameter-dependent contact assumption.

Interestingly, the calibrated formulation suggests a decreasing effective contact width for increasing dowel diameters. While this may be a consequence of curve fitting, it may also indicate that the effective bearing zone surrounding the dowel does not scale linearly with diameter.

This observation indicates that the improved agreement may not necessarily originate from a more accurate representation of the physical contact width. Instead, the calibration may be compensating for other modelling assumptions in either the analytical or finite-element formulations. Potential sources include the assumed extent of the embedment zone surrounding the dowel, the representation of local stress concentrations, or the mesh discretisation adopted around the dowel hole.

Consequently, while the modified formulation demonstrates that a substantially improved agreement between analytical and numerical results is possible, additional research is required before the proposed calibration can be considered physically validated. The observed behaviour should therefore be interpreted primarily as an indication of where the analytical assumptions may be refined rather than as a definitive replacement of the original formulation.

6.5. Conclusion

The finite element validation demonstrates that the analytical beam-on-elastic-foundation formulation captures the principal influence of dowel diameter and embedment length on the out-of-plane rotational stiffness of steel–timber dowel connections. Both approaches predict similar global trends, indicating that the analytical formulation provides a mechanically consistent representation of the governing deformation mechanisms.

The comparison further demonstrates that the analytical formulation tends to predict a stronger nonlinear increase in out-of-plane rotational stiffness than the finite element model. The remaining discrepancies are primarily attributable to the representation of the local embedment behaviour, including the assumed embedment-zone stiffness, the extent of the reduced-material region surrounding the dowel, and the idealised treatment of distributed bearing interaction. These observations indicate that the analytical formulation captures the governing mechanics but simplifies several local deformation mechanisms present in the numerical model.

Calibration of the analytical formulation demonstrates that substantially closer agreement with the finite-element results can be achieved by refining the diameter-dependent assumptions governing dowel–timber interaction. The calibrated formulation reduces the discrepancy with the numerical results to below approximately 5% while remaining predominantly conservative. However, the calibrated parameters should be regarded as empirical corrections rather than as physically validated material properties, since they may simultaneously compensate for several simplifying assumptions in both the analytical and numerical models.

Overall, the finite element validation supports the analytical formulation as a suitable basis for predicting the out-of-plane rotational stiffness of steel–timber dowel connections. At the same time, it identifies the principal assumptions that govern the remaining discrepancies and provides a clear direction for future refinement of the analytical model. The calibrated formulation, therefore, forms the basis for the practical connection design and verification presented in the following chapter.

7. Case Study: C30

7.1. Modelling Assumptions

The objective of this case study is to demonstrate how the analytical and numerical methodologies developed in the previous chapters can be applied to the design of a practical timber gridshell connection. A 28 × 28 m gridshell with a diagonal grid spacing of 2.475 m is considered (Figure 57). To accommodate practical connection layouts, C24 timber members with a cross-section of 320 × 160 mm are adopted. The loading assumptions remain consistent with those used in the global analyses. To isolate the influence of out-of-plane connection stiffness, the in-plane rotational stiffness is evaluated between fully hinged and fully fixed conditions.

The following response quantities are extracted from the numerical model:

- Maximum and minimum global deflections
- Governing unity checks
- Absolute values of axial force, shear force, torsion, and in-plane and out-of-plane bending moments
- Locations of the governing force effects
- Governing load combinations associated with the critical response

Absolute force values are used throughout the evaluation. For the present study, the magnitude of the force effect is of primary importance, whereas the sign of the response frequently changes as the connection stiffness decreases. The use of absolute values, therefore, provides a clearer representation of the governing structural behaviour and avoids unnecessary complexity in interpreting the results.

To reduce numerical scatter associated with geometric non-linear analysis and minor differences between converged solution states, each analysis was performed three times (v1, v2 and v3). The reported results correspond to the mean values obtained from these analyses.

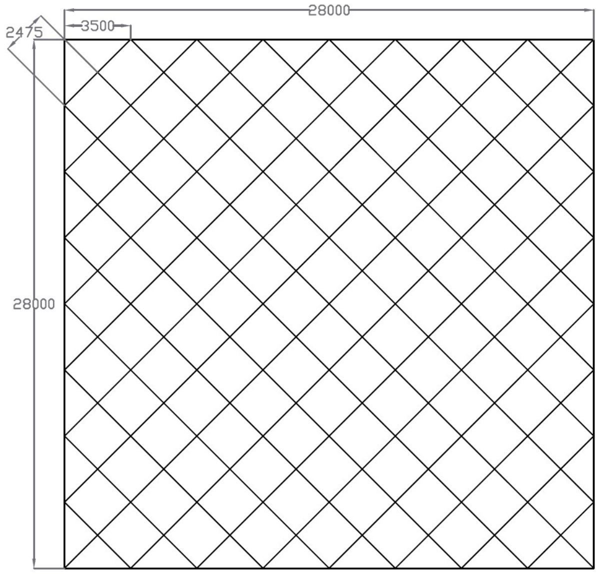

Figure 57: Plan view of the C30 gridshell geometry showing the overall dimensions and grid spacing.

7.1.1. Conversion to Connection Design Stiffness

Three stiffness definitions are required when translating global stiffness requirements into a practical connection design. The first corresponds to the ultimate limit state (ULS), which forms the basis of the global analysis and is therefore used to establish the target fixity factor.

Eurocode 5 relates the serviceability and ultimate stiffness through the expression:

$$K_{ser} = \frac{2}{3} K_u \tag{37}$$

Since the analytical connection model is formulated in terms of the serviceability stiffness and the output from the graphs is the ultimate stiffness, the relationship is rearranged as:

$$\frac{3}{2}C_u = C_{ser} \tag{38}$$

Consequently, the out-of-plane rotational stiffness obtained from the global analysis must be multiplied by a factor of 1.5 before comparison with the analytical stiffness predictions. Both stiffness definitions remain dependent on the density of the timber, for which the mean density values are adopted.

A second distinction concerns the stiffness values used for stability assessment. Structural stability verification is traditionally based on the 5th-percentile material properties, represented by $E_{0.05}$ and $\rho_{0.05}$. In the present model, the reduced Young's modulus affects the stiffness of the members, while the reduced density directly influences the out-of-plane rotational stiffness of the connections.

To ensure consistency between the global stability analysis and the analytical connection model, the stability-based serviceability stiffness is therefore expressed as:

$$\frac{3}{2}C_{u,0.05} = C_{ser,0.05} \tag{39}$$

This value is subsequently used as the stiffness target for the connection optimisation procedure.

7.2. Required global stiffness

7.2.1. **Global Behaviour and Stiffness Requirements**

Two critical stiffness thresholds can be identified from the global analyses. The first occurs at approximately α = 0.65–0.70, where the governing unity checks begin to increase rapidly due to growing bending moments and axial forces. The second occurs at approximately α = 0.37, below which the structure is dominated by bending moments and fails to converge in RFEM6.

The global and nodal force distributions shown in Figure 58 and Figure 59 do not exhibit the idealised moment redistribution that might initially be expected from the simplified arch analogy. Instead, the governing response is controlled by four critical corner regions, where relatively shallow shell inclinations coincide with significant force transfer between members. These regions generate elevated

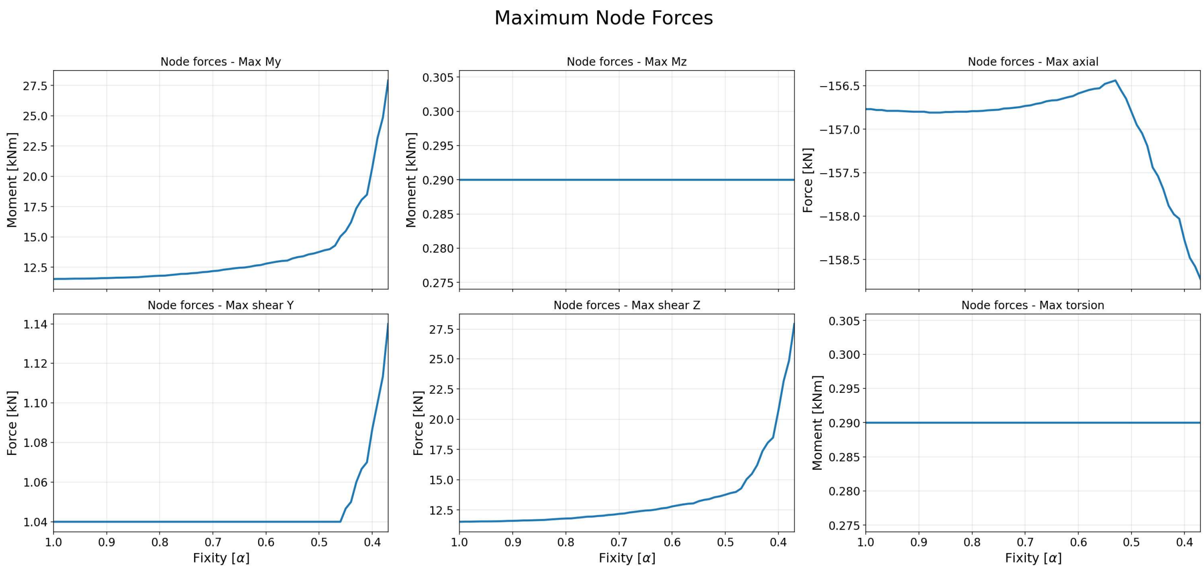

Figure 58: Maximum nodal force components as a function of the fixity factor α. Values are reported per node rather than per rotational spring.

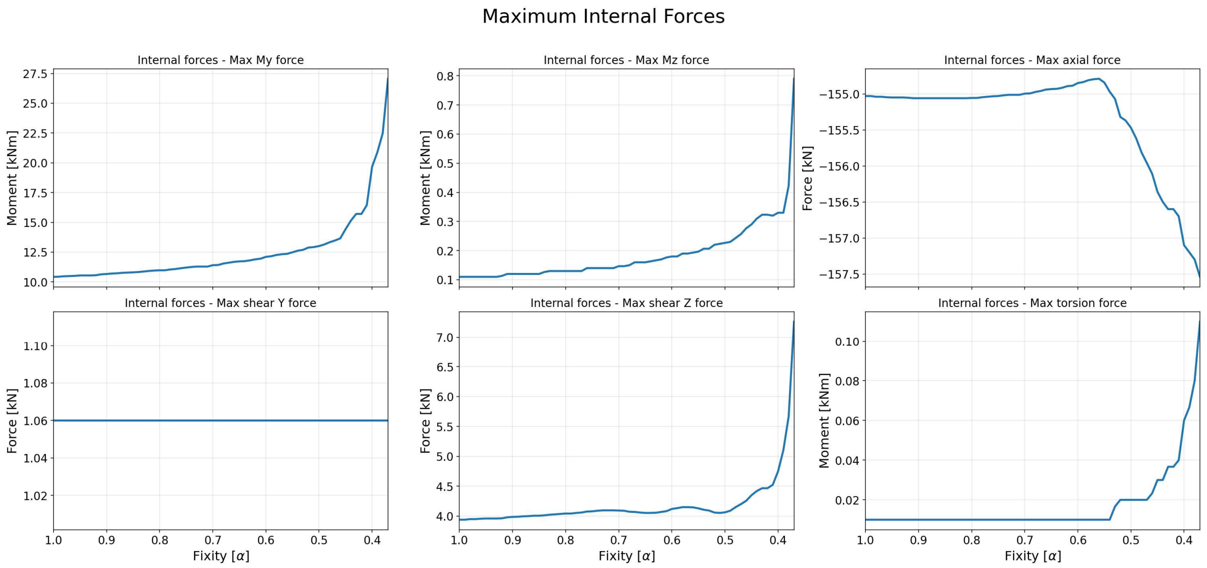

Figure 59: Development of the maximum internal forces in the gridshell as a function of the fixity factor α.

bending moments and axial forces that dominate the structural response. Consequently, the location of the governing moment does not transition as clearly with decreasing connection stiffness as suggested by the simplified global fixity study.

Nevertheless, the expected behaviour becomes visible when evaluating the moment distribution along the longest diagonal of the gridshell (Figure 60). At higher out-of-plane rotational stiffness values, distinct moment peaks develop at the nodes, indicating fixed-like behaviour. As the connection stiffness decreases, these peaks gradually diminish, and the structural response becomes increasingly governed by axial-force transfer.

The presented moment diagrams correspond to Load Combination 7 (quad-pyramid loading). Due to the asymmetric nature of this load case, the resulting moment distributions are not perfectly symmetric.

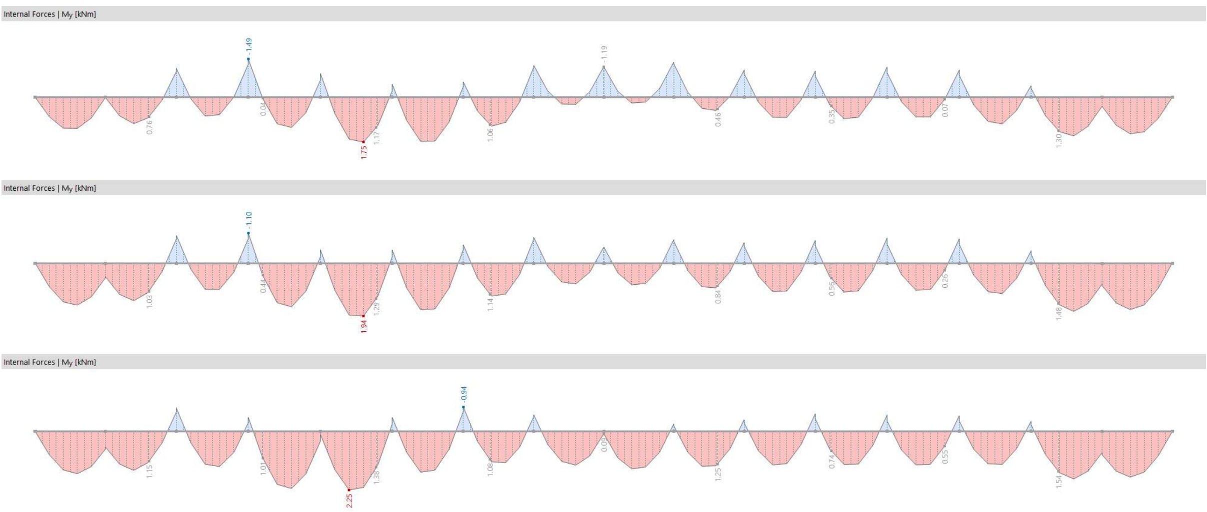

Figure 60: Bending moment diagrams of the central diagonal arch for decreasing fixity factors α, illustrating the redistribution of moments away from the nodes. From top to bottom: α = 1.0, 0.7 and 0.4.

In addition, localised effects occur near the edge elements, where lower stiffness values occasionally increase moment transfer between adjacent nodes. This behaviour appears to be related to the critical corner regions, where the shell curvature changes sign and may locally alter the influence of the out-of-plane rotational stiffness.

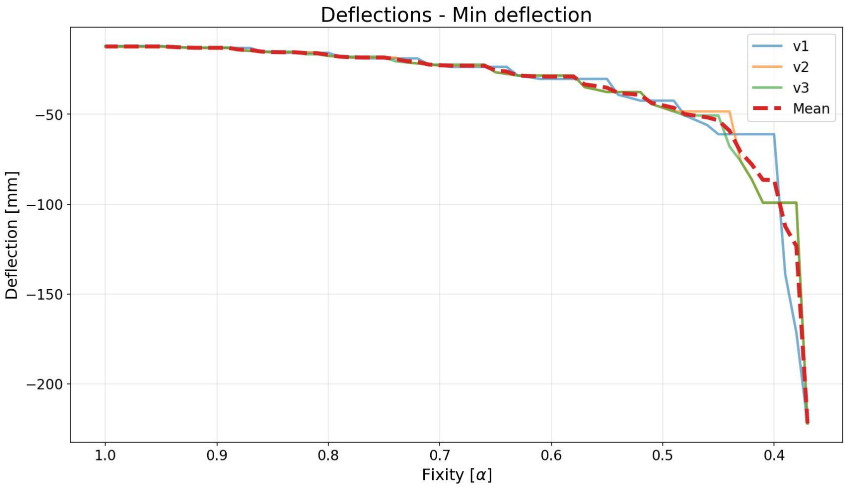

Figure 61: Maximum vertical deflection as a function of the fixity factor α for the three analysis runs and their mean value.

7.2.2. In-Plane Stiffness Effects

The previous analyses focused primarily on the influence of out-of-plane rotational stiffness, as this parameter was found to govern the gridshell's stability behaviour. However, the global parameter study also demonstrated that in-plane rotational restraint influences the required out-of-plane stiffness.

Preliminary analyses indicate that increasing in-plane stiffness reduces the out-of-plane stiffness required to achieve stable behaviour. However, directly increasing nodal in-plane rotational stiffness results in higher My, Mz, and torsional actions within the members. Consequently, additional global bracing appears to be a more efficient method of increasing shell stiffness than increasing the in-plane rotational stiffness of the connections themselves.

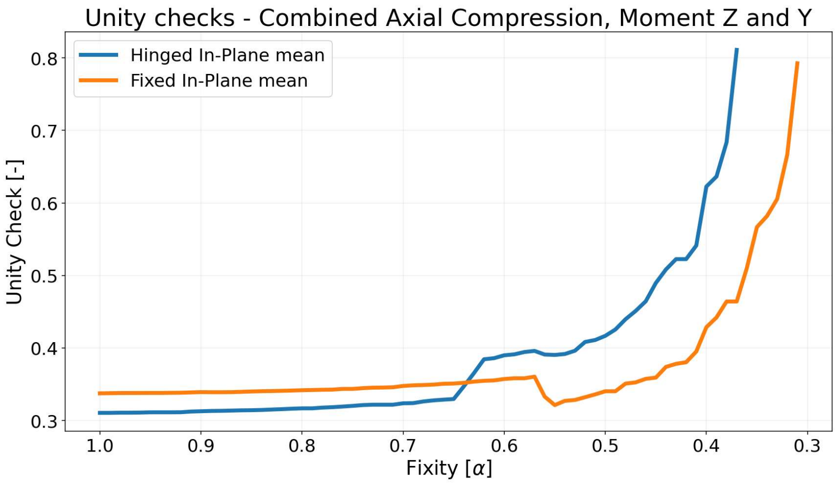

Figure 62: Development of the governing member unity check with decreasing fixity factor α.

The results further suggest that introducing additional bracing within the grid is generally more beneficial than increasing the nodes' in-plane rotational stiffness. Directly constraining in-plane rotation at the nodes significantly increases bending moments about the local z-axis and may generate additional torsional forces due to the differing rotational axes of intersecting members, as seen in Figure 62 and Figure 64 These effects can result in higher unity checks.

Consequently, where additional stiffness is required, introducing in-plane bracing may provide a more efficient means of improving stability than increasing the rotational stiffness of the connections. A detailed evaluation of these effects is presented in the following sections.

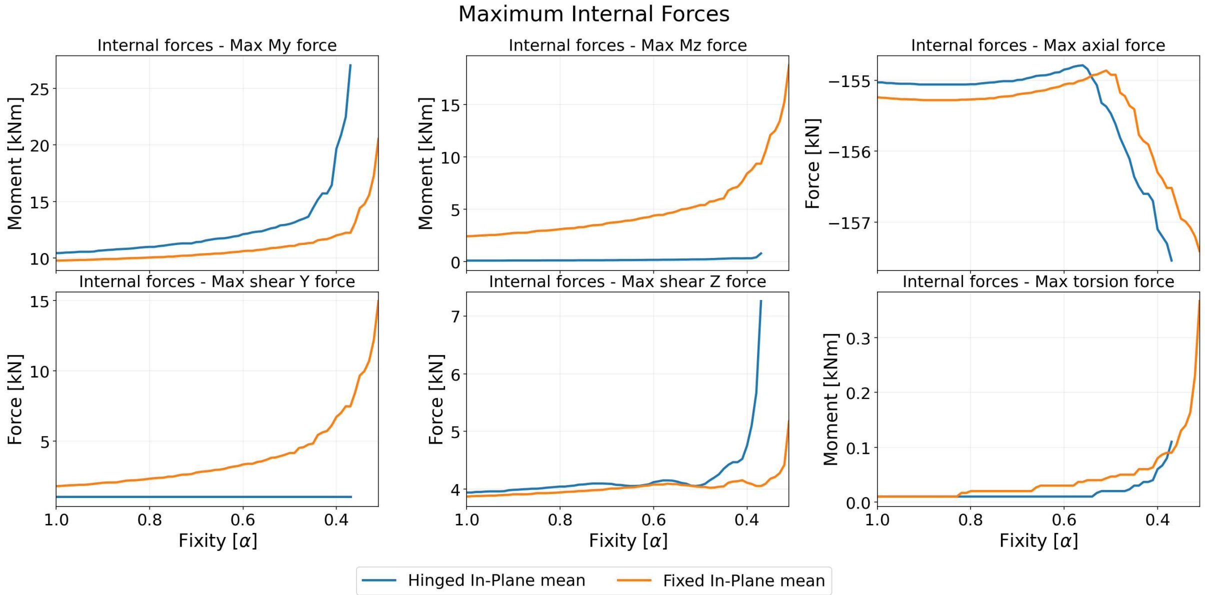

Figure 64: Development of the maximum internal force components with decreasing fixity factor α for hinged and fixed in-plane node.

7.2.3. **Stiffness Effects on Stability**

The stability of timber gridshells is strongly influenced by both geometric stiffness and the stiffness characteristics of the connection and beam system. Unlike conventional frame structures, gridshells derive a significant portion of their load-carrying capacity from their curved geometry and membrane action. Consequently, reductions in connection stiffness or the presence of geometric imperfections may significantly reduce stability and increase the structure's susceptibility to progressive collapse.

For the investigated gridshell, rotational stiffness is provided by the semi-rigid steel–timber knife-plate connections developed in the preceding chapters. In addition to the out-of-plane rotational stiffness, a limited amount of in-plane stiffness is provided by the welded plate connection. This stiffness contributes to the resistance against asymmetric deformation modes and progressive collapse. Additional in-plane stiffness could be introduced through local plate stiffeners or global bracing systems.

Creep buckling was not considered explicitly. Since the stability assessment is performed using characteristic material properties and reduced stiffness values corresponding to the ultimate limit state, the resulting behaviour is expected to remain conservative relative to long-term service conditions.

To obtain a reliable representation of the stability behaviour, multiple analysis methods were employed. Linear eigenvalue buckling analysis was used to identify the dominant instability modes and establish an initial estimate of the critical load factors. These analyses were subsequently supplemented with geometrically non-linear analyses incorporating imperfections, allowing the influence of connection stiffness and imperfection sensitivity to be evaluated more realistically.

In Eurocode 3, sway imperfections are generally neglected for critical load factors above 10, and combined sway and member imperfections become necessary below a factor of 4. Since gridshells are inherently imperfection-sensitive structures, a minimum reserve capacity of 10% above the design load was adopted in the present study.

Models with negligible in-plane stiffness exhibited severe convergence difficulties. Introducing representative in-plane stiffness values derived from the welded plate connection significantly improved convergence and produced more stable numerical behaviour, indicating that the in-plane stiffness contributes to the shell's physical stability rather than merely serving as a numerical stabilisation parameter.

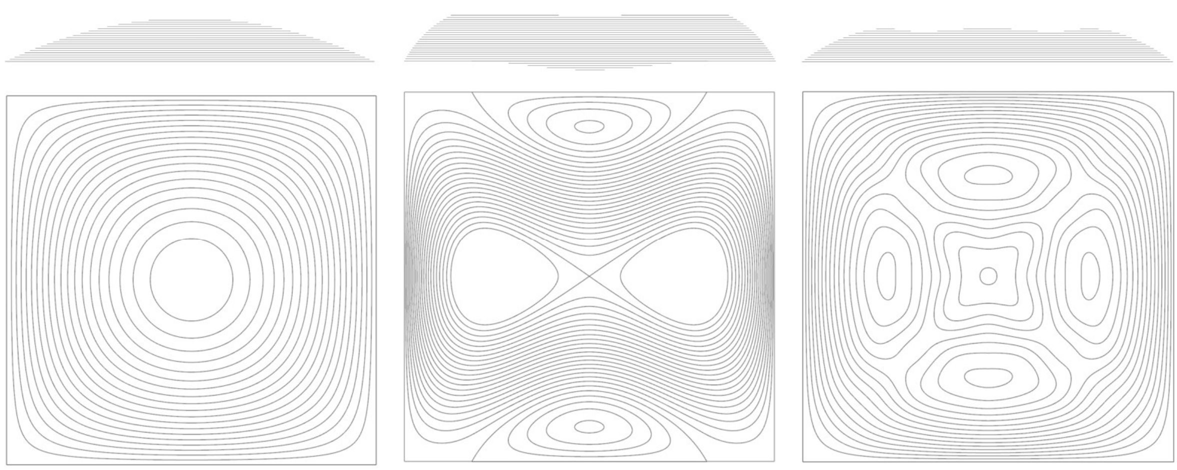

Figure 65: Isopleth lines of the original parabolic gridshell geometry and the applied symmetric and asymmetric imperfection shapes. The imperfection amplitudes have been exaggerated to 2 m for visual clarity.

To account for geometric imperfections, two representative imperfection modes were investigated, as illustrated in Figure 65.

The first mode consists of an asymmetric imperfection shape defined by

$$imperfection_{asym} = sin\left(\pi \cdot \frac{x}{28}\right) \cdot sin\left(\pi \cdot \frac{y}{28}\right) \cdot \left(\frac{(x-14)^2 - (y-14)^2}{14^2}\right)$$

The dimensions 28 m and 14 m correspond to the grid shell's plan dimensions. The second mode consists of a symmetric imperfection shape defined by

$$imperfection_{sym} = -cos(\pi \cdot \frac{\max\big(abs(x-14), abs(y-14)\big)}{14}) \cdot sin(\pi \cdot \frac{x}{28}) \cdot sin\left(\pi \cdot \frac{y}{28}\right)$$

Both imperfection shapes were scaled using an amplitude equal to

$$A = L_{eff} \cdot 0.0025$$

where L_{eff} represents the effective span between the points receiving zero imperfection. The resulting imperfection was applied to the original node coordinates according to

$$z_{imp,i} = z_i + imperfection \cdot \frac{L_{eff} \cdot 0.0025}{\max\big(abs(imperfection)\big)}$$

In addition to the global imperfection modes, a rotational imperfection of 0.005 rad was introduced along the elements to represent local fabrication and assembly tolerances. This imperfection was accumulated over consecutive elements sharing the same deformation direction, resulting in

$$z_{imp,i} = z_i + z_{imp,mode,i} + \tan(0.005) \cdot 2.475 \cdot n$$

where 2.475 m represents the average element length and (n) corresponds to the sequence number within a continuous region of equal sign.

An inverted asymmetric imperfection was also considered, as several loading combinations produced buckling modes closely resembling the inverse of the original imperfection pattern. Evaluating both directions, therefore, provided a more robust assessment of the imperfection sensitivity of the structure.

Initial linear eigenvalue analyses produced relatively low critical load factors, indicating that geometric non-linearity and imperfections would play an important role in the structural response. Subsequent geometrically non-linear analyses generally resulted in lower critical load factors than the corresponding linear analyses. Several load combinations, particularly the asymmetric imperfection cases, exhibited convergence difficulties during the geometrically non-linear analyses. These issues became significantly more severe when the in-plane stiffness was reduced to a hinge.

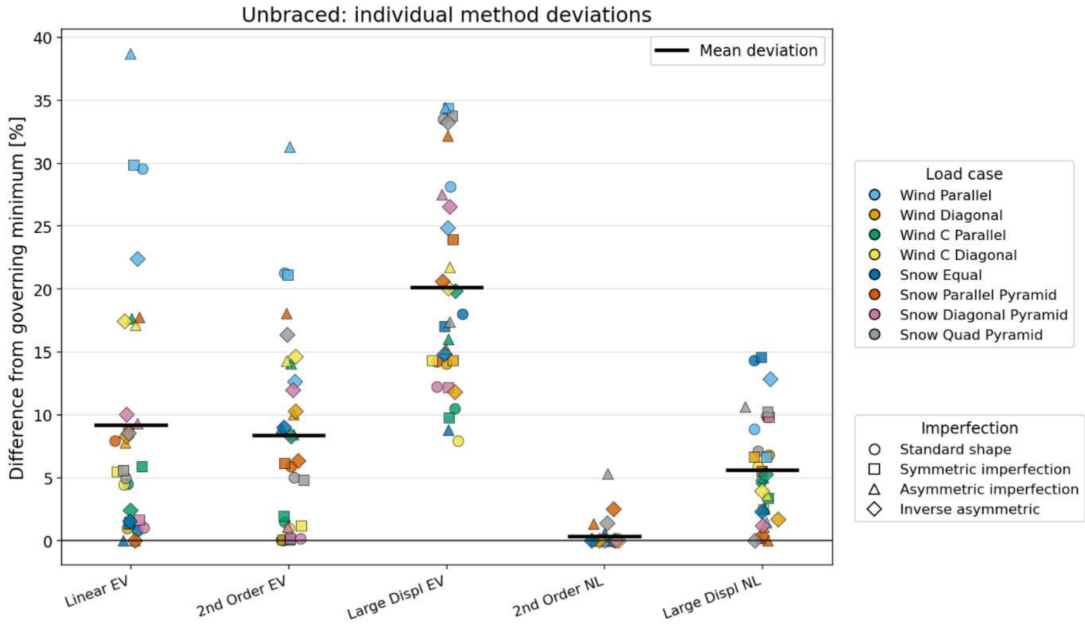

Figure 67: Comparison of stability analysis methods based on their deviation from the governing critical load factor. Deviations are calculated relative to the minimum critical load factor for each load case and imperfection case.

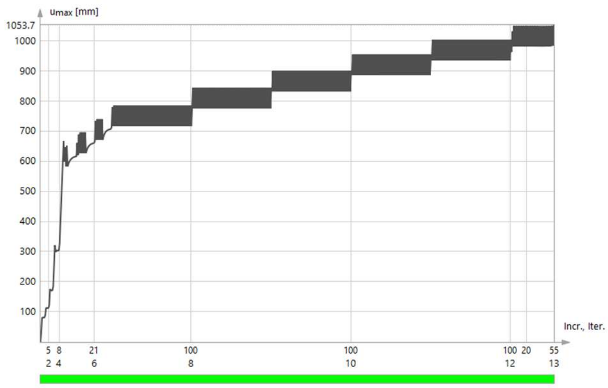

Figure 66: Convergence history of the second-order nonlinear analysis. The repeated oscillations between displacement levels indicate a sudden reduction in structural stiffness associated with a potential snap-through instability.

The convergence problems primarily occurred for the governing snow load cases and the parallel wind load case. The convergence histories displayed oscillations, seen in Figure 66, between displacement states, indicating a sudden reduction in structural stiffness associated with snap-through behaviour.

Large-displacement analyses confirmed that the shell possesses alternative post-critical equilibrium paths, including progressive inversion of the gridshell. This suggests that the observed non-convergence is linked to physical instability mechanisms rather than purely numerical effects. The stability analyses further demonstrated sensitivity to the selected load incrementation strategy. While the critical load factor remained nearly unchanged, with values of 1.220 and 1.228 differing by only approximately 0.7%, the corresponding deformation mode changed significantly. One solution followed the expected first-mode double-sine buckling shape, whereas the other showed a global inversion-type deformation of the gridshell, seen in Figure 68. This indicates that the structure operates close to a bifurcation point, where small numerical changes can cause the nonlinear solver to converge to different equilibrium branches. Consequently, the critical load factor is interpreted as robust in magnitude, whereas the post-critical deformation path appears sensitive to the numerical solution strategy.

Although the deformation paths differ substantially, both solutions correspond to nearly identical critical load factors. This suggests that the structure is approaching a bifurcation point at which multiple post-critical equilibrium paths become energetically comparable.

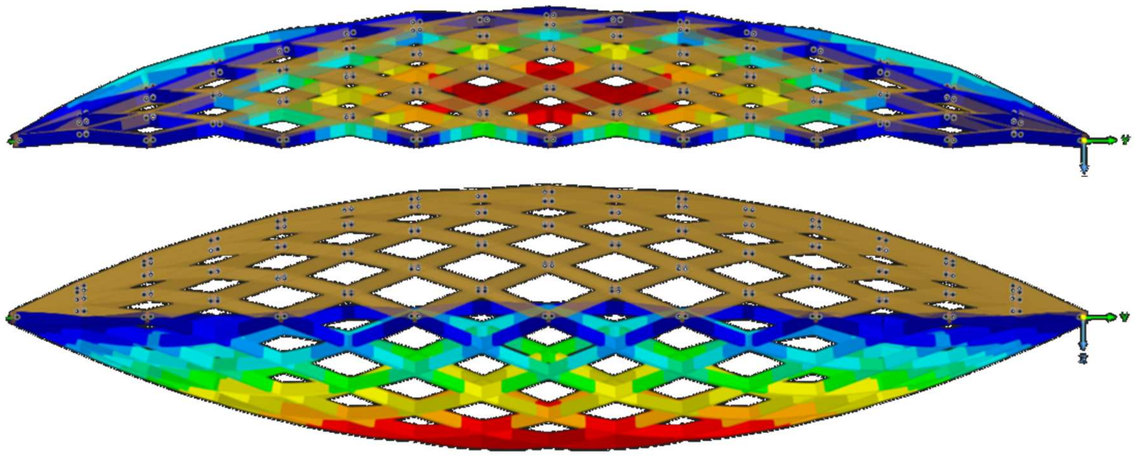

Figure 68: Buckling shapes obtained for the uniformly distributed snow load. The upper and lower solutions correspond to critical load factors of 1.220 and 1.228 respectively, illustrating the sensitivity of the post-buckling response to numerical solution parameters.

Increasing rotational stiffness generally resulted in higher critical load factors. However, stability was influenced more strongly by the available in-plane stiffness than by out-of-plane rotational stiffness alone. While stiffer connections improved capacity, the governing instability mechanisms remained global shell instabilities rather than local connection or member instabilities.

No distinct local in-plane failure mechanism was observed. Instead, instability was characterised by progressive distortion of the square grid cells into diamond-shaped configurations associated with the first global buckling mode. This behaviour suggests that the in-plane stiffness contributes primarily to maintaining shell geometry, stabilising asymmetric loading, and resisting progressive collapse.

The braced configurations exhibited additional complexity in their stability behaviour. Several buckling modes had very similar critical load factors, which may result in combined failure, as noted by Bulenda(Bulenda and Knippers, 2001). This observation is consistent with previous studies on gridshell stability that report closely spaced eigenmodes. In several cases, the braced system appeared to bypass the global first buckling mode and instead converged towards a more localised instability involving a single quadrant of the gridshell. For the governing load case, uniformly distributed snow, however, the deformation shape remained comparable to the unbraced configuration. In contrast, the magnitude of the deformation was reduced due to the increased stiffness of the shell centre.

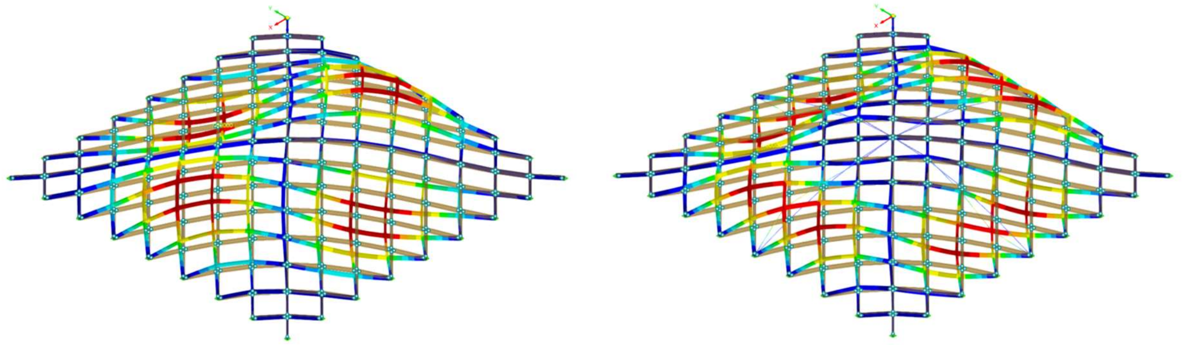

Figure 70: Influence of diagonal bracing on the first buckling mode of the gridshell under uniformly distributed snow loading.

The asymmetric imperfection cases proved most critical from a convergence perspective. The uniformly distributed snow load consistently governed the critical load factor for the converged analyses and produced the lowest reserve capacities when combined with the symmetric imperfection. When combined with the symmetric imperfection mode, the available reserve capacity reduced from approximately 15–16% to 11.6–13.1%. Although these values remain marginally above the adopted 10% threshold, they indicate limited robustness when geometric imperfections and nonlinear effects are accounted for.

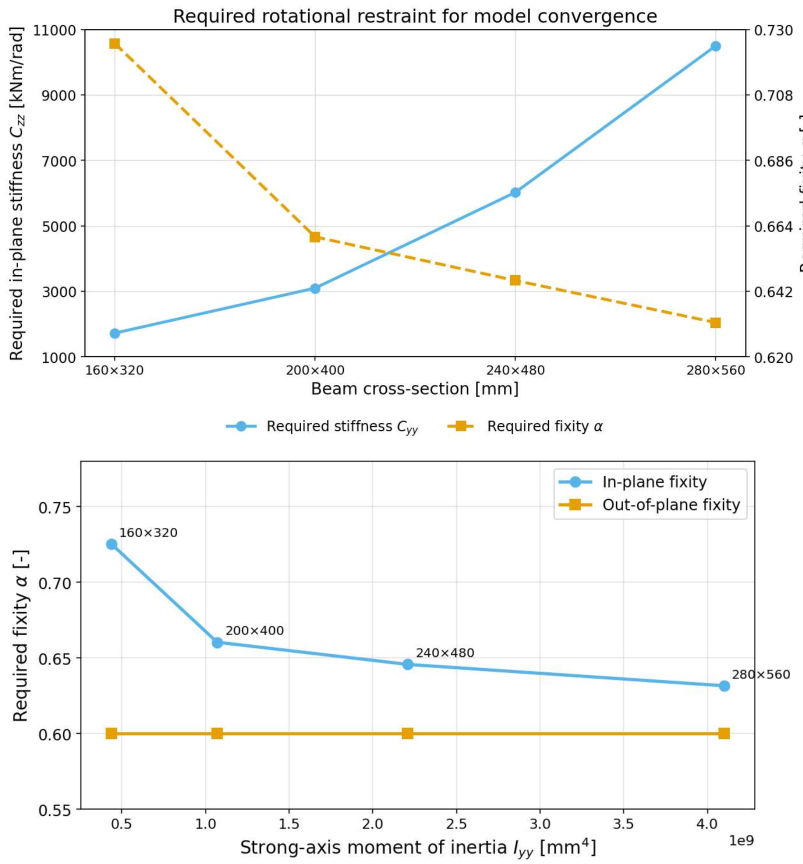

Figure 69: Relationship between beam stiffness and the minimum in-plane restraint required to achieve stable nonlinear convergence for a constant out-of-plane fixity factor.

For comparison of the stability results, only the first global instability mode was considered. The higher modes primarily introduce additional half-wave deformations rather than fundamentally different instability mechanisms. Since the objective of the present study is to evaluate the influence of connection stiffness on global stability, the first mode was considered most representative of the governing behaviour.

Geometrically non-linear second-order analyses generally produced the lowest critical load factors and therefore represent the most conservative assessment of stability. The only exceptions occurred for load cases affected by convergence difficulties, in which linear eigenvalue analyses occasionally yielded lower values than the corresponding large-displacement analyses. Despite these differences, the variation between analysis methods remained relatively limited, indicating that the overall stability behaviour is captured consistently.

Additional parameter studies showed that the minimum in-plane stiffness required for stable nonlinear behaviour increases with increasing member stiffness and out-of-plane rotational stiffness(Figure 69). Rather than converging towards a fully hinged solution, the models consistently required a finite proportion of in-plane stiffness, suggesting the existence of a practical lower limit for in-plane restraint below which stable equilibrium paths cannot be reliably established.

Interestingly, increasing in-plane stiffness had only a limited influence on the critical load factors themselves. Its primary effect was to improve the displacement behaviour of the geometrically non-linear solution and reduce the severity of second-order effects. This suggests that some of the higher critical load factors obtained from non-converged analyses may not represent physically realistic solutions. The complete result tables are in Appendix 7.

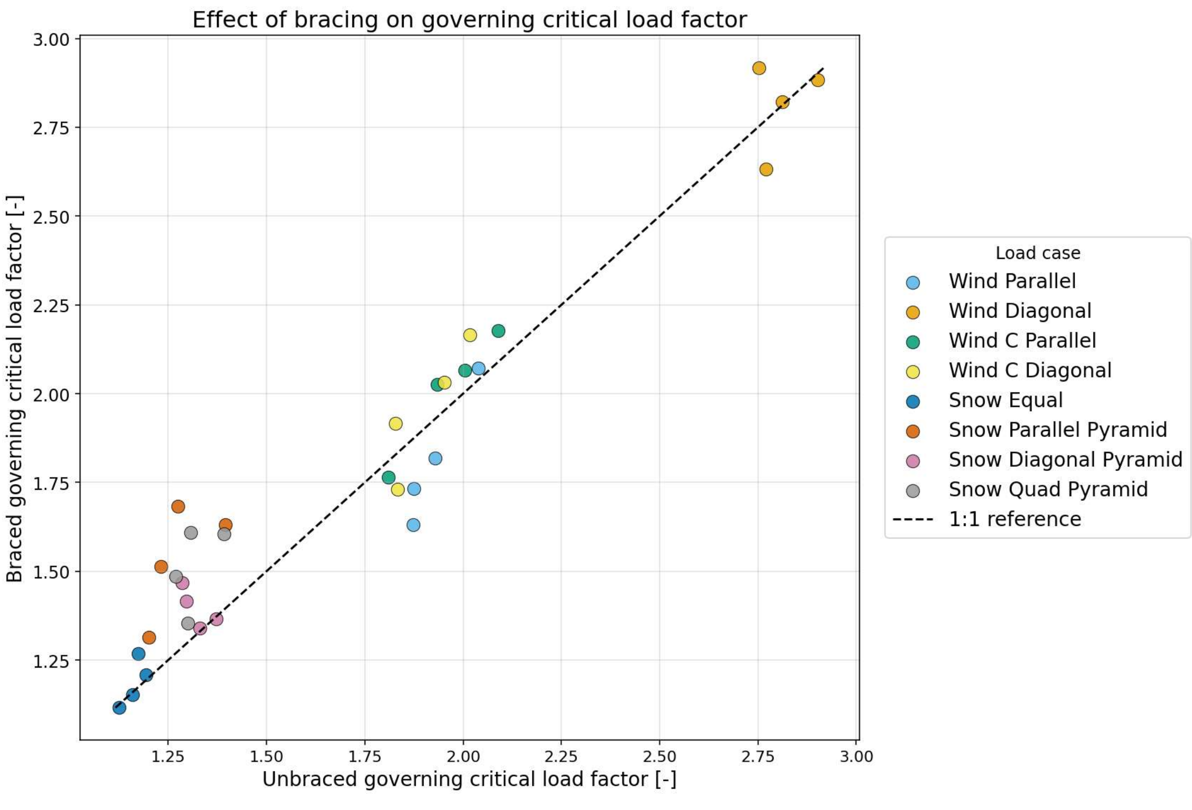

Figure 71: Comparison of the governing critical load factors for the braced and unbraced configurations. The dashed line indicates equal performance; points above the line represent load cases for which the braced configuration achieved a higher critical load factor.

The investigated gridshell, therefore, possesses only a limited reserve capacity beyond the design load level. If a larger safety margin is required, the most effective measures are to increase timber stiffness by using a higher strength class or to increase the member depth. The latter option proved particularly effective, as an increase of approximately 80 mm in member depth not only improved the global shell stiffness but also allowed larger connection details and additional dowels, increasing both local and global stiffness. This modification increased the governing critical load factor to approximately 2.38, corresponding to a reserve capacity of approximately 138%.

Overall, the results demonstrate that gridshell stability is governed by the interaction between out-of-plane rotational stiffness, in-plane rotational stiffness, geometric imperfections, and global shell behaviour. While increased rotational stiffness generally improves the critical load factor, a minimum level of in-plane stiffness appears necessary to obtain stable nonlinear behaviour and prevent snap-through mechanisms. Consequently, the design of semi-rigid gridshell connections should not focus solely on rotational stiffness but also consider their contribution to the shell's overall in-plane stability. These findings suggest that some form of additional in-plane restraint, whether through connection detailing, local stiffening, or global bracing, is likely required for robust practical applications.

7.2.4. Selection of Design Fixity

To proceed with the connection design, a target fixity factor must be selected. Based on the global response analyses, $\alpha = 0.55$ was adopted as the design target. At this stiffness level, the gridshell remains within the stable response region while avoiding the rapid increase in internal forces observed for lower fixity values. Furthermore, $\alpha = 0.55$ corresponds closely to the transition between the two response plateaus identified in the global stiffness study, making it a practical compromise between structural performance and connection feasibility.

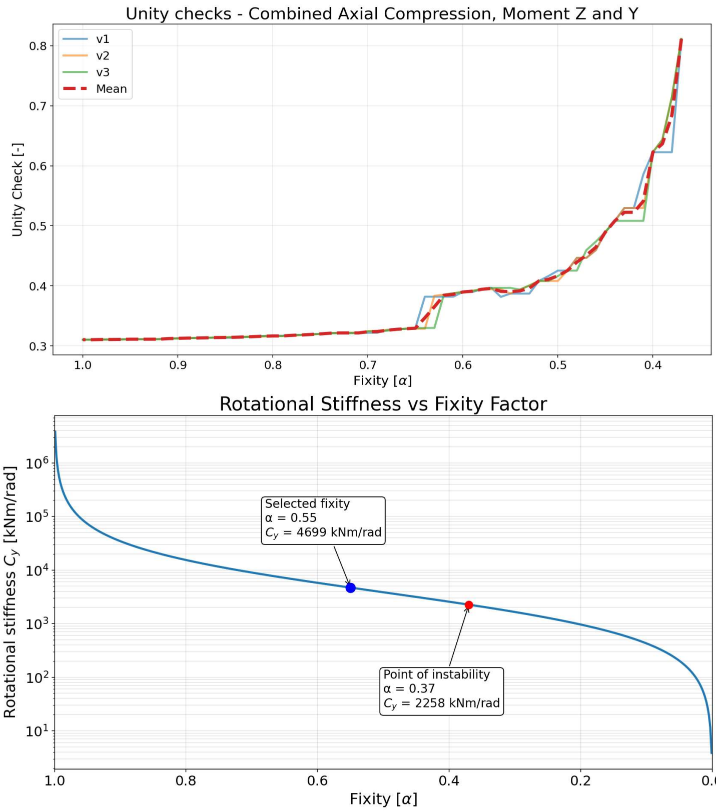

Figure 72: Governing unity check and corresponding rotational stiffness as a function of the fixity factor α. The selected design fixity (α = 0.55) and the point of instability (α = 0.37) are indicated.

A slightly higher target of α = 0.60 could be considered more conservative, as it lies at the beginning of the second response plateau (Figure 72). However, achieving this level of stiffness with the investigated connection configurations would significantly restrict the range of feasible solutions. For the selected 320 × 160 mm C24 member, only the stiffest investigated connection configuration (3×4 pattern with 20 mm dowels) exceeds this threshold. While this solution provides sufficient stiffness, it leaves little flexibility for practical optimisation of the connection geometry.

When evaluating the stability results, the influence of characteristic material properties must also be considered. Stability verification is based on the reduced material properties. $E_{0.05}$ and $\rho_{0.05}$, resulting in a lower effective stiffness than that obtained from mean material properties. Consequently, connection configurations that appear adequate based on serviceability stiffness alone may provide only limited reserve capacity when geometric non-linearity and imperfections are considered.

For example, the 320 × 160 mm C24 member combined with a 3×4 pattern of 20 mm dowels corresponds approximately to a fixity factor of α = 0.58(Figure 73) when evaluated using mean material properties and α = 0.62 when evaluated using characteristic properties(Figure 74). This configuration produced a governing critical load factor of 1.125 or 1.116 for braced systems, corresponding to a reserve capacity of approximately 11.6% beyond the design load. Although this satisfies the adopted stability criterion, the limited reserve capacity and the observed convergence difficulties suggest that additional robustness is desirable.

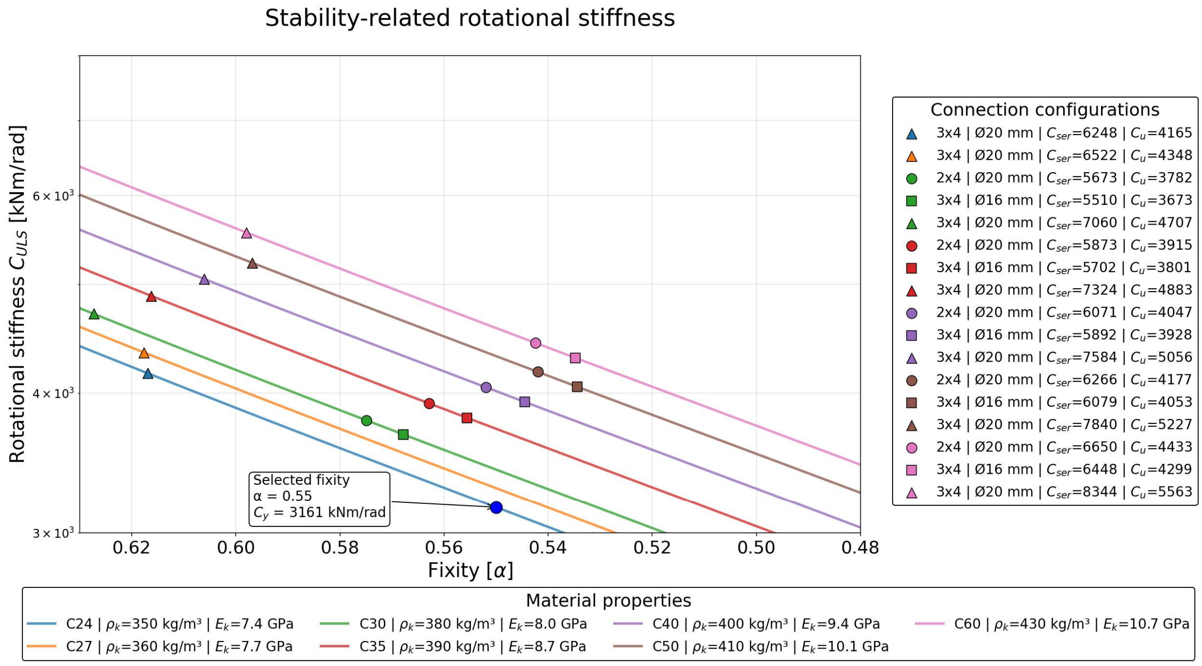

Figure 73: The reduced rotational stiffnesses for stability analysis with respect to the characteristic Young's modulus

Increasing the out-of-plane rotational stiffness further is difficult within the geometric constraints of the selected member size. Introducing a fifth column of dowels would substantially increase the width of the connection and require a significantly larger steel plate. Alternatively, increasing the timber strength class improves the structure's overall stiffness. For example, replacing the C24 members with C60 timber increases the governing critical load factor to approximately 1.57. Although this represents a significant improvement, it remains below the capacity achievable by increasing the member size.

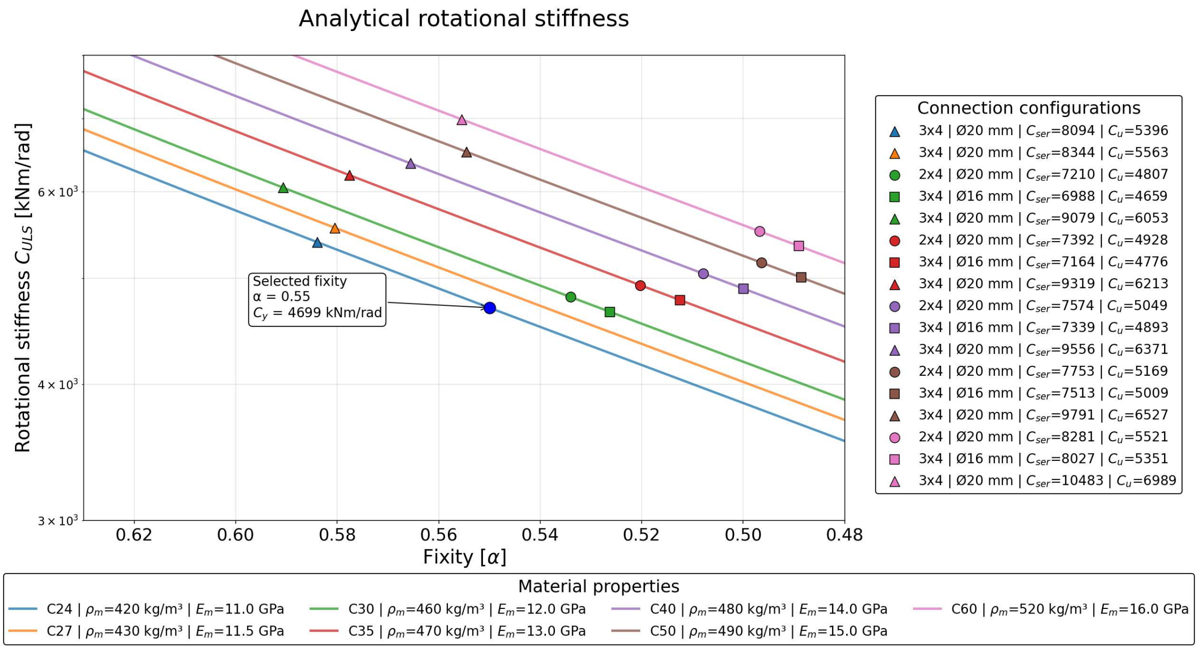

Figure 74: Comparison of the rotational stiffness and corresponding fixity of the investigated connection configurations. The highlighted point indicates the preferred connection stiffness to be used for the subsequent structural verification.

For this reason, increasing the member dimensions was considered the most effective design strategy. Adopting a 400 × 200 mm C24 section combined with a 4×4 dowel pattern using 16 mm dowels increases the available connection stiffness to approximately. $C_{u,0.05}$ = 5928 kNm/rad and C_u = 7427 kNm/rad. These stiffnesses correspond to fixity factors of approximately α = 0.48 and α = 0.43, respectively. More importantly, the governing critical load factor increases to approximately 2.011, providing substantial reserve capacity and significantly improving the design's robustness.

The 16 mm dowel diameter was selected in preference to larger fasteners because it leaves additional flexibility for future refinement of the connection design. Should subsequent capacity checks indicate insufficient strength, the connection can still be strengthened by increasing dowel diameter or making minor modifications to the dowel-group geometry, without requiring a fundamental redesign of the connection concept.

For additional robustness, diagonal cross-bracing may be introduced within the gridshell. Incorporating this bracing system increases the governing critical load factor to approximately 2.521. In addition to increasing load-carrying capacity, the bracing provides in-plane restraint, reducing the structure's sensitivity to geometric imperfections and asymmetric loading conditions. Consequently, the braced configuration not only exhibits a larger stability reserve but also demonstrates a more robust structural response against global instability mechanisms.

7.3. Connection Design

7.3.1. Design Parameters

The parameter studies presented in Chapters 4 and 5 identified four primary variables governing the rotational stiffness of the connection: dowel diameter, dowel-group geometry, timber density, and embedment length. In addition, the comparison between the analytical and numerical results led to a modified analytical formulation that improved the agreement between both approaches. For the present case study, this calibrated formulation is adopted to provide a more conservative estimate of rotational stiffness while retaining the additional parameter interactions that appear to be absent from the Eurocode 5 stiffness definition.

Among the investigated local parameters, dowel diameter had the greatest influence on the stiffness. The modified formulation, however, indicates a closer relationship between dowel diameter and timber density than the original analytical model suggests. For loading parallel to the grain, both parameters contribute significantly to stiffness development, while the influence of embedment length remains comparatively small. For loading perpendicular to the grain, the relative importance of timber density increases further, and embedment length becomes more influential due to the reduced effectiveness of increasing dowel diameter.

Achieving high stiffness generally requires larger dowel diameters; however, the effectiveness of increasing dowel size depends strongly on the grain direction and associated embedment stiffness. As a result, dowel-group geometry becomes increasingly important for configurations subjected to significant perpendicular-to-grain loading, where the distribution of forces among the fasteners governs the overall stiffness response.

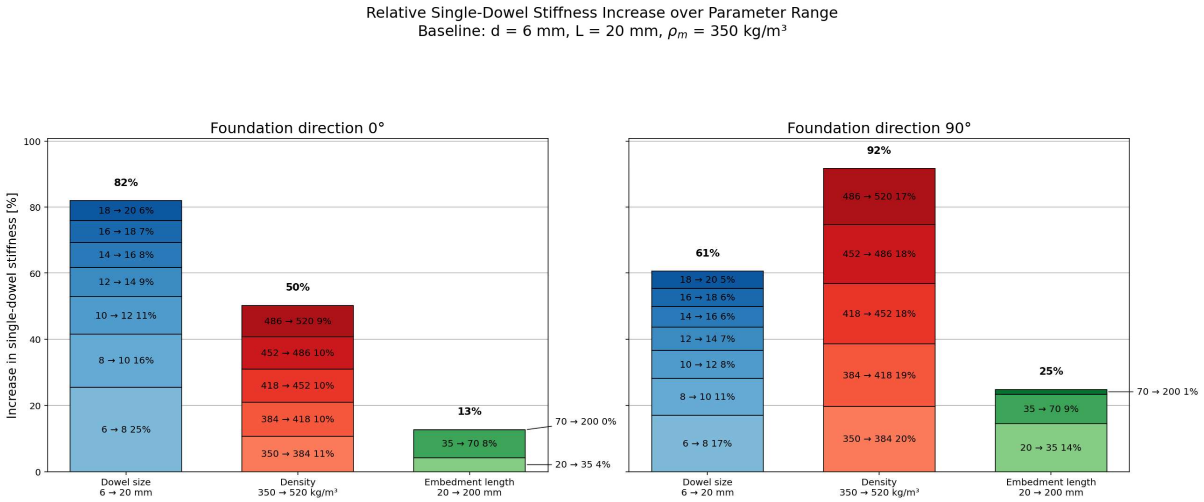

Figure 75: Relative modified contribution of dowel diameter, timber density, and embedment length to single-dowel stiffness development for loading parallel and perpendicular to the grain.

Unlike timber density or embedment length, modifications to the dowel pattern can often be implemented without substantially affecting the surrounding structural configuration. Dowel-group geometry, therefore, offers an attractive design variable to improve rotational stiffness while maintaining practical manufacturability. For this reason, dowel-group geometry and dowel diameter are treated as the primary optimisation variables within the present study. In contrast, timber density and embedment length are considered secondary parameters that may be adjusted when additional stiffness is required.

Although timber density and embedment length both contribute to stiffness development, they are associated with additional practical constraints. Increasing timber density generally requires using higher-strength timber grades, which increases material costs. Increasing embedment length, on the other hand, requires larger member dimensions and therefore affects the overall structural design. Furthermore, the parameter studies indicate that the stiffness gains associated with embedment lengths exceeding approximately 70 mm diminish progressively. Beyond this point, increasing embedment length results in diminishing returns relative to the additional material required.

This observation also suggests alternative design strategies for deeper members. Rather than increasing the embedment length of a single plate, it may be more efficient to introduce additional plates distributed across the cross-section, thereby making more effective use of the available embedment length while maintaining practical connection dimensions.

7.3.2. Node Modelling Assumptions and Plate Correction

An important modelling consideration concerns the representation of the steel knife plate within the global stiffness formulation. In the analytical model, the rotational spring is located at the end of the beam element, whereas the physical centre of rotation is located within the connection itself. Consequently, part of the timber member deformation is implicitly included in the rotational stiffness representation.

For the investigated connection geometry, the stiffness ratio between the timber member and the steel plate exceeds approximately 2:1 in the governing direction. This indicates that the adopted modelling approach may underestimate the steel plate's contribution to stiffness. Rather than directly correcting the rotational stiffness, the resulting conservatism is retained throughout the case study as a safety margin.

If a more accurate representation of the connection stiffness is required, the additional stiffness contribution of the steel plate can be incorporated through the reciprocal stiffness relationship developed in Chapter 5.

Compared to the formulation presented in Chapter 5, the stiffness relationship is applied differently within the global model. In the analytical derivation, the rotational stiffness is formulated by combining the stiffness contributions of the timber member and the steel plate. Within the finite element model, however, the region represented by the eccentricity a It is already included in the timber beam element. Consequently, a direct application of the analytical formulation would result in a partial double-counting of the stiffness contribution of this segment.

To avoid this effect, the timber contribution is removed from the correction formulation through the ratio r, which expresses the relative stiffness of the timber and steel components based on the relative material stiffness and section thickness, assuming equal plate and member heights. The rotational spring stiffness C_s represents the additional stiffness contribution of the steel plate. The stiffness ratio and plate stiffness are defined as

$$r = \frac{E_s b_s}{E_t b_t}$$

$$C_s = \frac{E_s I_s}{a}$$

where a denotes the distance between the support location and the rotational centre of the connection. The corrected out-of-plane rotational stiffness is subsequently obtained from

$$C_{adj} = \frac{1}{\frac{1}{C_{yy}} + \frac{1-r}{C_s}} \tag{40}$$

The stiffness correction introduces a nonlinear amplification of the out-of-plane rotational stiffness. Since the correction is formulated in terms of a reciprocal stiffness relationship, the relative contribution of the steel plate increases with increasing connection stiffness. Consequently, larger dowel diameters, which already produce higher out-of-plane rotational stiffnesses, experience proportionally greater increases after application of the plate correction. The resulting stiffness development, therefore, exhibits an accelerating hyperbolic trend, visible in Figure 76, rather than a linear increase.

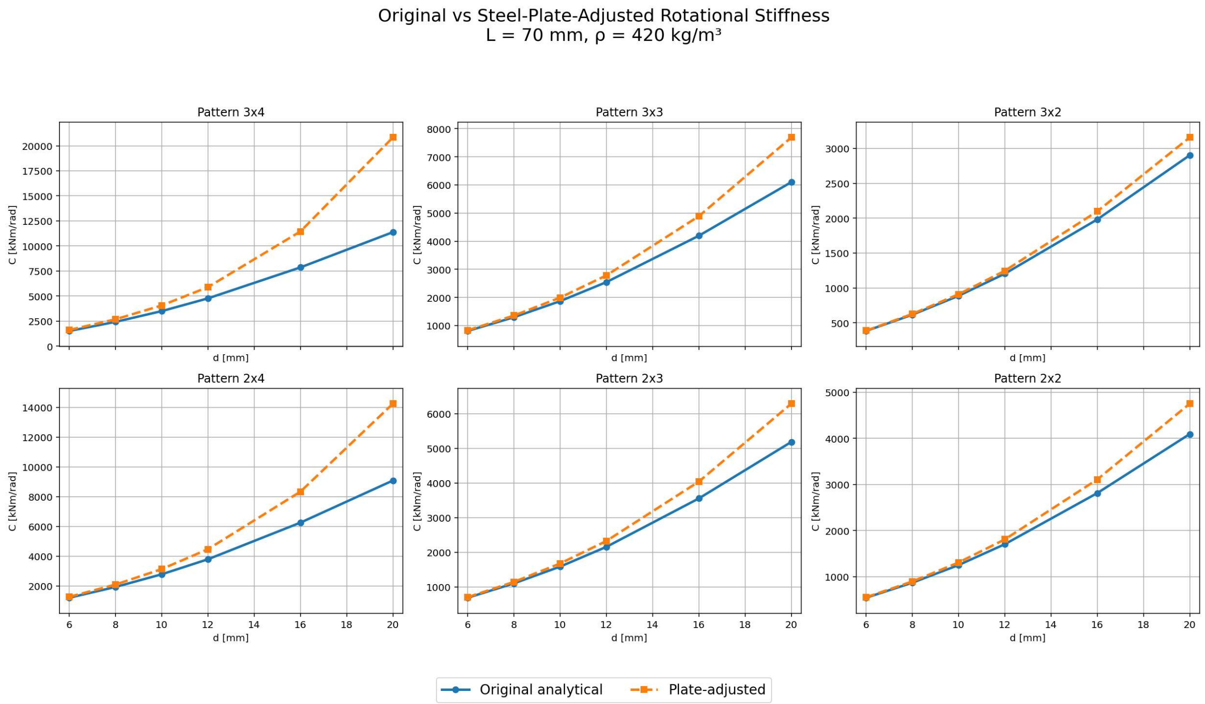

Figure 76: Comparison between the original analytical stiffness and the plate-adjusted stiffness according to the setup of the RFEM6 model.

The lateral rotational stiffness C_{zz} may be derived analogously by evaluating the plate stiffness about the local z-axis. However, the rotational stiffness of the dowel group in this direction is significantly larger than the corresponding plate flexibility, such that the overall response is governed primarily by the plate stiffness. In practice, this contribution is small relative to the primary rotational stiffness and may therefore be neglected. Nevertheless, a nominal stiffness of $14\ kNm/rad$ is retained within the numerical model to improve solver stability and convergence.

Although the correction formulation is presented for completeness, the uncorrected stiffness values are retained in the subsequent optimisation. Neglecting the additional plate stiffness yields a conservative estimate of the connection stiffness, thereby providing an inherent safety margin in the design process.

The connection node seen in Figure 77 is represented by a square hollow section (SHS) profile with dimensions 100 × 100 × 10 mm. This profile was selected in preference to a circular hollow section (CHS) due to its practical fabrication advantages. In particular, the flat faces of the SHS provide more accessible welding surfaces for the connection plates and simplify node assembly.

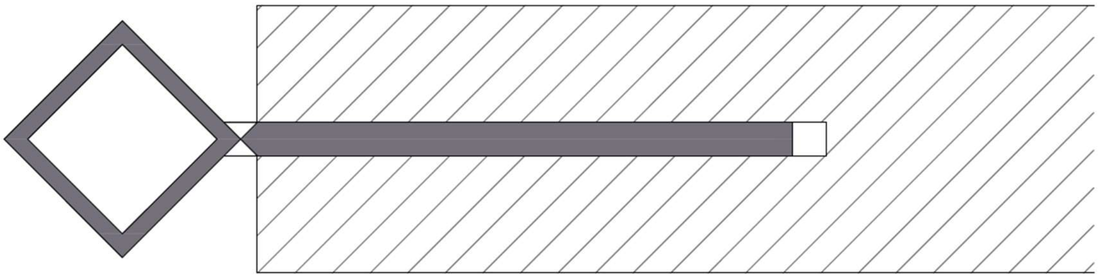

Figure 77: Top view of the proposed connection detail showing the RHS node, welded knife plate and timber beam.

From a structural perspective, the SHS geometry also provides a more direct load path between opposing connection plates. In contrast, a curved CHS surface would introduce additional local bending effects and less favourable force transfer between the connected members. The selected SHS profile, therefore, provides a stiffer and more predictable connection detail for the present study.

To ensure that the node itself remains significantly stiffer than the surrounding connection components, welded end plates are provided at both ends of the hollow section. These stiffening plates minimise local deformation of the node and support the modelling assumption that the rotational flexibility of the connection is governed primarily by the dowel group, steel plate deformation, and timber embedment behaviour rather than by deformation of the node itself.

7.4. Design Verification

7.4.1. **Beam Verification**

The final design adopts a 400 × 200 mm C24 timber section. Although this profile was initially selected to improve the global stiffness and stability behaviour of the gridshell, it is necessary to verify that the member also satisfies the ultimate limit state requirements.

The verification was performed using the governing internal forces extracted from the numerical model. Separate checks were carried out for axial force, shear force, bending about both principal axes, torsion, and a combined axial force and bending verification in accordance with Eurocode 5. The complete set of governing values and unity checks is presented in Table 7.

Check	Governing Load combination	Internal Force	Unity Check
N	ULS Snow Equally	$-165.46\ kN$	$0.14 \leq 1.0$
V_y	ULS Wind C Diagonal	$5.23\ kN$	$0.04 \leq 1.0$
V_z	ULS Wind Parallel	$5.93\ kN$	$0.06 \leq 1.0$
M_{yy}	ULS Wind Parallel	$12.81\ kNm$	$0.18 \leq 1.0$
M_{zz}	ULS Snow Equally	$0.67\ kNm$	$0.02 \leq 1.0$
T	ULS Snow Quad Pyramid	$-5.77\ kNm$	$0.06 \leq 1.0$
$N + M_{yy} + M_{zz}$	ULS Wind Parallel	$-91.93 + 12.81 + 0.37$	$0.19 \leq 1.0$

Table 7: Governing ultimate limit state load combinations, internal forces, and corresponding unity checks for the selected 400 × 200 mm C24 member.

The results indicate that all governing unity checks remain well below the design limit of 1.0. The highest utilisation is obtained for bending about the local y-axis, resulting in a unity check of 0.18. When combined with the governing axial force, the maximum utilisation increases only marginally to 0.19. This low value is partly attributable to the Eurocode 5 interaction formulation, which permits the compressive stress term to be squared, thereby accounting for the plastic compression capacity of timber:

$$\left(\frac{\frac{N}{A}}{f_{c,0,d}}\right)^2 + \frac{\frac{M_{yy}}{W_{yy}}}{f_{m,0,d}} + \frac{\frac{M_{zz}}{W_{zz}}}{f_{m,0,d}} \leq 1.0 \tag{41}$$

These results demonstrate that ultimate strength requirements do not govern the selected beam section. Similar conclusions were obtained for the previously evaluated 320 × 160 mm section during the fixity analysis. Instead, the member dimensions are governed primarily by stiffness and stability considerations. This observation is consistent with the findings of the previous chapters, where connection stiffness and global stability behaviour were shown to influence the design more strongly than member capacity.

Consequently, the adopted 400 × 200 mm C24 section provides a substantial strength reserve while supplying the increased stiffness required to achieve the desired global stability performance.

7.4.2. Connection Verification

The final connection design is verified using the hinge forces obtained from the global analyses. As discussed in the previous sections, three stiffness definitions are required throughout the design process. The serviceability stiffness is used to evaluate the rotational response of the connection, the ultimate stiffness forms the basis of the connection verification, and the characteristic stiffness is adopted during the global stability assessment. For the selected connection, consisting of a 400 × 200 mm C24 timber member, a 20 mm steel knife plate, a 90 mm embedment length and a 4 × 4 arrangement of M16 grade 4.6 dowels, the corresponding out-of-plane rotational stiffnesses are

$$C_{ser} = 11247\ kNm/rad$$

$$C_u = 7498\ kNm/rad$$

$$C_{u,0.05} = 5964\ kNm/rad$$

Using the ultimate stiffness, the governing hinge forces are extracted from the global model. The governing load combinations, internal hinge forces and corresponding unity checks are summarised in Table 8. These actions form the basis for the subsequent verification of the timber connection, steel plate and fasteners.

Check	Governing Load combination	Internal Hinge Force	Unity Check
N	ULS Snow Equally	$-165.47\ kN$	$0.37 \leq 1.0$
V_y	ULS Snow Diagonal Pyramid	$1.09\ kN$	$0.01 \leq 1.0$
V_z	ULS Wind Parallel	$6.17\ kN$	$0.02 \leq 1.0$
M_{yy}	ULS Wind Parallel	$11.44\ kNm$	$0.37 \leq 1.0$
M_{zz}	ULS Wind Parallel	$0.04\ kNm$	$0.00 \leq 1.0$
T	ULS Snow Diagonal Pyramid	$-0.36\ kNm$	$-$

Table 8: Governing internal hinge forces for each action and their corresponding unity checks.

Unlike the beam verification, the connection is subjected to a combined state of loading consisting of axial compression, shear and bending. Consequently, the individual actions cannot be verified independently; they must be evaluated by the resultant force acting on each dowel. Following the stiffness-based force distribution procedure developed in Chapter 5, the hinge actions are converted into the corresponding forces acting on the individual fasteners.

The resulting force distribution for the governing bending moment of 11.44 kNm is presented in Table 9.

Dowel	Load-to-grain angle [°]	Force per shear plane [kN]
1	51.34	5.041
2	75.07	3.226
3	75.07	3.226
4	51.34	5.041
5	22.62	4.369
6	51.34	1.680
7	51.34	1.680
8	22.62	4.369
9	22.62	4.369
10	51.34	1.680
11	51.34	1.680
12	22.62	4.369
13	51.34	5.041
14	75.07	3.226
15	75.07	3.226
16	51.34	5.041

Table 9: Force distribution and corresponding grain angles for each dowel under the governing bending moment of 11.44 kNm.

As expected, the outer corner dowels carry the largest proportion of the applied moment owing to their larger lever arms. In contrast, the inner dowels contribute primarily to the overall out-of-plane rotational stiffness of the connection. The resultant force acting on each dowel, containing moment, axial and shear force, together with its corresponding grain angle, is subsequently used for the Eurocode 5 bearing verification. Torsional loading is neglected because it arises primarily from preventing member spin in the global model and contributes only marginally to the combined dowel forces.

The timber verification comprises dowel bearing resistance and verification against splitting perpendicular to the grain. Bearing resistance is evaluated according to the Eurocode 5 Johansen yield formulation using the resultant force acting on each shear plane. The effective number of fasteners is determined using the Eurocode 5 reduction procedure described in Chapter 5. Since smooth dowels installed in tight-fitting holes are assumed, rope effects are neglected, and the connection resistance is governed entirely by bearing, splitting and dowel yielding.

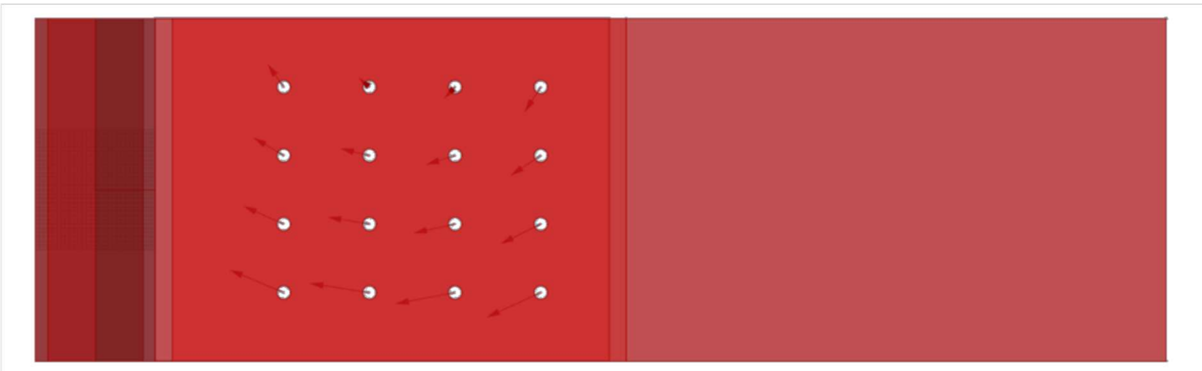

Figure 78: Governing vector configuration for the timber embedment check

To account for the reduction in effectiveness of fasteners placed within the same row, the effective number of dowels is determined according to the Eurocode 5 expression. The average loading angle of the dowel group is subsequently incorporated to obtain an angle-dependent effective number of fasteners, resulting in a uniform reduction of the bearing capacity for all dowels within the row.

The governing failure mechanism corresponds to the Johansen failure mode (b) and the splitting failure mode (g)(Figure 79 and Figure 80. Verification of every dowel under every governing load combination demonstrates that sufficient reserve capacity remains throughout the connection. The highest utilisation occurs for the ULS Wind Parallel load combination, resulting in a maximum timber bearing utilisation of 0.58, seen in Table 10.

Load Combination	Highest Unity Check per Dowel
ULS Wind Parallel	$0.58 \leq 1.0$
ULS Wind Diagonal	$0.32 \leq 1.0$
ULS Wind C Parallel	$0.40 \leq 1.0$
ULS Wind C Diagonal	$0.45 \leq 1.0$
ULS Snow Equally	$0.48 \leq 1.0$
ULS Snow Parallel Pyramid	$0.49 \leq 1.0$
ULS Snow Diagonal Pyramid	$0.42 \leq 1.0$
ULS Snow Quad Pyramid	$0.55 \leq 1.0$

Table 10: Governing timber bearing unity checks for the individual dowels under each ultimate limit state load combination.

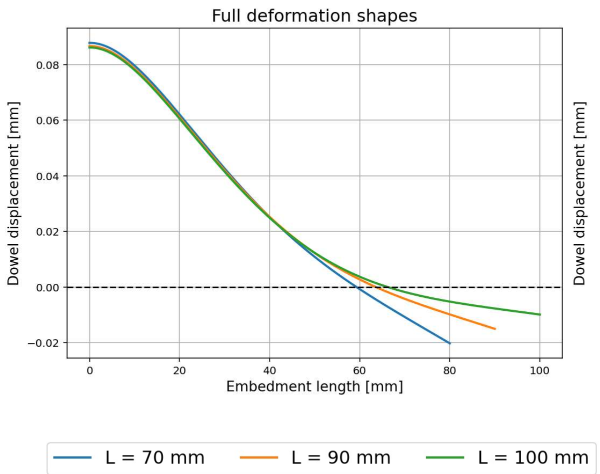

Figure 79: The deformation shapes for a 16 mm dowel for different embedment lengths.

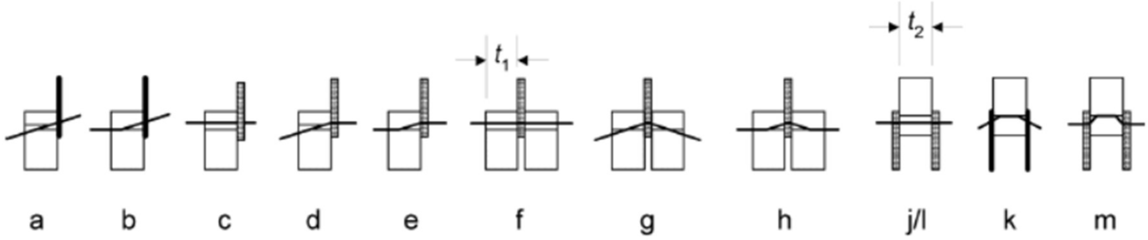

Figure 80: Failure modes for steel to timber connections

In addition to dowel bearing, splitting perpendicular to the grain is evaluated. The maximum splitting force generated within the outer dowel rows equals approximately 22 kN. Although the timber's characteristic splitting resistance is exceeded locally, the additional tensile force can be effectively resisted by introducing fully threaded reinforcement screws. A single centrally positioned 120 × 8 mm fully threaded screw provides approximately 11.9 kN of additional tensile capacity and is therefore sufficient to prevent premature splitting. To ensure symmetric behaviour, identical reinforcement is provided on both sides of the connection, as displayed in Figure 81.

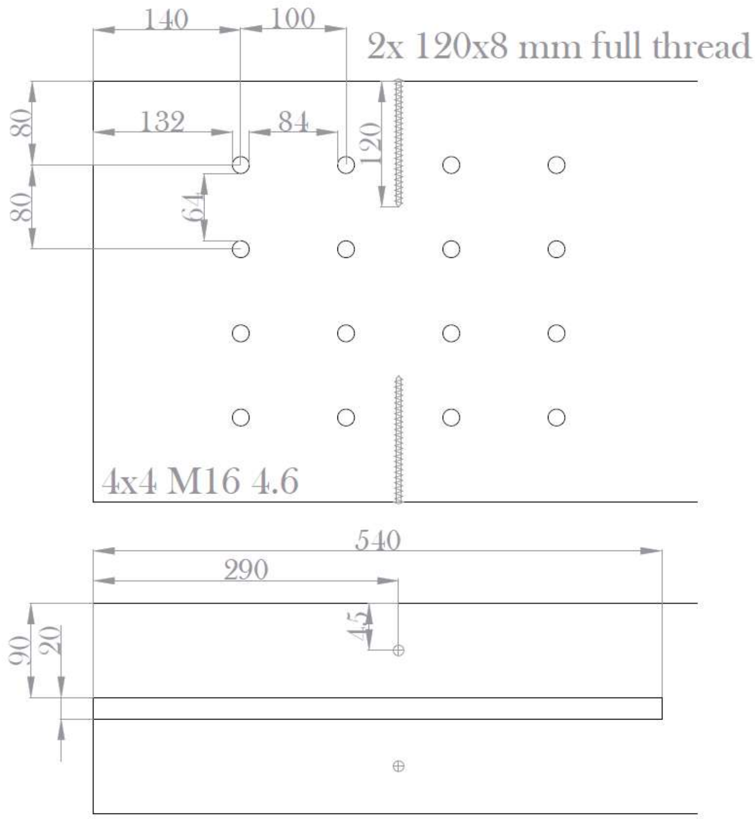

Figure 81: Final connection design

The governing timber verification therefore remains below the design resistance, demonstrating that the proposed reinforcement allows the dowel group's full bearing capacity to be mobilised.

The steel components are verified through separate checks of the knife plate, the dowels and the local bearing stresses surrounding the dowel holes.

Because the selected plate geometry permits full-penetration butt welds, the welds do not govern the design. The knife plate is therefore verified by converting the governing axial force, shear force and bending moment into equivalent stresses. Additional moments generated by the eccentricity between the dowel group and the plate centreline are included through

$$V \cdot a = M_V \tag{42}$$

$$N \cdot a \cdot \tan(\theta) = M_N \tag{43}$$

$$M_{tot} = M_N + M_V + M_{yy} \tag{44}$$

The resulting stress state is evaluated using the von Mises yield criterion(NEN 1993, 2016). The maximum plate utilisation equals 0.19, seen in Table 11, indicating that substantial reserve capacity remains within the steel plate. Although the calculations demonstrate that the plate thickness could theoretically be reduced to approximately 8 mm, the adopted 20 mm thickness is retained to provide the out-of-plane rotational stiffness assumed throughout the analytical and numerical investigations.

Load Combination	Highest Unity Check per Dowel
ULS Wind Parallel	$0.19 \leq 1.0$
ULS Wind Diagonal	$0.11 \leq 1.0$
ULS Wind C Parallel	$0.13 \leq 1.0$
ULS Wind C Diagonal	$0.15 \leq 1.0$
ULS Snow Equally	$0.16 \leq 1.0$
ULS Snow Parallel Pyramid	$0.17 \leq 1.0$
ULS Snow Diagonal Pyramid	$0.15 \leq 1.0$
ULS Snow Quad Pyramid	$0.19 \leq 1.0$

Table 11: Governing von Mises plate unity checks for each ultimate-limit-state load combination.

The dowels themselves are subsequently verified in shear. Since rope effects are neglected, only the shear force acting within each shear plane is considered. The governing utilisation equals 0.38, seen in Table 12, demonstrating that the dowel strength exceeds the required design resistance by a considerable margin.

Load Combination	Highest Unity Check per Dowel
ULS Wind Parallel	$0.38 \leq 1.0$
ULS Wind Diagonal	$0.21 \leq 1.0$
ULS Wind C Parallel	$0.26 \leq 1.0$
ULS Wind C Diagonal	$0.30 \leq 1.0$
ULS Snow Equally	$0.32 \leq 1.0$
ULS Snow Parallel Pyramid	$0.32 \leq 1.0$
ULS Snow Diagonal Pyramid	$0.27 \leq 1.0$
ULS Snow Quad Pyramid	$0.36 \leq 1.0$

Table 12: Governing dowel shearing unity checks for each ultimate limit state load combination.

Finally, the local bearing resistance of the steel plate surrounding the dowel holes is evaluated. All investigated load combinations remain well below the available bearing resistance, with the highest utilisation remaining below 0.10. Consequently, neither the steel plate nor the dowels governs the connection design.

Overall, the connection verification demonstrates that all components satisfy the relevant Eurocode 5 design requirements. The governing verification corresponds to the dowel group's timber bearing resistance, resulting in a maximum utilisation of 0.58, while the steel plate, welds, dowels, and local bearing stresses all exhibit substantially lower utilisation ratios.

These results demonstrate that the final connection is governed primarily by stiffness rather than strength. The adopted geometry therefore provides sufficient reserve capacity while simultaneously achieving the out-of-plane rotational stiffness required by the global stability analyses. When combined with the beam and stability verifications presented in the previous sections, the proposed connection demonstrates that the stiffness requirements established throughout this research can be translated into a practical, structurally feasible engineering design.

7.4.3. **Stability and Serviceability Verification**

The final design was verified using the geometrically non-linear stability procedures established in the previous sections. The lowest critical load factors obtained for each governing load combination are summarised in Table 13. All analysed cases converged successfully without additional bracing, indicating that the selected member dimensions and connection stiffness provide sufficient global stability for the investigated loading scenarios.

Load Combination	Imperfection Case	Critical Load Factor [-]	Mode Shape
ULS Wind Parallel	No Imperfections	2.322	A
ULS Wind Diagonal	Inverse Asymmetric	4.535	B
ULS Wind C Parallel	Asymmetric	3.123	C
ULS Wind C Diagonal	Asymmetric	3.162	D
ULS Snow Equally	Symmetric	1.993	E
ULS Snow Parallel Pyramid	Symmetric	2.158	F
ULS Snow Diagonal Pyramid	Asymmetric	2.273	G
ULS Snow Quad Pyramid	Inverse Asymmetric	2.328	H

Table 13: Governing critical load factors, corresponding imperfection cases, and buckling mode shapes for each ultimate limit state load combination.

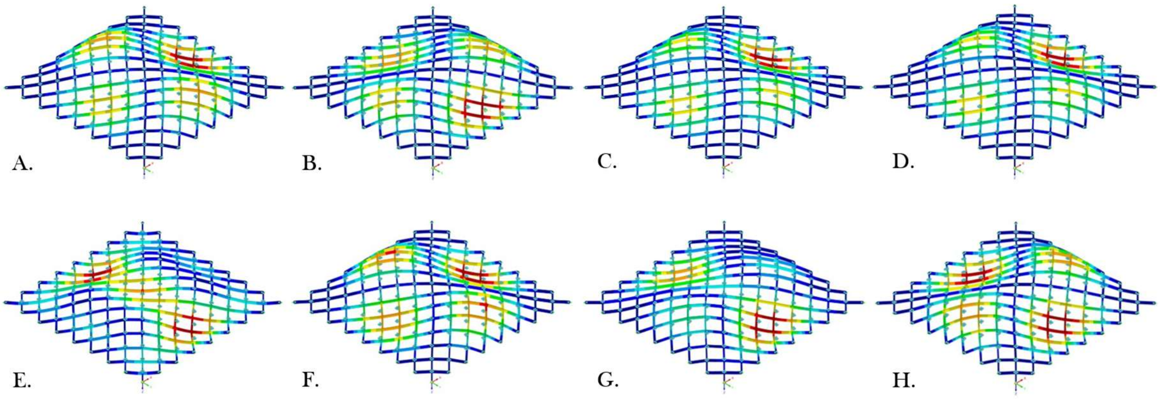

Figure 82: The buckling modes assigned to the lowest critical load factors of the different load cases amplified by their governing imperfections

The governing critical load factor is obtained for the uniformly distributed snow load combined with the symmetric imperfection, yielding 1.993. This indicates that the structure possesses a global stability reserve of approximately 100% beyond the design load before reaching global instability. The remaining load combinations exhibit significantly larger stability reserves. Furthermore, the governing buckling modes correspond closely with the mode shapes identified during the preliminary stability investigations, indicating that the selected design remains consistent with the previously established global stability behaviour.

Although the global stability analysis demonstrates adequate reserve capacity, the member verification must also account for the additional bending moments generated by second-order effects. Although the governing internal forces are extracted from a second-order analysis, this procedure only accounts for the geometric non-linearity arising from the applied loading. The additional effects of initial geometric imperfections are not explicitly included in the member verification. Furthermore, directly applying the internal forces obtained from the stability analysis would overestimate the member utilisation because the stability analyses are performed using reduced characteristic stiffnesses. Consequently, a modified interaction check based on the governing critical load factor is adopted, in which the axial force is amplified using an equivalent eccentricity representing both the initial member imperfection and the global buckling deformation.

The governing interaction is therefore evaluated according to

$$\frac{\frac{n}{n-1}\cdot\frac{F\left(e_0+e_{imp}\right)}{W_{yy}}+\frac{M_{yy}}{W_{yy}}+\frac{M_{zz}}{W_{zz}}}{f_{m,0,d}}+\frac{\frac{F}{A}}{f_{c,0,d}}\leq 1.0 \tag{45}$$

where the equivalent eccentricity is taken as

$$e_0+e_{imp}=\frac{17660}{300}+72=131.7\ mm$$

The adopted imperfection length corresponds to the largest global buckling half-sine observed during the stability analyses, consisting of eight elements with a total length of approximately 17.66 m. The diagonal buckling mode was not adopted because the neutral axis passes through the centre of the shell, reducing the eccentricities experienced by the members. Although this approach does not necessarily represent the most conservative eccentricity, it provides a physically representative estimate of the global buckling deformation. It therefore allows the second-order effects to be incorporated consistently within the member verification.

The verification results are summarised in Table 14. Without considering stability effects, the governing member utilisation is only 0.19, as previously established during the beam verification. After incorporating the amplified second-order effects, the governing utilisation increases to 0.80, with the uniformly distributed snow load becoming the governing load combination. This increase is primarily due to the conversion of axial force into additional bending moments via the assumed global eccentricity.

Stability	Check	Governing Load combination	Internal Force	Unity Check
No	$F+M_{yy}+M_{zz}$	ULS Wind Parallel	$-91.93+12.81+0.37$	$0.19\leq 1.0$
Yes	$F+M_{yy}+M_{zz}$	ULS Snow Equally	$-164.27+3.12+0.62$	$0.80\leq 1.0$

Table 14: Comparison of the governing member verification with and without the inclusion of second-order and imperfection effects.

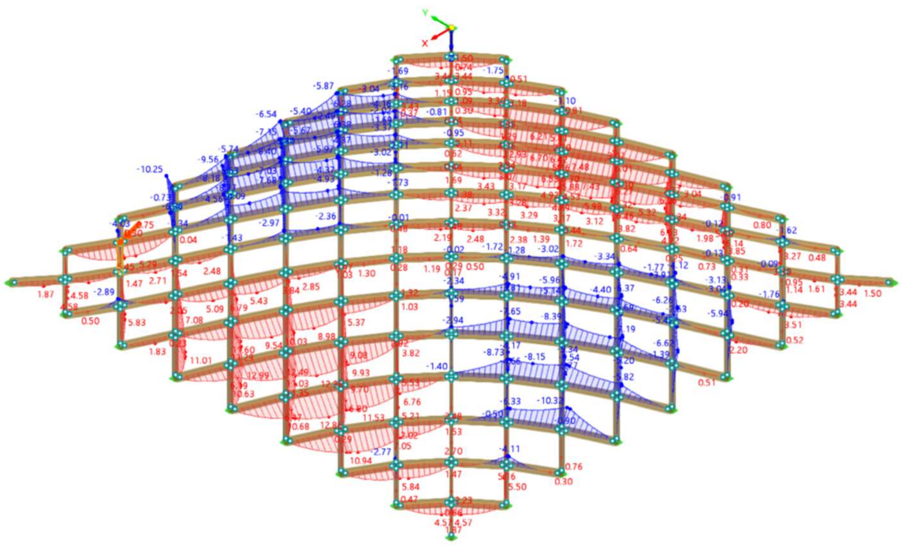

Figure 83: The governing combined load combination Parallel wind with peak moments occurring in the left quadrant

This verification demonstrates that the selected member dimensions provide sufficient reserve against both material failure and instability. Although the adopted imperfection amplitude slightly overestimates the bending moments, because the largest bending moments occur closer to the shell edges than the assumed maximum eccentricity, the resulting utilisation remains comfortably below the design limit. Consequently, the selected 400 × 200 mm C24 members provide an adequate level of robustness against second-order effects.

The serviceability behaviour of the final design was evaluated using the governing displacement combinations. Owing to the increased beam stiffness and the relatively high connection stiffness adopted in the final design, the resulting displacements remain significantly smaller than the equivalent eccentricities assumed in the stability verification.

The largest vertical displacements occur under the parallel wind-load case, consistent with the governing asymmetric loading behaviour observed throughout the stability analyses. The in-plane displacements remain relatively small and satisfy the conventional sway criterion of approximately (L/300) when evaluated over the local element length.

For vertical displacement, conventional span-based limits are less representative because a gridshell's deformation is governed by its global shell behaviour rather than by that of an individual beam. The observed deformation shapes closely resemble the governing global buckling modes, suggesting that an effective span corresponding to approximately half the shell width provides a more representative measure of allowable displacement. Based on this assumption, an allowable vertical displacement of approximately 20–25 mm is obtained, which compares favourably with the calculated maximum displacement of approximately 21 mm. The comparison can be seen in Table 15.

Deformation	Load case	Min Displacement	Max Displacement	Allowed
u_Y	SLS Wind Parallel	-7.6	+5.1	±8.2
u_X	SLS Quad pyramid snow	-5.3	+5.2	±8.2
u_Z	SLS Wind Parallel	-8.7	+20.9	±25-20
$\lvert u_{tot} \rvert$	SLS Wind Parallel	22.1		23.1

Table 15: Governing serviceability load cases together with the corresponding minimum, maximum, and allowable displacements.

Overall, the stability verification demonstrates that the final design satisfies both global and local stability requirements. The selected member dimensions provide sufficient reserve against second-order effects while maintaining acceptable serviceability behaviour. Combined with the connection verification presented in the previous section, these results indicate that the proposed design satisfies both stiffness and strength requirements without additional global bracing.

Overall, the stability verification demonstrates that the final design satisfies the adopted global stability criterion while maintaining acceptable member utilisation and serviceability behaviour. Taken together with the connection and beam verifications presented in the previous sections, the results demonstrate that the proposed design successfully translates the stiffness requirements derived from the global analyses into a practical, structurally feasible connection solution.

7.5. Learning from Application

The case study demonstrates that the analytical and numerical methodology developed throughout this research can be translated into a practical connection design while maintaining consistency between the local connection behaviour and the global structural response. Rather than treating connection design and structural analysis as separate tasks, the developed workflow allows the required in- and out-of-plane rotational stiffness to be established from the global structural behaviour and subsequently converted into a feasible steel–timber connection configuration.

The application further illustrates that the interaction between connection stiffness, member geometry, and global stability governs the available design space. The required in- and out-of-plane rotational stiffness is determined not only by the connection itself but also by the stiffness and utilisation of the supporting members. In practice, member depth is one of the most influential design parameters, as it controls both the available lever arm within the connection and the achievable embedment length. Consequently, increasing the member depth simultaneously improves the global stiffness of the gridshell and expands the range of feasible connection configurations.

The case study also demonstrates that a practical range of out-of-plane rotational stiffness exists in which stable gridshell behaviour can be achieved using realistic steel–timber knife-plate connections. Beyond this range, further increases in connection stiffness provide diminishing improvements to the global structural response, whereas insufficient stiffness rapidly reduces the available stability margin. Where higher stability is required, introducing additional in-plane restraint through bracing or local plate stiffeners may be more effective than increasing the connection's out-of-plane rotational stiffness alone.

Finally, the application confirms that timber splitting is a governing design consideration for heavily loaded semi-rigid dowel connections. Although the dowel, steel plate, and member capacities all exhibited substantial reserve capacity, additional reinforcement perpendicular to the grain was required to mobilise the available bearing resistance of the connection fully. This demonstrates that stiffness optimisation alone is insufficient and that practical detailing, particularly regarding splitting reinforcement, remains an essential aspect of the final connection design.

The application also highlights the efficiency of combining analytical formulations with parametric modelling tools. Rather than treating each design iteration as an independent analysis, changes to the connection geometry, member dimensions, or material properties are propagated automatically through both the local connection calculations and the global structural model. This significantly reduces the effort required to evaluate alternative design solutions and enables rapid optimisation of both the connection and the overall gridshell. In the present study, this integrated workflow reduced the entire design and verification process to approximately two weeks while still allowing numerous design iterations and sensitivity studies.

7.6. Conclusions

The case study demonstrates that the proposed design methodology can be used to develop a practical steel–timber connection that satisfies both the local connection requirements and the global stability requirements of the investigated gridshell. The selected 400 × 200 mm C24 members combined with the 4 × 4 arrangement of 16 mm dowels provide sufficient out-of-plane rotational stiffness to achieve the required global fixity while remaining well within the governing ultimate limit state checks for the timber members, connection components, and steel plate.

The global stability verification further shows that the final design remains stable for all investigated load combinations, including the governing imperfection cases. Serviceability and ultimate limit state requirements are satisfied, demonstrating that the analytical stiffness formulation can be translated successfully into a practical connection design.

Some uncertainty nevertheless remains regarding the exact critical load factors because a limited number of stability analyses did not converge consistently. Although the adopted design provides adequate reserve capacity, additional confidence could be obtained through experimental validation or by introducing supplementary stabilisation measures, such as cross-bracing or increased in-plane rotational stiffness. These measures would reduce the structure's sensitivity to imperfections and further improve the robustness of the global response.

8. Discussion

Several limitations should be considered when interpreting the results presented in this research. Both the analytical and numerical formulations assume linear elastic material behaviour and therefore do not capture local timber splitting, plastic embedment deformation, frictional effects, or progressive damage development. In practical applications, some of these mechanisms may be mitigated through appropriate connection detailing, such as reinforcement screws (as shown in the C30 case study) or steel confinement elements. Nevertheless, these effects fall outside the scope of the present study.

The analytical and numerical formulations further neglect axial fastener action, rope effects, and the detailed interaction between the steel plate and the surrounding timber. Although the steel plate's flexibility is accounted for analytically, the finite element model omits the plate from the local discretisation to reduce computational effort and analytical complexity. Consequently, local stress concentrations and contact interactions within the steel components are not explicitly represented.

At the global scale, the gridshell behaviour is represented using equivalent rotational springs. This idealisation enables a direct relationship to be established between the rotational stiffness of the connection and the structural response of the gridshell. However, it does not account for nonlinear moment–rotation relationships or progressive stiffness degradation that may occur as the connection approaches failure. Despite these simplifications, the combined analytical and numerical methodology provides a consistent framework for relating local connection mechanics to the global structural behaviour of semi-rigid timber gridshells. Rather than treating the connection and the structural system as independent design problems, the proposed workflow establishes a direct link between the required global rotational stiffness and the geometric and material parameters that govern the behaviour of the individual dowels and the connection as a whole.

An important outcome of this work is the demonstration that connection stiffness can be treated as a design variable rather than as an assumed boundary condition. The analytical formulations allow the influence of individual parameters to be evaluated rapidly, while the numerical models provide confidence that the governing stiffness trends are representative of the physical behaviour. Combined with the parametric workflow, this enables efficient exploration of a large design space while maintaining a clear physical interpretation of the governing mechanisms.

More broadly, this research illustrates the value of integrating analytical modelling, finite element analysis and parametric design. The analytical formulations provide rapid physical insight into the governing parameters, the finite element models verify the underlying assumptions, and the global parametric analyses translate the resulting stiffness into structural performance. Together, these methods enable a substantially more efficient exploration of the design space than would be achievable using numerical modelling alone.

9. Conclusion

This research developed and validated a combined analytical, numerical, and parametric methodology for relating the rotational stiffness of semi-rigid steel–timber knife-plate connections to the global behaviour of timber gridshell structures. By integrating global parametric analyses, analytical beam-on-elastic-foundation formulations, finite element simulations, and practical connection design, the study established a consistent multi-scale framework linking local connection mechanics to structural performance.

The use of parametric modelling proved essential for investigating both local connection behaviour and global structural response. Centralised control of geometric, material, and stiffness parameters enabled the efficient generation and evaluation of large numbers of design configurations. Combined with automated post-processing using Python(Codex,-), this approach significantly reduced the time required to investigate extensive parameter ranges. It demonstrated the value of parametric workflows for exploring the large solution spaces associated with semi-rigid connection design.

The global analyses demonstrated that the structural response of timber gridshells is strongly influenced by the rotational stiffness of their connections. For both investigated grid configurations, reducing the out-of-plane rotational stiffness resulted in increased deflections, member utilisation, and second-order bending effects. The influence of the in-plane rotational stiffness was shown to depend strongly on the structural topology. Whereas the diagonal gridshell remained governed primarily by the out-of-plane rotational stiffness, the orthogonal configuration exhibited a coupled dependence on both in-plane and out-of-plane stiffness. Consequently, the diagonal configuration provided the most suitable reference system for investigating the proposed knife-plate connection, whose in-plane rotational stiffness is inherently limited.

The analytical investigations demonstrated that dowel diameter, timber density, embedment length, and bolt-group geometry all influence the rotational stiffness of steel–timber dowel connections. Among the investigated parameters, dowel diameter had the greatest influence on stiffness development, while embedment length exhibited the most complex behaviour. In contrast to the approximately monotonic increases in stiffness with dowel diameter and timber density, the embedment-length response exhibited multiple plateau regions and nonlinear transitions reflecting changes in the dowel–timber contact mechanism. These observations indicate that rotational stiffness cannot be adequately described by local bearing behaviour alone but depends on the interaction among dowel bending, distributed timber support, and the evolution of the contact zone along the embedded length.

Comparison with the Eurocode 5 slip-modulus formulation demonstrated systematic differences between the analytical and empirical approaches. Because the analytical formulation explicitly accounts for finite embedment length and distributed dowel–timber interaction, it predicts progressively greater rotational stiffness than Eurocode 5 as embedment length increases. The results, therefore, suggest that the Eurocode 5 formulation provides a practical and conservative, design-oriented stiffness approximation but does not explicitly represent several of the mechanical mechanisms that govern the rotational behaviour of dowel-type connections. However, when a connection is loaded, the embedment can start yielding over the dowel for larger dowel diameters, providing less capacity than anticipated.

The finite element investigations confirmed the general stiffness trends predicted by the analytical formulation. Both approaches demonstrated increasing rotational stiffness with increasing dowel diameter and embedment length, while the numerical simulations verified the importance of

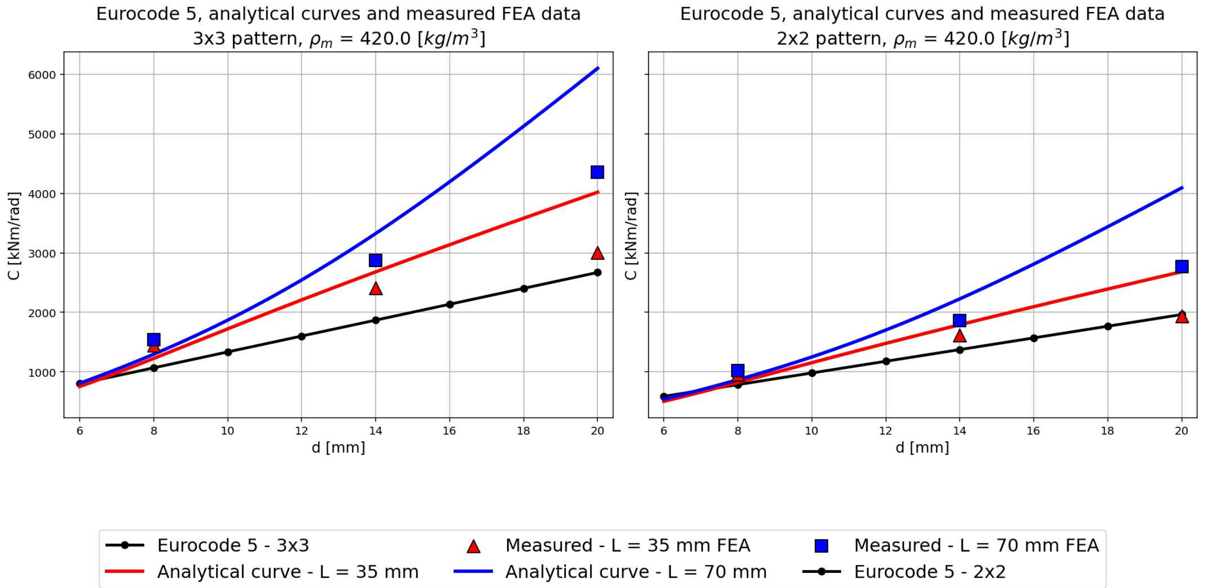

Figure 84: Comparison of Eurocode 5, analytical, and finite element out-of-plane rotational stiffness predictions for the 2×2 and 3×3 dowel patterns at embedment lengths of 35 mm and 70 mm.

embedment-dependent behaviour. Although the finite element results generally occupied an intermediate position between the analytical formulation and the Eurocode 5 predictions, calibration of the analytical model reduced the remaining discrepancy to approximately 5%. This indicates that the analytical formulation captures the stiffness mechanisms successfully while highlighting the need for further research into local contact behaviour, stress concentrations, and nonlinear embedment effects.

The practical case study demonstrated that the developed methodology can be applied directly within engineering design. The required global rotational stiffness was translated into a feasible steel–timber knife-plate connection that subsequently satisfied the structural verification requirements while providing the stiffness needed for global stability. The study further demonstrated that the governing design criterion was the required rotational stiffness, rather than the ultimate strength of individual connection components, underscoring the importance of explicitly accounting for connection stiffness in the design process.

Overall, this research demonstrates that material and geometric parameters strongly influence the rotational stiffness of semi-rigid steel–timber connections, and that this stiffness, in turn, directly affects the global behaviour, stability, and feasible design space of timber gridshell structures. Rather than treating connection stiffness as an assumed modelling parameter, the proposed methodology establishes a direct relationship between the global structural requirements of an unbraced gridshell geometry and the local connection mechanics. The developed framework, therefore, provides a practical basis for stiffness-informed analysis and design of timber gridshells while offering a foundation for future research into semi-rigid timber connections and their integration within computational structural design workflows.

10. Recommendations for Future Research

1. **Extension towards nonlinear connection behaviour**

The present analytical formulation assumes linear elastic material behaviour. Future research should extend the beam-on-elastic-foundation formulation to incorporate nonlinear embedment behaviour, plastic dowel yielding, and progressive stiffness degradation. A bi-linear or multi-linear moment–rotation formulation could provide a more realistic representation of the connection response beyond the elastic range and enable direct assessment of ultimate capacity and post-yield redistribution within timber gridshells.

2. **Development of nonlinear analytical foundation models**

The analytical formulation currently represents the timber using a linear elastic foundation. Incorporating nonlinear foundation behaviour would allow local crushing, stress redistribution, and changes in contact conditions to be represented more accurately, particularly for larger embedment lengths, where contact evolution becomes increasingly important.

3. **Investigation of the embedment contact mechanism**

The analytical formulation predicts multiple plateau regions associated with changes in the dowel–timber contact mechanism. Although these mechanisms are supported by the deformation shapes observed in the analytical model, further numerical and experimental research is required to verify the physical development of the contact zones and their influence on rotational stiffness.

4. **Improved modelling of the complete knife-plate connection**

Although the steel plate's flexibility was accounted for analytically, the local finite element model did not explicitly include the steel plate geometry. Future work should investigate the combined influence of plate thickness, local plate deformation, weld geometry, and contact interactions on the rotational stiffness and stress distribution of the complete knife-plate connection.

5. **Experimental validation**

The proposed analytical formulations and numerical models should be validated through physical testing of both individual dowels and complete multi-dowel knife-plate connections. Experimental results would enable verification of the predicted stiffness development, embedment mechanisms, and force distributions while providing data for further calibration of the analytical model.

6. **Extension of the global parametric framework**

The global parameter study considered only two grid topologies and a single reference geometry. Future research should investigate a wider range of gridshell geometries, grid densities, span-to-rise ratios, support conditions, and loading scenarios to establish more generally applicable stiffness requirements for semi-rigid timber gridshells.

7. **Combined stiffness and stability design**

The present research focused primarily on the influence of rotational stiffness on the global structural response. Future studies should investigate the interaction between connection stiffness, member capacity, and global stability, allowing stability to be incorporated directly as a design criterion alongside conventional strength verification.

8. **Relationship between connection stiffness and global restraint**

The investigated knife-plate connection provides only limited in-plane rotational stiffness. Future research should establish a direct relationship between the required in-plane stiffness and practical stabilisation measures, such as diagonal bracing, local plate stiffeners, or alternative connection details. Such relationships would enable global stiffness requirements to be translated directly into practical detailing recommendations.

Sources

Adriaenssens, Sigrid., Block, Philippe., Veenendaal, Diederik. and Williams, Chris. (2014) *Shell structures for architecture : form finding and optimization*. Routledge/ Taylor & Francis Group.

Block, Philippe., Mele, T. van., Rippmann, Matthias. and Paulson, N.C.. (2017) "Beyond bending : reimagining compression shells," p. 190.

Bulenda, T. and Knippers, J. (2001) *Stability of grid shells*. Stuttgart. Available at: www.elsevier.com/locate/compstruc.

Chen, C., Kuang, Y., Zhu, S., Burgert, I., Keplinger, T., Gong, A., Li, T., Berglund, L., Eichhorn, S.J. and Hu, L. (2020) "Structure–property–function relationships of natural and engineered wood," *Nature Reviews Materials*, 5(9), pp. 642–666. Available at: https://doi.org/10.1038/S41578-020-0195-Z;SUBJMETA.

Chen, Z., Zhao, J., Zhao, S., Wang, X., Liu, H., Zhang, L. and Xu, Q. (2022) "Experimental study and theoretical analysis on the rotational performance of large-size glulam bolted joints with slotted-in steel plates," *Construction and Building Materials*, 341. Available at: https://doi.org/10.1016/j.conbuildmat.2022.127785.

Dyvik, S.H., Manum, B. and Rønnquist, A. (2021) "Gridshells in recent research—a systematic mapping study," *Applied Sciences (Switzerland)*, 11(24). Available at: https://doi.org/10.3390/app112411731.

Fan, F., Ma, H., Cao, Z. and Shen, S. (2011) "A new classification system for the joints used in lattice shells," *Thin-Walled Structures*, 49(12), pp. 1544–1553. Available at: https://doi.org/10.1016/j.tws.2011.08.002.

Fu, H., He, M., Alhaddad, W. and Shen, Z. (2024) "Numerical simulation and design method of dowel-type timber joints connecting laminated veneer lumber," *Structures*, 62, p. 106172. Available at: https://doi.org/10.1016/J.ISTRUC.2024.106172.

Gikonyo, J.W., Schweigler, M. and Bader, T.K. (2025) "Numerical simulation of the group effect in the slip modulus of laterally loaded multiple fastener cross-laminated timber connections," *Construction and Building Materials*, 484. Available at: https://doi.org/10.1016/j.conbuildmat.2025.141536.

Harada, H., Nakajima, S., Yamazaki, Y., Matsui, R., Hayashi, K., Sakata, H. and Takeuchi, T. (2018) "Rotational stiffness and bending strength of steel connections in timber lattice shell," *Journal of Structural and Construction Engineering*, 83(746), pp. 577–587. Available at: https://doi.org/10.3130/aijs.83.577.

Hetényi, M. (1946) "Beams On Elastic Foundation: Theory With Applications In The Fields Of Civil And Mechanical-Engineering."

Holzer, S.M., Loferski, J.R. and Dillard, D.A. (1988) *A REVIEW OF CREEP IN WOOD: CONCEPTS RELEVANT TO DEVELOP LONG-TERM BEHAVIOR PREDICTIONS FOR WOOD STRUCTURES.*

Isufi F. (2021) *Parametric design of a grid shell roof over existing buildings, with a focus on connection design.*

Kekeliak, M., An, J.V. and Gocál, J. (2013) *On numerical modelling of dowel type timber connections.*

Larsson, S. (2018) *Design Implications of Rigid Timber Gridshells: A Method for the Planning and Manufacture of Load-carrying, Rigid, Freeform Structures of Timber.* Sweden.

Li, R., Chen, A., Yang, L., He, G. and Wang, H. (2025) "Experimental study on long-term performance of simply-supported Glulam beams connected with steel joining plates and bolts," *Structures*, 73. Available at: https://doi.org/10.1016/j.istruc.2025.108439.

Nakajima, S., Terazawa, Y., Takeuchi, T., Ogawa, T., Yamazaki, Y. and Sakata, H. (2019) "Elastic buckling strength of timber lattice shell with steel connections considering rotational stiffness," *Journal of Structural and Construction Engineering*, 84(762), pp. 1081–1091. Available at: https://doi.org/10.3130/aijs.84.1081.

Nakajima, S., Yamazaki, Y., Sakata, H., Takeuchi, T., Harada, H. and Hayashi, K. (2019) "Rotational stiffness of steel connections for timber lattice shell in negative out-of-plane and in-plane directions," *Journal of Structural and Construction Engineering*, 84(760), pp. 831–841. Available at: https://doi.org/10.3130/aijs.84.831.

NEN 1993 (2016) *NEN-EN 1993-1-1:2006+A1:2014+NB:2016 Staal - Algemene regels.* NEN.

NEN 1995 (2014) *NEN-EN 1995-1-1:2005+A2:2014+NB:2013 Hout - Algemeen, BRISwarenhuis.* Available at: https://www.briswarenhuis.nl/docs/norm/nen-en1995-1-1-2005[3] (Accessed: October 16, 2025).

OECD (2019) *Global Material Resources Outlook to 2060: Economic Drivers and Environmental Consequences.* Paris: OECD Publishing. Available at: https://doi.org/10.1787/9789264307452-en.

Rahim, N.L., Raftery, G.M. and Quenneville, P. (2018) "Stiffness of Bolted Timber Connection," *WCTE 2018 World Conference on Timber Engineering.* Seoul : WTCE.

Saad, K. and Lengyel, A. (2022) "Strengthening Timber Structural Members with CFRP and GFRP: A State-of-the-Art Review," *Polymers.* MDPI. Available at: https://doi.org/10.3390/polym14122381.

Sandhaas, C. and Van De Kuilen, J.W.G. (2013) *Material model for wood.*

Sandhaas, C., Munch-Andersen, J. and Dietsch, P. (2018) *Design of Connections in Timber Structures: A state-of-the-art report by COST Action FP1402 / WG3.*

Skotny, L. and Hidalgo, B.M. (2018) *Blas Molero on Enterfea HERTZ Contact in FEMAP: CGAP elements.* Available at: https://enterfea.com/hertz-contact-cgap-elements/ (Accessed: May 28, 2026).

Spengler van F. (2024) *Parametric design of grid shell structures: A design method considering semi-rigid joints and stiffness based connection design.*

Stahl, J.A. and Rosenkranz, C. (2024) "REHABILITATION OF THE MANNHEIM MULTIHALLE," *Journal of the International Association for Shell and Spatial Structures*, 65(1), pp. 1–12. Available at: https://doi.org/10.20898/j.iass.2023.020.

Tao, H., Yang, H., Ju, G. and Shi, B. (2021) "Elastic stiffness of timber joints with dowel-type fasteners and slotted-in steel plate based on the theory of beam on elastic foundation," *Construction and Building Materials*, 294. Available at: https://doi.org/10.1016/j.conbuildmat.2021.123569.

Todd, G. (2026) *Stress Concentrations at Holes*, *fracturemechanics.org*. Available at: https://www.fracturemechanics.org/hole.html (Accessed: June 11, 2026).

UNEP (2023) *Building materials and the climate: constructing a new future*. United Nations Environment Programme. Available at: https://wedocs.unep.org/20.500.11822/43293 (Accessed: October 14, 2025).

Wang, X.T., Zhu, E.C., Niu, S. and Wang, H.J. (2021) "Analysis and test of stiffness of bolted connections in timber structures," *Construction and Building Materials*, 303, p. 124495. Available at: https://doi.org/10.1016/J.CONBUILDMAT.2021.124495.

Williams, C. (2017) *Decisions to be made in the design and analysis of gridshell structures*. France: École Nationale des Ponts et Chaussées. Available at: https://www.youtube.com/watch?v=VPSw3dRE6xQ (Accessed: October 14, 2025).

Wilson, C. (2023) *Arch Analysis – How to Analyse Determinate and Indeterminate Arches*, *www.engineeringskills.com*.

Yuan, P.F., Jin, J., Han, L. and Chai, H. (2019) "Structural design of gridshells aiming at lightweight design and rapid assembly," *IASS Symposium 2019 - 60th Anniversary Symposium of the International Association for Shell and Spatial Structures; Structural Membranes 2019 - 9th International Conference on Textile Composites and Inflatable Structures, FORM and FORCE*, pp. 1539–1546.

Appendix

1. Boundary Stiffness as a Function of Fixity

The horizontal stiffness of the gridshell boundary is described using an equivalent arch model, visualised in Figure 4. The edge of the gridshell is idealised as a simply supported curved element spanning a horizontal distance L with rise h. The horizontal restraint at the supports is represented by axial springs with stiffness k_t.

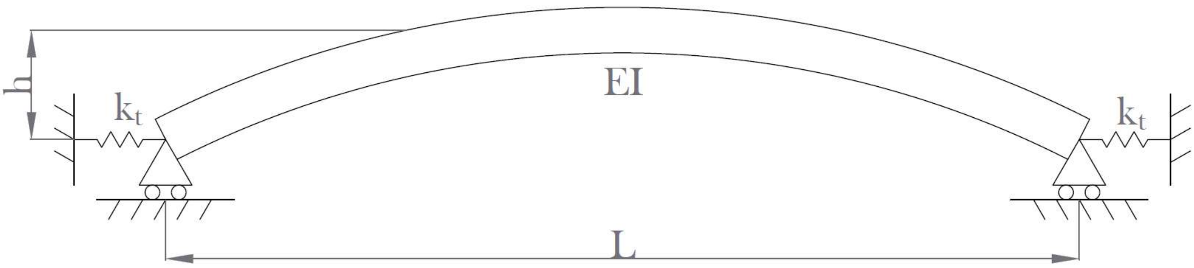

Figure 85: Equivalent tied-arch model with horizontal springs.

The derivation follows a strain-energy approach in which the axial stiffness of a tie is replaced by equivalent horizontal springs, as proposed by Wilson (Wilson, 2023).

The horizontal thrust of the arch is first expressed as:

$$H = \frac{wL^2}{8h} \cdot \frac{8E_tA_th^2}{8E_tA_th^2 + 15EI}$$

where E_tA_t is the axial stiffness of the equivalent tie.

For two horizontal springs acting at the supports, the tie stiffness is replaced by

$$E_tA_t = \frac{k_tL}{2}$$

Substitution gives:

$$H = \frac{wL^2}{8h} \cdot \frac{4k_tLh^2}{4k_tLh^2 + 15EI}$$

Introducing the boundary fixity parameter α, the horizontal thrust can be written as

$$H = \alpha \cdot \frac{wL^2}{8h}$$

$$\alpha = \frac{4k_tLh^2}{4k_tLh^2 + 15EI} = \frac{1}{1 + \frac{15EI}{4k_tLh^2}}$$

Solving for the horizontal spring stiffness gives:

$$k_t = \frac{\alpha}{1-\alpha} \cdot \frac{15EI}{4h^2L}$$

This expression is used to assign horizontal edge stiffnesses in the global gridshell model. As with the rotational fixity parameter, this formulation expresses the boundary stiffness relative to the bending stiffness and geometry of the structural system, rather than as an isolated dimensional spring value. The reason why the rotational springs of the nodes are not included in the formulation is to establish the effects of an uninfluenced result equally.

$$k_t = \frac{\alpha}{1-\alpha} \cdot \frac{15EI}{4h^2L}$$

Results of Incorporating Boundary Stiffness

It is to be noted that in the tested formulation the 1/L was missing from the stiffness derivation. Resulting in unreliable results.

The global fixity parameter study generated a large dataset containing deflections, internal forces, and stability responses for combinations of rotational and boundary stiffness parameters C_{yy}, C_{zz}, and k_t. Due to the high dimensionality of the parameter space, the complete response is difficult to represent directly. A more detailed evaluation of the structural response is therefore presented in the later case study, where the boundary stiffness parameter is fixed, and the behaviour can be evaluated more clearly in two dimensions.

The primary outcome of the global parameter study is the identification of the solution space that describes combinations of stiffness parameters for which the gridshell remains stable, as shown in Figure 18. Second-order and inextensional effects primarily govern the resulting stability boundaries. Near these stability limits, stresses and deformations increase rapidly, typically resulting in large bending moments within the members. Consequently, configurations near the stability boundary may become structurally infeasible due to material failure before the global system becomes unstable.

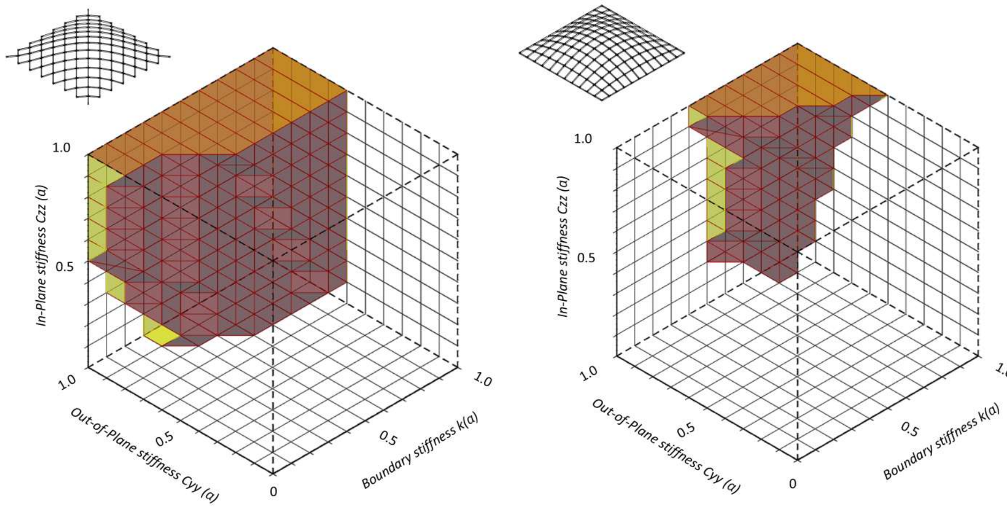

Figure 86: Stability boundaries for the diagonal (left) and orthogonal (right) grids expressed in terms of boundary restraint and rotational stiffness parameters.

Distinct differences are observed between the diagonal and orthogonal grid configurations. The diagonal grids exhibit significantly greater stability regions, indicating the influence of geometric stiffening mechanisms that develop along the boundary of the gridshell.

The out-of-plane rotational stiffness parameter $C_{yy}$is observed to govern the global response more strongly than the in-plane rotational stiffness parameter C_{zz}, particularly for configurations approaching the stability boundary.

2. Connection Design Optimisation Procedure

The preceding analyses establish a direct relationship between global structural behaviour and local connection stiffness. To demonstrate the practical application of the developed methodology, a connection optimisation tool was implemented in Grasshopper. The objective of this tool is to generate connection layouts that achieve a prescribed rotational stiffness while minimising material use and promoting efficient force distribution among fasteners.

The optimisation procedure is based on a discretised search space representing the available connection plate area. A rectangular grid with a spacing of 2 × 2 mm is generated, providing a set of candidate fastener locations for the optimisation algorithm to select from. The candidate points are sorted radially from the centre of the connection to establish a consistent ordering of potential fastener positions and facilitate the optimisation process.

The primary objective is to minimise the total steel volume required for the connection, expressed as:

$$V_{tot} = V_d + V_p$$

where V_d represents the steel volume of the dowels and V_p represents the steel volume of the connection plate.

In addition to material efficiency, practical detailing constraints must be satisfied. Minimum fastener spacing requirements are enforced in accordance with Eurocode 5 to reduce the risk of timber splitting and local interaction effects. Rather than incorporating these constraints directly into the optimisation objective, they are implemented as a preprocessing step. Any candidate locations violating the required spacing criteria are removed from the available solution space using a Python routine. This approach reduces the computational complexity of the optimisation while ensuring that only feasible connection layouts are evaluated.

A second constraint is introduced to prevent solutions containing fewer than two active fasteners, as such configurations cannot provide rotational restraint and therefore behave as idealised hinges. Such configurations are assigned a large penalty value to ensure the optimisation process rejects them.

The optimisation objective is formulated as a fitness function consisting of the steel volume and a series of penalty terms:

$$Fitness = V_{tot} + \sum P_i$$

The first penalty term evaluates the ability of the connection to achieve the target rotational stiffness. The resulting dowel-group stiffness $C_{yy,1}$ is combined with the plate bending stiffness $C_{yy,2}$ through a reciprocal stiffness relationship to obtain the total connection stiffness C_0:

$$C_{yy,1} = \frac{M}{\theta} = \sum r_i^2 k_i$$

$$C_{yy,2} = \frac{EI_{yy}}{e}$$

$$C_0 = \frac{1}{\dfrac{1}{C_{yy,1}} + \dfrac{1-r}{C_{yy,2}}}$$

The resulting stiffness is compared with the target stiffness C_{ref}. Undershooting the required stiffness is penalised more heavily than overshooting it, reflecting the design objective of achieving a minimum stiffness requirement:

$$P_C = \alpha \cdot abs\left(C_0 - C_{ref}\right) + \beta \cdot \max\left(0, \left(C_{ref} - C_0\right)\right)^2$$

The weighting factors α and β are selected such that the stiffness penalty remains comparable in magnitude to the volume objective.

A second penalty term is introduced to encourage efficient utilisation of the fasteners. Fasteners located near the centre of rotation contribute relatively little to the rotational stiffness and may therefore result in inefficient use of material. Since the contribution of an individual fastener is proportional to the square of its distance from the centre of rotation, fasteners located close to the centroid contribute relatively little to the overall rotational stiffness while still increasing material usage. To account for this effect, a utilisation ratio is defined for each fastener:

$$\omega_i = \frac{r_i}{C_0 \cdot \sum_i \frac{r_i}{C_0}}$$

The penalty term is formulated using the maximum utilisation ratio within the connection group:

$$P_u = \gamma \cdot (n \cdot \max(\omega_i) - 1)$$

where n is the number of active fasteners and γ is a weighting factor selected to balance the influence of the utilisation penalty relative to the stiffness and volume objectives.

The final optimisation objective becomes:

$$Fitness = V_{tot} + P_C + P_u$$

The optimisation is solved using a simulated annealing algorithm implemented through Galapagos. A simulated annealing approach was selected because it offers greater ability to escape local optima than conventional evolutionary search strategies, thereby increasing the likelihood of identifying globally efficient fastener configurations.

The resulting connection layouts therefore represent a compromise between material efficiency, rotational stiffness requirements, and fastener utilisation. These optimised configurations are subsequently compared with conventional connection layouts to evaluate the effectiveness of the proposed stiffness-based design methodology.

The optimisation process produces connection layouts that satisfy the stiffness and material objectives but do not necessarily result in practical or easily reproducible connection geometries. Since multiple near-optimal solutions may exist, the raw optimisation output is therefore subjected to a post-processing procedure aimed at improving constructability and geometric regularity.

Three post-processing strategies are investigated. The first enforces symmetry by splitting the connection along the x-axis and mirroring the side with the most fasteners. The second establishes a regular grid by generating a bounding box around the optimised layout, subdividing this region according to the number of active fasteners, and relocating the fasteners to the nearest grid positions. The third method seeks to identify dominant alignment directions within the optimised layout, constructs a best-fit grid based on these axes, and then relocates the fasteners accordingly.

The resulting connection layouts are subsequently re-evaluated using the analytical stiffness model to determine the extent to which constructability-driven regularisation influences the predicted rotational stiffness.

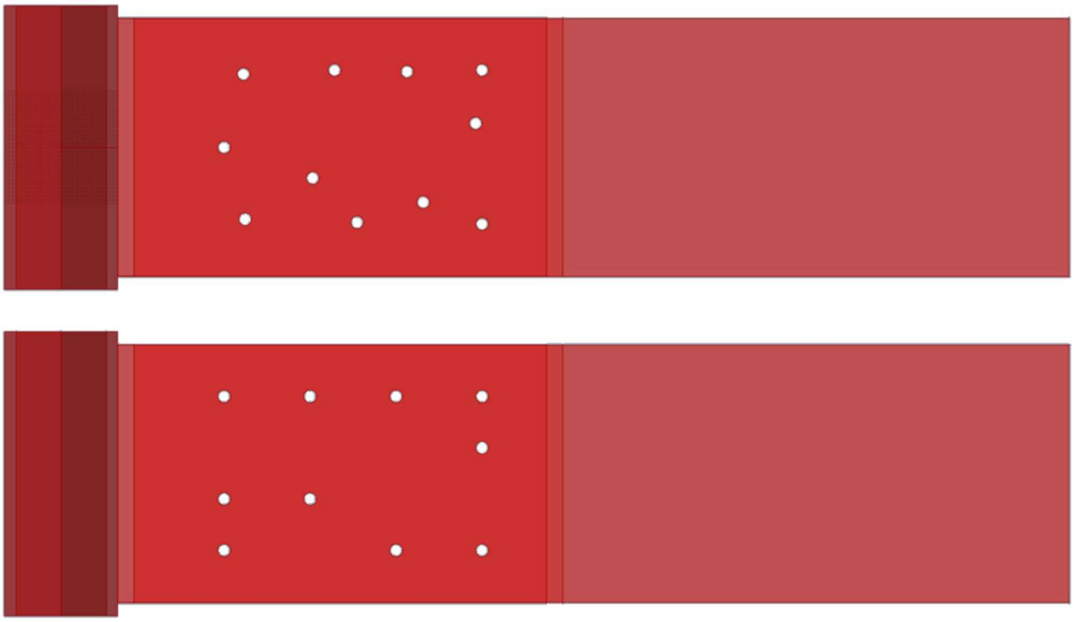

Figure 87: Comparison between the raw optimisation result and the post-processed connection detail using 16 mm dowels for the selected design stiffness (α = 0.55, C_Y = 4699 kNm/rad).

3. Derivation Beam Fixity Factor

Formulation of the displacement function in relation to the external load q_z

$$\frac{d^2}{dx^2}(EI\frac{d^2w(x)}{dx^2}) = q_z$$

Since EI is constant over the length of the beam

$$EI\frac{d^4w(x)}{dx^4} = q_z$$

$$\frac{d^4w(x)}{dx^4} = \hat{q}_z$$

With $\hat{q}_z = \frac{q_z}{EI}$

Integrated by the lowest derivative of the initial function

$$w(x) = \iint\iint \hat{q}_z = \frac{\hat{q}_z x^4}{24} + \frac{C_1x^3}{6} + \frac{C_2x^2}{2} + C_3x + C_4$$

$$w(x) = \iint\iint \hat{q}_z = \frac{\hat{q}_z x^4}{24} + A_1x^3 + A_2x^2 + A_3x + A_4$$

Integrate to get the functions that are related to the boundary conditions

$$w(x) = \frac{\hat{q}_z x^4}{24} + A_1x^3 + A_2x^2 + A_3x + A_4$$

$$\frac{dw(x)}{dx} = \frac{\hat{q}_z x^3}{6} + 3A_1x^2 + 2A_2x + A_3$$

$$\frac{d^2w(x)}{dx^2} = \frac{\hat{q}_z x^2}{2} + 6A_1x + 2A_2$$

Hinged boundary conditions

$$w(0) = 0$$

$$\frac{d^2w(0)}{dx^2} = 0$$

$$w(l) = 0$$

$$\frac{d^2w(l)}{dx^2} = 0$$

$$w(0) = \frac{\hat{q}_z x^4}{24} + A_1x^3 + A_2x^2 + A_3x + A_4 = 0$$

$$\boldsymbol{A_4 = 0}$$

$$\frac{d^2w(0)}{dx^2} = \frac{\hat{q}_z x^2}{2} + 6A_1x + 2A_2 = 0$$

$$\boldsymbol{A_2 = 0}$$

$$w(l) = \frac{\hat{q}_z x^4}{24} + A_1x^3 + A_2x^2 + A_3x + A_4 = 0$$

$$\frac{\hat{q}_z l^4}{24} + A_1l^3 + A_3l = 0$$

$$\frac{d^2w(l)}{dx^2} = \frac{\hat{q}_z x^2}{2} + 6A_1x = 0$$

$$\frac{\hat{q}_z l^2}{2} + 6A_1l = 0$$

$$\boldsymbol{A_1 = -\frac{\hat{q}_z l}{12}}$$

$$\frac{\hat{q}_z l^4}{24} + A_1l^3 + A_3l = 0$$

$$\frac{\hat{q}_z l^4}{24} - \frac{\hat{q}_z l^4}{12} + A_3l = 0$$

$$A_3 = \frac{\hat{q}_z l^3}{24}$$

Insert solutions for A1 to A4 into the initial deformation equation

$$A_4 = 0$$

$$A_2 = 0$$

$$A_1 = -\frac{\hat{q}_z l}{12}$$

$$A_3 = \frac{\hat{q}_z l^3}{24}$$

$$w(x) = \frac{\hat{q}_z}{24}x^4 - \frac{\hat{q}_z l}{12}x^3 + \frac{\hat{q}_z l^3}{24}x$$

$$w(x) = \frac{\hat{q}_z}{24}x^4 - \frac{\hat{q}_z l}{12}x^3 + \frac{\hat{q}_z l^3}{24}x$$

Maximum deflection occurs at midspan

$$w_{max}\left(\frac{1}{2}l\right) = \frac{\hat{q}_z l^4}{384} - \frac{\hat{q}_z l^4}{96} + \frac{\hat{q}_z l^4}{48}$$

$$w_{max}\left(\frac{1}{2}l\right) = \frac{5\hat{q}_z l^4}{384} = \frac{5q_z l^4}{384EI}$$

Semi-rigid boundary conditions

$$w(0) = 0$$

$$-EI\frac{d^2w(0)}{dx^2} + C_r\frac{dw(0)}{dx} = 0$$

$$w(l) = 0$$

$$EI\frac{d^2w(l)}{dx^2} + C_r\frac{dw(l)}{dx} = 0$$

$$w(0) = \frac{\hat{q}_z x^4}{24} + A_1x^3 + A_2x^2 + A_3x + A_4 = 0$$

$$A_4 = 0$$

$$-EI\frac{d^2w(0)}{dx^2} + C_r\frac{dw(0)}{dx} = -EI\left(\frac{\hat{q}_z x^2}{2} + 6A_1x + 2A_2\right) + C_r\left(\frac{\hat{q}_z x^3}{6} + 3A_1x^2 + 2A_2x + A_3\right) = 0$$

$$-2A_2EI + A_3C_r = 0$$

$$\boldsymbol{A_2 = A_3\frac{C_r}{2EI}}$$

$$w(l) = \frac{\hat{q}_z x^4}{24} + A_1x^3 + A_2x^2 + A_3x + A_4 = 0$$

$$\frac{\hat{q}_z l^4}{24} + A_1l^3 + A_2l^2 + A_3l = 0$$

$$\frac{\hat{q}_z l^4}{24} + A_1 l^3 + A_3 \frac{C_r}{2EI} l^2 + A_3 l = 0$$

$$-A_1 l^3 = \frac{\hat{q}_z l^4}{24} + A_3 \frac{C_r}{2EI} l^2 + A_3 l$$

$$\boldsymbol{A_1 = -\frac{\hat{q}_z l}{24} - A_3 \left(\frac{C_r}{2EIl} + \frac{1}{l^2}\right)}$$

$$EI \frac{d^2 w(l)}{dx^2} + C_r \frac{dw(l)}{dx} = EI \left(\frac{\hat{q}_z x^2}{2} + 6A_1 x + 2A_2\right) + C_r \left(\frac{\hat{q}_z x^3}{6} + 3A_1 x^2 + 2A_2 x + A_3\right) = 0$$

$$EI \left(\frac{\hat{q}_z l^2}{2} + 6A_1 l + 2A_2\right) + C_r \left(\frac{\hat{q}_z l^3}{6} + 3A_1 l^2 + 2A_2 l + A_3\right) = 0$$

$$\boldsymbol{A_4 = 0}$$

$$\boldsymbol{A_2 = A_3 \frac{C_r}{2EI}}$$

$$\boldsymbol{A_1 = -\frac{\hat{q}_z l}{24} - A_3 \left(\frac{C_r}{2EIl} + \frac{1}{l^2}\right)}$$

$$\frac{\hat{q}_z l^2 EI}{2} + 6EIA_1 l + 2EIA_2 + \frac{\hat{q}_z C_r l^3}{6} + 3C_r A_1 l^2 + 2C_r A_2 l + C_r A_3 = 0$$

$$\frac{\hat{q}_z l^2 EI}{2} + 6EIA_1 l + C_r A_3 + \frac{\hat{q}_z C_r l^3}{6} + 3C_r A_1 l^2 + A_3 \frac{C_r^2 l}{EI} + C_r A_3 = 0$$

$$\frac{\hat{q}_z EIl^2}{2} + \frac{\hat{q}_z C_r l^3}{6} + A_1 (6EIl + 3C_r l^2) + A_3 \left(2C_r + \frac{C_r^2 l}{EI}\right) = 0$$

$$\frac{\hat{q}_z EIl^2}{2} + \frac{\hat{q}_z C_r l^3}{6} + (-\frac{\hat{q}_z l}{24} - A_3 \left(\frac{C_r}{2EIl} + \frac{1}{l^2}\right)) (6EIl + 3C_r l^2) + A_3 \left(2C_r + \frac{C_r^2 l}{EI}\right) = 0$$

$$\frac{\hat{q}_z EIl^2}{2} + \frac{\hat{q}_z C_r l^3}{6} - \frac{\hat{q}_z EIl^2}{4} - 3C_r A_3 - A_3 \frac{6EI}{l} - \frac{\hat{q}_z C_r l^3}{8} - A_3 \frac{3C_r^2 l}{2EI} - 3C_r A_3 \ + A_3 \left(2C_r + \frac{C_r^2 l}{EI}\right) = 0$$

$$\frac{\hat{q}_z EIl^2}{2} + \frac{\hat{q}_z C_r l^3}{6} - \frac{\hat{q}_z EIl^2}{4} - \frac{\hat{q}_z C_r l^3}{8} + A_3 (-3C_r - \frac{6EI}{l} - \frac{3C_r^2 l}{2EI} - 3C_r) \ + A_3 \left(2C_r + \frac{C_r^2 l}{EI}\right) = 0$$

$$\frac{\hat{q}_z EIl^2}{4} + \frac{\hat{q}_z C_r l^3}{24} + A_3 \left(\frac{C_r^2 l}{EI} - 4C_r - \frac{6EI}{l} - \frac{3C_r^2 l}{2EI}\right) = 0$$

$$A_3 \left(-4C_r - \frac{6EI}{l} - \frac{C_r^2 l}{2EI}\right) = -\frac{\hat{q}_z EIl^2}{4} - \frac{\hat{q}_z C_r l^3}{24}$$

$$A_3 \left(-\frac{96 C_r l EI}{EI} - \frac{144 E^2 I^2}{EI} - \frac{12 C_r^2 l^2}{EI}\right) = -\hat{q}_z l^3 (6EI + C_r l)$$

$$A_3 \frac{96C_r lEI + 144E^2I^2 + 12C_r^2 l^2}{EI} = \hat{q}_z l^3 (6EI + C_r l)$$

$$A_3 \frac{(C_r l + 6EI)(12C_r l + 24EI)}{EI} = \hat{q}_z l^3 (6EI + C_r l)$$

$$\boldsymbol{A_3 = \frac{\hat{q}_z l^3 EI}{12(C_r l + 2EI)}}$$

Insert solution for A3 into existing solutions for A1 to A4

$$\boldsymbol{A_4 = 0}$$

$$A_2 = A_3 \frac{C_r}{2EI}$$

$$A_2 = \frac{\hat{q}_z l^3 EI}{12(C_r l + 2EI)} \frac{C_r}{2EI}$$

$$\boldsymbol{A_2 = \frac{\hat{q}_z l^3 C_r}{24(C_r l + 2EI)}}$$

$$A_1 = -\frac{\hat{q}_z l}{24} - A_3 \left(\frac{C_r}{2EIl} + \frac{1}{l^2}\right)$$

$$A_1 = -\frac{\hat{q}_z l}{24} - A_3 \frac{C_r}{2EIl} - A_3 \frac{1}{l^2}$$

$$A_1 = -\frac{\hat{q}_z l}{24} - \frac{\hat{q}_z l^2 C_r}{24(C_r l + 2EI)} - \frac{\hat{q}_z lEI}{12(C_r l + 2EI)}$$

$$A_1 = -\frac{\hat{q}_z l(C_r l + 2EI)}{24(C_r l + 2EI)} - \frac{\hat{q}_z l(C_r l)}{24(C_r l + 2EI)} - \frac{\hat{q}_z l(2EI)}{24(C_r l + 2EI)}$$

$$A_1 = -\frac{\hat{q}_z l(C_r l + 2EI)}{12(C_r l + 2EI)}$$

$$\boldsymbol{A_1 = -\frac{\hat{q}_z l}{12}}$$

$$w(x) = \frac{\hat{q}_z x^4}{24} + A_1 x^3 + A_2 x^2 + A_3 x + A_4$$

$$w(x) = \frac{\hat{q}_z x^4}{24} - \frac{\hat{q}_z l}{12} x^3 + \frac{\hat{q}_z l^2 C_r l}{24(C_r l + 2EI)} x^2 + \frac{\hat{q}_z l^3 EI}{12(C_r l + 2EI)} x$$

$$w(x) = \frac{q_z x^4}{24EI} - \frac{q_z l}{12EI} x^3 + \frac{q_z l^2 C_r l}{24EI(C_r l + 2EI)} x^2 + \frac{q_z l^3}{12(C_r l + 2EI)} x$$

$$\frac{dw(x)}{dx}=\frac{q_z x^3}{6EI}-\frac{q_z l}{4EI}x^2+\frac{q_z l^2 C_r l}{12EI(C_r l+2EI)}x+\frac{q_z l^3}{12(C_r l+2EI)}$$

$$\frac{d^2w(x)}{dx^2}=\frac{q_z x^2}{2EI}-\frac{q_z l}{2EI}x+\frac{q_z l^2 C_r l}{12EI(C_r l+2EI)}$$

$$-EI\frac{d^2w(0)}{dx^2}=\frac{q_z 0^2}{2}-\frac{q_z l}{2}0+\frac{q_z l^2 C_r l}{12(C_r l+2EI)}$$

$$-EI\frac{d^2w(0)}{dx^2}=\frac{q_z l^2 C_r l}{12(C_r l+2EI)}=\frac{q_z l^2}{12}\cdot\frac{C_r l}{C_r l+2EI}$$

$$\frac{C_r l}{C_r l+2EI}=\frac{1}{1+\frac{2EI}{C_r l}}=k$$

$$\frac{2EI}{C_r l}=\lambda$$

$$\frac{1}{C_r l+2EI}=\frac{\frac{1}{C_r l}}{1+\frac{2EI}{C_r l}}=\frac{k}{C_r l}$$

$$C_r=\frac{k}{1-k}\cdot\frac{2EI}{l}$$

Maximum deflection occurs at midspan

$$w_{max}\left(\frac{1}{2}l\right)=\frac{q_z x^4}{24EI}-\frac{q_z l}{12EI}x^3+\frac{q_z l^2 C_r l}{24EI(C_r l+2EI)}x^2+\frac{q_z l^3}{12(C_r l+2EI)}x$$

$$w_{max}\left(\frac{1}{2}l\right)=\frac{q_z l^4}{384EI}-\frac{q_z l^4}{96EI}+\frac{q_z l^4 C_r l}{48EI(C_r l+2EI)}+\frac{q_z l^4}{24(C_r l+2EI)}$$

$$w_{max}\left(\frac{1}{2}l\right)=\frac{q_z l^4}{384EI}-\frac{4q_z l^4}{384EI}+\frac{8q_z l^4 C_r l}{384EI(C_r l+2EI)}+\frac{16q_z l^4}{384(C_r l+2EI)}$$

$$w_{max}\left(\frac{1}{2}l\right)=\frac{q_z l^4}{384EI}-\frac{4q_z l^4}{384EI}+\frac{8q_z l^4}{384EI}\cdot\frac{C_r l}{(C_r l+2EI)}+\frac{16q_z l^4}{384}\cdot\frac{1}{(C_r l+2EI)}$$

$$w_{max}\left(\frac{1}{2}l\right)=-\frac{3q_z l^4}{384EI}+\frac{8q_z l^4}{384EI}\cdot\frac{C_r l}{(C_r l+2EI)}+\frac{16q_z l^4}{384}\cdot\frac{1}{(C_r l+2EI)}$$

$$w_{max}\left(\frac{1}{2}l\right)=\frac{q_z l^4}{384EI}-\frac{4q_z l^4}{384EI}+\frac{8q_z l^4}{384EI}\cdot k+\frac{16q_z l^4}{384C_r l}\cdot k$$

$$w_{max}\left(\frac{1}{2}l\right)=\frac{q_z l^4}{384EI}-\frac{4q_z l^4}{384EI}+\frac{8q_z l^4}{384EI}\cdot\frac{C_r l}{(C_r l+2EI)}+\frac{16q_z l^4}{384}\cdot\frac{1}{(C_r l+2EI)}$$

Fixed boundary conditions

$$w(0)=0$$

$$\frac{dw(0)}{dx}=0$$

$$w(l)=0$$

$$\frac{dw(l)}{dx}=0$$

$$w(x)=\frac{\hat{q}_z x^4}{24}+A_1x^3+A_2x^2+A_3x+A_4$$

$$\frac{dw(x)}{dx}=\frac{\hat{q}_z x^3}{6}+3A_1x^2+2A_2x+A_3$$

$$\frac{d^2w(x)}{dx^2}=\frac{\hat{q}_z x^2}{2}+6A_1x+2A_2$$

$$w(0)=\frac{\hat{q}_z x^4}{24}+A_1x^3+A_2x^2+A_3x+A_4=0$$

$$\boldsymbol{A_4=0}$$

$$\frac{dw(0)}{dx}=\frac{\hat{q}_z x^3}{6}+3A_1x^2+2A_2x+A_3=0$$

$$\boldsymbol{A_3=0}$$

$$w(l)=\frac{\hat{q}_z x^4}{24}+A_1x^3+A_2x^2+A_3x+A_4=0$$

$$\frac{\hat{q}_z l^4}{24}+A_1l^3+A_2l^2=0$$

$$\boldsymbol{A_2=-\frac{\hat{q}_z l^2}{24}-A_1 l}$$

$$\frac{dw(l)}{dx} = \frac{\hat{q}_z x^3}{6} + 3A_1 x^2 + 2A_2 x + A_3 = 0$$

$$\frac{\hat{q}_z l^3}{6} + 3A_1 l^2 + 2A_2 l = 0$$

$$\frac{\hat{q}_z l^3}{6} + 3A_1 l^2 - \frac{\hat{q}_z l^3}{12} - 2A_1 l^2 = 0$$

$$A_1 l^2 = -\frac{\hat{q}_z l^3}{12}$$

$$A_1 = -\frac{\hat{q}_z l}{12}$$

$$A_2 = -\frac{\hat{q}_z l^2}{24} + \frac{\hat{q}_z l^2}{12}$$

$$A_2 = \frac{\hat{q}_z l^2}{24}$$

$$w(x) = \frac{\hat{q}_z x^4}{24} - \frac{\hat{q}_z l}{12} x^3 + \frac{\hat{q}_z l^2}{24} x^2$$

$$\frac{dw(x)}{dx} = \frac{\hat{q}_z x^3}{6} - \frac{\hat{q}_z l}{4} x^2 + \frac{\hat{q}_z l^2}{12} x$$

$$\frac{d^2 w(x)}{dx^2} = \frac{\hat{q}_z x^2}{2} - \frac{\hat{q}_z l}{2} x + \frac{\hat{q}_z l^2}{12}$$

Maximum deflection occurs at midspan

$$w_{max}\left(\frac{1}{2}l\right) = \frac{\hat{q}_z l^4}{384} - \frac{\hat{q}_z l^4}{96} + \frac{\hat{q}_z l^4}{96}$$

$$w_{max}\left(\frac{1}{2}l\right) = \frac{\hat{q}_z l^4}{384} - \frac{4\hat{q}_z l^4}{384} + \frac{4\hat{q}_z l^4}{384}$$

$$w_{max}\left(\frac{1}{2}l\right) = \frac{5\hat{q}_z l^4}{384} - \frac{4\hat{q}_z l^4}{384}$$

Find the common parts of the deflection equations and how the spring stiffness affects this relation

$$\frac{C_r l}{C_r l + 2EI} = \frac{1}{1 + \frac{2EI}{C_r l}} = \frac{1}{1 + \lambda} = k$$

$$\frac{1}{k} - 1 = \lambda$$

$$C_r = \frac{2EIk}{l(1-k)}$$

$$C_r = \frac{2EIk}{l(1-k)}$$

$$\frac{2EI}{C_r l} = \lambda$$

$$\frac{C_r l}{2EI + \frac{4E^2I^2}{C_r l}} = \frac{2EI}{C_r l} k = \lambda k$$

$$w(x) = \frac{q_z}{24EI}x^4 - \frac{\hat{q}_z l}{12EI}x^3 + \frac{\hat{q}_z l^3}{24EI}x$$

$$w(x) = \frac{q_z}{24EI}x^4 - \frac{q_z l}{12EI}x^3 + \frac{q_z l^2}{24EI}x^2 \cdot k + \frac{q_z l^3}{24EI}x \cdot \lambda k$$

$$w(x) = \frac{q_z}{24EI}x^4 - \frac{\hat{q}_z l}{12EI}x^3 + \frac{\hat{q}_z l^2}{24EI}x^2$$

Arch horizontal spring configuration

$$M_B = \frac{wL^2}{8} \cdot \alpha$$

$$\alpha = 1 - \frac{1}{1 + \frac{15EI}{8f^2E_tA_t}}$$

$$E_tA_t = \frac{k_tL}{2}$$

$$\alpha = 1 - \frac{1}{1 + \frac{15EI}{4f^2k_tL}}$$

$$\alpha = 1 - \frac{4f^2k_tL}{4f^2k_tL + 15EI}$$

$$k_t = \frac{15EI}{4f^2L}\frac{1-\alpha}{\alpha}$$

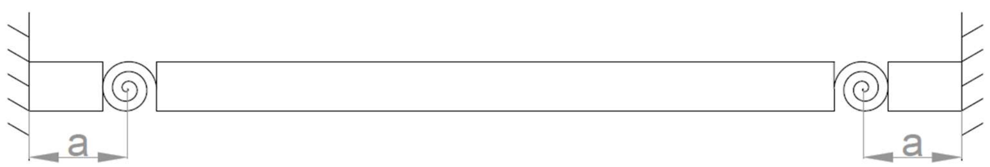

4. Beam-on-elastic-foundation Derrivaton

Beam on an elastic foundation derivation with free ends except for a rotational constraint in the symmetry axis using Hetényi (1946) effects of the round profile are neglected due to complexity, significantly stiffened using plates.

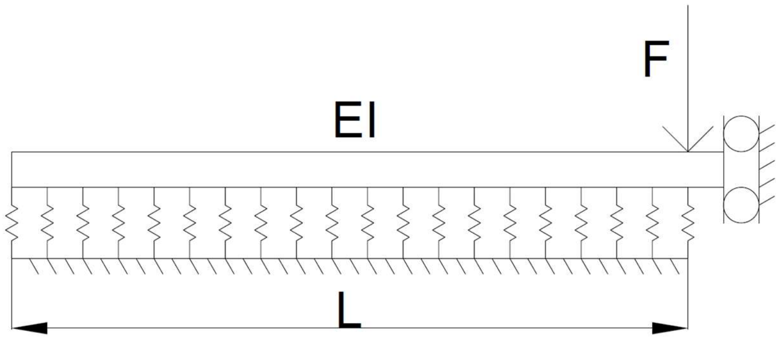

$$EI\frac{d^4u}{dx^4} + k_y u = p(x)$$

$$\lambda = \sqrt[4]{\frac{k}{4EI}}, \qquad \check{p}(x) = \frac{p(x)}{EI}$$

Where k is multiplied by the dowel diameter to give a proper extraction of the foundation stiffness.

$$\frac{d^4u}{dx^4} + 4\lambda^4 u = \check{p}(x)$$

$u_0(x) = e^{\lambda x}[C_1\cos(\lambda x) + C_2\sin(\lambda x)] + e^{-\lambda x}[C_3\cos(\lambda x) + C_4\sin(\lambda x)]$

The generalised solution can be rewritten using the relation

$$\cosh(\lambda x) = \frac{e^{\lambda x} + e^{-\lambda x}}{2}, \quad \sinh(\lambda x) = \frac{e^{\lambda x} - e^{-\lambda x}}{2},$$

From this relation we determine that

$$\cosh(\lambda x) + \sinh(\lambda x) = e^{\lambda x}$$

$$\cosh(\lambda x) - \sinh(\lambda x) = e^{-\lambda x}$$

Substitute into the initial form of the deformation equation w(x)

$$u_0(x) = e^{\lambda x}[C_1\cos(\lambda x) + C_2\sin(\lambda x)] + e^{-\lambda x}[C_3\cos(\lambda x) + C_4\sin(\lambda x)]$$

$$\begin{aligned} u_0(x) &= [\cosh(\lambda x) + \sinh(\lambda x)][C_1\cos(\lambda x) + C_2\sin(\lambda x)] \\ &+ [\cosh(\lambda x) - \sinh(\lambda x)][C_3\cos(\lambda x) + C_4\sin(\lambda x)] \end{aligned}$$

$$\begin{aligned} u_0(x) &= [C_1\cos(\lambda x)\cosh(\lambda x) + C_1\cos(\lambda x)\sinh(\lambda x)] \\ &+ [C_2\sin(\lambda x)\cosh(\lambda x) + C_2\sin(\lambda x)\sinh(\lambda x)] \\ &+ [C_3\cos(\lambda x)\cosh(\lambda x) - C_3\cos(\lambda x)\sinh(\lambda x)] \\ &+ [C_4\sin(\lambda x)\cosh(\lambda x) - C_4\sin(\lambda x)\sinh(\lambda x)] \end{aligned}$$

$$u_0(x) = (C_1 + C_3)\cos(\lambda x)\cosh(\lambda x) + (C_1 - C_3)\cos(\lambda x)\sinh(\lambda x) + (C_2 + C_4)\sin(\lambda x)\cosh(\lambda x) + (C_2 - C_4)\sin(\lambda x)\sinh(\lambda x)$$

Can be rewritten using new constants

$$C_1 + C_3 = A_1, \qquad C_1 - C_3 = A_2, \qquad C_2 + C_4 = A_3, \qquad C_2 - C_4 = A_4$$

$$u_0(x) = A_1\cos(\lambda x)\cosh(\lambda x) + A_2\cos(\lambda x)\sinh(\lambda x) + A_3\sin(\lambda x)\cosh(\lambda x) + A_4\sin(\lambda x)\sinh(\lambda x)$$

$$\frac{du_0(x)}{dx} = \lambda[A_1(-\sin(\lambda x)\cosh(\lambda x) + \cos(\lambda x)\sinh(\lambda x)) + A_2(-\sin(\lambda x)\sinh(\lambda x) + \cos(\lambda x)\cosh(\lambda x)) + A_3(\cos(\lambda x)\cosh(\lambda x) + \sin(\lambda x)\sinh(\lambda x)) + A_4(\cos(\lambda x)\sinh(\lambda x) + \sin(\lambda x)\cosh(\lambda x))]$$

$$\frac{d^2u_0(x)}{dx^2} = 2\lambda^2[-A_1\sin(\lambda x)\sinh(\lambda x) - A_2\sin(\lambda x)\cosh(\lambda x) + A_3\cos(\lambda x)\sinh(\lambda x) + A_4\cos(\lambda x)\cosh(\lambda x)]$$

$$\frac{d^3u_0(x)}{dx^3} = 2\lambda^3[-A_1(\cos(\lambda x)\sinh(\lambda x) + \sin(\lambda x)\cosh(\lambda x)) - A_2(\cos(\lambda x)\cosh(\lambda x) + \sin(\lambda x)\sinh(\lambda x)) + A_3(\cos(\lambda x)\cosh(\lambda x) - \sin(\lambda x)\sinh(\lambda x)) + A_4(\cos(\lambda x)\sinh(\lambda x) - \sin(\lambda x)\cosh(\lambda x))]$$

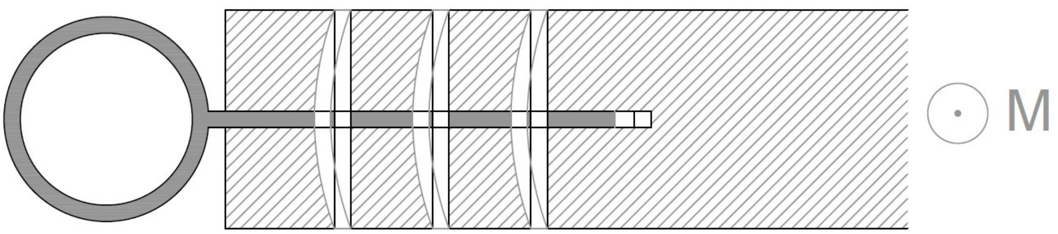

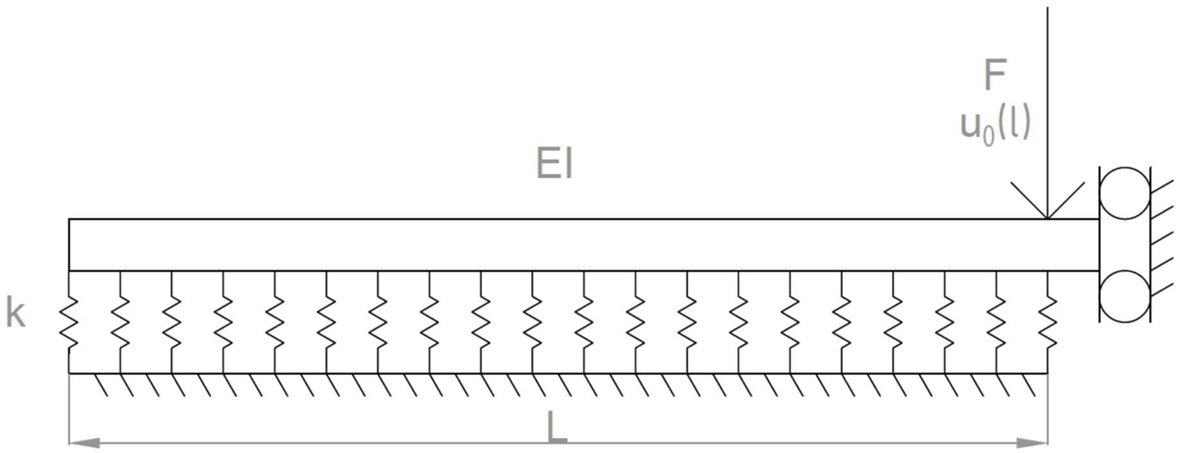

Double shear plane symmetric dowel gives the boundary conditions:

$$\frac{du_0(l)}{dx} = 0$$

$$-EI\frac{d^2u_0(0)}{dx^2} = 0$$

$$-EI\frac{d^3u_0(0)}{dx^3} = 0$$

$$\frac{d^3u_0(l)}{dx^3} = \frac{F}{EI}$$

$$-EI\frac{d^2u_0(0)}{dx^2} = 2\lambda^2[-A_1\sin(\lambda x)\sinh(\lambda x) - A_2\sin(\lambda x)\cosh(\lambda x) + A_3\cos(\lambda x)\sinh(\lambda x) + A_4\cos(\lambda x)\cosh(\lambda x)] = 0$$

$$2\lambda^2[-A_1\sin(0)\sinh(0) - A_2\sin(0)\cosh(0) + A_3\cos(0)\sinh(0) + A_4\cos(0)\cosh(0)] = 0$$

$$A_4 = 0$$

$$\frac{d^3u_0(0)}{dx^3} = 2\lambda^3[-A_1(\cos(\lambda x)\sinh(\lambda x) + \sin(\lambda x)\cosh(\lambda x)) - A_2(\cos(\lambda x)\cosh(\lambda x) + \sin(\lambda x)\sinh(\lambda x)) + A_3(\cos(\lambda x)\cosh(\lambda x) - \sin(\lambda x)\sinh(\lambda x))] = 0$$

$$2\lambda^3[-A_1(\cos(0)\sinh(0) + \sin(0)\cosh(0)) - A_2(\cos(0)\cosh(0) + \sin(0)\sinh(0)) + A_3(\cos(0)\cosh(0) - \sin(0)\sinh(0))] = 0$$

$$2\lambda^3[-A_2 + A_3] = 0$$

$$A_3 = A_2$$

$$\frac{d^3u_0(l)}{dx^3} = 2\lambda^3[-A_1(\cos(\lambda x)\sinh(\lambda x) + \sin(\lambda x)\cosh(\lambda x)) - A_2(\cos(\lambda x)\cosh(\lambda x) + \sin(\lambda x)\sinh(\lambda x)) + A_3(\cos(\lambda x)\cosh(\lambda x) - \sin(\lambda x)\sinh(\lambda x)) + A_4(\cos(\lambda x)\sinh(\lambda x) - \sin(\lambda x)\cosh(\lambda x))] = \frac{F}{EI}$$

$$\frac{d^3u_0(l)}{dx^3} = 2\lambda^3[-A_1(\cos(\lambda l)\sinh(\lambda l) + \sin(\lambda l)\cosh(\lambda l)) - A_2(\cos(\lambda l)\cosh(\lambda l) + \sin(\lambda l)\sinh(\lambda l)) + A_2(\cos(\lambda l)\cosh(\lambda l) - \sin(\lambda l)\sinh(\lambda l))] = \frac{F}{EI}$$

$$\frac{d^3u_0(l)}{dx^3} = -A_1(\cos(\lambda l)\sinh(\lambda l) + \sin(\lambda l)\cosh(\lambda l)) - 2A_2\sin(\lambda l)\sinh(\lambda l)) = \frac{F}{2\lambda^3 EI}$$

$$\frac{du_0(l)}{dx} = \lambda[A_1(-\sin(\lambda x)\cosh(\lambda x) + \cos(\lambda x)\sinh(\lambda x)) + A_2(-\sin(\lambda x)\sinh(\lambda x) + \cos(\lambda x)\cosh(\lambda x)) + A_3(\cos(\lambda x)\cosh(\lambda x) + \sin(\lambda x)\sinh(\lambda x)) + A_4(\cos(\lambda x)\sinh(\lambda x) + \sin(\lambda x)\cosh(\lambda x))] = 0$$

$$A_1(-\sin(\lambda l)\cosh(\lambda l) + \cos(\lambda l)\sinh(\lambda l)) + A_2(-\sin(\lambda l)\sinh(\lambda l) + \cos(\lambda l)\cosh(\lambda l)) + A_2(\cos(\lambda l)\cosh(\lambda l) + \sin(\lambda l)\sinh(\lambda l)) = 0$$

$$A_1(-\sin(\lambda l)\cosh(\lambda l) + \cos(\lambda l)\sinh(\lambda l)) + 2A_2\cos(\lambda l)\cosh(\lambda l) = 0$$

$$A_1 = -\frac{2A_2\cos(\lambda l)\cosh(\lambda l)}{\cos(\lambda l)\sinh(\lambda l) - \sin(\lambda l)\cosh(\lambda l)}$$

Substitute the function for A1 in $\frac{d^3u_0(l)}{dx^3} = 0$

$$\frac{2A_2\cos(\lambda l)\cosh(\lambda l)}{\cos(\lambda l)\sinh(\lambda l) - \sin(\lambda l)\cosh(\lambda l)}(\cos(\lambda l)\sinh(\lambda l) + \sin(\lambda l)\cosh(\lambda l)) - 2A_2\sin(\lambda l)\sinh(\lambda l)) = \frac{F}{2\lambda^3 EI}$$

$$A_2(\frac{\cos(\lambda l)\cosh(\lambda l)\,(\cos(\lambda l)\sinh(\lambda l) + \sin(\lambda l)\cosh(\lambda l))}{\cos(\lambda l)\sinh(\lambda l) - \sin(\lambda l)\cosh(\lambda l)} - \sin(\lambda l)\sinh(\lambda l)) = \frac{F}{4\lambda^3 EI}$$

$$A_2(\frac{\cos(\lambda l)\cosh(\lambda l)\,(\cos(\lambda l)\sinh(\lambda l) + \sin(\lambda l)\cosh(\lambda l))}{\cos(\lambda l)\sinh(\lambda l) - \sin(\lambda l)\cosh(\lambda l)} - \frac{\sin(\lambda l)\sinh(\lambda l)\,(\cos(\lambda l)\sinh(\lambda l) - \sin(\lambda l)\cosh(\lambda l))}{\cos(\lambda l)\sinh(\lambda l) - \sin(\lambda l)\cosh(\lambda l)}) = \frac{F}{4\lambda^3 EI}$$

$$A_2\frac{\sinh(\lambda l)\cosh(\lambda l) + \sin(\lambda l)\cos(\lambda l)}{\cos(\lambda l)\sinh(\lambda l) - \sin(\lambda l)\cosh(\lambda l)} = \frac{F}{4\lambda^3 EI}$$

$$A_2 = \frac{F(\cos(\lambda l)\sinh(\lambda l) - \sin(\lambda l)\cosh(\lambda l))}{4\lambda^3 EI(\sinh(\lambda l)\cosh(\lambda l) + \sin(\lambda l)\cos(\lambda l))}$$

Which give for the other constants the following results

$$A_3 = A_2 = \frac{F(\cos(\lambda l)\sinh(\lambda l) - \sin(\lambda l)\cosh(\lambda l))}{2\lambda^3 EI(\sinh(2\lambda l) + \sin(2\lambda l))}$$

$$A_4 = 0$$

$$A_1 = -A_2 \frac{2\cos(\lambda l)\cosh(\lambda l)}{\cos(\lambda l)\sinh(\lambda l) - \sin(\lambda l)\cosh(\lambda l)}$$

$$A_1 = -\frac{F(\cos(\lambda l)\sinh(\lambda l) - \sin(\lambda l)\cosh(\lambda l))}{2\lambda^3 EI(\sinh(2\lambda l) + \sin(2\lambda l))} \cdot \frac{2\cos(\lambda l)\cosh(\lambda l)}{\cos(\lambda l)\sinh(\lambda l) - \sin(\lambda l)\cosh(\lambda l)}$$

$$A_1 = -\frac{F(\cos(\lambda l)\sinh(\lambda l) - \sin(\lambda l)\cosh(\lambda l))(2\cos(\lambda l)\cosh(\lambda l))}{2\lambda^3 EI(\sinh(2\lambda l) + \sin(2\lambda l))(\cos(\lambda l)\sinh(\lambda l) - \sin(\lambda l)\cosh(\lambda l))}$$

$$A_1 = -\frac{F\cos(\lambda l)\cosh(\lambda l)}{\lambda^3 EI(\sinh(2\lambda l) + \sin(2\lambda l))}$$

Insert the solutions for A1 to A3 into the initial deformation equation

$$A_1 = -\frac{F\cos(\lambda l)\cosh(\lambda l)}{\lambda^3 EI(\sinh(2\lambda l) + \sin(2\lambda l))}$$

$$A_2 = A_3 = \frac{F(\cos(\lambda l)\sinh(\lambda l) - \sin(\lambda l)\cosh(\lambda l))}{2\lambda^3 EI(\sinh(2\lambda l) + \sin(2\lambda l))}$$

$$A_4 = 0$$

$$u_0(x) = A_1\cos(\lambda x)\cosh(\lambda x) + A_2\cos(\lambda x)\sinh(\lambda x) + A_3\sin(\lambda x)\cosh(\lambda x) + A_4\sin(\lambda x)\sinh(\lambda x)$$

$$u_0(x) = -\frac{F\cos(\lambda l)\cosh(\lambda l)\cos(\lambda x)\cosh(\lambda x)}{\lambda^3 EI(\sinh(2\lambda l) + \sin(2\lambda l))} + \frac{F(\cos(\lambda l)\sinh(\lambda l) - \sin(\lambda l)\cosh(\lambda l))}{2\lambda^3 EI(\sinh(2\lambda l) + \sin(2\lambda l))}(\cos(\lambda x)\sinh(\lambda x) + \sin(\lambda x)\cosh(\lambda x))$$

$$u_0(x) = -\frac{F}{EI\lambda^3(\sinh(2\lambda l) + \sin(2\lambda l))}\Big[\cos(\lambda l)\cosh(\lambda l)\cos(\lambda x)\cosh(\lambda x) + \frac{1}{2}(\sin(\lambda l)\cosh(\lambda l) - \cos(\lambda l)\sinh(\lambda l))(\cos(\lambda x)\sinh(\lambda x) + \sin(\lambda x)\cosh(\lambda x))\Big]$$

The peak deformation is expected to be at the point load of cause by the shear plane as such $u_0(x)$ is maximum at $u_0(l)$

$$u_0(l) = -\frac{F}{EI\lambda^3(\sinh(2\lambda l) + \sin(2\lambda l))}\Big[\cos(\lambda l)\cosh(\lambda l)\cos(\lambda l)\cosh(\lambda l) + \frac{1}{2}(\sin(\lambda l)\cosh(\lambda l) - \cos(\lambda l)\sinh(\lambda l))(\cos(\lambda l)\sinh(\lambda l) + \sin(\lambda l)\cosh(\lambda l))\Big]$$

$$u_0(l) = -\frac{F}{2EI\lambda^3(\sinh(2\lambda l) + \sin(2\lambda l))}[2\cos^2(\lambda l)\cosh(\lambda l) + (\sin^2(\lambda l)\cosh(\lambda l)^2 - \cos^2(\lambda l)\sinh(\lambda l)^2)]$$

$$u_0(l) = -\frac{F(\cos^2(\lambda l) + \cosh^2(\lambda l)}{2EI\lambda^3(\sinh(2\lambda l) + \sin(2\lambda l))}$$

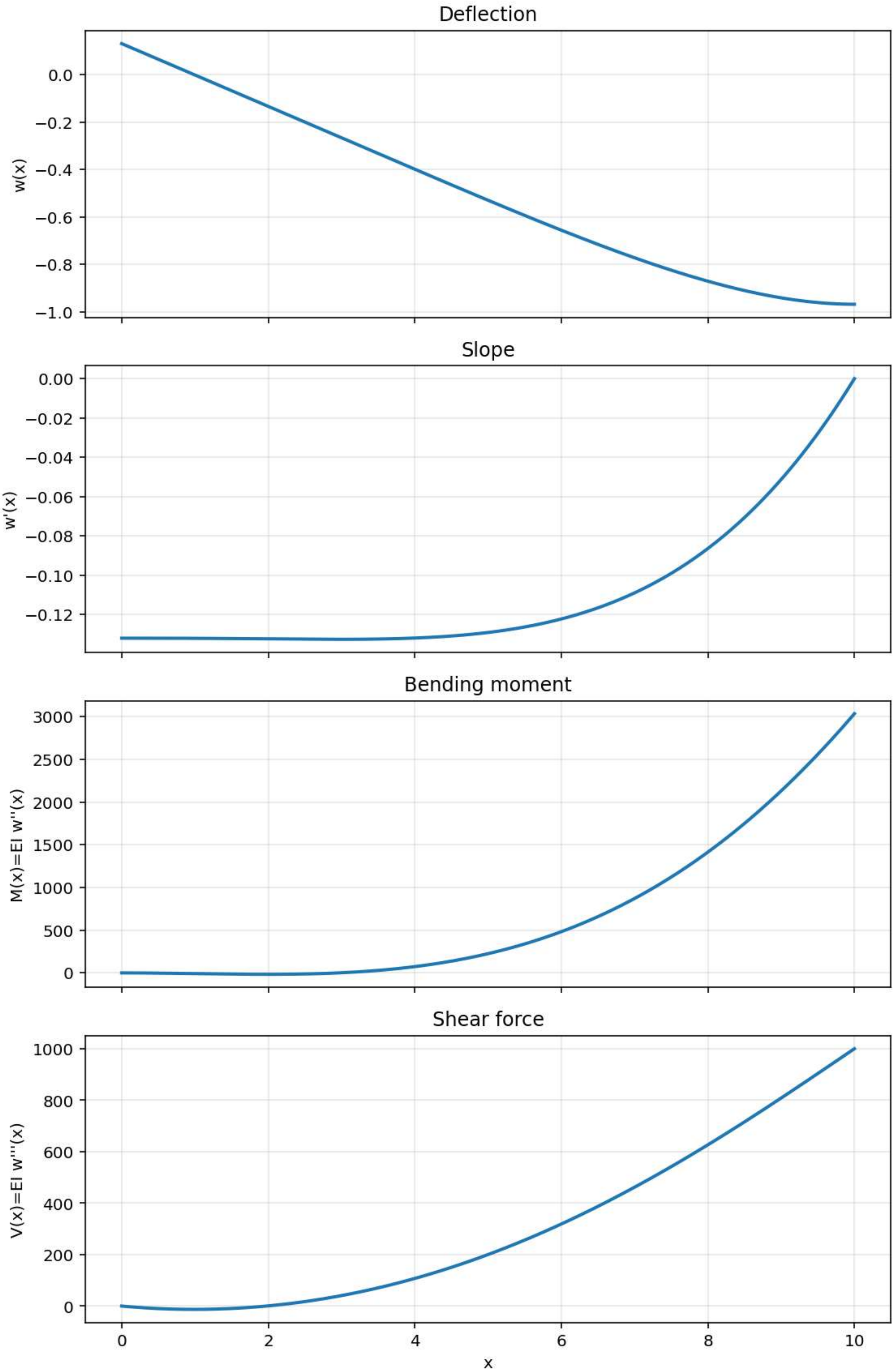
Deflection
w(x)
0.0
−0.2
−0.4
−0.6
−0.8
−1.0
Slope
w'(x)
0.00
−0.02
−0.04
−0.06
−0.08
−0.10
−0.12
Bending moment
M(x)=EI w''(x)
3000
2500
2000
1500
1000
500
0
Shear force
V(x)=EI w'''(x)
1000
800
600
400
200
0
0
2
4
6
8
10
x

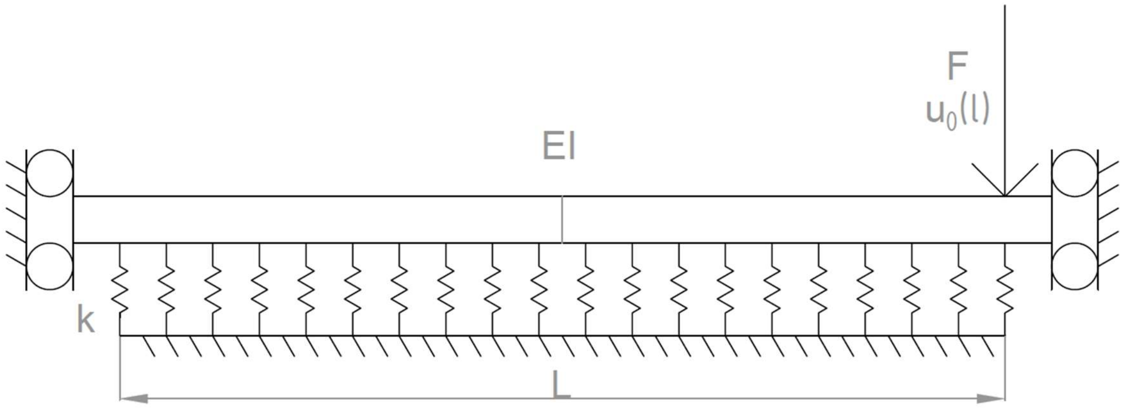

Double shear plane symmetric bolt gives the boundary conditions

$$-EI\frac{du_0(0)}{dx} = 0$$

$$-EI\frac{d^3u_0(0)}{dx^3} = 0$$

$$-EI\frac{du_0(l)}{dx} = 0$$

$$\frac{d^3u_0(l)}{dx^3} = \frac{F}{EI}$$

$$\begin{aligned}-EI\frac{du_0(0)}{dx} = \lambda[&A_1(-\sin(\lambda x)\cosh(\lambda x) + \cos(\lambda x)\sinh(\lambda x)) + A_2(-\sin(\lambda x)\sinh(\lambda x)\\ &+ \cos(\lambda x)\cosh(\lambda x)) + A_3(\cos(\lambda x)\cosh(\lambda x) + \sin(\lambda x)\sinh(\lambda x))\\ &+ A_4(\cos(\lambda x)\sinh(\lambda x) + \sin(\lambda x)\cosh(\lambda x))] = 0\end{aligned}$$

$$\boldsymbol{A_2 + A_3 = 0}$$

$$\begin{aligned}-EI\frac{d^3u_0(0)}{dx^3} = 2\lambda^3[&-A_1(\cos(\lambda x)\sinh(\lambda x) + \sin(\lambda x)\cosh(\lambda x)) - A_2(\cos(\lambda x)\cosh(\lambda x)\\ &+ \sin(\lambda x)\sinh(\lambda x)) + A_3(\cos(\lambda x)\cosh(\lambda x) - \sin(\lambda x)\sinh(\lambda x))\\ &+ A_4(\cos(\lambda x)\sinh(\lambda x) - \sin(\lambda x)\cosh(\lambda x))] = 0\end{aligned}$$

$$\boldsymbol{-A_2 + A_3 = 0}$$

Only holds for $\boldsymbol{A_2 = A_3 = 0}$

$$\begin{aligned}-EI\frac{du_0(l)}{dx} = \lambda[&A_1(-\sin(\lambda x)\cosh(\lambda x) + \cos(\lambda x)\sinh(\lambda x)) + A_2(-\sin(\lambda x)\sinh(\lambda x)\\ &+ \cos(\lambda x)\cosh(\lambda x)) + A_3(\cos(\lambda x)\cosh(\lambda x) + \sin(\lambda x)\sinh(\lambda x))\\ &+ A_4(\cos(\lambda x)\sinh(\lambda x) + \sin(\lambda x)\cosh(\lambda x))] = 0\end{aligned}$$

$$A_1(-\sin(\lambda l)\cosh(\lambda l)+\cos(\lambda l)\sinh(\lambda l))+A_4(\cos(\lambda l)\sinh(\lambda l)+\sin(\lambda l)\cosh(\lambda l))=0$$

$$\boldsymbol{A_1=A_4\frac{\cos(\lambda l)\sinh(\lambda l)+\sin(\lambda l)\cosh(\lambda l)}{\sin(\lambda l)\cosh(\lambda l)-\cos(\lambda l)\sinh(\lambda l)}}$$

$$\begin{aligned}\frac{d^3u_0(l)}{dx^3}=2\lambda^3[&-A_1(\cos(\lambda x)\sinh(\lambda x)+\sin(\lambda x)\cosh(\lambda x))-A_2(\cos(\lambda x)\cosh(\lambda x)\\&+\sin(\lambda x)\sinh(\lambda x))+A_3(\cos(\lambda x)\cosh(\lambda x)-\sin(\lambda x)\sinh(\lambda x))\\&+A_4(\cos(\lambda x)\sinh(\lambda x)-\sin(\lambda x)\cosh(\lambda x))]=\frac{F}{EI}\end{aligned}$$

$$\boldsymbol{\begin{aligned}-A_1(\cos(\lambda l)\sinh(\lambda l)+\sin(\lambda l)\cosh(\lambda l))+A_4(\cos(\lambda l)\sinh(\lambda l)-\sin(\lambda l)\cosh(\lambda l))\\=\frac{F}{2\lambda^3EI}\end{aligned}}$$

Insert Solution 3 into A1

$$\boldsymbol{A_1=A_4\frac{\cos(\lambda l)\sinh(\lambda l)+\sin(\lambda l)\cosh(\lambda l)}{\sin(\lambda l)\cosh(\lambda l)-\cos(\lambda l)\sinh(\lambda l)}}$$

$$\begin{aligned}-A_4\frac{\cos(\lambda l)\sinh(\lambda l)+\sin(\lambda l)\cosh(\lambda l)}{\sin(\lambda l)\cosh(\lambda l)-\cos(\lambda l)\sinh(\lambda l)}(\cos(\lambda l)\sinh(\lambda l)+\sin(\lambda l)\cosh(\lambda l))\\+A_4(\cos(\lambda l)\sinh(\lambda l)-\sin(\lambda l)\cosh(\lambda l))=\frac{F}{2\lambda^3EI}\end{aligned}$$

$$\begin{aligned}-A_4\frac{\cos(\lambda l)\sinh(\lambda l)+\sin(\lambda l)\cosh(\lambda l)}{\sin(\lambda l)\cosh(\lambda l)-\cos(\lambda l)\sinh(\lambda l)}(\cos(\lambda l)\sinh(\lambda l)+\sin(\lambda l)\cosh(\lambda l))\\+A_4(\cos(\lambda l)\sinh(\lambda l)-\sin(\lambda l)\cosh(\lambda l))=\frac{F}{2\lambda^3EI}\end{aligned}$$

$$A_4\frac{-2\sin^2(\lambda l)\cosh^2(\lambda l)-2\cos^2(\lambda l)\sinh^2(\lambda l)}{\sin(\lambda l)\cosh(\lambda l)-\cos(\lambda l)\sinh(\lambda l)}=\frac{F}{2\lambda^3EI}$$

$$A_4=\frac{F(\sin(\lambda l)\cosh(\lambda l)-\cos(\lambda l)\sinh(\lambda l))}{2\lambda^3EI(-2\sin^2(\lambda l)\cosh^2(\lambda l)-2\cos^2(\lambda l)\sinh^2(\lambda l))}$$

$$\boldsymbol{A_4=-\frac{F(\sin(\lambda l)\cosh(\lambda l)-\cos(\lambda l)\sinh(\lambda l))}{4\lambda^3EI(\sin^2(\lambda l)\cosh^2(\lambda l)+\cos^2(\lambda l)\sinh^2(\lambda l))}}$$

$$A_1=-\frac{F(\sin(\lambda l)\cosh(\lambda l)-\cos(\lambda l)\sinh(\lambda l))}{4\lambda^3EI(\sin^2(\lambda l)\cosh^2(\lambda l)+\cos^2(\lambda l)\sinh^2(\lambda l))}\frac{\cos(\lambda l)\sinh(\lambda l)+\sin(\lambda l)\cosh(\lambda l)}{\sin(\lambda l)\cosh(\lambda l)-\cos(\lambda l)\sinh(\lambda l)}$$

$$A_1=-\frac{F(\cos(\lambda l)\sinh(\lambda l)+\sin(\lambda l)\cosh(\lambda l))}{4\lambda^3EI(\sin^2(\lambda l)\cosh^2(\lambda l)+\cos^2(\lambda l)\sinh^2(\lambda l))}$$

$$-\frac{F(-\cos^2(\lambda l)\sinh(\lambda l)^2+\sin^2(\lambda l)\cosh(\lambda l)^2)}{4\lambda^3 EI(\sin^3(\lambda l)\cosh^3(\lambda l)+\sin(\lambda l)\cosh(\lambda l)\cos^2(\lambda l)\sinh^2(\lambda l)-\cos(\lambda l)\sinh(\lambda l)\sin^2(\lambda l)\cosh^2(\lambda l)-\cos^3(\lambda l)\sinh^3(\lambda l))}$$

$$\boldsymbol{A_4=-\frac{F(\sin(\lambda l)\cosh(\lambda l)-\cos(\lambda l)\sinh(\lambda l))}{2\lambda^3 EI\big(cosh(2\lambda l)-cos(2\lambda l)\big)}}$$
$$\boldsymbol{A_1=-\frac{F(\cos(\lambda l)\sinh(\lambda l)+\sin(\lambda l)\cosh(\lambda l))}{2\lambda^3 EI\big(cosh(2\lambda l)-cos(2\lambda l)\big)}}$$

$$u_0(x)=A_1\cos(\lambda x)\cosh(\lambda x)+A_2\cos(\lambda x)\sinh(\lambda x)+A_3\sin(\lambda x)\cosh(\lambda x)$$
$$+A_4\sin(\lambda x)\sinh(\lambda x)$$

$$u_0(x)=A_1\cos(\lambda x)\cosh(\lambda x)+A_4\sin(\lambda x)\sinh(\lambda x)$$

$$u_0(x)=-\frac{F(\cos(\lambda l)\sinh(\lambda l)+\sin(\lambda l)\cosh(\lambda l))}{2\lambda^3 EI\big(cosh(2\lambda l)-cos(2\lambda l)\big)}\cos(\lambda x)\cosh(\lambda x)$$
$$+-\frac{F(\sin(\lambda l)\cosh(\lambda l)-\cos(\lambda l)\sinh(\lambda l))}{2\lambda^3 EI\big(cosh(2\lambda l)-cos(2\lambda l)\big)}\sin(\lambda x)\sinh(\lambda x)$$

$$\boldsymbol{u_0(x)=\frac{F}{2\lambda^3 EI\big(cosh(2\lambda l)-cos(2\lambda l)\big)}[-(\sin(\lambda l)\cosh(\lambda l)}$$
$$\boldsymbol{+\cos(\lambda l)\sinh(\lambda l))\cos(\lambda x)\cosh(\lambda x)}$$
$$\boldsymbol{+(\cos(\lambda l)\sinh(\lambda l)-\sin(\lambda l)\cosh(\lambda l))\sin(\lambda x)\sinh(\lambda x)]}$$

Evaluated at x=l where the max displacement is expected to occur

$$u_0(l)=-\frac{F(\cos(\lambda l)\sinh(\lambda l)+\sin(\lambda l)\cosh(\lambda l))}{2\lambda^3 EI\big(cosh(2\lambda l)-cos(2\lambda l)\big)}\cos(\lambda l)\cosh(\lambda l)$$
$$-\frac{F(\sin(\lambda l)\cosh(\lambda l)-\cos(\lambda l)\sinh(\lambda l))}{2\lambda^3 EI\big(cosh(2\lambda l)-cos(2\lambda l)\big)}\sin(\lambda l)\sinh(\lambda l)$$

$$u_0(l)=-F\frac{\sin(2\lambda l)+\sinh(2\lambda l)}{4\lambda^3 EI\big(cosh(2\lambda l)-cos(2\lambda l)\big)}$$

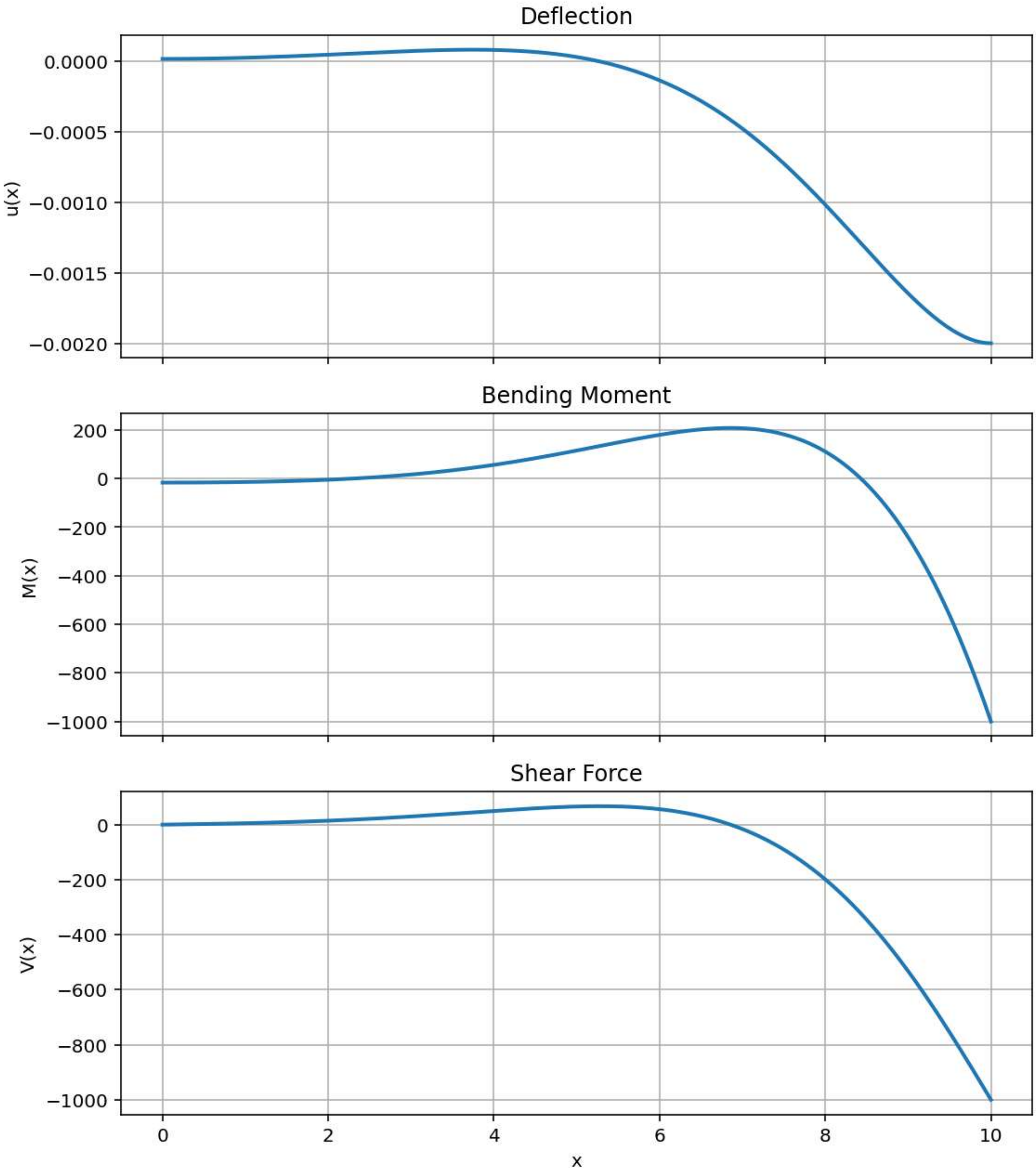
Deflection
0.0000
−0.0005
−0.0010
−0.0015
−0.0020
u(x)
Bending Moment
200
0
−200
−400
−600
−800
−1000
M(x)
Shear Force
0
−200
−400
−600
−800
−1000
V(x)
0
2
4
6
8
10
x

Symmetric lateral moment condition dowel without plate effects:

$$-EI\frac{d^2u_0(0)}{dx^2} = 0$$

$$-EI\frac{d^3u_0(0)}{dx^3} = 0$$

$$-EI\frac{d^2u_0(l)}{dx^2} = 0$$

$$u_0(l) = 0$$

$$EI\frac{d^4u}{dx^4} + k_y u = p(x)$$

The total displacement function consist out of a homogenous and particular solution

$$EI\frac{d^4u}{dx^4} + k_y u = p(x)$$

$$With\, p(x) = q_1 + \frac{q_2 - p_0}{l}x$$

$$u(x) = u_h(x) + u_p(x)$$

The particular solution is derived from the foundation stiffness term

$$u_p(x) = \frac{1}{k_y}\left(q_1 + \frac{q_2 - p_0}{l}x\right)$$

And the homogenous term is derived from the bending term as

$$u_h(x) = A_1\cos(\lambda x)\cosh(\lambda x) + A_2\cos(\lambda x)\sinh(\lambda x) + A_3\sin(\lambda x)\cosh(\lambda x) + A_4\sin(\lambda x)\sinh(\lambda x)$$

Combined gives

$$u(x) = A_1\cos(\lambda x)\cosh(\lambda x) + A_2\cos(\lambda x)\sinh(\lambda x) + A_3\sin(\lambda x)\cosh(\lambda x) + A_4\sin(\lambda x)\sinh(\lambda x) + \frac{1}{k_y}\left(q_1 + \frac{q_2 - q_1}{l}x\right)$$

However for the higher order derivatives of this function the particular solution disappears as it is linear. To solve this function the boundary conditions are inserted and provide the following results for the constants.

$$-EI\frac{d^2u_0(0)}{dx^2} = 2\lambda^2[-A_1\sin(\lambda x)\sinh(\lambda x) - A_2\sin(\lambda x)\cosh(\lambda x) + A_3\cos(\lambda x)\sinh(\lambda x) + A_4\cos(\lambda x)\cosh(\lambda x)] = 0$$

$$\boldsymbol{A_4 = 0}$$

$$
\begin{aligned}
-EI\frac{d^3u_0(0)}{dx^3} = 2\lambda^3[&-A_1(\cos(\lambda x)\sinh(\lambda x)+\sin(\lambda x)\cosh(\lambda x)) - A_2(\cos(\lambda x)\cosh(\lambda x)\\
&+\sin(\lambda x)\sinh(\lambda x)) + A_3(\cos(\lambda x)\cosh(\lambda x)-\sin(\lambda x)\sinh(\lambda x))\\
&+A_4(\cos(\lambda x)\sinh(\lambda x)-\sin(\lambda x)\cosh(\lambda x))] = 0
\end{aligned}
$$

$$-A_2 + A_3 = 0$$

$$\boldsymbol{A_2 = A_3}$$

$$
\begin{aligned}
-EI\frac{d^2u_0(l)}{dx^2} = 2\lambda^2[&-A_1\sin(\lambda x)\sinh(\lambda x) - A_2\sin(\lambda x)\cosh(\lambda x) + A_3\cos(\lambda x)\sinh(\lambda x)\\
&+A_4\cos(\lambda x)\cosh(\lambda x)] = 0
\end{aligned}
$$

$$-A_1\sin(\lambda l)\sinh(\lambda l) - A_2\sin(\lambda l)\cosh(\lambda l) + A_3\cos(\lambda l)\sinh(\lambda l) + A_4\cos(\lambda l)\cosh(\lambda l) = 0$$

$$-A_1\sin(\lambda l)\sinh(\lambda l) + A_3(\cos(\lambda l)\sinh(\lambda l) - \sin(\lambda l)\cosh(\lambda l)) = 0$$

$$\boldsymbol{A_3 = A_1\frac{\sin(\lambda l)\sinh(\lambda l)}{\cos(\lambda l)\sinh(\lambda l) - \sin(\lambda l)\cosh(\lambda l)}}$$

$$
\begin{aligned}
u_0(l) = A_1\cos(\lambda x)\cosh(\lambda x) &+ A_2\cos(\lambda x)\sinh(\lambda x) + A_3\sin(\lambda x)\cosh(\lambda x) + A_4\sin(\lambda x)\sinh(\lambda x)\\
&+\frac{1}{k_y}\left(q_1 + \frac{q_2-q_1}{l}x\right) = 0
\end{aligned}
$$

$$
\begin{aligned}
A_1\cos(\lambda l)\cosh(\lambda l) &+ A_2\cos(\lambda l)\sinh(\lambda l) + A_3\sin(\lambda l)\cosh(\lambda l) + A_4\sin(\lambda l)\sinh(\lambda l)\\
&+\frac{1}{k_y}\left(q_1 + \frac{q_2-q_1}{l}l\right) = 0
\end{aligned}
$$

$$\boldsymbol{A_1\cos(\lambda l)\cosh(\lambda l) + A_2(\cos(\lambda l)\sinh(\lambda l) + \sin(\lambda l)\cosh(\lambda l)) + \frac{q_2}{k_y} = 0}$$

Insert the solution for A3 into the displacement function

$$
\begin{aligned}
A_1&\cos(\lambda l)\cosh(\lambda l)\\
&+A_1\frac{\sin(\lambda l)\sinh(\lambda l)}{\cos(\lambda l)\sinh(\lambda l)-\sin(\lambda l)\cosh(\lambda l)}(\cos(\lambda l)\sinh(\lambda l)+\sin(\lambda l)\cosh(\lambda l))\\
&+\frac{q_2}{k_y} = 0
\end{aligned}
$$

$$A_1\cos(\lambda l)\cosh(\lambda l) + A_1\frac{\sin(\lambda l)\sinh(\lambda l)\,(\cos(\lambda l)\sinh(\lambda l)+\sin(\lambda l)\cosh(\lambda l))}{\cos(\lambda l)\sinh(\lambda l)-\sin(\lambda l)\cosh(\lambda l)} + \frac{q_2}{k_y} = 0$$

$$
\begin{aligned}
A_1\Bigg(&\frac{\cos(\lambda l)\cosh(\lambda l)\,(\cos(\lambda l)\sinh(\lambda l)-\sin(\lambda l)\cosh(\lambda l))}{\cos(\lambda l)\sinh(\lambda l)-\sin(\lambda l)\cosh(\lambda l)}\\
&+\frac{\sin(\lambda l)\sinh(\lambda l)\,(\cos(\lambda l)\sinh(\lambda l)+\sin(\lambda l)\cosh(\lambda l))}{\cos(\lambda l)\sinh(\lambda l)-\sin(\lambda l)\cosh(\lambda l)}\Bigg) + \frac{q_2}{k_y} = 0
\end{aligned}
$$

$$A_1\frac{\sinh(\lambda l)\cosh(\lambda l)\,(\cos^2(\lambda l)+\sin^2(\lambda l)) - \sin(\lambda l)\cos(\lambda l)\,(\cosh^2(\lambda l)-\sinh^2(\lambda l))}{\cos(\lambda l)\sinh(\lambda l)-\sin(\lambda l)\cosh(\lambda l)} + \frac{q_2}{k_y} = 0$$

$$A_1 \frac{\sinh(\lambda l)\cosh(\lambda l) - \sin(\lambda l)\cos(\lambda l)}{\cos(\lambda l)\sinh(\lambda l) - \sin(\lambda l)\cosh(\lambda l)} + \frac{q_2}{k_y} = 0$$

$$A_1 = -\frac{q_2(\cos(\lambda l)\sinh(\lambda l) - \sin(\lambda l)\cosh(\lambda l))}{k_y(\sinh(\lambda l)\cosh(\lambda l) - \sin(\lambda l)\cos(\lambda l))}$$

$$\boldsymbol{A_1} = -\frac{\mathbf{2}\boldsymbol{q_2}(\mathbf{sin}(\boldsymbol{\lambda l})\,\mathbf{cosh}(\boldsymbol{\lambda l}) - \mathbf{cos}(\boldsymbol{\lambda l})\,\mathbf{sinh}(\boldsymbol{\lambda l}))}{\boldsymbol{k_y}(\mathbf{sin}(\mathbf{2}\boldsymbol{\lambda l}) - \mathbf{sinh}(\mathbf{2}\boldsymbol{\lambda l}))}$$

$$A_3 = A_2 = A_1 \frac{\sin(\lambda l)\sinh(\lambda l)}{\cos(\lambda l)\sinh(\lambda l) - \sin(\lambda l)\cosh(\lambda l)}$$

$$\boldsymbol{A_3} = \boldsymbol{A_2} = \frac{\mathbf{2}\boldsymbol{q_2}\,\mathbf{sin}(\boldsymbol{\lambda l})\,\mathbf{sinh}(\boldsymbol{\lambda l})}{\boldsymbol{k_y}(\mathbf{sin}(\mathbf{2}\boldsymbol{\lambda l}) - \mathbf{sinh}(\mathbf{2}\boldsymbol{\lambda l}))}$$

$$u(x) = A_1\cos(\lambda x)\cosh(\lambda x) + A_2\cos(\lambda x)\sinh(\lambda x) + A_3\sin(\lambda x)\cosh(\lambda x) + A_4\sin(\lambda x)\sinh(\lambda x) + \frac{1}{k_y}\left(q_1 + \frac{q_2 - q_1}{l}x\right)$$

$$\begin{aligned} u(x) = &-\frac{2q_2(\sin(\lambda l)\cosh(\lambda l) - \cos(\lambda l)\sinh(\lambda l))}{k_y(\sin(2\lambda l) - \sinh(2\lambda l))}\cos(\lambda x)\cosh(\lambda x) \\ &+ \frac{2q_2\sin(\lambda l)\sinh(\lambda l)}{k_y(\sin(2\lambda l) - \sinh(2\lambda l))}(\cos(\lambda x)\sinh(\lambda x) + \sin(\lambda x)\cosh(\lambda x)) \\ &+ \frac{1}{k_y}\left(q_1 + \frac{q_2 - q_1}{l}x\right) \end{aligned}$$

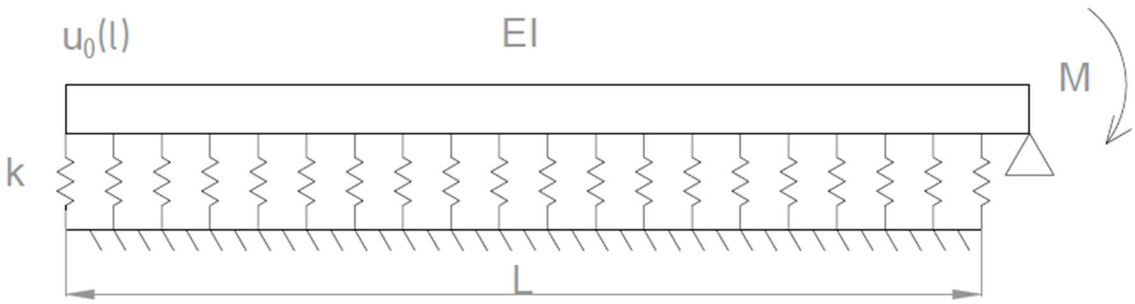

Turning of the bolt due to lateral action without plate effects

$$-EI\frac{d^2u_0(0)}{dx^2} = 0$$

$$-EI\frac{d^3u_0(0)}{dx^3} = 0$$

$$-EI\frac{d^2u_0(l)}{dx^2} = M$$

$$u_0(l) = 0$$

$$EI\frac{d^4u}{dx^4} + k_y u = p(x)$$

The total displacement function consist out of a homogenous and particular solution

$$EI\frac{d^4u}{dx^4} + k_y u = p(x)$$

$$With\ p(x) = 0$$

$$u(x) = u_h(x) + u_p(x)$$

$$u_p(x) = 0$$

To complete the full function the particular part is derived from the spring term

And the homogenous term is derived from the bending term as

$$u_h(x) = A_1\cos(\lambda x)\cosh(\lambda x) + A_2\cos(\lambda x)\sinh(\lambda x) + A_3\sin(\lambda x)\cosh(\lambda x) + A_4\sin(\lambda x)\sinh(\lambda x)$$

$$-EI\frac{d^2u_0(0)}{dx^2} = 2\lambda^2[-A_1\sin(\lambda x)\sinh(\lambda x) - A_2\sin(\lambda x)\cosh(\lambda x) + A_3\cos(\lambda x)\sinh(\lambda x) + A_4\cos(\lambda x)\cosh(\lambda x)] = 0$$

$$\boldsymbol{A_4 = 0}$$

$$-EI\frac{d^3u_0(0)}{dx^3} = 2\lambda^3[-A_1(\cos(\lambda x)\sinh(\lambda x) + \sin(\lambda x)\cosh(\lambda x)) - A_2(\cos(\lambda x)\cosh(\lambda x) + \sin(\lambda x)\sinh(\lambda x)) + A_3(\cos(\lambda x)\cosh(\lambda x) - \sin(\lambda x)\sinh(\lambda x)) + A_4(\cos(\lambda x)\sinh(\lambda x) - \sin(\lambda x)\cosh(\lambda x))] = 0$$

$$\boldsymbol{A_3 = A_2}$$

$$-EI\frac{d^2u_0(l)}{dx^2} = 2\lambda^2[-A_1\sin(\lambda x)\sinh(\lambda x) - A_2\sin(\lambda x)\cosh(\lambda x) + A_3\cos(\lambda x)\sinh(\lambda x) + A_4\cos(\lambda x)\cosh(\lambda x)] = M$$

$$-A_1\sin(\lambda l)\sinh(\lambda l) - A_2\sin(\lambda l)\cosh(\lambda l) + A_3\cos(\lambda l)\sinh(\lambda l) = -\frac{M}{2\lambda^2 EI}$$

$$\boldsymbol{-A_1\sin(\lambda l)\sinh(\lambda l) + A_3(\cos(\lambda l)\sinh(\lambda l) - \sin(\lambda l)\cosh(\lambda l)) = -\frac{M}{2\lambda^2 EI}}$$

$$u_0(l) = A_1\cos(\lambda x)\cosh(\lambda x) + A_2\cos(\lambda x)\sinh(\lambda x) + A_3\sin(\lambda x)\cosh(\lambda x) + A_4\sin(\lambda x)\sinh(\lambda x) = 0$$

$$A_1\cos(\lambda l)\cosh(\lambda l) + A_2\cos(\lambda l)\sinh(\lambda l) + A_3\sin(\lambda l)\cosh(\lambda l) = 0$$

$$A_1\cos(\lambda l)\cosh(\lambda l) + A_3(\cos(\lambda l)\sinh(\lambda l) + \sin(\lambda l)\cosh(\lambda l)) = 0$$

$$\boldsymbol{A_1 = -\frac{A_3(\cos(\lambda l)\sinh(\lambda l) + \sin(\lambda l)\cosh(\lambda l))}{\cos(\lambda l)\cosh(\lambda l)}}$$

$$-A_1\sin(\lambda l)\sinh(\lambda l) + A_3(\cos(\lambda l)\sinh(\lambda l) - \sin(\lambda l)\cosh(\lambda l)) = -\frac{M}{2\lambda^2 EI}$$

$$A_3\frac{(\cos(\lambda l)\sinh(\lambda l) + \sin(\lambda l)\cosh(\lambda l))}{\cos(\lambda l)\cosh(\lambda l)}\sin(\lambda l)\sinh(\lambda l) + A_3(\cos(\lambda l)\sinh(\lambda l) - \sin(\lambda l)\cosh(\lambda l)) = -\frac{M}{2\lambda^2 EI}$$

$$A_3\frac{(\cos(\lambda l)\sinh(\lambda l) + \sin(\lambda l)\cosh(\lambda l))}{\cos(\lambda l)\cosh(\lambda l)}\sin(\lambda l)\sinh(\lambda l) + A_3\frac{\cos(\lambda l)\cosh(\lambda l)\,(\cos(\lambda l)\sinh(\lambda l) - \sin(\lambda l)\cosh(\lambda l))}{\cos(\lambda l)\cosh(\lambda l)} = -\frac{M}{2\lambda^2 EI}$$

$$A_3 \frac{(\sin(\lambda l)\cos(\lambda l)\sinh^2(\lambda l) + \sin^2(\lambda l)\sinh(\lambda l)\cosh(\lambda l))}{\cos(\lambda l)\cosh(\lambda l)} + A_3 \frac{(\cos^2(\lambda l)\sinh(\lambda l)\cosh(\lambda l) - \cos(\lambda l)\sin(\lambda l)\cosh^2(\lambda l))}{\cos(\lambda l)\cosh(\lambda l)} = -\frac{M}{2\lambda^2 EI}$$

$$A_3 \frac{\sinh(\lambda l)\cosh(\lambda l) - \cos(\lambda l)\sin(\lambda l)}{\cos(\lambda l)\cosh(\lambda l)} = -\frac{M}{2\lambda^2 EI}$$

$$\boldsymbol{A_3 = -\frac{M\cos(\lambda l)\cosh(\lambda l)}{2\lambda^2 EI(\sinh(\lambda l)\cosh(\lambda l) - \cos(\lambda l)\sin(\lambda l))}}$$

$$A_1 = -A_3 \frac{(\cos(\lambda l)\sinh(\lambda l) + \sin(\lambda l)\cosh(\lambda l))}{\cos(\lambda l)\cosh(\lambda l)}$$

$$\boldsymbol{A_1 = \frac{M(\cos(\lambda l)\sinh(\lambda l) + \sin(\lambda l)\cosh(\lambda l))}{2\lambda^2 EI(\sinh(\lambda l)\cosh(\lambda l) - \cos(\lambda l)\sin(\lambda l))}}$$

$$u_h(x) = A_1\cos(\lambda x)\cosh(\lambda x) + A_2\cos(\lambda x)\sinh(\lambda x) + A_3\sin(\lambda x)\cosh(\lambda x) + A_4\sin(\lambda x)\sinh(\lambda x)$$

$$u_h(x) = \frac{M(\cos(\lambda l)\sinh(\lambda l) + \sin(\lambda l)\cosh(\lambda l))}{2\lambda^2 EI(\sinh(\lambda l)\cosh(\lambda l) - \cos(\lambda l)\sin(\lambda l))}\cos(\lambda x)\cosh(\lambda x) - \frac{M\cos(\lambda l)\cosh(\lambda l)}{2\lambda^2 EI(\sinh(\lambda l)\cosh(\lambda l) - \cos(\lambda l)\sin(\lambda l))}(\cos(\lambda x)\sinh(\lambda x) + \sin(\lambda x)\cosh(\lambda x))$$

$$\boldsymbol{u_h(x) = \frac{M}{2\lambda^2 EI(\sinh(\lambda l)\cosh(\lambda l) - \cos(\lambda l)\sin(\lambda l))}[(\cos(\lambda l)\sinh(\lambda l) + \sin(\lambda l)\cosh(\lambda l))\cos(\lambda x)\cosh(\lambda x) - \cos(\lambda l)\cosh(\lambda l)(\cos(\lambda x)\sinh(\lambda x) + \sin(\lambda x)\cosh(\lambda x))]}$$

$$u_h^{\prime(x)} = \frac{M}{2\lambda EI}\frac{\cosh^2(\lambda l) + \cos^2(\lambda l)}{\sinh(\lambda l)\cosh(\lambda l) - \sin(\lambda l)\cos(\lambda l)}$$

The clamping effect of the plate is a highly conservative approach that results in roughly a net zero deformation for small widths and for large widths the result can also be considered to be net zero.

Turning of the bolt due to lateral action without plate effects

$$-\frac{du_0(0)}{dx} = 0$$

$$-EI\frac{d^3u_0(0)}{dx^3} = 0$$

$$-EI\frac{d^2u_0(l)}{dx^2} = M$$

$$u_0(l) = 0$$

$$EI\frac{d^4u}{dx^4} + k_y u = p(x)$$

The total displacement function consist out of a homogenous and particular solution

$$EI\frac{d^4u}{dx^4} + k_y u = p(x)$$

$$With\, p(x) = 0$$

$$u(x) = u_h(x) + u_p(x)$$

$$u_p(x) = 0$$

To complete the full function the particular part is derived from the spring term

And the homogenous term is derived from the bending term as

$$u_h(x) = A_1\cos(\lambda x)\cosh(\lambda x) + A_2\cos(\lambda x)\sinh(\lambda x) + A_3\sin(\lambda x)\cosh(\lambda x) + A_4\sin(\lambda x)\sinh(\lambda x)$$

$$-\frac{du_0(0)}{dx} = \lambda[A_1(-\sin(\lambda x)\cosh(\lambda x) + \cos(\lambda x)\sinh(\lambda x)) + A_2(-\sin(\lambda x)\sinh(\lambda x) + \cos(\lambda x)\cosh(\lambda x)) + A_3(\cos(\lambda x)\cosh(\lambda x) + \sin(\lambda x)\sinh(\lambda x)) + A_4(\cos(\lambda x)\sinh(\lambda x) + \sin(\lambda x)\cosh(\lambda x))] = 0$$

$$A_2 + A_3 = 0$$

$$\boldsymbol{A_2 = -A_3}$$

$$-EI\frac{d^3u_0(0)}{dx^3} = 2\lambda^3[-A_1(\cos(\lambda x)\sinh(\lambda x) + \sin(\lambda x)\cosh(\lambda x)) - A_2(\cos(\lambda x)\cosh(\lambda x) + \sin(\lambda x)\sinh(\lambda x)) + A_3(\cos(\lambda x)\cosh(\lambda x) - \sin(\lambda x)\sinh(\lambda x)) + A_4(\cos(\lambda x)\sinh(\lambda x) - \sin(\lambda x)\cosh(\lambda x))] = 0$$

$$-A_2 + A_3 = 0$$

$$\boldsymbol{A_3 = A_2}$$

Holds only for $A_3 = A_2 = 0$

$$-EI\frac{d^2u_0(l)}{dx^2} = 2\lambda^2[-A_1\sin(\lambda x)\sinh(\lambda x) - A_2\sin(\lambda x)\cosh(\lambda x) + A_3\cos(\lambda x)\sinh(\lambda x) + A_4\cos(\lambda x)\cosh(\lambda x)] = -\frac{M}{EI}$$

$$\boldsymbol{-A_1\sin(\lambda l)\sinh(\lambda x) + A_4\cos(\lambda l)\cosh(\lambda l) = -\frac{M}{2\lambda^2 EI}}$$

$$u_0(l) = A_1\cos(\lambda x)\cosh(\lambda x) + A_2\cos(\lambda x)\sinh(\lambda x) + A_3\sin(\lambda x)\cosh(\lambda x) + A_4\sin(\lambda x)\sinh(\lambda x) = 0$$

$$A_1\cos(\lambda l)\cosh(\lambda l) + A_4\sin(\lambda l)\sinh(\lambda l) = 0$$

$$\boldsymbol{A_1 = -A_4\frac{\sin(\lambda l)\sinh(\lambda l)}{\cos(\lambda l)\cosh(\lambda l)}}$$

$$-A_1\sin(\lambda l)\sinh(\lambda x) + A_4\cos(\lambda l)\cosh(\lambda l) = -\frac{M}{2\lambda^2 EI}$$

$$A_4\frac{\sin(\lambda l)\sinh(\lambda l)}{\cos(\lambda l)\cosh(\lambda l)}\sin(\lambda l)\sinh(\lambda x) + A_4\cos(\lambda l)\cosh(\lambda l) = -\frac{M}{2\lambda^2 EI}$$

$$A_4\frac{\sin(\lambda l)\sinh(\lambda l)}{\cos(\lambda l)\cosh(\lambda l)}\sin(\lambda l)\sinh(\lambda x) + A_4\frac{\cos(\lambda l)\cosh(\lambda l)}{\cos(\lambda l)\cosh(\lambda l)}\cos(\lambda l)\cosh(\lambda l) = -\frac{M}{2\lambda^2 EI}$$

$$A_4\left(\frac{\sin^2(\lambda l)\sinh^2(\lambda l)}{\cos(\lambda l)\cosh(\lambda l)} + \frac{\cos^2(\lambda l)\cosh(\lambda l)^2}{\cos(\lambda l)\cosh(\lambda l)}\right) = -\frac{M}{2\lambda^2 EI}$$

$$A_4\frac{\sin^2(\lambda l)\sinh^2(\lambda l) + \cos^2(\lambda l)\cosh(\lambda l)^2}{\cos(\lambda l)\cosh(\lambda l)} = -\frac{M}{2\lambda^2 EI}$$

$$A_4 = -\frac{M\cos(\lambda l)\cosh(\lambda l)}{2\lambda^2 EI(\sin^2(\lambda l)\sinh^2(\lambda l) + \cos^2(\lambda l)\cosh(\lambda l)^2)}$$

$$A_1 = -A_4\frac{\sin(\lambda l)\sinh(\lambda l)}{\cos(\lambda l)\cosh(\lambda l)}$$

$$A_1 = \frac{M\cos(\lambda l)\cosh(\lambda l)}{2\lambda^2 EI(\sin^2(\lambda l)\sinh^2(\lambda l) + \cos^2(\lambda l)\cosh(\lambda l)^2)} \frac{\sin(\lambda l)\sinh(\lambda l)}{\cos(\lambda l)\cosh(\lambda l)}$$

$$A_1 = \frac{M\sin(\lambda l)\sinh(\lambda l)}{2\lambda^2 EI(\sin^2(\lambda l)\sinh^2(\lambda l) + \cos^2(\lambda l)\cosh(\lambda l)^2)}$$

$$u_h(x) = A_1\cos(\lambda x)\cosh(\lambda x) + A_2\cos(\lambda x)\sinh(\lambda x) + A_3\sin(\lambda x)\cosh(\lambda x) + A_4\sin(\lambda x)\sinh(\lambda x)$$

$$u_h(x) = \frac{M}{2\lambda^2 EI(\sin^2(\lambda l)\sinh^2(\lambda l) + \cos^2(\lambda l)\cosh(\lambda l)^2)}[\sin(\lambda l)\sinh(\lambda l)\cos(\lambda x)\cosh(\lambda x) - \cos(\lambda l)\cosh(\lambda l)\sin(\lambda x)\sinh(\lambda x)]$$

$$u_h'(l) = -\frac{M}{4\lambda EI}\frac{\sinh(2\lambda l) + \sin(2\lambda l)}{\sin^2(\lambda l)\sinh^2(\lambda l) + \cos^2(\lambda l)\cosh^2(\lambda l)}$$

5. Derivation Dowel Group Stiffness

The parametric formula for the bearing deformation due to the out-of-plane moments of a bolt based on the bolt stiffness $\boldsymbol{EI}$ the length of the bolt contacting the material and $\boldsymbol{\lambda} = \sqrt[4]{\frac{\boldsymbol{dk}}{\boldsymbol{4EI}}}$

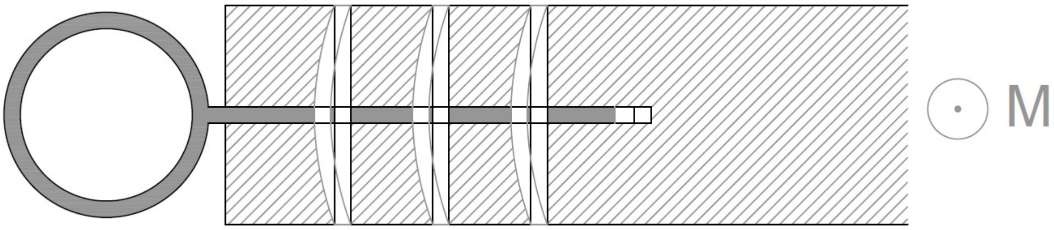

$$M = K_0\theta$$

$$\frac{M}{\theta} = K_0$$

$$u_i(x) = F_i c_i$$

$$u_i(x) = r_i\theta$$

$$\frac{r_i\theta}{c_i} = F_i$$

$$M = 2\sum_i F_i r_i$$

$$M = 2\sum_i \frac{r_i^2\theta}{c_i}$$

$$\frac{M}{\theta} = 2\sum_i r_i^2 k_i = C_0$$

$$\frac{1}{c_i} = k_i$$

$$F_i = \frac{k_i r_i}{2\sum_i r_i^2 k_i} M$$

$$2\sum_i \frac{r_i^2}{c_i} = C_0$$

$$2\sum_i r_i^2 k_i = C_0$$

$$u_D(l) = F \cdot -\frac{\cos^2(\lambda l) + \cosh^2(\lambda l)}{2EI\lambda^3(\sinh(2\lambda l) + \sin(2\lambda l))}$$

$$k_i = -\frac{2EI\lambda^3(\sinh(2\lambda l) + \sin(2\lambda l))}{\cos^2(\lambda l) + \cosh^2(\lambda l)}$$

$$u_B(l) = -F\frac{\sin(2\lambda l) + \sinh(2\lambda l)}{4\lambda^3 EI\big(cosh(2\lambda l) - cos(2\lambda l)\big)}$$

$$k_i = -\frac{4\lambda^3 EI\big(cosh(2\lambda l) - cos(2\lambda l)\big)}{\sin(2\lambda l) + \sinh(2\lambda l)}$$

BE AWARE this expression is per shear plane, as such the total moment it can resist stays the same but the effects of a moment force on the plate should be doubled, and the thickness of the bolt should be included in the definition of the foundation stiffness by multiplying it by d or 2r, also ensure that there is sufficient space between the node, the plate and the timber of them to rotate without contact outside of the calculated area since this will likely result in much stiffer behaviour and stress concentrations in those contact areas

This result clearly depicts the effect of the foundation decay length where for large width ratios the prediction of the deformation is minimal for the prediction of internal forces of the bolt however this does have effect.

There appears to be a lack of the difference between fibre directions in the formulation according to EC5 of Kser assuming only the main direction

A similar approach can be used to calculate the lateral stiffness of the bolt. Here however it is a much simpler relation due to the expected deflection of the bolt, where the rotation at the interface between the plate and the beam is governing. As this allows the plate and the beam to rotate against each other. As the bolt is continuous the rotation sign caused by the moment has a negative sign on the other side resulting in a diagonal symmetry plane across the steel plate

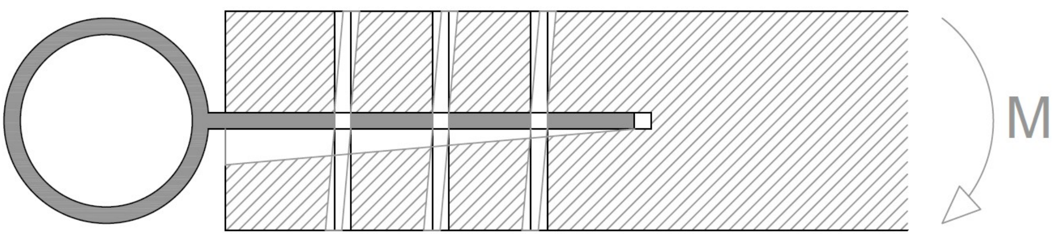

$$\frac{M}{\theta} = C$$

Where we are considering the full dowel and its rotational effect at the interface so evaluated at x=l

$$u_B{}'(l) = \frac{M}{2\lambda EI(\sinh(\lambda l)\cosh(\lambda l) - \cos(\lambda l)\sin(\lambda l))}\big[(\cos(\lambda l)\sinh(\lambda l) + \sin(\lambda l)\cosh(\lambda l))(-\sin(\lambda l)\cosh(\lambda l) + \cos(\lambda l)\sinh(\lambda l)) - \cos(\lambda l)\cosh(\lambda l)\big((-\sin(\lambda l)\sinh(\lambda l) + \cos(\lambda x)\cosh(\lambda x)) + (\cos(\lambda l)\cosh(\lambda l) + \sin(\lambda l)\sinh(\lambda l))\big)\big]$$

$$u_B{}'(l) = \frac{M}{2\lambda EI(\sinh(\lambda l)\cosh(\lambda l) - \cos(\lambda l)\sin(\lambda l))}[\cos^2(\lambda l)\sinh^2(\lambda l) - \sin^2(\lambda l)\cosh^2(\lambda l) - 2\cos^2(\lambda l)\cosh^2(\lambda l)]$$

Fill solution into the relation between rotation and moment to derive the rotational stiffness, due to the two shear planes however there is twice the stiffness coming from the bolts thus we include a factor 2

$$\frac{2M}{\theta} = C$$

$$\frac{4\lambda EI(\sinh(\lambda l)\cosh(\lambda l) - \cos(\lambda l)\sin(\lambda l))}{\cos^2(\lambda l)\sinh^2(\lambda l) - \sin^2(\lambda l)\cosh^2(\lambda l) - 2\cos^2(\lambda l)\cosh^2(\lambda l)} = C_{zz,1,d}$$

Where we are considering the full bolt and its rotational effect at the interface so evaluated at x=l

$$\frac{du_0(l)}{dx} = \frac{M}{2\lambda EI(\sin^2(\lambda l)\sinh^2(\lambda l) + \cos^2(\lambda l)\cosh(\lambda l)^2)}[\sin(\lambda l)\sinh(\lambda l)\,(-\sin(\lambda x)\cosh(\lambda x) + \cos(\lambda x)\sinh(\lambda x)) - \cos(\lambda l)\cosh(\lambda l)\,(\cos(\lambda x)\sinh(\lambda x) + \sin(\lambda x)\cosh(\lambda x))]$$

$$\theta_l = -\frac{M(\sinh(\lambda l)\cosh(\lambda l) + \sin(\lambda l)\cos(\lambda l))}{2\lambda EI(\sin^2(\lambda l)\sinh^2(\lambda l) + \cos^2(\lambda l)\cosh(\lambda l)^2)}$$

Fill solution into the relation between rotation and moment to derive the rotational stiffness, due to the two shear planes however there is twice the stiffness coming from the bolts thus we include a factor 2 and sum the rotational stiffness of the bolts together

$$\frac{2M}{\theta} = C$$

$$\frac{4\lambda EI(\sin^2(\lambda l)\sinh^2(\lambda l) + \cos^2(\lambda l)\cosh(\lambda l)^2)}{\sinh(\lambda l)\cosh(\lambda l) + \sin(\lambda l)\cos(\lambda l)} = C_{zz,1,b}$$

$$C_{zz,1,b,tot} = \sum_i C_{zz,1,i}$$

The other components from the stiffness come from the plate which is a simple equation based on a rotational spring from the plate itself and from the bearing of the timber on the steel plate. This expression is the same system as the bolt bending however instead of being plotted over the dowel foundation depth equal to the bolt length it is equal to the height of the crossection and with the plate as its stiffness

$$C_{zz,2} = \frac{EI_{zz}}{e}$$

$$\frac{2\lambda EI(\sin^2(\lambda l)\sinh^2(\lambda l) + \cos^2(\lambda l)\cosh(\lambda l)^2)}{\sinh(\lambda l)\cosh(\lambda l) + \sin(\lambda l)\cos(\lambda l)} = C_{zz,3}$$

This combined with the series spring combination expression of the plate results in a sum of stiffnesses to determine the total C_{yy} where $C_{zz,1,i} and\ C_{zz,3}$ are added directly as they share the angle of rotation on which they act.

$$\frac{1}{\frac{1}{\sum_i C_{zz,1,i} + C_{zz,3}} + \frac{1}{C_{zz,2}}} = C_{yy}$$

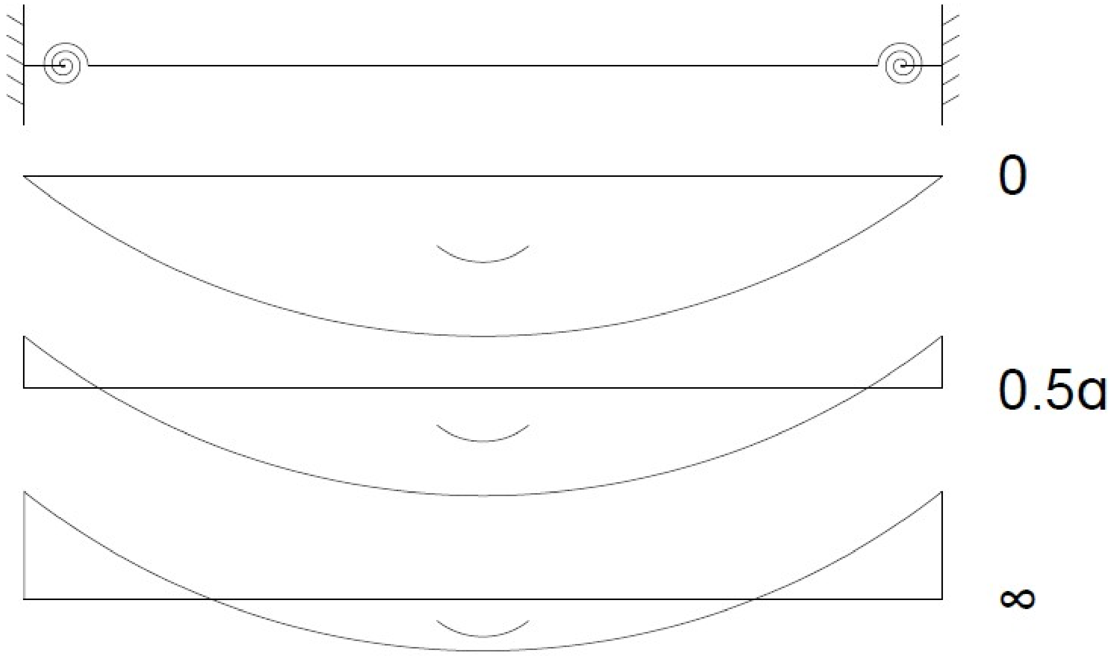

All internal and node force plots for $C_{zz} = 0$ and $k = 1$

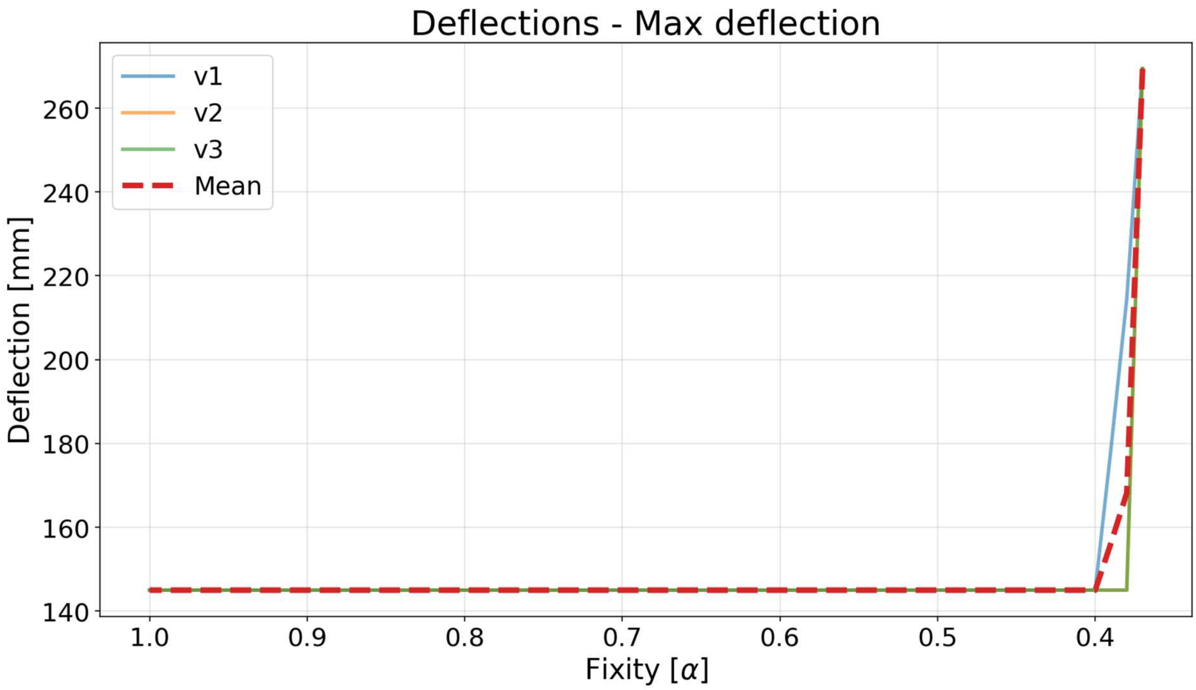

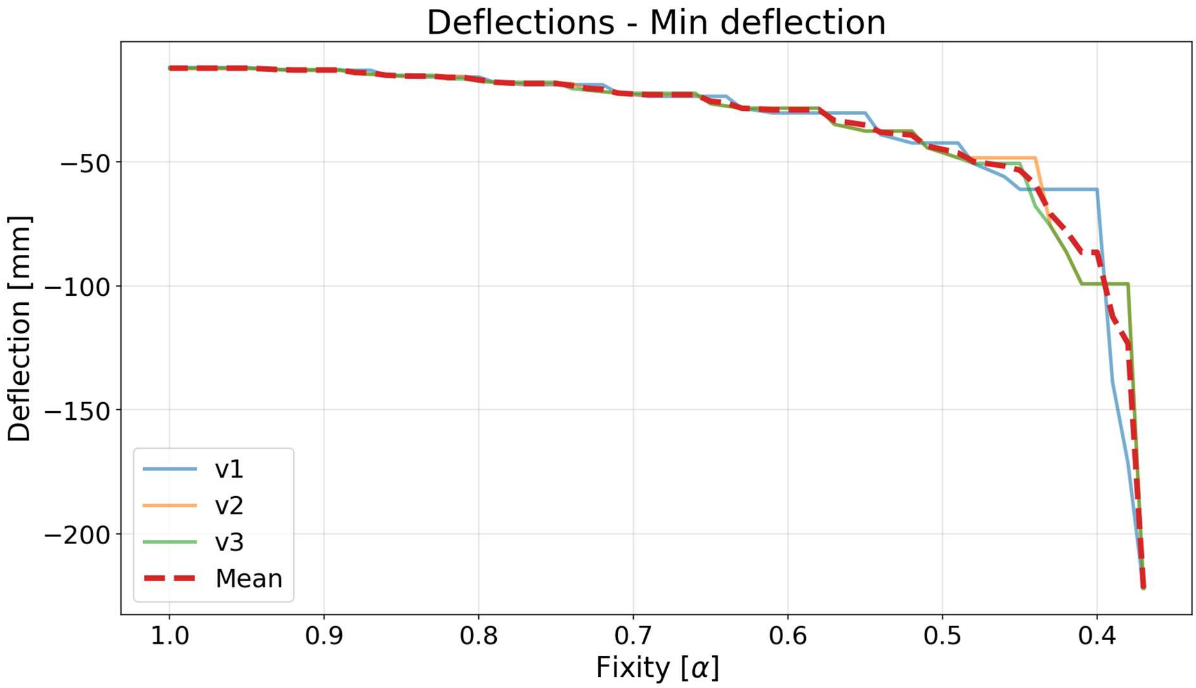

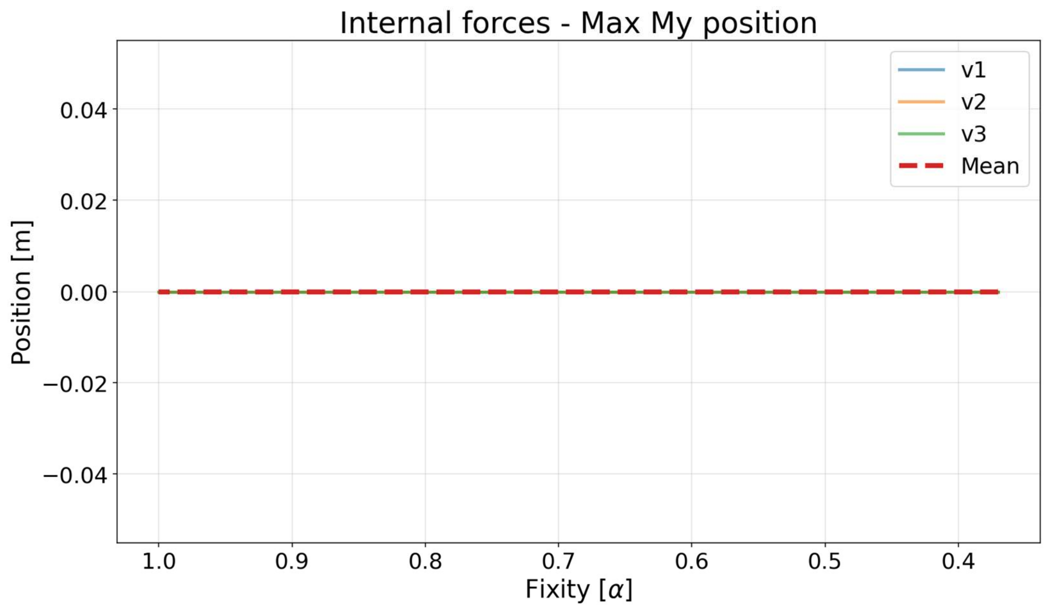

Internal forces - Max My position
Position [m]
Fixity [α]
v1
v2
v3
Mean

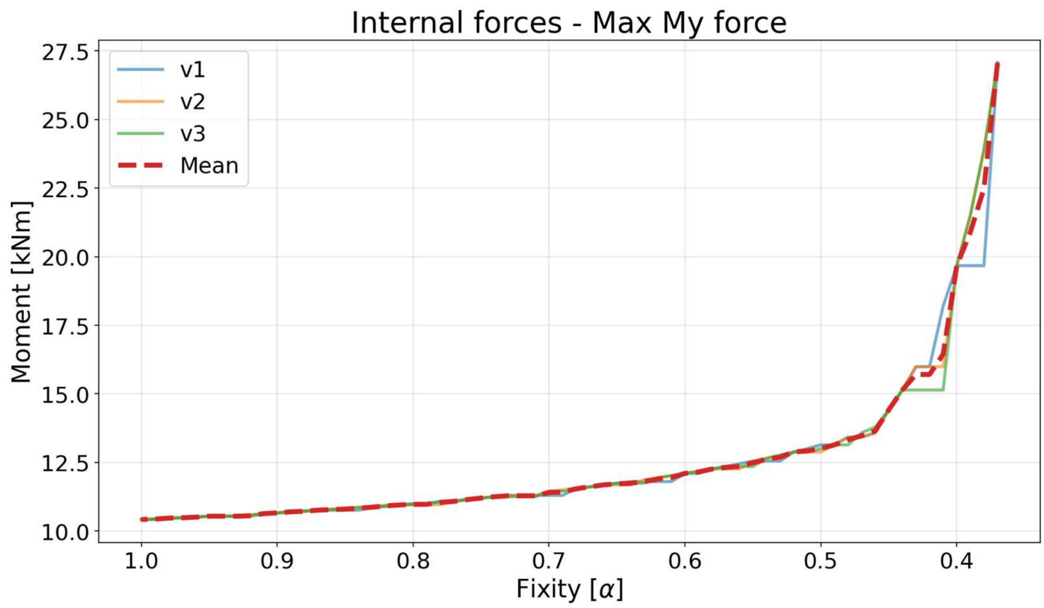

Internal forces - Max My force
Moment [kNm]
Fixity [α]
v1
v2
v3
Mean

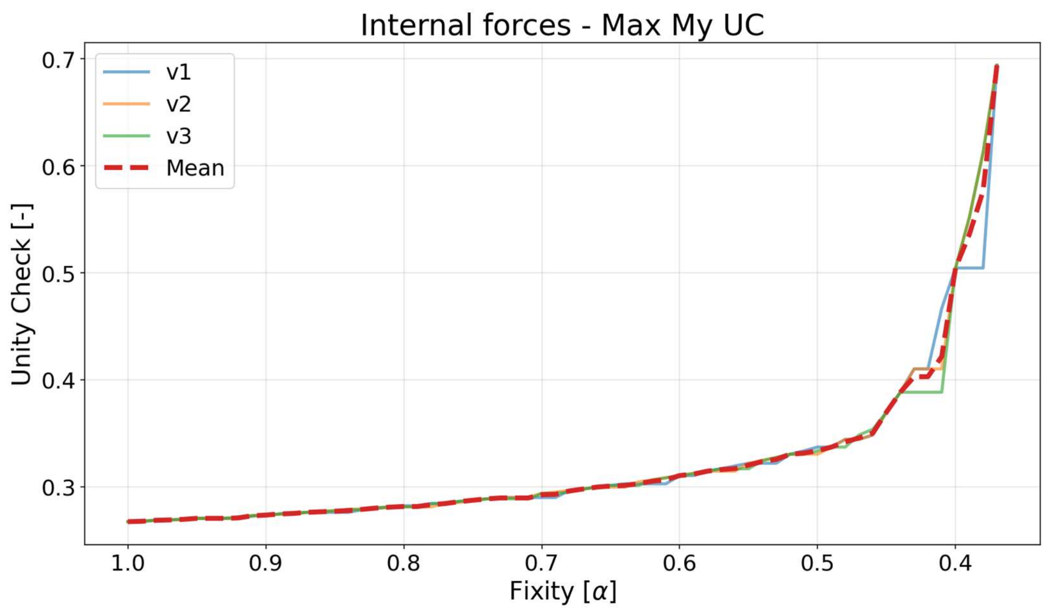

Internal forces - Max My UC
Unity Check [-]
Fixity [α]
v1
v2
v3
Mean

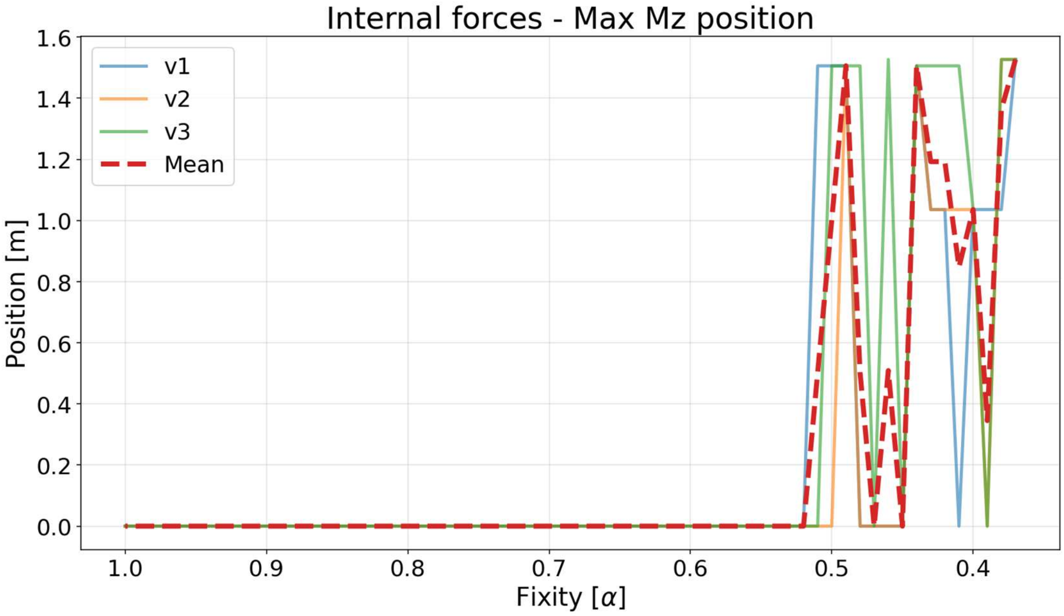
Internal forces - Max Mz position
Position [m]
Fixity [α]
v1
v2
v3
Mean
1.6
1.4
1.2
1.0
0.8
0.6
0.4
0.2
0.0
1.0
0.9
0.8
0.7
0.6
0.5
0.4

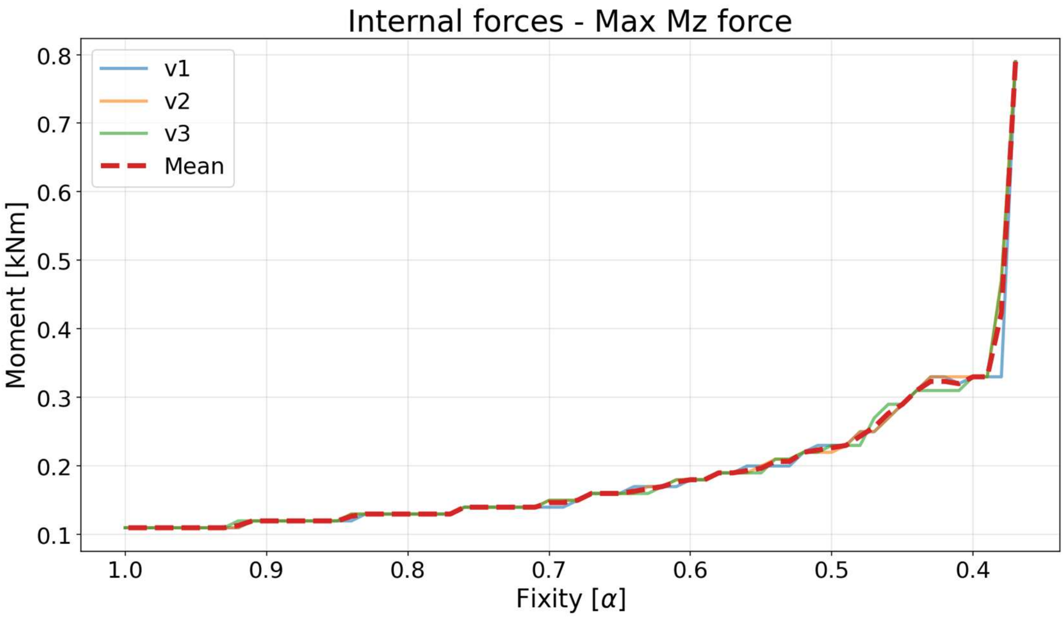
Internal forces - Max Mz force
Moment [kNm]
Fixity [α]
v1
v2
v3
Mean
0.8
0.7
0.6
0.5
0.4
0.3
0.2
0.1
1.0
0.9
0.8
0.7
0.6
0.5
0.4

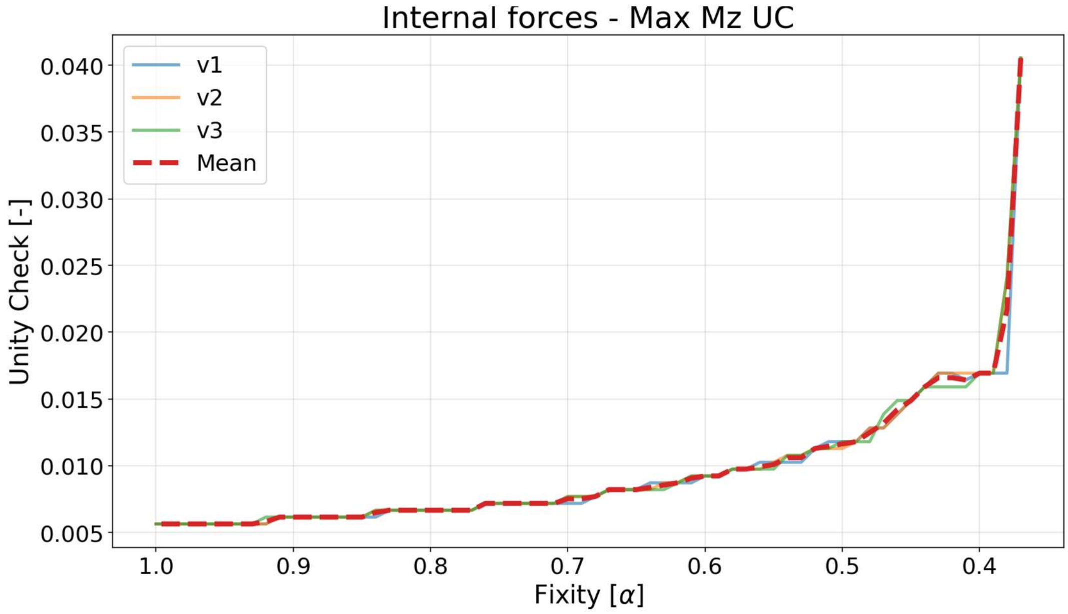
Internal forces - Max Mz UC
Unity Check [-]
Fixity [α]
v1
v2
v3
Mean
0.040
0.035
0.030
0.025
0.020
0.015
0.010
0.005
1.0
0.9
0.8
0.7
0.6
0.5
0.4

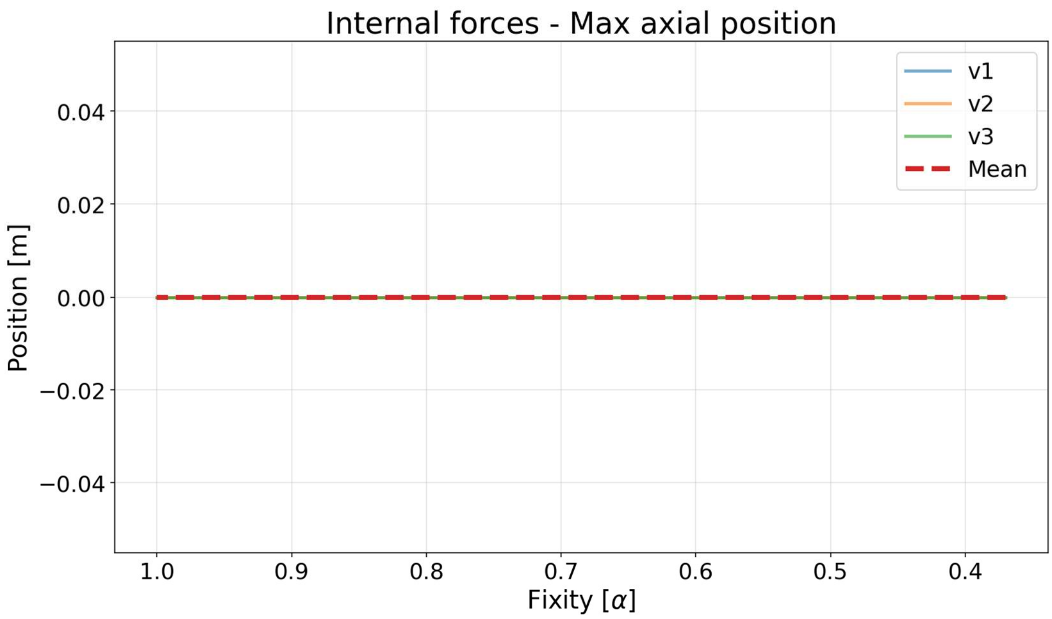
Internal forces - Max axial position
Position [m]
Fixity [α]
v1
v2
v3
Mean
0.04
0.02
0.00
−0.02
−0.04
1.0
0.9
0.8
0.7
0.6
0.5
0.4

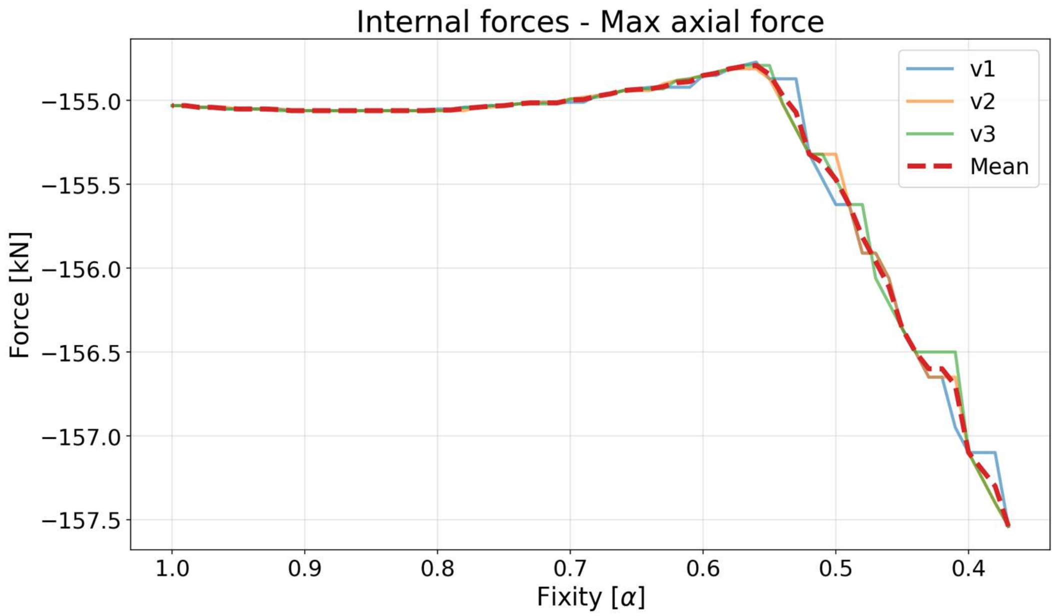
Internal forces - Max axial force
Force [kN]
Fixity [α]
v1
v2
v3
Mean
−155.0
−155.5
−156.0
−156.5
−157.0
−157.5
1.0
0.9
0.8
0.7
0.6
0.5
0.4

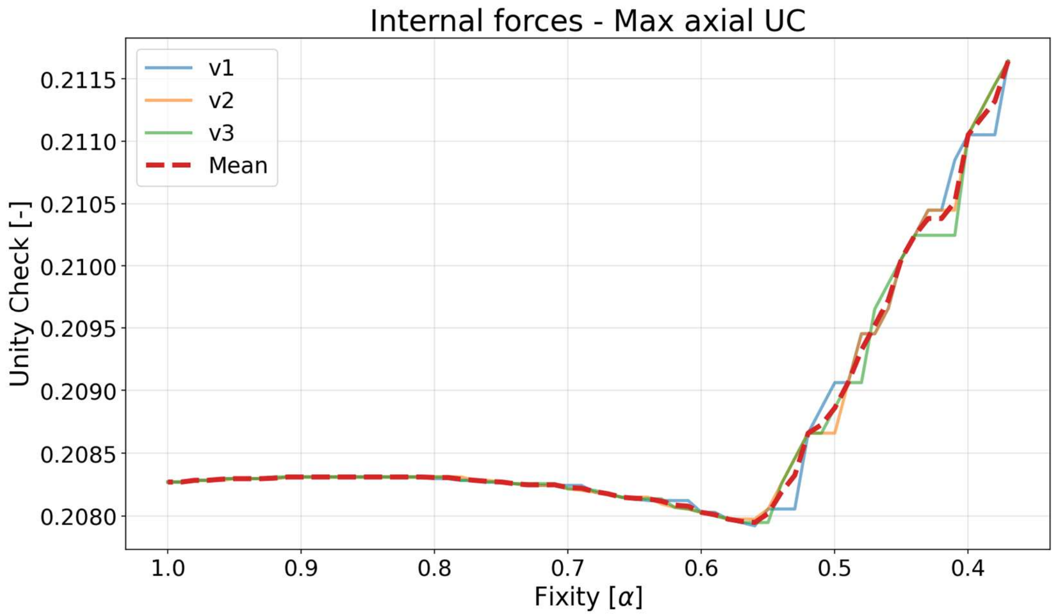
Internal forces - Max axial UC
Unity Check [-]
Fixity [α]
v1
v2
v3
Mean
0.2115
0.2110
0.2105
0.2100
0.2095
0.2090
0.2085
0.2080
1.0
0.9
0.8
0.7
0.6
0.5
0.4

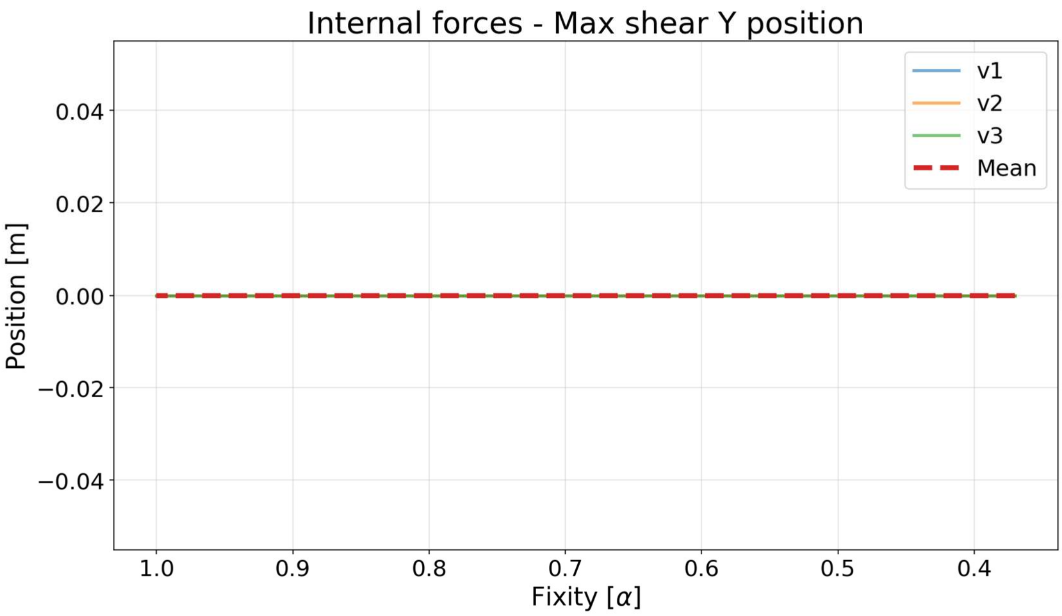
Internal forces - Max shear Y position
v1
v2
v3
Mean
Position [m]
0.04
0.02
0.00
−0.02
−0.04
1.0
0.9
0.8
0.7
0.6
0.5
0.4
Fixity [α]

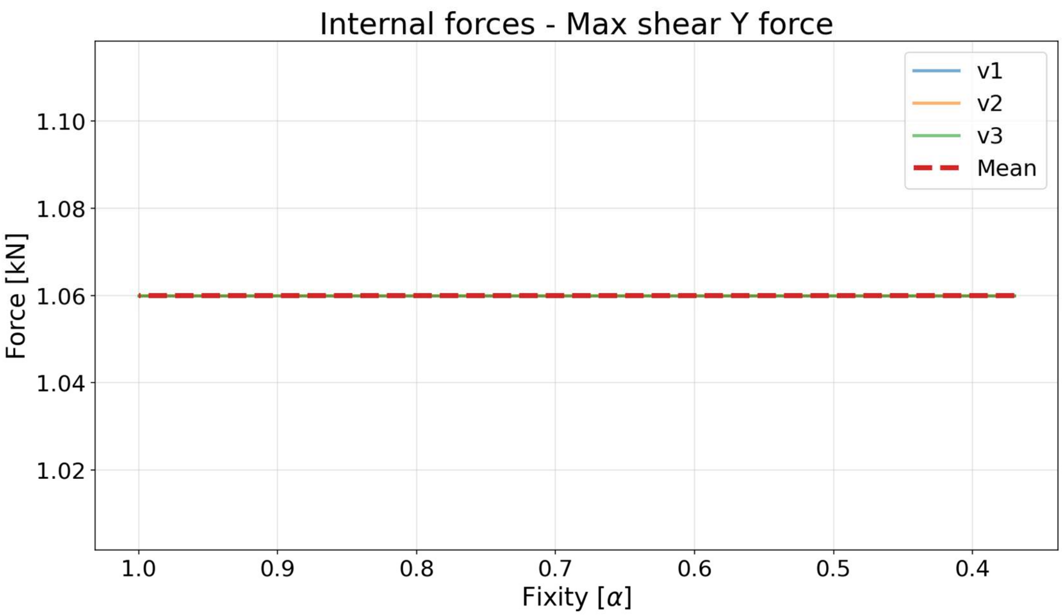
Internal forces - Max shear Y force
v1
v2
v3
Mean
Force [kN]
1.10
1.08
1.06
1.04
1.02
1.0
0.9
0.8
0.7
0.6
0.5
0.4
Fixity [α]

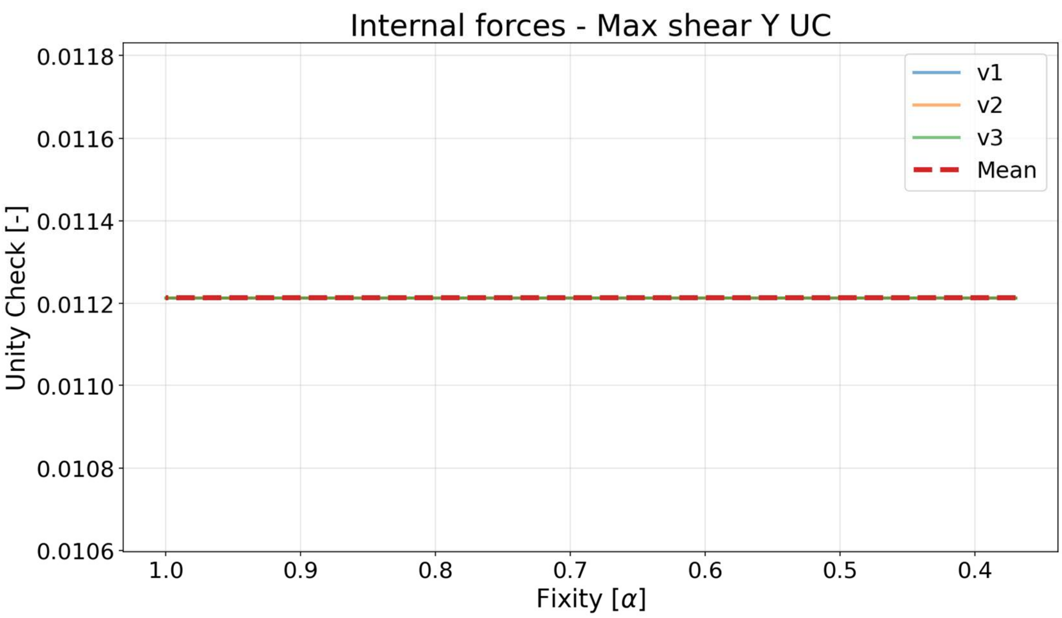
Internal forces - Max shear Y UC
v1
v2
v3
Mean
Unity Check [-]
0.0118
0.0116
0.0114
0.0112
0.0110
0.0108
0.0106
1.0
0.9
0.8
0.7
0.6
0.5
0.4
Fixity [α]

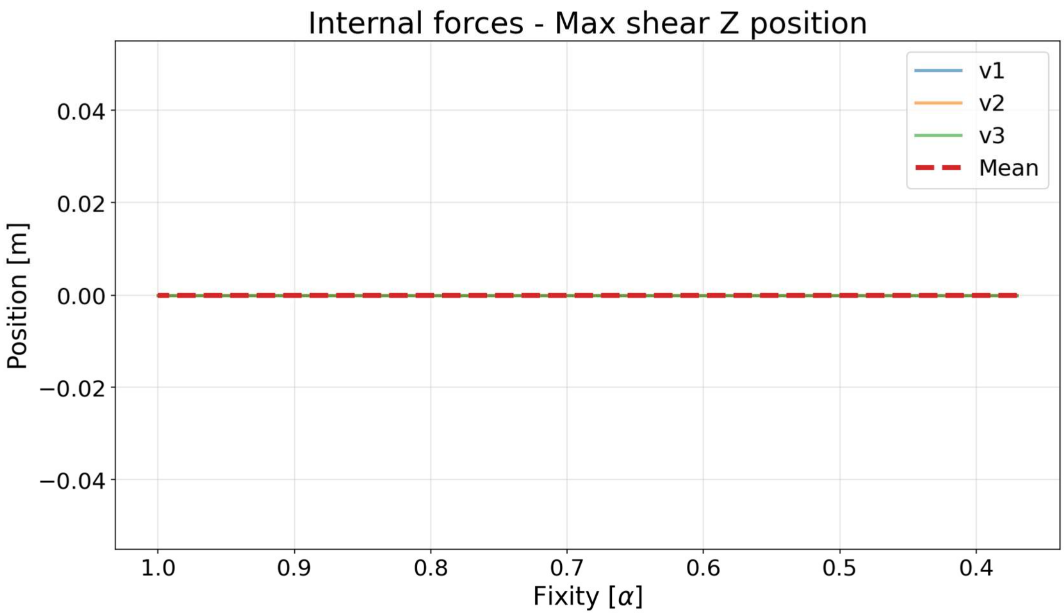
Internal forces - Max shear Z position
v1
v2
v3
Mean
Position [m]
0.04
0.02
0.00
−0.02
−0.04
1.0
0.9
0.8
0.7
0.6
0.5
0.4
Fixity [α]

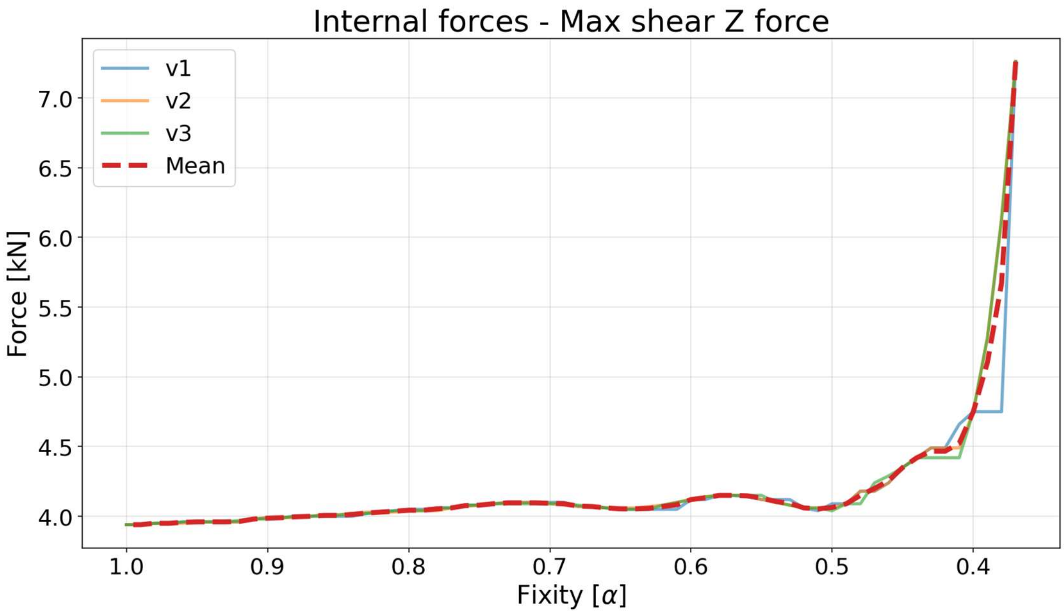
Internal forces - Max shear Z force
v1
v2
v3
Mean
Force [kN]
7.0
6.5
6.0
5.5
5.0
4.5
4.0
1.0
0.9
0.8
0.7
0.6
0.5
0.4
Fixity [α]

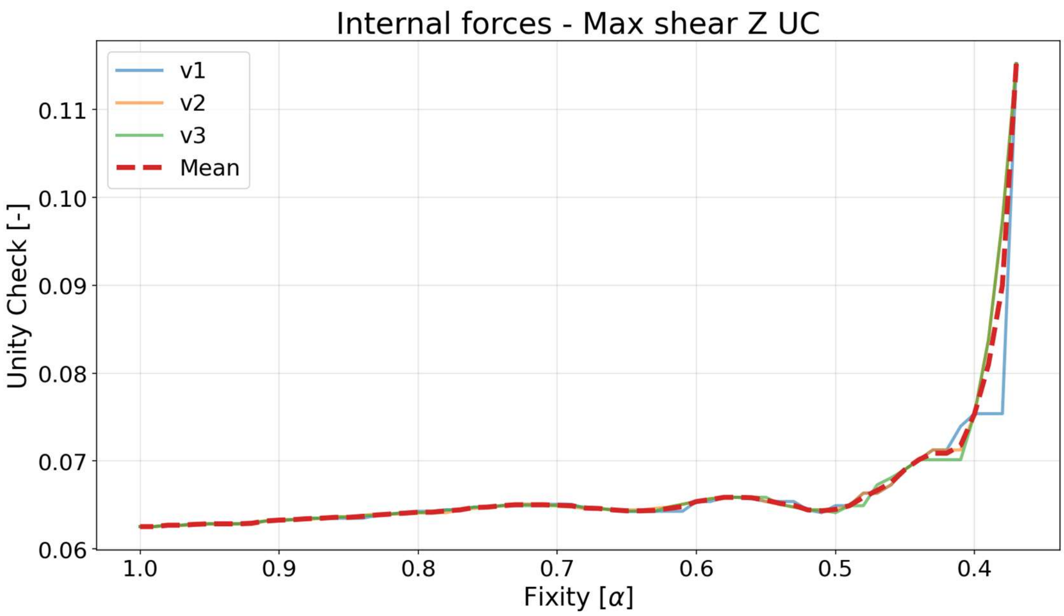
Internal forces - Max shear Z UC
v1
v2
v3
Mean
Unity Check [-]
0.11
0.10
0.09
0.08
0.07
0.06
1.0
0.9
0.8
0.7
0.6
0.5
0.4
Fixity [α]

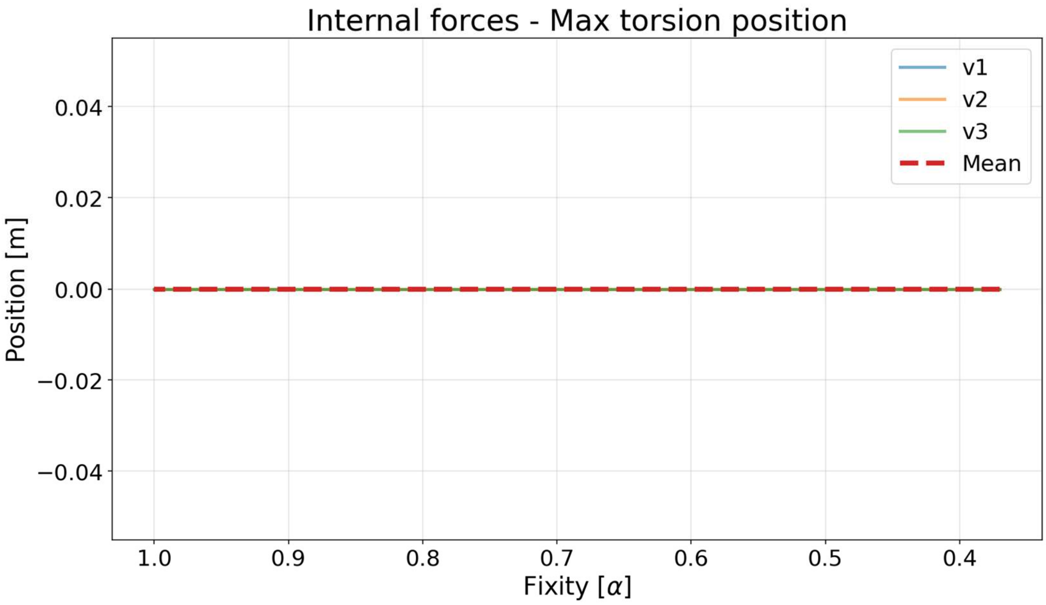
Internal forces - Max torsion position
Position [m]
Fixity [α]
v1
v2
v3
Mean

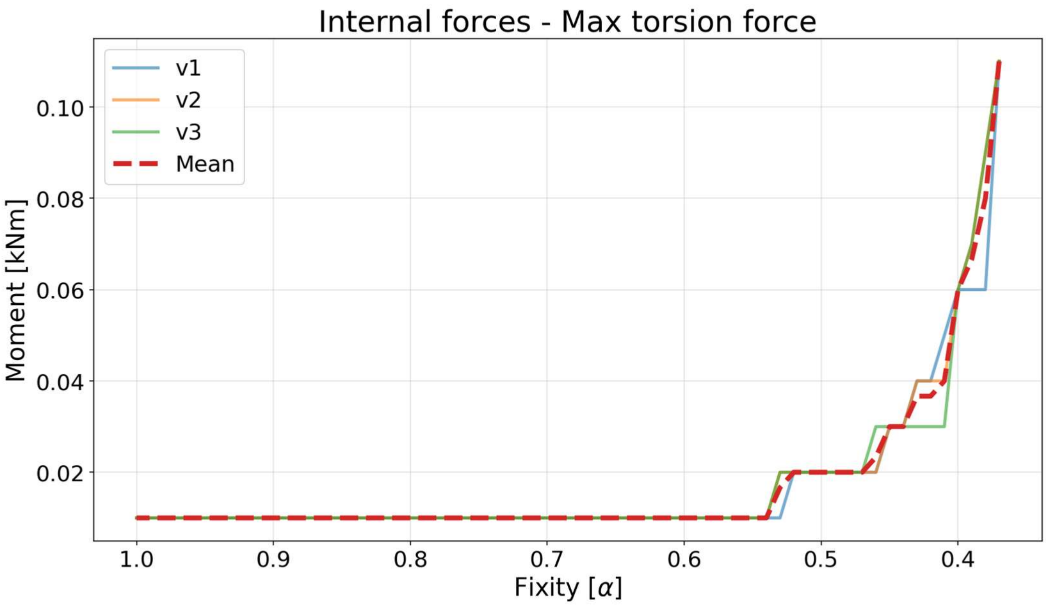
Internal forces - Max torsion force
Moment [kNm]
Fixity [α]
v1
v2
v3
Mean

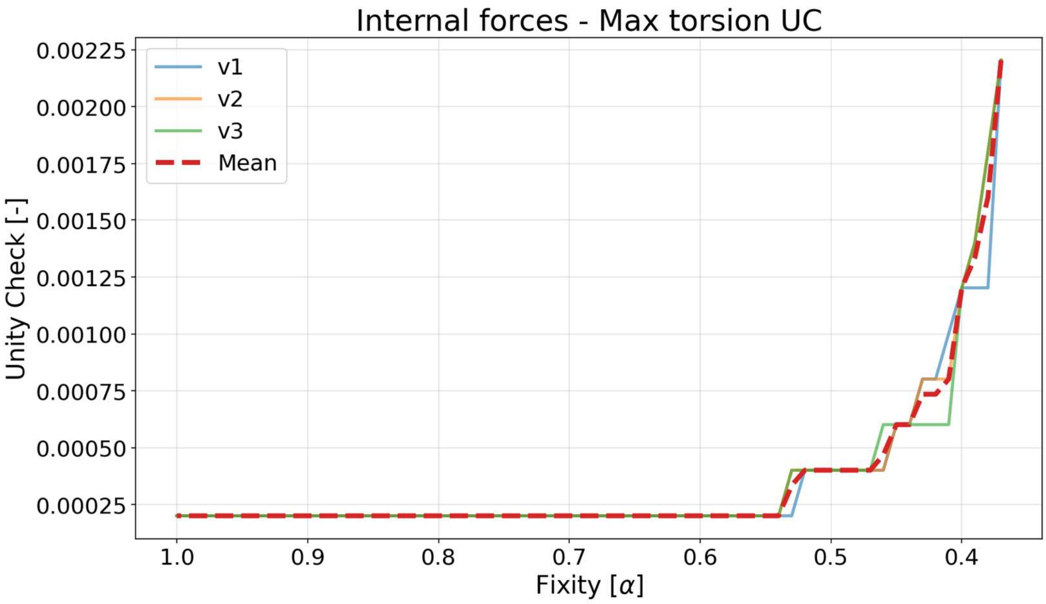
Internal forces - Max torsion UC
Unity Check [-]
Fixity [α]
v1
v2
v3
Mean

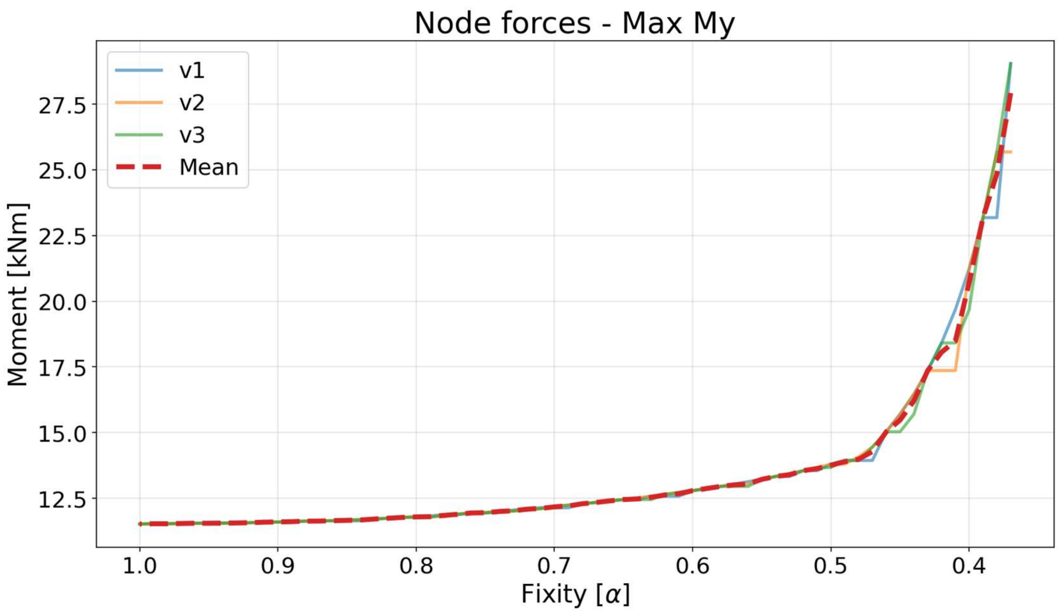
Node forces - Max My
v1
v2
v3
Mean
Moment [kNm]
27.5
25.0
22.5
20.0
17.5
15.0
12.5
1.0
0.9
0.8
0.7
0.6
0.5
0.4
Fixity [α]

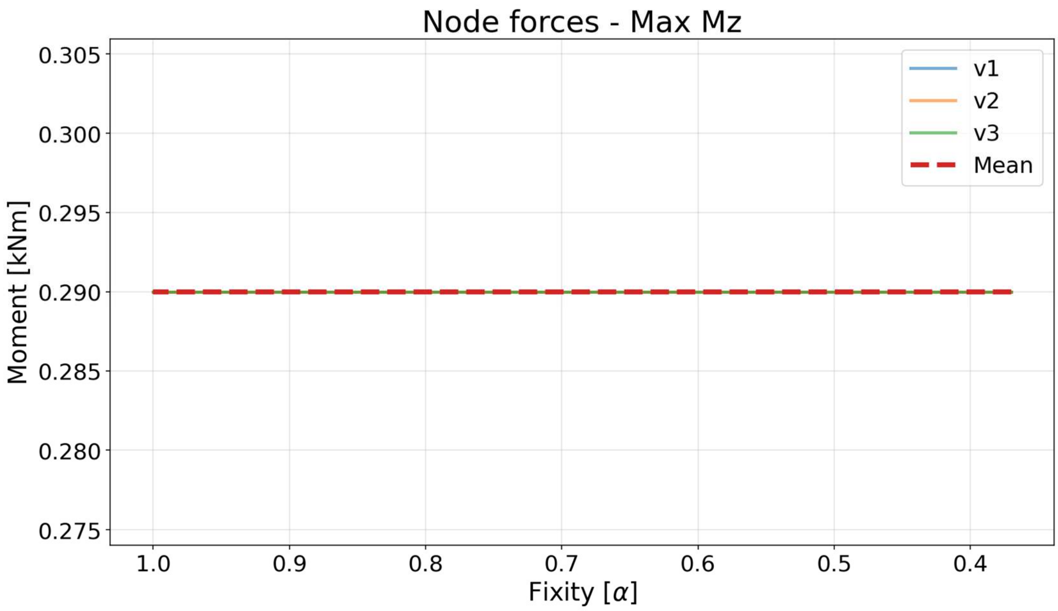
Node forces - Max Mz
v1
v2
v3
Mean
Moment [kNm]
0.305
0.300
0.295
0.290
0.285
0.280
0.275
1.0
0.9
0.8
0.7
0.6
0.5
0.4
Fixity [α]

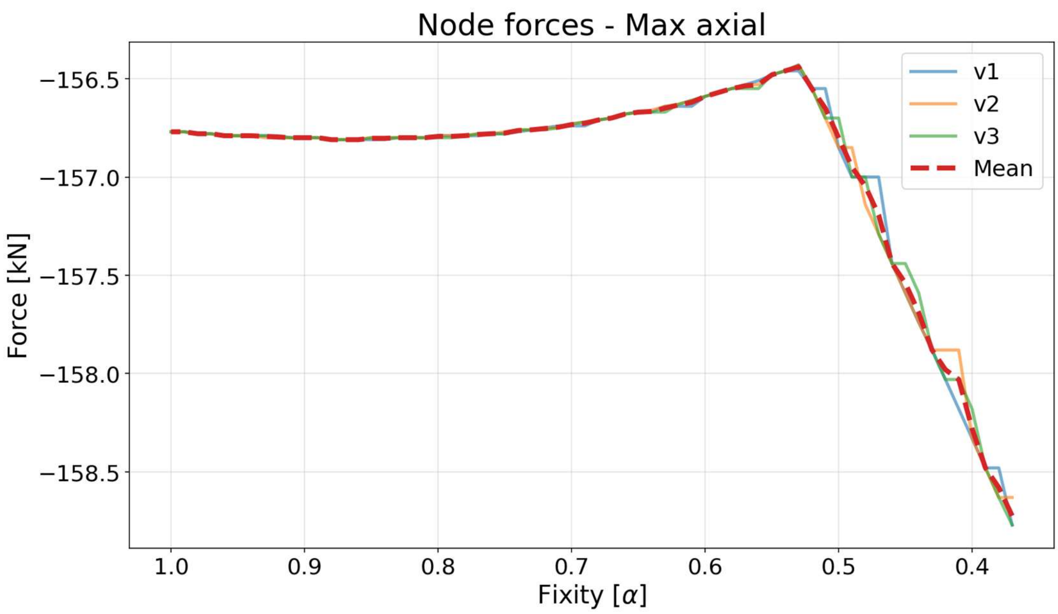
Node forces - Max axial
v1
v2
v3
Mean
Force [kN]
−156.5
−157.0
−157.5
−158.0
−158.5
1.0
0.9
0.8
0.7
0.6
0.5
0.4
Fixity [α]

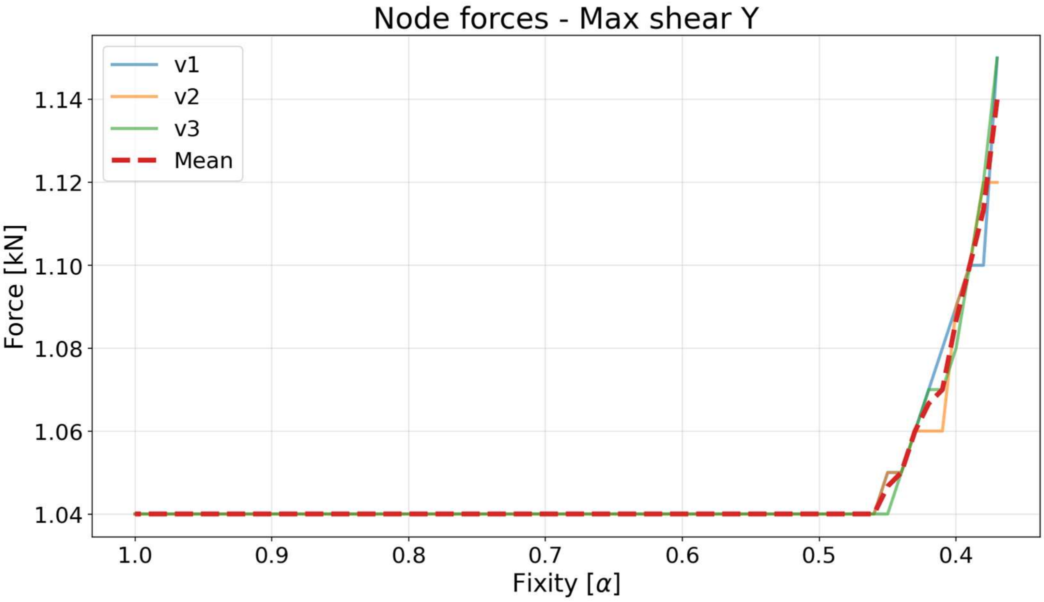

Node forces - Max shear Y
v1
v2
v3
Mean
Force [kN]
Fixity [α]

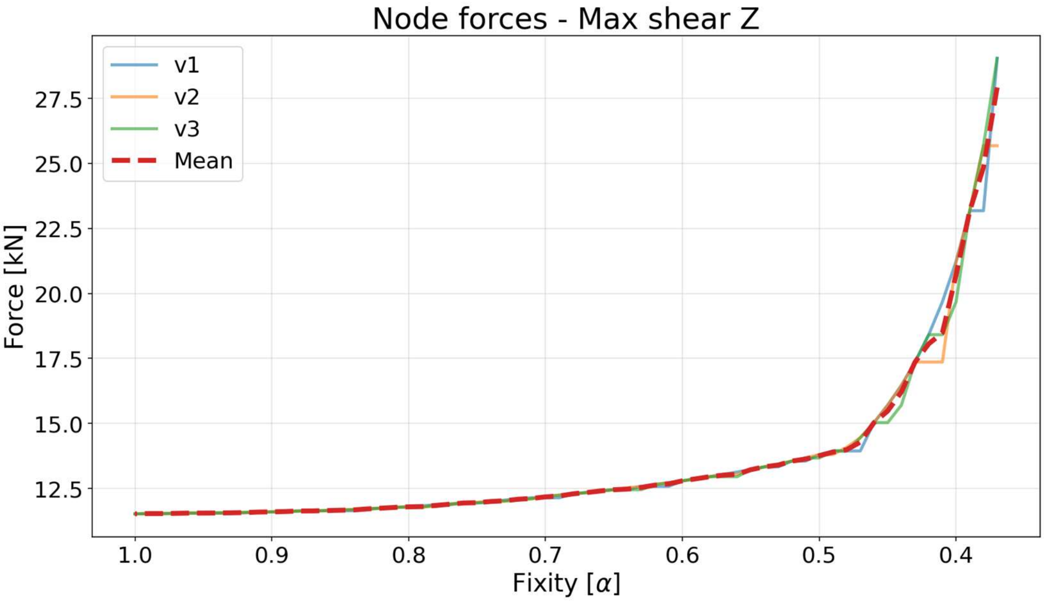

Node forces - Max shear Z
v1
v2
v3
Mean
Force [kN]
Fixity [α]

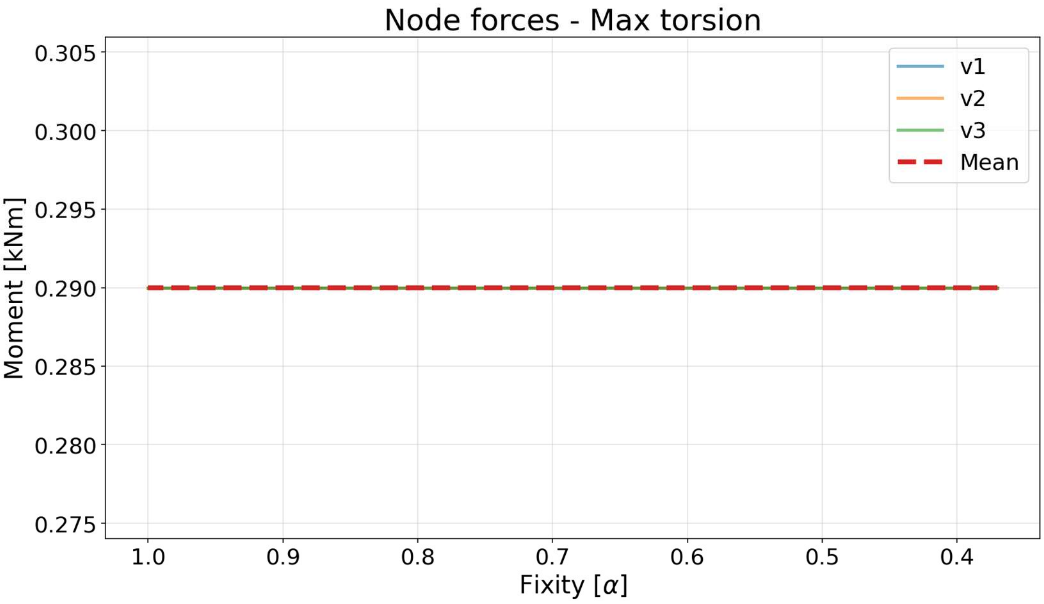

Node forces - Max torsion
v1
v2
v3
Mean
Moment [kNm]
Fixity [α]

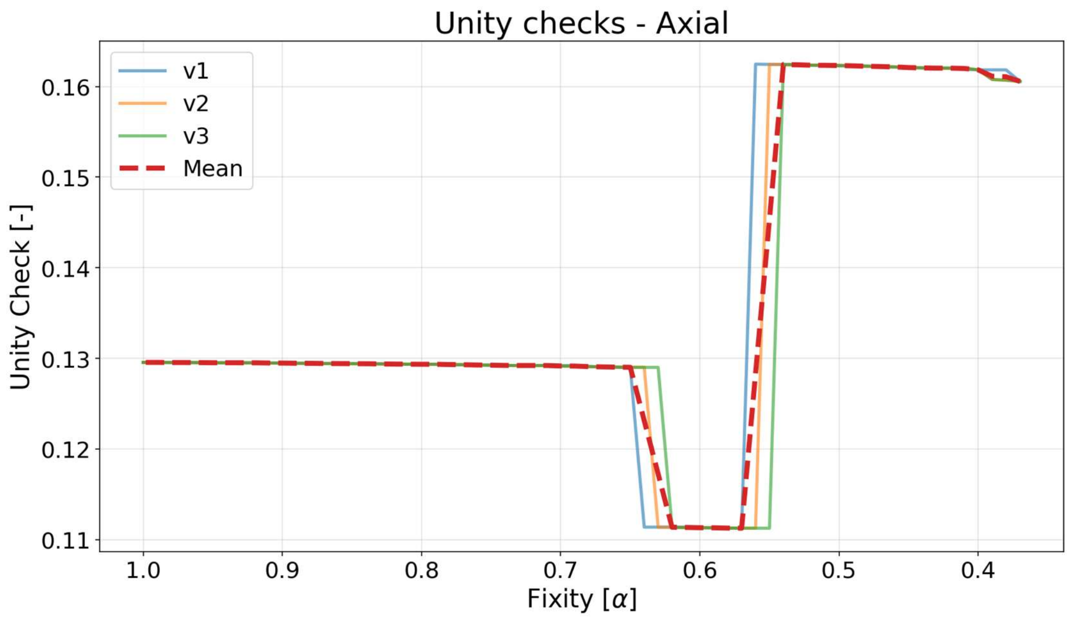
Unity checks - Axial
v1
v2
v3
Mean
Unity Check [-]
0.16
0.15
0.14
0.13
0.12
0.11
1.0
0.9
0.8
0.7
0.6
0.5
0.4
Fixity [α]

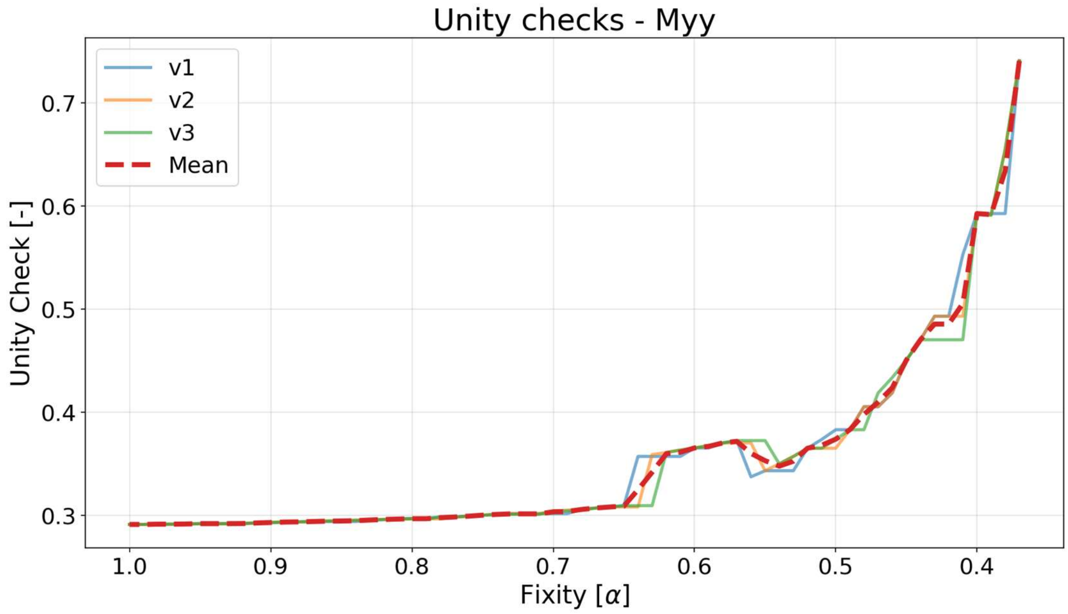
Unity checks - Myy
v1
v2
v3
Mean
Unity Check [-]
0.7
0.6
0.5
0.4
0.3
1.0
0.9
0.8
0.7
0.6
0.5
0.4
Fixity [α]

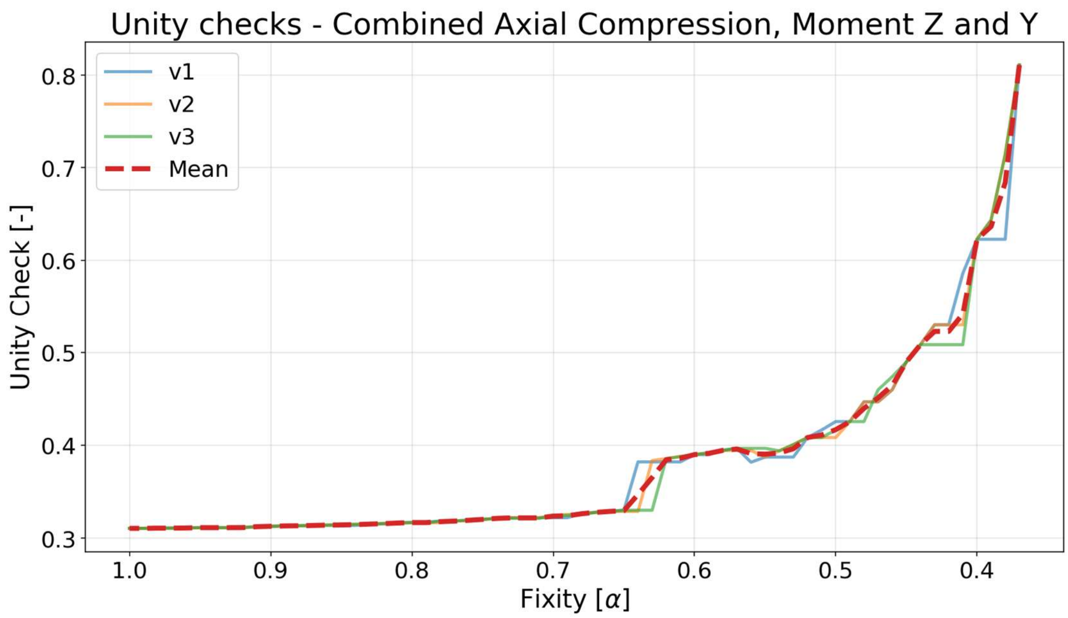
Unity checks - Combined Axial Compression, Moment Z and Y
v1
v2
v3
Mean
Unity Check [-]
0.8
0.7
0.6
0.5
0.4
0.3
1.0
0.9
0.8
0.7
0.6
0.5
0.4
Fixity [α]

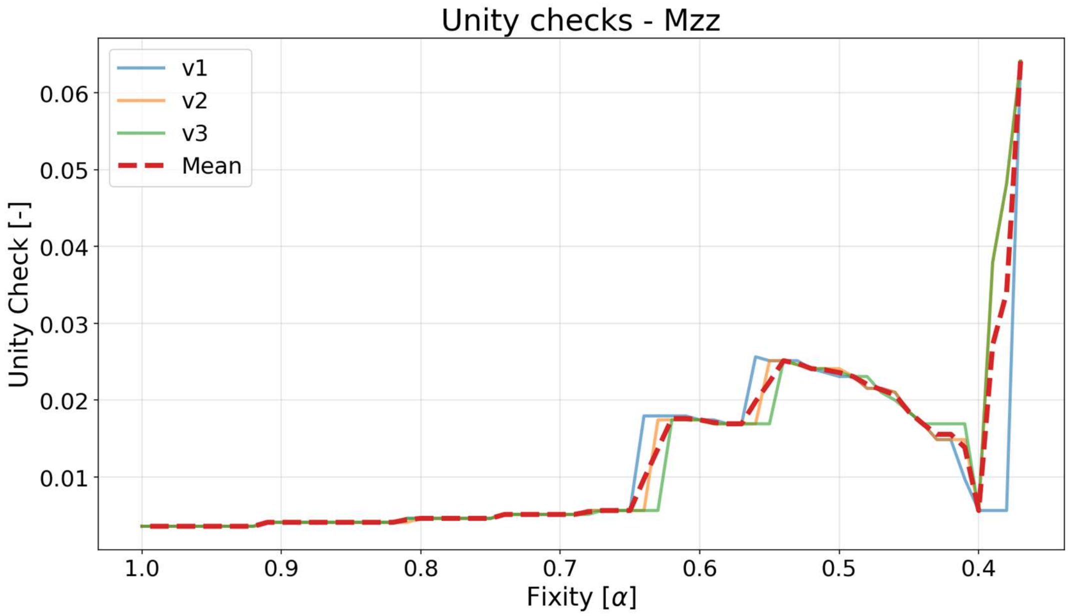
Unity checks - Mzz
v1
v2
v3
Mean
Unity Check [-]
Fixity [α]
0.01
0.02
0.03
0.04
0.05
0.06
1.0
0.9
0.8
0.7
0.6
0.5
0.4

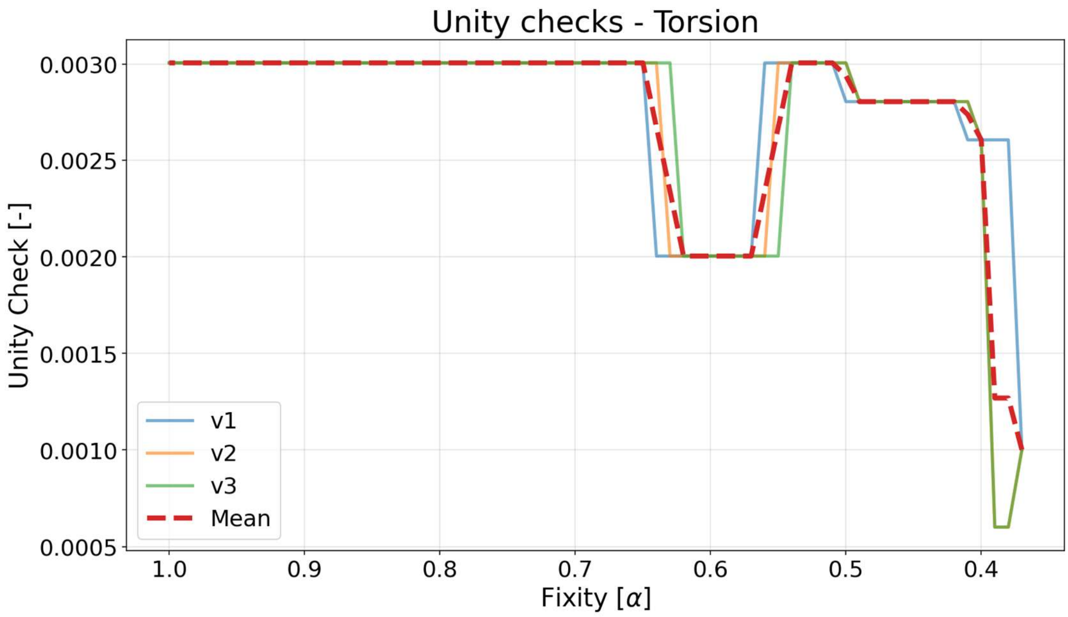
Unity checks - Torsion
v1
v2
v3
Mean
Unity Check [-]
Fixity [α]
0.0005
0.0010
0.0015
0.0020
0.0025
0.0030
1.0
0.9
0.8
0.7
0.6
0.5
0.4

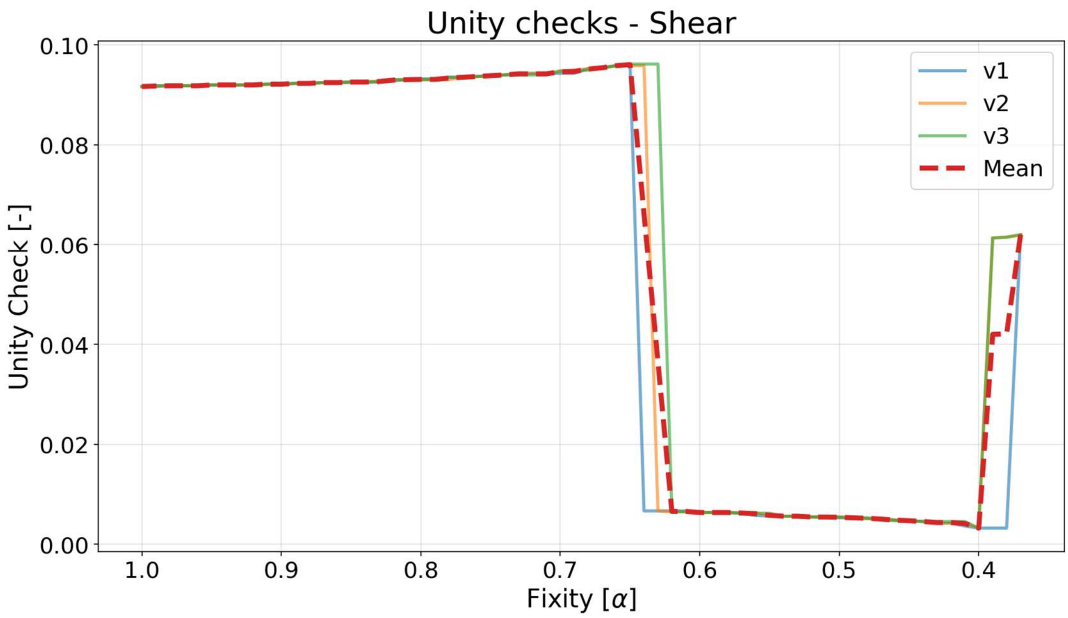
Unity checks - Shear
v1
v2
v3
Mean
Unity Check [-]
Fixity [α]
0.00
0.02
0.04
0.06
0.08
0.10
1.0
0.9
0.8
0.7
0.6
0.5
0.4

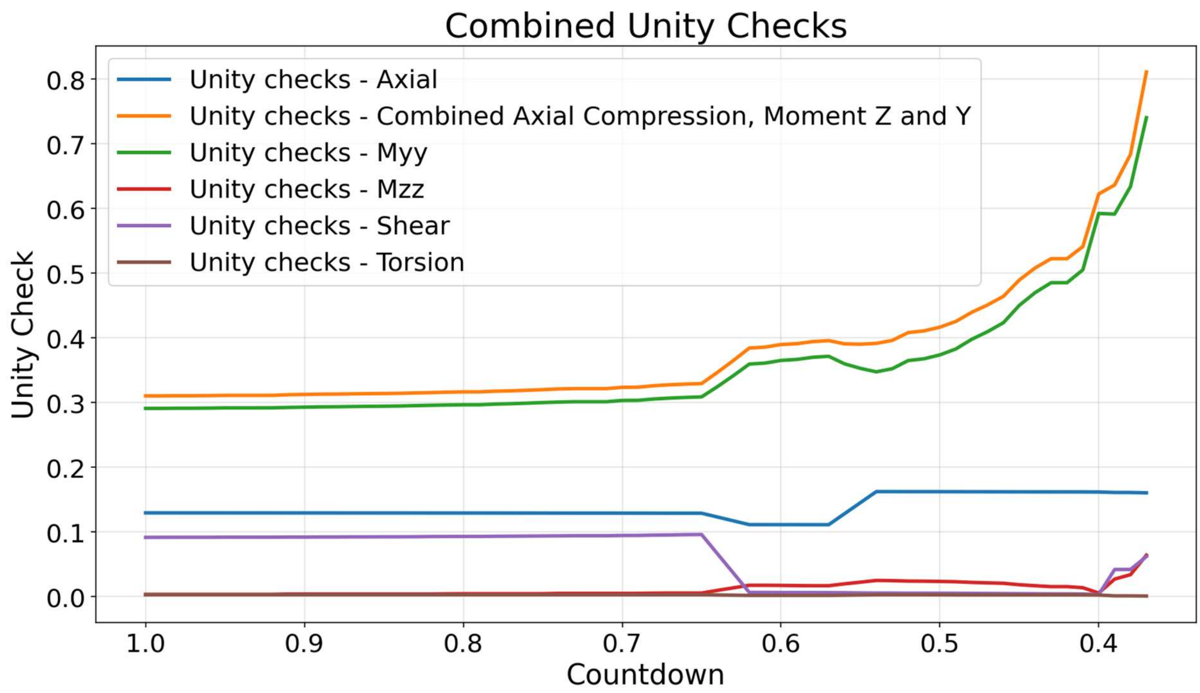
Combined Unity Checks
Unity checks - Axial
Unity checks - Combined Axial Compression, Moment Z and Y
Unity checks - Myy
Unity checks - Mzz
Unity checks - Shear
Unity checks - Torsion
Unity Check
Countdown

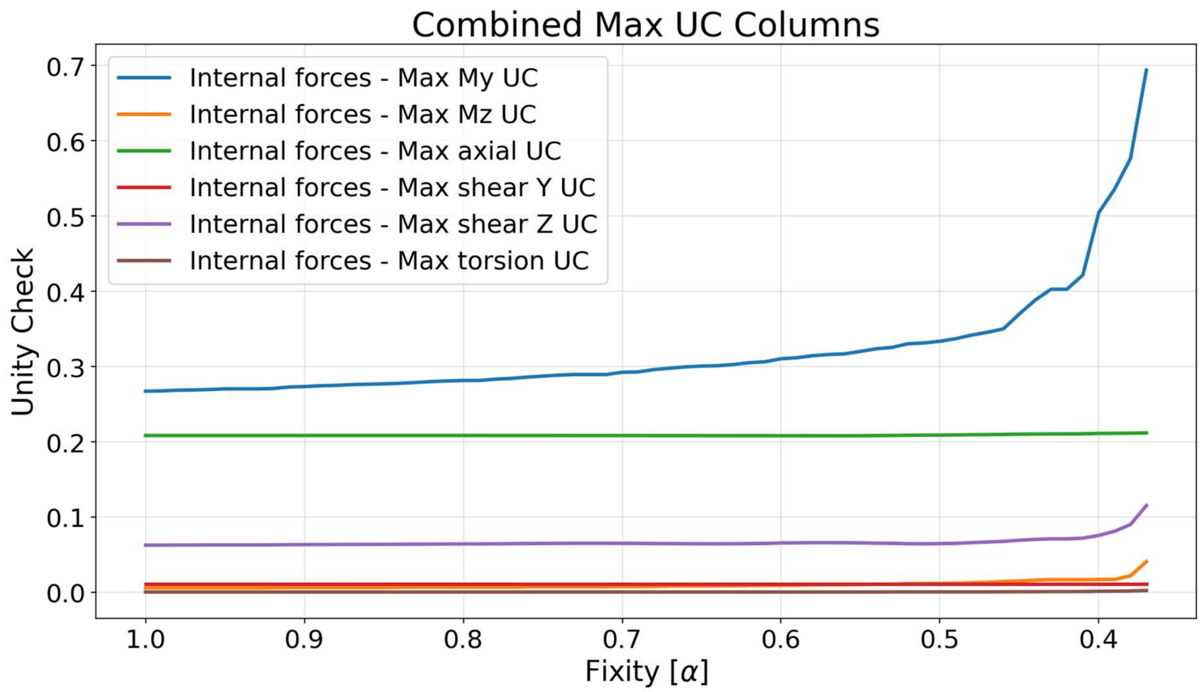
Combined Max UC Columns
Internal forces - Max My UC
Internal forces - Max Mz UC
Internal forces - Max axial UC
Internal forces - Max shear Y UC
Internal forces - Max shear Z UC
Internal forces - Max torsion UC
Unity Check
Fixity [α]

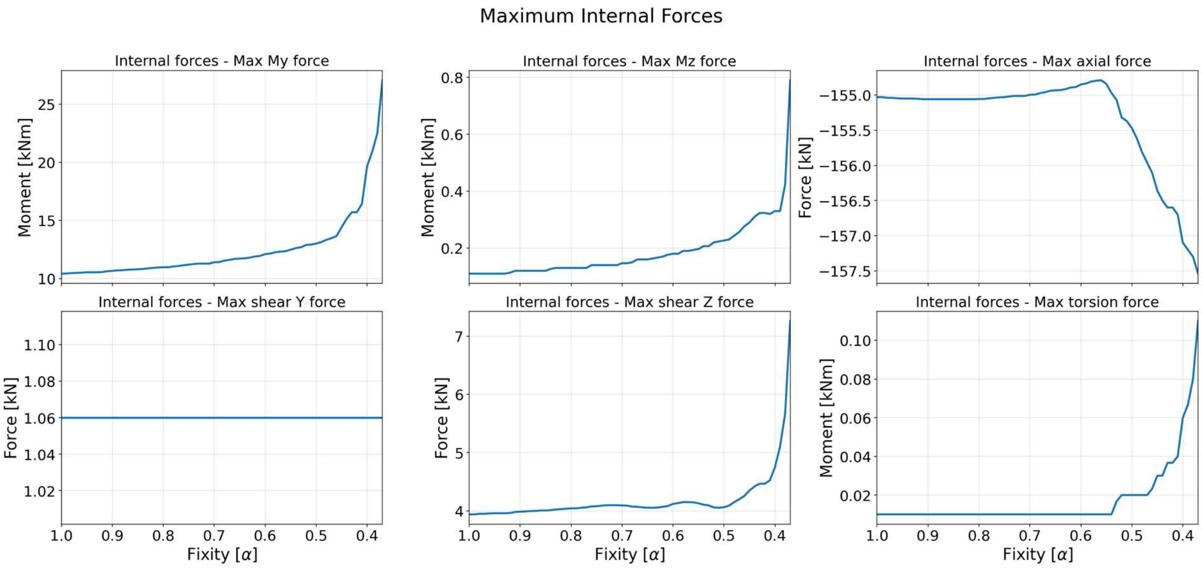
Maximum Internal Forces
Internal forces - Max My force
Internal forces - Max Mz force
Internal forces - Max axial force
Internal forces - Max shear Y force
Internal forces - Max shear Z force
Internal forces - Max torsion force
Moment [kNm]
Force [kN]
Fixity [α]

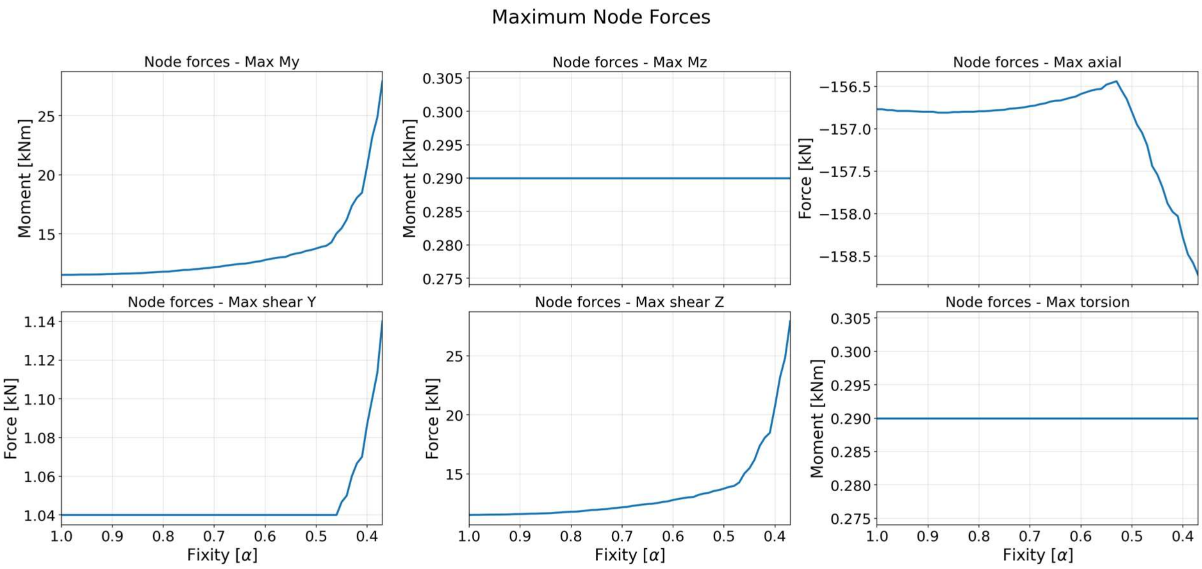
Maximum Node Forces
Node forces - Max My
Node forces - Max Mz
Node forces - Max axial
Node forces - Max shear Y
Node forces - Max shear Z
Node forces - Max torsion
Moment [kNm]
Force [kN]
Fixity [α]

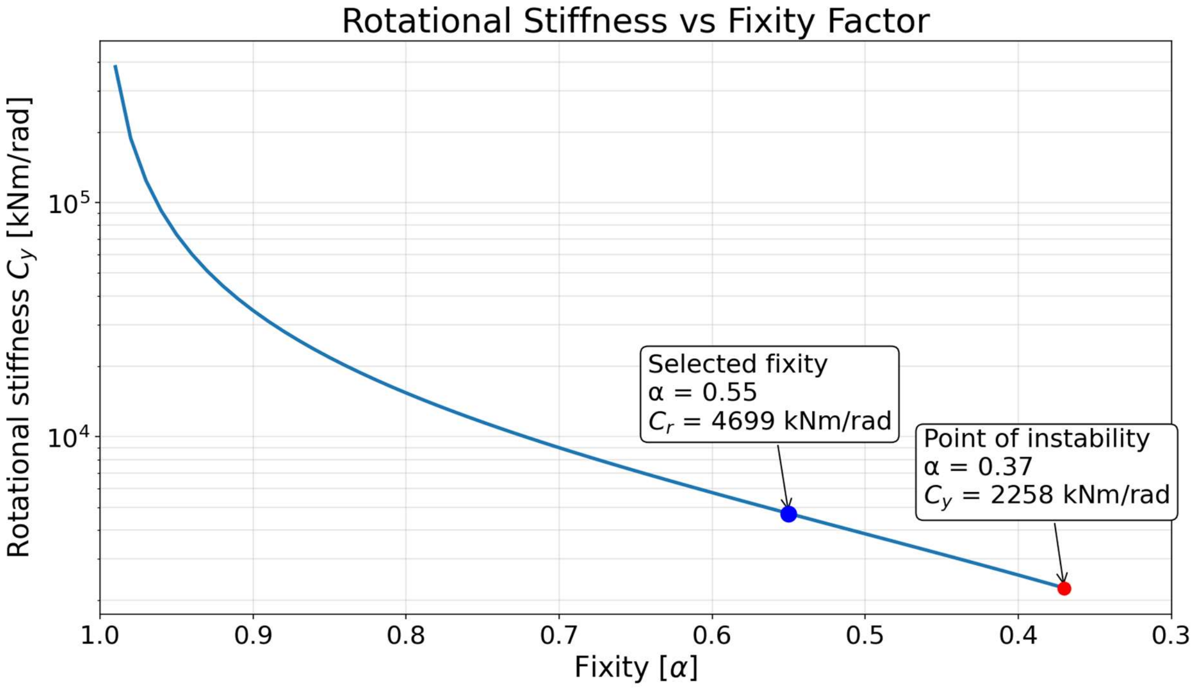
Rotational Stiffness vs Fixity Factor
Rotational stiffness C_y [kNm/rad]
Fixity [α]
Selected fixity
α = 0.55
C_r = 4699 kNm/rad
Point of instability
α = 0.37
C_y = 2258 kNm/rad

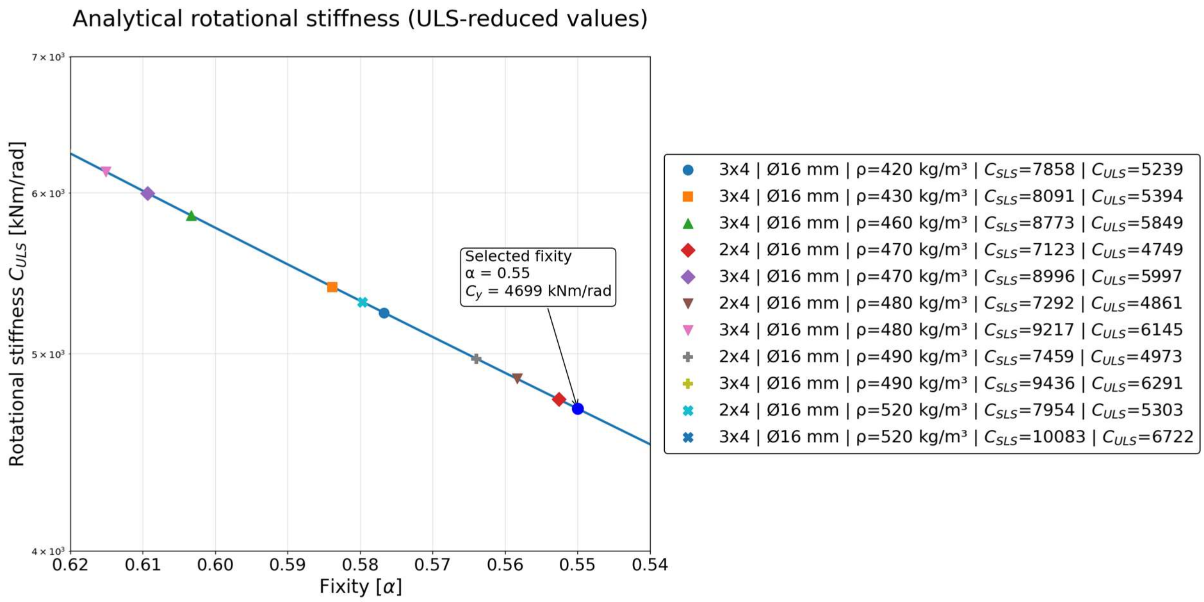
Analytical rotational stiffness (ULS-reduced values)
Rotational stiffness C_{ULS} [kNm/rad]
Fixity [α]
Selected fixity
α = 0.55
C_y = 4699 kNm/rad
3x4 | Ø16 mm | ρ=420 kg/m³ | C_{SLS}=7858 | C_{ULS}=5239
3x4 | Ø16 mm | ρ=430 kg/m³ | C_{SLS}=8091 | C_{ULS}=5394
3x4 | Ø16 mm | ρ=460 kg/m³ | C_{SLS}=8773 | C_{ULS}=5849
2x4 | Ø16 mm | ρ=470 kg/m³ | C_{SLS}=7123 | C_{ULS}=4749
3x4 | Ø16 mm | ρ=470 kg/m³ | C_{SLS}=8996 | C_{ULS}=5997
2x4 | Ø16 mm | ρ=480 kg/m³ | C_{SLS}=7292 | C_{ULS}=4861
3x4 | Ø16 mm | ρ=480 kg/m³ | C_{SLS}=9217 | C_{ULS}=6145
2x4 | Ø16 mm | ρ=490 kg/m³ | C_{SLS}=7459 | C_{ULS}=4973
3x4 | Ø16 mm | ρ=490 kg/m³ | C_{SLS}=9436 | C_{ULS}=6291
2x4 | Ø16 mm | ρ=520 kg/m³ | C_{SLS}=7954 | C_{ULS}=5303
3x4 | Ø16 mm | ρ=520 kg/m³ | C_{SLS}=10083 | C_{ULS}=6722

Fixed Middle beam results per load case Fixity factor 0.4 0.7 1.0

CO1

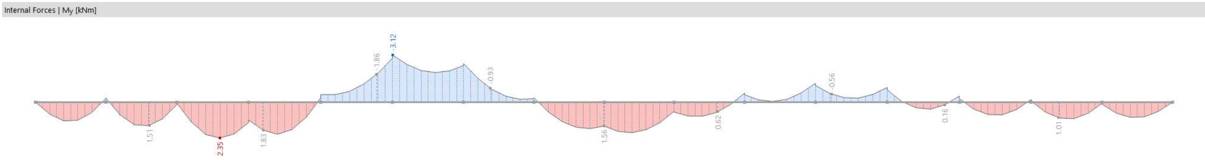

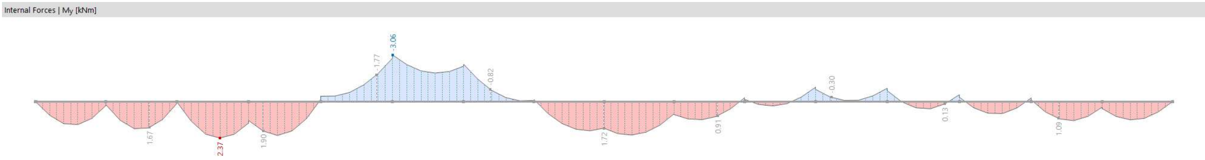

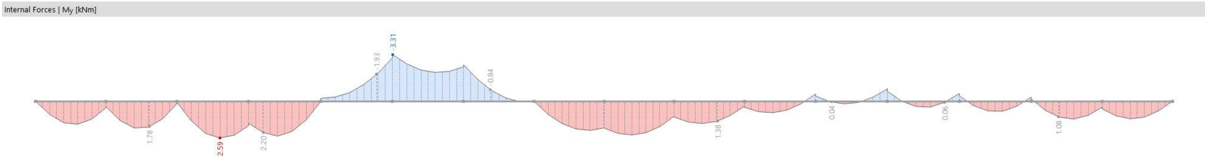

CO2

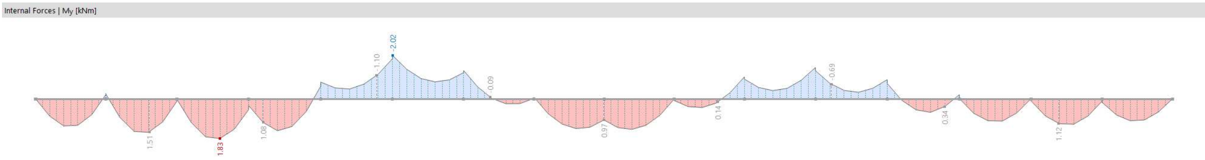

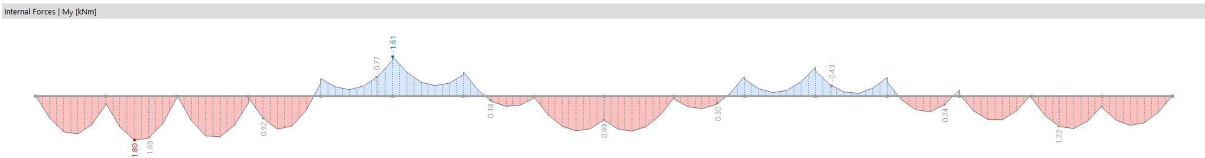

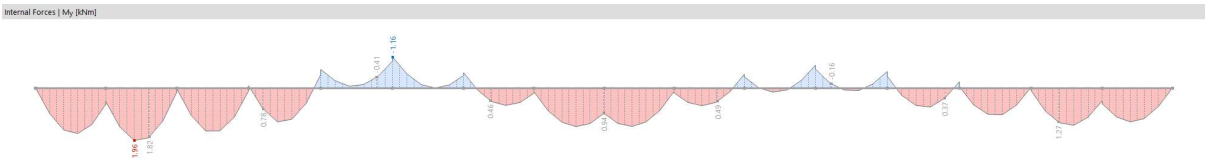

CO3

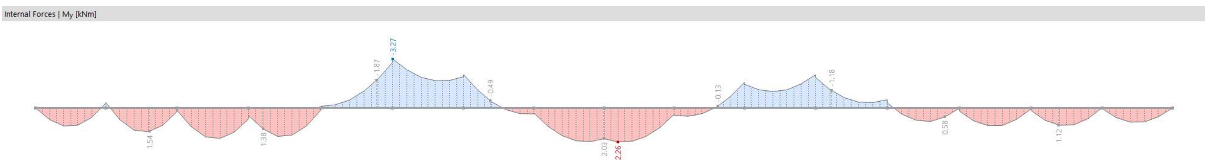

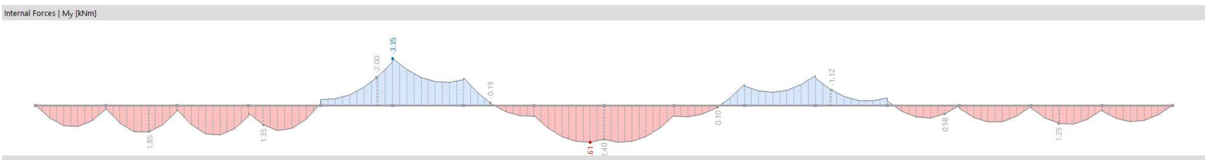

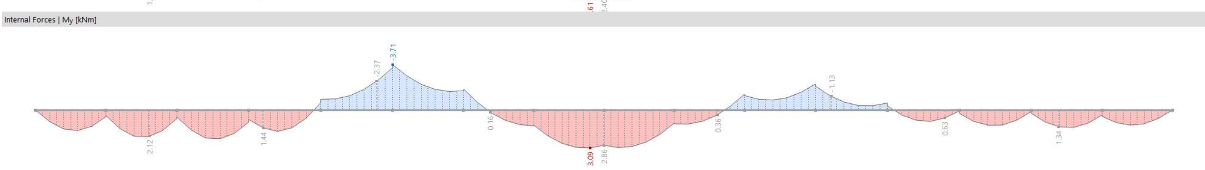

CO4

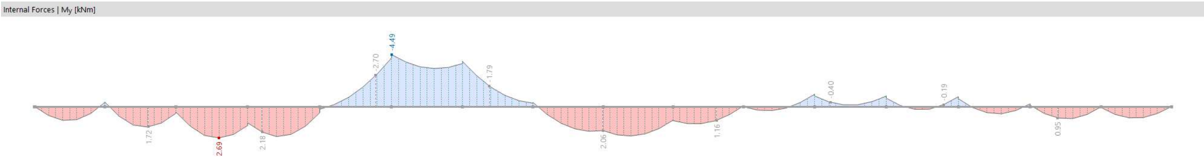

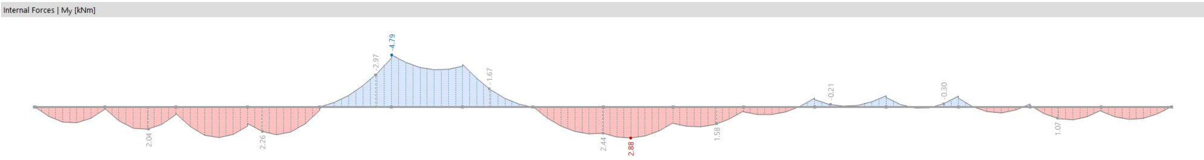

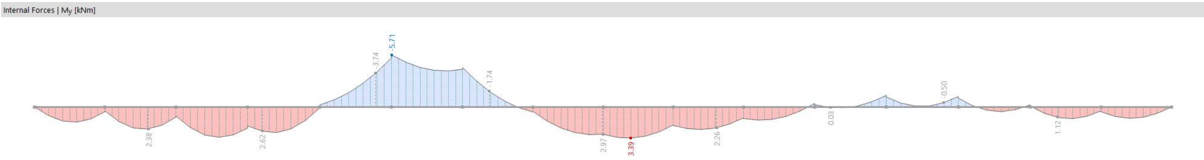

CO5

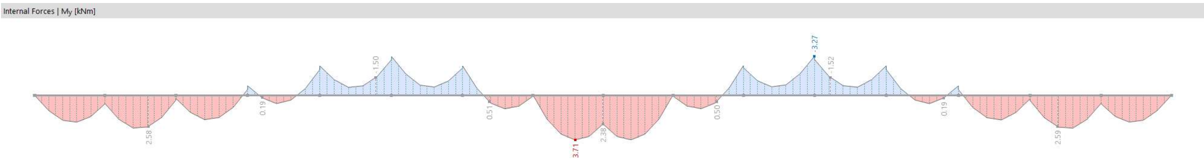

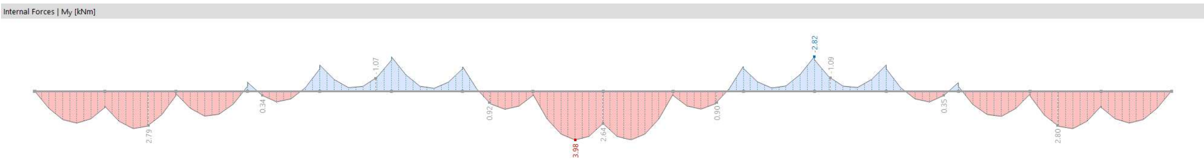

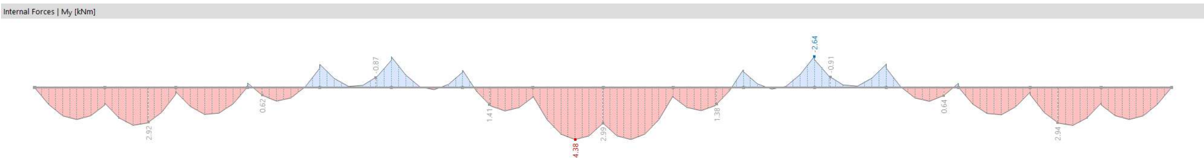

CO6 1.0, 0.7, 0.4

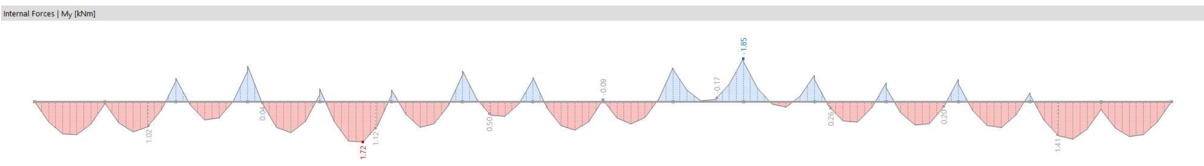

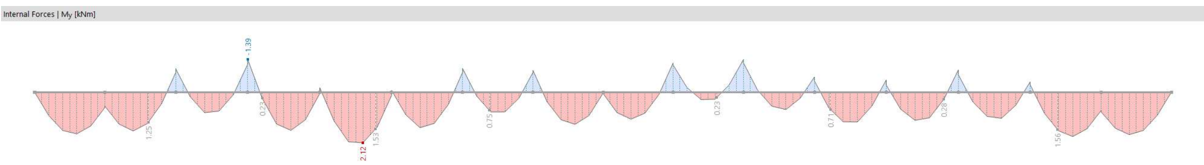

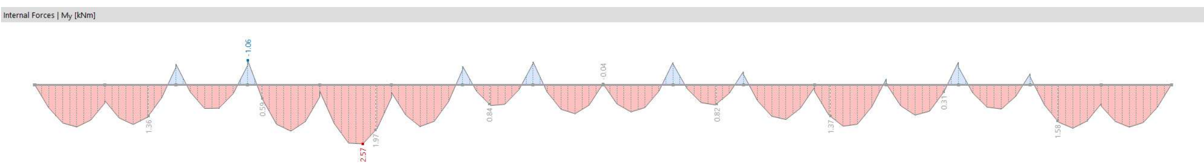

CO7

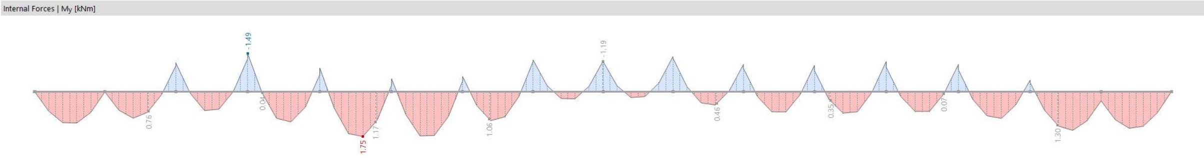
Internal Forces | My [kNm]

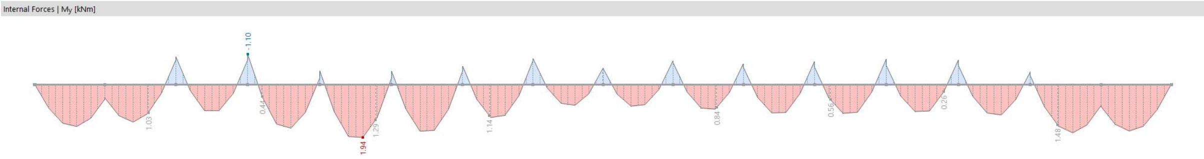
Internal Forces | My [kNm]

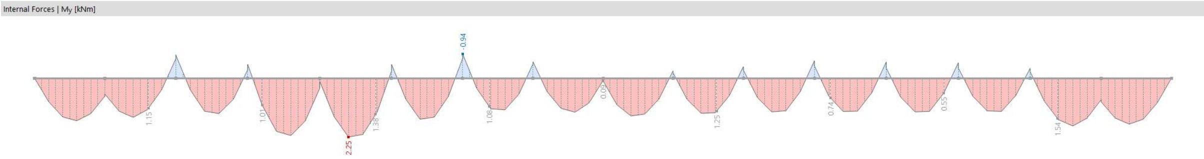
Internal Forces | My [kNm]

CO8

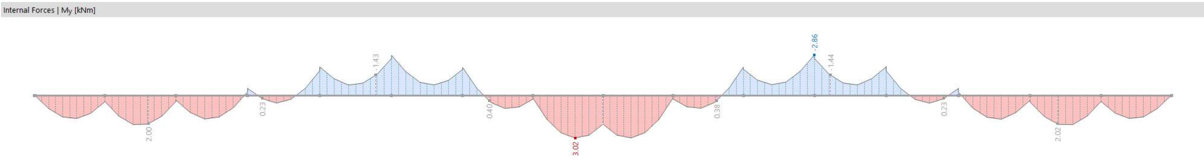
Internal Forces | My [kNm]

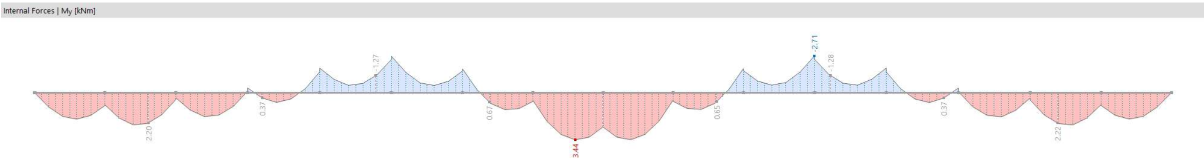
Internal Forces | My [kNm]

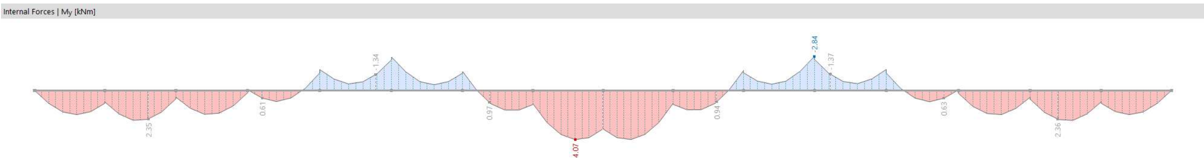
Internal Forces | My [kNm]

7. Case Study: C30 Stability Analysis

Unbraced Minimal in-plane stiffness

Mode 1 Load Combination	Linear elastic Eigenvalue Critical Load Factor	Non-linear 2nd Order Critical load factor	Non-linear Large Displ Critical load factor
ULS Wind Parallel	2.499	1.929	2.100
ULS Wind Diagonal	2.930	2.902	3.100
ULS Wind C Parallel	2.096	2.005	2.100
ULS Wind C Diagonal	2.108	2.018	2.137
ULS Snow Equally	1.168	1.159	1.325
ULS Snow Parallel Pyramid	1.375	1.274	1.400
ULS Snow Diagonal Pyramid	1.386	1.372	1.507
ULS Snow Quad Pyramid	1.372	1.307	1.400

$320 \times 160, 3 \times 4\ 20\ mm, C_{yy} = 4165\ kNm/rad\ , C_{zz} = 14\ kNm/rad, E_{0.05} = 7400$ Standard shape

Mode 1 Load Combination	Linear elastic Eigenvalue Critical Load Factor	Non-linear 2nd Order Critical load factor	Non-linear Large Displ Critical load factor
ULS Wind Parallel	2.435	1.875	2.000
ULS Wind Diagonal	2.854	2.812	3.000
ULS Wind C Parallel	2.048	1.934	2.000
ULS Wind C Diagonal	2.059	1.952	2.000
ULS Snow Equally	1.140	1.125	1.289
ULS Snow Parallel Pyramid	1.339	1.232	1.300
ULS Snow Diagonal Pyramid	1.353	1.331	1.462
ULS Snow Quad Pyramid	1.341	1.270	1.400

$320 \times 160, 3 \times 4\ 20\ mm, C_{yy} = 4165\ kNm/rad\ , C_{zz} = 14\ kNm/rad, E_{0.05} = 7400$ Symmetric Imperfection

Mode 1 Load Combination	Linear elastic Eigenvalue Critical Load Factor	Non-linear 2nd Order Critical load factor	Non-linear Large Displ Critical load factor
ULS Wind Parallel	2.598	1.873	1.900
ULS Wind Diagonal	2.986	2.770	2.800
ULS Wind C Parallel	2.128	1.809	1.900
ULS Wind C Diagonal	2.147	1.833	1.900
ULS Snow Equally	1.194	1.201	1.225
ULS Snow Parallel Pyramid	1.413	1.216	1.200
ULS Snow Diagonal Pyramid	1.418	1.297	1.300
ULS Snow Quad Pyramid	1.392	1.466	1.540

$320 \times 160, 3 \times 4\ 20\ mm, C_{yy} = 4165\ kNm/rad\ , C_{zz} = 14\ kNm/rad, E_{0.05} = 7400$ Asymmetric Imperfection

Mode 1 Load Combination	Linear elastic Eigenvalue Critical Load Factor	Non-linear 2nd Order Critical load factor	Non-linear Large Displ Critical load factor
ULS Wind Parallel	2.495	2.038	2.300
ULS Wind Diagonal	2.981	2.753	2.800
ULS Wind C Parallel	2.141	2.090	2.200
ULS Wind C Diagonal	2.147	1.828	1.900
ULS Snow Equally	1.191	1.173	1.200
ULS Snow Parallel Pyramid	1.395	1.430	1.400
ULS Snow Diagonal Pyramid	1.414	1.285	1.300
ULS Snow Quad Pyramid	1.411	1.318	1.300

$320 \times 160, 3 \times 4\ 20\ mm, C_{yy} = 4165\ kNm/rad\ , C_{zz} = 14\ kNm/rad, E_{0.05} = 7400$ Inverse Asymmetric

Unbraced Minimal in-plane stiffness

Mode 1 Load Combination	Linear elastic Eigenvalue Critical Load Factor	2^{nd} Order Eigenvalue Critical load factor	Large Displ Eigenvalue Critical load factor
ULS Wind Parallel	2.499	2.340	2.472
ULS Wind Diagonal	2.930	2.903	3.311
ULS Wind C Parallel	2.096	2.035	2.215
ULS Wind C Diagonal	2.108	2.038	2.178
ULS Snow Equally	1.168	1.160	1.368
ULS Snow Parallel Pyramid	1.375	1.349	1.455
ULS Snow Diagonal Pyramid	1.386	1.374	1.540
ULS Snow Quad Pyramid	1.372	1.373	1.745

$320 \times 160, 3 \times 4\ 20\ mm, C_{yy} =\ 4165\ kNm/rad\ , C_{zz}\ = 14\ kNm/rad, E_{0.05} = 7400$ Standard shape

Mode 1 Load Combination	Linear elastic Eigenvalue Critical Load Factor	2^{nd} Order Eigenvalue Critical load factor	Large Displ Eigenvalue Critical load factor
ULS Wind Parallel	2.435	2.271	2.520
ULS Wind Diagonal	2.854	2.814	3.215
ULS Wind C Parallel	2.048	1.972	2.123
ULS Wind C Diagonal	2.059	1.975	2.232
ULS Snow Equally	1.140	1.126	1.317
ULS Snow Parallel Pyramid	1.339	1.308	1.527
ULS Snow Diagonal Pyramid	1.353	1.333	1.493
ULS Snow Quad Pyramid	1.341	1.331	1.699

$320 \times 160, 3 \times 4\ 20\ mm, C_{yy} =\ 4165\ kNm/rad\ , C_{zz}\ = 14\ kNm/rad, E_{0.05} = 7400$ Symmetric Imperfection

Mode 1 Load Combination	Linear elastic Eigenvalue Critical Load Factor	2^{nd} Order Eigenvalue Critical load factor	Large Displ Eigenvalue Critical load factor
ULS Wind Parallel	2.598	2.459	2.518
ULS Wind Diagonal	2.986	3.048	3.192
ULS Wind C Parallel	2.128	2.064	2.099
ULS Wind C Diagonal	2.147	2.095	2.232
ULS Snow Equally	1.194	1.301	1.299
ULS Snow Parallel Pyramid	1.413	1.417	1.586
ULS Snow Diagonal Pyramid	1.418	1.311	1.654
ULS Snow Quad Pyramid	1.392	1.510	1.634

$320 \times 160, 3 \times 4\ 20\ mm, C_{yy} =\ 4165\ kNm/rad\ , C_{zz}\ = 14\ kNm/rad, E_{0.05} = 7400$ Asymmetric Imperfection

Mode 1 Load Combination	Linear elastic Eigenvalue Critical Load Factor	2^{nd} Order Eigenvalue Critical load factor	Large Displ Eigenvalue Critical load factor
ULS Wind Parallel	2.495	2.296	2.545
ULS Wind Diagonal	2.981	3.036	3.079
ULS Wind C Parallel	2.141	2.263	2.505
ULS Wind C Diagonal	2.147	2.096	2.195
ULS Snow Equally	1.191	1.279	1.347
ULS Snow Parallel Pyramid	1.395	1.484	1.683
ULS Snow Diagonal Pyramid	1.414	1.439	1.626
ULS Snow Quad Pyramid	1.411	1.513	1.732

$320 \times 160, 3 \times 4\ 20\ mm, C_{yy} =\ 4165\ kNm/rad\ , C_{zz}\ = 14\ kNm/rad, E_{0.05} = 7400$ Inverse Asymmetric

LINEAR ANALYSIS

Load Combination	Mode 1 Eigenvalue Critical Load Factor
ULS Wind Parallel	2.499
ULS Wind Diagonal	2.930
ULS Wind C Parallel	2.096
ULS Wind C Diagonal	2.108
ULS Snow Equally	1.168
ULS Snow Parallel Pyramid	1.375
ULS Snow Diagonal Pyramid	1.386
ULS Snow Quad Pyramid	1.372

$320 \times 160, 3 \times 4\ 20\ mm, C_{yy} = 4165\ kNm/rad\ , C_{zz} = 14\ kNm/rad, E_{0.05} = 7400$ Normal Shape Linear elastic Eigenvalue analysis

Load Combination	Mode 1 Eigenvalue Critical Load Factor
ULS Wind Parallel	2.435
ULS Wind Diagonal	2.854
ULS Wind C Parallel	2.048
ULS Wind C Diagonal	2.059
ULS Snow Equally	1.140
ULS Snow Parallel Pyramid	1.339
ULS Snow Diagonal Pyramid	1.353
ULS Snow Quad Pyramid	1.341

$320 \times 160, 3 \times 4\ 20\ mm, C_{yy} = 4165\ kNm/rad\ , C_{zz} = 14\ kNm/rad, E_{0.05} = 7400$ Symmetric Imperfection Linear elastic Eigenvalue analysis

Load Combination	Mode 1 Eigenvalue Critical Load Factor
ULS Wind Parallel	2.598
ULS Wind Diagonal	2.986
ULS Wind C Parallel	2.128
ULS Wind C Diagonal	2.147
ULS Snow Equally	1.194
ULS Snow Parallel Pyramid	1.413
ULS Snow Diagonal Pyramid	1.418
ULS Snow Quad Pyramid	1.392

$320 \times 160, 3 \times 4\ 20\ mm, C_{yy} = 4165\ kNm/rad\ , C_{zz} = 14\ kNm/rad, E_{0.05} = 7400$ Asymmetric Imperfection Linear elastic Eigenvalue analysis

Load Combination	Mode 1 Eigenvalue Critical Load Factor
ULS Wind Parallel	2.495
ULS Wind Diagonal	2.981
ULS Wind C Parallel	2.141
ULS Wind C Diagonal	2.147
ULS Snow Equally	1.191
ULS Snow Parallel Pyramid	1.395
ULS Snow Diagonal Pyramid	1.414
ULS Snow Quad Pyramid	1.411

$320 \times 160, 3 \times 4\ 20\ mm, C_{yy} = 4165\ kNm/rad\ , C_{zz} = 14\ kNm/rad, E_{0.05} = 7400$ Inverse Asymmetric Imperfection Linear elastic Eigenvalue analysis

2[ND] ORDER ANALYSIS

Load Combination	Mode 1 Eigenvalue Critical Load Factor	Mode 1 Non-linear Critical load factor
ULS Wind Parallel	2.340	1.929
ULS Wind Diagonal	2.903	2.902
ULS Wind C Parallel	2.035	2.005
ULS Wind C Diagonal	2.038	2.018
ULS Snow Equally	1.160	1.159
ULS Snow Parallel Pyramid	1.349	1.274
ULS Snow Diagonal Pyramid	1.374	1.372
ULS Snow Quad Pyramid	1.373	1.307

$320 \times 160, 3 \times 4\ 20\ mm, C_{yy} =\ 4165\ kNm/rad\ , C_{zz}\ = 14\ kNm/rad, E_{0.05} = 7400$ 2[nd] Order Incremental method with eigenvalue and nonlinear stability analysis

Load Combination	Mode 1 Eigenvalue Critical Load Factor	Mode 1 Non-linear Critical load factor
ULS Wind Parallel	2.271	1.875
ULS Wind Diagonal	2.814	2.812
ULS Wind C Parallel	1.972	1.934
ULS Wind C Diagonal	1.975	1.952
ULS Snow Equally	1.126	1.125
ULS Snow Parallel Pyramid	1.308	1.232
ULS Snow Diagonal Pyramid	1.333	1.331
ULS Snow Quad Pyramid	1.331	1.270

$320 \times 160, 3 \times 4\ 20\ mm, C_{yy} =\ 4165\ kNm/rad\ , C_{zz}\ = 14\ kNm/rad, E_{0.05} = 7400$ Symmetric Imperfection 7400 Incremental method with eigenvalue and nonlinear stability analysis (Lanczos) 2[nd] Order

Load Combination	Mode 1 Eigenvalue Critical Load Factor	Mode 1 Non-linear Critical load factor
ULS Wind Parallel	2.459	1.873
ULS Wind Diagonal	3.048	2.770
ULS Wind C Parallel	2.064	1.809
ULS Wind C Diagonal	2.095	1.833
ULS Snow Equally	1.301	1.201
ULS Snow Parallel Pyramid	1.417	1.216
ULS Snow Diagonal Pyramid	1.311	1.297
ULS Snow Quad Pyramid	1.510	1.466

$320 \times 160, 3 \times 4\ 20\ mm, C_{yy} =\ 4165\ kNm/rad\ , C_{zz}\ = 14\ kNm/rad, E_{0.05} = 7400$ Asymmetric Imperfection 7400 Incremental method with eigenvalue and nonlinear stability analysis (Lanczos) 2[nd] Order

CO5 CO7 CO8 convergence errors

Load Combination	Mode 1 Eigenvalue Critical Load Factor	Mode 1 Non-linear Critical load factor
ULS Wind Parallel	2.296	2.038
ULS Wind Diagonal	3.036	2.753
ULS Wind C Parallel	2.263	2.090
ULS Wind C Diagonal	2.096	1.828
ULS Snow Equally	1.279	1.173
ULS Snow Parallel Pyramid	1.484	1.430
ULS Snow Diagonal Pyramid	1.439	1.285
ULS Snow Quad Pyramid	1.513	1.318

$320 \times 160, 3 \times 4\ 20\ mm, C_{yy} =\ 4165\ kNm/rad\ , C_{zz}\ = 14\ kNm/rad, E_{0.05} = 7400$ Inverse Asymmetric Imperfection 7400 Incremental method with eigenvalue and nonlinear stability analysis (Lanczos) 2[nd] Order

CO3 CO6 convergence errors

LARGE DISPLACEMENTS

Load Combination	Mode 1 Eigenvalue Critical Load Factor	Mode 1 Non-linear Critical load factor
ULS Wind Parallel	2.472	2.100
ULS Wind Diagonal	3.311	3.100
ULS Wind C Parallel	2.215	2.100
ULS Wind C Diagonal	2.178	2.137
ULS Snow Equally	1.368	1.325
ULS Snow Parallel Pyramid	1.455	1.400
ULS Snow Diagonal Pyramid	1.540	1.507
ULS Snow Quad Pyramid	1.745	1.400

$320 \times 160, 3 \times 4\ 20\ mm, C_{yy} =\ 4165\ kNm/rad\ , C_{zz}\ = 14\ kNm/rad, E_{0.05} = 7400$ Incremental method with eigenvalue and nonlinear stability analysis (Lanczos) Large displacements Load increase capped at 3000mm displacement

Load Combination	Mode 1 Eigenvalue Critical Load Factor	Mode 1 Non-linear Critical load factor
ULS Wind Parallel	2.520	2.000
ULS Wind Diagonal	3.215	3.000
ULS Wind C Parallel	2.123	2.000
ULS Wind C Diagonal	2.232	2.000
ULS Snow Equally	1.317	1.289
ULS Snow Parallel Pyramid	1.527	1.300
ULS Snow Diagonal Pyramid	1.493	1.462
ULS Snow Quad Pyramid	1.699	1.400

$320 \times 160, 3 \times 4\ 20\ mm, C_{yy} =\ 4165\ kNm/rad\ , C_{zz}\ = 14\ kNm/rad, E_{0.05} = 7400$ Symmetric Imperfection Incremental method with eigenvalue and nonlinear stability analysis (Lanczos) Large displacements Load increase capped at 3000mm displacement

Load Combination	Mode 1 Eigenvalue Critical Load Factor	Mode 1 Non-linear Critical load factor
ULS Wind Parallel	2.518	1.900
ULS Wind Diagonal	3.192	2.800
ULS Wind C Parallel	2.099	1.900
ULS Wind C Diagonal	2.232	1.900
ULS Snow Equally	1.299	1.225
ULS Snow Parallel Pyramid	1.586	1.200
ULS Snow Diagonal Pyramid	1.654	1.300
ULS Snow Quad Pyramid	1.634	1.540

$320 \times 160, 3 \times 4\ 20\ mm, C_{yy} =\ 4165\ kNm/rad\ , C_{zz}\ = 14\ kNm/rad, E_{0.05} = 7400$ Asymmetric Imperfection Incremental method with eigenvalue and nonlinear stability analysis (Lanczos) Large displacements Load increase capped at 3000mm displacement

Load Combination	Mode 1 Eigenvalue Critical Load Factor	Mode 1 Non-linear Critical load factor
ULS Wind Parallel	2.545	2.300
ULS Wind Diagonal	3.079	2.800
ULS Wind C Parallel	2.505	2.200
ULS Wind C Diagonal	2.195	1.900
ULS Snow Equally	1.347	1.200
ULS Snow Parallel Pyramid	1.683	1.400
ULS Snow Diagonal Pyramid	1.626	1.300
ULS Snow Quad Pyramid	1.732	1.300

$320 \times 160, 3 \times 4\ 20\ mm, C_{yy} =\ 4165\ kNm/rad\ , C_{zz}\ = 14\ kNm/rad, E_{0.05} = 7400$ Inverse Asymmetric Imperfection Incremental method with eigenvalue and nonlinear stability analysis (Lanczos) Large displacements Load increase capped at 3000mm displacement

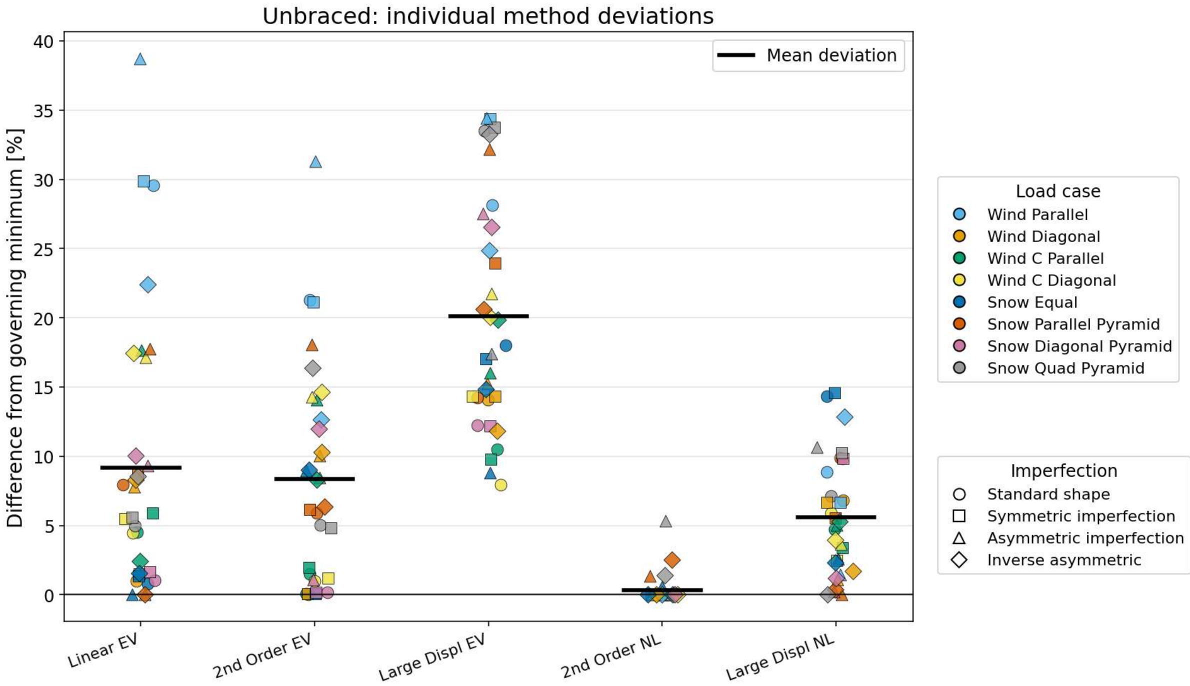
Unbraced: individual method deviations
Difference from governing minimum [%]
0
5
10
15
20
25
30
35
40
Mean deviation
Linear EV
2nd Order EV
Large Displ EV
2nd Order NL
Large Displ NL
Load case
Wind Parallel
Wind Diagonal
Wind C Parallel
Wind C Diagonal
Snow Equal
Snow Parallel Pyramid
Snow Diagonal Pyramid
Snow Quad Pyramid
Imperfection
Standard shape
Symmetric imperfection
Asymmetric imperfection
Inverse asymmetric

Diagonal bracing 30/H S235

Mode 1 Load Combination	Linear elastic Eigenvalue Critical Load Factor	Non-linear 2nd Order Critical load factor	Non-linear Large Displ Critical load factor
ULS Wind Parallel	3.460	2.270	1.818
ULS Wind Diagonal	2.884	3.704	3.632
ULS Wind C Parallel	2.065	2.435	2.219
ULS Wind C Diagonal	2.336	2.396	2.166
ULS Snow Equally	1.153	1.649	1.598
ULS Snow Parallel Pyramid	1.969	1.758	1.683
ULS Snow Diagonal Pyramid	1.367	1.911	1.876
ULS Snow Quad Pyramid	2.039	1.708	1.609

$320 \times 160, 3 \times 4\ 20\ mm, C_{yy} = 4165\ kNm/rad, C_{zz} = 1(braced)\ kNm/rad, E_{0.05} = 7400$ Standard shape

Mode 1 Load Combination	Linear elastic Eigenvalue Critical Load Factor	Non-linear 2nd Order Critical load factor	Non-linear Large Displ Critical load factor
ULS Wind Parallel	3.278	2.134	1.732
ULS Wind Diagonal	2.822	3.455	3.366
ULS Wind C Parallel	2.027	2.256	2.049
ULS Wind C Diagonal	2.253	2.245	2.032
ULS Snow Equally	1.131	1.116	1.451
ULS Snow Parallel Pyramid	1.842	1.600	1.514
ULS Snow Diagonal Pyramid	1.340	1.738	1.692
ULS Snow Quad Pyramid	1.895	1.570	1.485

$320 \times 160, 3 \times 4\ 20\ mm, C_{yy} = 4165\ kNm/rad, C_{zz} = 1(braced)\ kNm/rad, E_{0.05} = 7400$ Symmetric Imperfection

Mode 1 Load Combination	Linear elastic Eigenvalue Critical Load Factor	Non-linear 2nd Order Critical load factor	Non-linear Large Displ Critical load factor
ULS Wind Parallel	3.425	2.018	1.632
ULS Wind Diagonal	3.959	3.136	2.633
ULS Wind C Parallel	2.823	2.053	1.764
ULS Wind C Diagonal	2.640	2.057	1.731
ULS Snow Equally	1.755	1.355	1.208
ULS Snow Parallel Pyramid	2.007	1.455	1.315
ULS Snow Diagonal Pyramid	2.048	1.563	1.415
ULS Snow Quad Pyramid	1.717	1.749	1.606

$320 \times 160, 3 \times 4\ 20\ mm, C_{yy} = 4165\ kNm/rad, C_{zz} = 1(braced)\ kNm/rad, E_{0.05} = 7400$ Asymmetric Imperfection

Mode 1 Load Combination	Linear elastic Eigenvalue Critical Load Factor	Non-linear 2nd Order Critical load factor	Non-linear Large Displ Critical load factor
ULS Wind Parallel	3.385	2.572	2.071
ULS Wind Diagonal	3.961	3.128	2.918
ULS Wind C Parallel	3.000	2.294	2.178
ULS Wind C Diagonal	2.635	2.058	1.917
ULS Snow Equally	1.750	1.351	1.268
ULS Snow Parallel Pyramid	2.048	1.721	1.632
ULS Snow Diagonal Pyramid	2.042	1.557	1.467
ULS Snow Quad Pyramid	2.142	1.442	1.355

$320 \times 160, 3 \times 4\ 20\ mm, C_{yy} = 4165\ kNm/rad, C_{zz} = 1(braced)\ kNm/rad, E_{0.05} = 7400$ Inverse Asymmetric

Mode 1 Load Combination	Linear elastic Eigenvalue Critical Load Factor	2nd Order Eigenvalue Critical load factor	Large Displ Eigenvalue Critical load factor
ULS Wind Parallel	3.460	3.761	3.007
ULS Wind Diagonal	2.884	4.361	4.194
ULS Wind C Parallel	2.065	3.452	2.946
ULS Wind C Diagonal	2.336	3.519	2.924
ULS Snow Equally	1.153	2.149	1.864
ULS Snow Parallel Pyramid	1.969	2.387	2.060
ULS Snow Diagonal Pyramid	1.367	2.508	2.161
ULS Snow Quad Pyramid	2.039	2.419	1.911

$320 \times 160, 3 \times 4\ 20\ mm, C_{yy} = 4165\ kNm/rad, C_{zz} = 1(braced)\ kNm/rad, E_{0.05} = 7400$ Standard shape

Mode 1 Load Combination	Linear elastic Eigenvalue Critical Load Factor	2nd Order Eigenvalue Critical load factor	Large Displ Eigenvalue Critical load factor
ULS Wind Parallel	3.278	3.475	2.732
ULS Wind Diagonal	2.822	4.168	3.769
ULS Wind C Parallel	2.027	3.196	2.638
ULS Wind C Diagonal	2.253	3.242	2.635
ULS Snow Equally	1.131	2.022	1.669
ULS Snow Parallel Pyramid	1.842	2.232	1.825
ULS Snow Diagonal Pyramid	1.340	2.339	1.886
ULS Snow Quad Pyramid	1.895	2.321	1.748

$320 \times 160, 3 \times 4\ 20\ mm, C_{yy} = 4165\ kNm/rad, C_{zz} = 1(braced)\ kNm/rad, E_{0.05} = 7400$ Symmetric Imperfection

Mode 1 Load Combination	Linear elastic Eigenvalue Critical Load Factor	2nd Order Eigenvalue Critical load factor	Large Displ Eigenvalue Critical load factor
ULS Wind Parallel	3.425	3.415	2.514
ULS Wind Diagonal	3.959	4.110	3.973
ULS Wind C Parallel	2.823	3.136	2.502
ULS Wind C Diagonal	2.640	3.237	2.544
ULS Snow Equally	1.755	1.923	1.627
ULS Snow Parallel Pyramid	2.007	2.135	1.673
ULS Snow Diagonal Pyramid	2.048	2.272	1.809
ULS Snow Quad Pyramid	1.717	2.400	2.022

$320 \times 160, 3 \times 4\ 20\ mm, C_{yy} = 4165\ kNm/rad, C_{zz} = 1(braced)\ kNm/rad, E_{0.05} = 7400$ Asymmetric Imperfection

Mode 1 Load Combination	Linear elastic Eigenvalue Critical Load Factor	2nd Order Eigenvalue Critical load factor	Large Displ Eigenvalue Critical load factor
ULS Wind Parallel	3.385	4.077	3.547
ULS Wind Diagonal	3.961	4.101	3.294
ULS Wind C Parallel	3.000	3.316	2.478
ULS Wind C Diagonal	2.635	3.207	2.170
ULS Snow Equally	1.750	1.894	1.452
ULS Snow Parallel Pyramid	2.048	2.309	1.846
ULS Snow Diagonal Pyramid	2.042	2.247	1.592
ULS Snow Quad Pyramid	2.142	2.160	1.577

$320 \times 160, 3 \times 4\ 20\ mm, C_{yy} = 4165\ kNm/rad, C_{zz} = 1(braced)\ kNm/rad, E_{0.05} = 7400$ Inverse Asymmetric

LINEAR ANALYSIS

Load Combination	Mode 1 Eigenvalue Critical Load Factor
ULS Wind Parallel	3.460
ULS Wind Diagonal	2.884
ULS Wind C Parallel	2.065
ULS Wind C Diagonal	2.336
ULS Snow Equally	1.153
ULS Snow Parallel Pyramid	1.969
ULS Snow Diagonal Pyramid	1.367
ULS Snow Quad Pyramid	2.039

$320 \times 160, 3 \times 4\ 20\ mm, C_{yy} =\ 4165\ kNm/rad\ , C_{zz}\ = 14\ kNm/rad, E_{0.05} = 7400$ Normal Shape Linear elastic Eigenvalue analysis

Load Combination	Mode 1 Eigenvalue Critical Load Factor
ULS Wind Parallel	3.278
ULS Wind Diagonal	2.822
ULS Wind C Parallel	2.027
ULS Wind C Diagonal	2.253
ULS Snow Equally	1.131
ULS Snow Parallel Pyramid	1.842
ULS Snow Diagonal Pyramid	1.340
ULS Snow Quad Pyramid	1.895

$320 \times 160, 3 \times 4\ 20\ mm, C_{yy} =\ 4165\ kNm/rad\ , C_{zz}\ = 14\ kNm/rad, E_{0.05} = 7400$ Symmetric Imperfection Linear elastic Eigenvalue analysis

Load Combination	Mode 1 Eigenvalue Critical Load Factor
ULS Wind Parallel	3.425
ULS Wind Diagonal	3.959
ULS Wind C Parallel	2.823
ULS Wind C Diagonal	2.640
ULS Snow Equally	1.755
ULS Snow Parallel Pyramid	2.007
ULS Snow Diagonal Pyramid	2.048
ULS Snow Quad Pyramid	1.717

$320 \times 160, 3 \times 4\ 20\ mm, C_{yy} =\ 4165\ kNm/rad\ , C_{zz}\ = 14\ kNm/rad, E_{0.05} = 7400$ Asymmetric Imperfection Linear elastic Eigenvalue analysis

Load Combination	Mode 1 Eigenvalue Critical Load Factor
ULS Wind Parallel	3.385
ULS Wind Diagonal	3.961
ULS Wind C Parallel	3.000
ULS Wind C Diagonal	2.635
ULS Snow Equally	1.750
ULS Snow Parallel Pyramid	2.048
ULS Snow Diagonal Pyramid	2.042
ULS Snow Quad Pyramid	2.142

$320 \times 160, 3 \times 4\ 20\ mm, C_{yy} =\ 4165\ kNm/rad\ , C_{zz}\ = 14\ kNm/rad, E_{0.05} = 7400$ Inverse Asymmetric Imperfection Linear elastic Eigenvalue analysis

2ND ORDER ANALYSIS

Load Combination	Mode 1 Eigenvalue Critical Load Factor	Mode 1 Non-linear Critical load factor
ULS Wind Parallel	3.761	2.270
ULS Wind Diagonal	4.361	3.704
ULS Wind C Parallel	3.452	2.435
ULS Wind C Diagonal	3.519	2.396
ULS Snow Equally	2.149	1.649
ULS Snow Parallel Pyramid	2.387	1.758
ULS Snow Diagonal Pyramid	2.508	1.911
ULS Snow Quad Pyramid	2.419	1.708

$320 \times 160, 3 \times 4\ 20\ mm, C_{yy} =\ 4165\ kNm/rad\ , C_{zz}\ = 14\ kNm/rad, E_{0.05} = 7400$ 2nd Order Incremental method with eigenvalue and nonlinear stability analysis

Load Combination	Mode 1 Eigenvalue Critical Load Factor	Mode 1 Non-linear Critical load factor
ULS Wind Parallel	3.475	2.134
ULS Wind Diagonal	4.168	3.455
ULS Wind C Parallel	3.196	2.256
ULS Wind C Diagonal	3.242	2.245
ULS Snow Equally	2.022	1.116
ULS Snow Parallel Pyramid	2.232	1.600
ULS Snow Diagonal Pyramid	2.339	1.738
ULS Snow Quad Pyramid	2.321	1.570

$320 \times 160, 3 \times 4\ 20\ mm, C_{yy} =\ 4165\ kNm/rad\ , C_{zz}\ = 14\ kNm/rad, E_{0.05} = 7400$ Symmetric Imperfection 7400 Incremental method with eigenvalue and nonlinear stability analysis (Lanczos) 2nd Order

Load Combination	Mode 1 Eigenvalue Critical Load Factor	Mode 1 Non-linear Critical load factor
ULS Wind Parallel	3.415	2.018
ULS Wind Diagonal	4.110	3.136
ULS Wind C Parallel	3.136	2.053
ULS Wind C Diagonal	3.237	2.057
ULS Snow Equally	1.923	1.355
ULS Snow Parallel Pyramid	2.135	1.455
ULS Snow Diagonal Pyramid	2.272	1.563
ULS Snow Quad Pyramid	2.400	1.749

$320 \times 160, 3 \times 4\ 20\ mm, C_{yy} =\ 4165\ kNm/rad\ , C_{zz}\ = 14\ kNm/rad, E_{0.05} = 7400$ Asymmetric Imperfection 7400 Incremental method with eigenvalue and nonlinear stability analysis (Lanczos) 2nd Order

Load Combination	Mode 1 Eigenvalue Critical Load Factor	Mode 1 Non-linear Critical load factor
ULS Wind Parallel	4.077	2.572
ULS Wind Diagonal	4.101	3.128
ULS Wind C Parallel	3.316	2.294
ULS Wind C Diagonal	3.207	2.058
ULS Snow Equally	1.894	1.351
ULS Snow Parallel Pyramid	2.309	1.721
ULS Snow Diagonal Pyramid	2.247	1.557
ULS Snow Quad Pyramid	2.160	1.442

$320 \times 160, 3 \times 4\ 20\ mm, C_{yy} =\ 4165\ kNm/rad\ , C_{zz}\ = 14\ kNm/rad, E_{0.05} = 7400$ Inverse Asymmetric Imperfection 7400 Incremental method with eigenvalue and nonlinear stability analysis (Lanczos) 2nd Order

LARGE DISPLACEMENTS

Load Combination	Mode 1 Eigenvalue Critical Load Factor	Mode 1 Non-linear Critical load factor
ULS Wind Parallel	3.007	1.818
ULS Wind Diagonal	4.194	3.632
ULS Wind C Parallel	2.946	2.219
ULS Wind C Diagonal	2.924	2.166
ULS Snow Equally	1.864	1.598
ULS Snow Parallel Pyramid	2.060	1.683
ULS Snow Diagonal Pyramid	2.161	1.876
ULS Snow Quad Pyramid	1.911	1.609

$320 \times 160, 3 \times 4\ 20\ mm, C_{yy} =\ 4165\ kNm/rad\ , C_{zz}\ = 14\ kNm/rad, E_{0.05} = 7400$ Incremental method with eigenvalue and nonlinear stability analysis (Lanczos) Large displacements Load increase capped at 3000mm displacement

Load Combination	Mode 1 Eigenvalue Critical Load Factor	Mode 1 Non-linear Critical load factor
ULS Wind Parallel	2.732	1.732
ULS Wind Diagonal	3.769	3.366
ULS Wind C Parallel	2.638	2.049
ULS Wind C Diagonal	2.635	2.032
ULS Snow Equally	1.669	1.451
ULS Snow Parallel Pyramid	1.825	1.514
ULS Snow Diagonal Pyramid	1.886	1.692
ULS Snow Quad Pyramid	1.748	1.485

$320 \times 160, 3 \times 4\ 20\ mm, C_{yy} =\ 4165\ kNm/rad\ , C_{zz}\ = 14\ kNm/rad, E_{0.05} = 7400$ Symmetric Imperfection Incremental method with eigenvalue and nonlinear stability analysis (Lanczos) Large displacements Load increase capped at 3000mm displacement

Load Combination	Mode 1 Eigenvalue Critical Load Factor	Mode 1 Non-linear Critical load factor
ULS Wind Parallel	2.514	1.632
ULS Wind Diagonal	3.973	2.633
ULS Wind C Parallel	2.502	1.764
ULS Wind C Diagonal	2.544	1.731
ULS Snow Equally	1.627	1.208
ULS Snow Parallel Pyramid	1.673	1.315
ULS Snow Diagonal Pyramid	1.809	1.415
ULS Snow Quad Pyramid	2.022	1.606

$320 \times 160, 3 \times 4\ 20\ mm, C_{yy} =\ 4165\ kNm/rad\ , C_{zz}\ = 14\ kNm/rad, E_{0.05} = 7400$ Asymmetric Imperfection Incremental method with eigenvalue and nonlinear stability analysis (Lanczos) Large displacements Load increase capped at 3000mm displacement

Load Combination	Mode 1 Eigenvalue Critical Load Factor	Mode 1 Non-linear Critical load factor
ULS Wind Parallel	3.547	2.071
ULS Wind Diagonal	3.294	2.918
ULS Wind C Parallel	2.478	2.178
ULS Wind C Diagonal	2.170	1.917
ULS Snow Equally	1.452	1.268
ULS Snow Parallel Pyramid	1.846	1.632
ULS Snow Diagonal Pyramid	1.592	1.467
ULS Snow Quad Pyramid	1.577	1.355

$320 \times 160, 3 \times 4\ 20\ mm, C_{yy} =\ 4165\ kNm/rad\ , C_{zz}\ = 14\ kNm/rad, E_{0.05} = 7400$ Inverse Asymmetric Imperfection Incremental method with eigenvalue and nonlinear stability analysis (Lanczos) Large displacements Load increase capped at 3000mm displacement

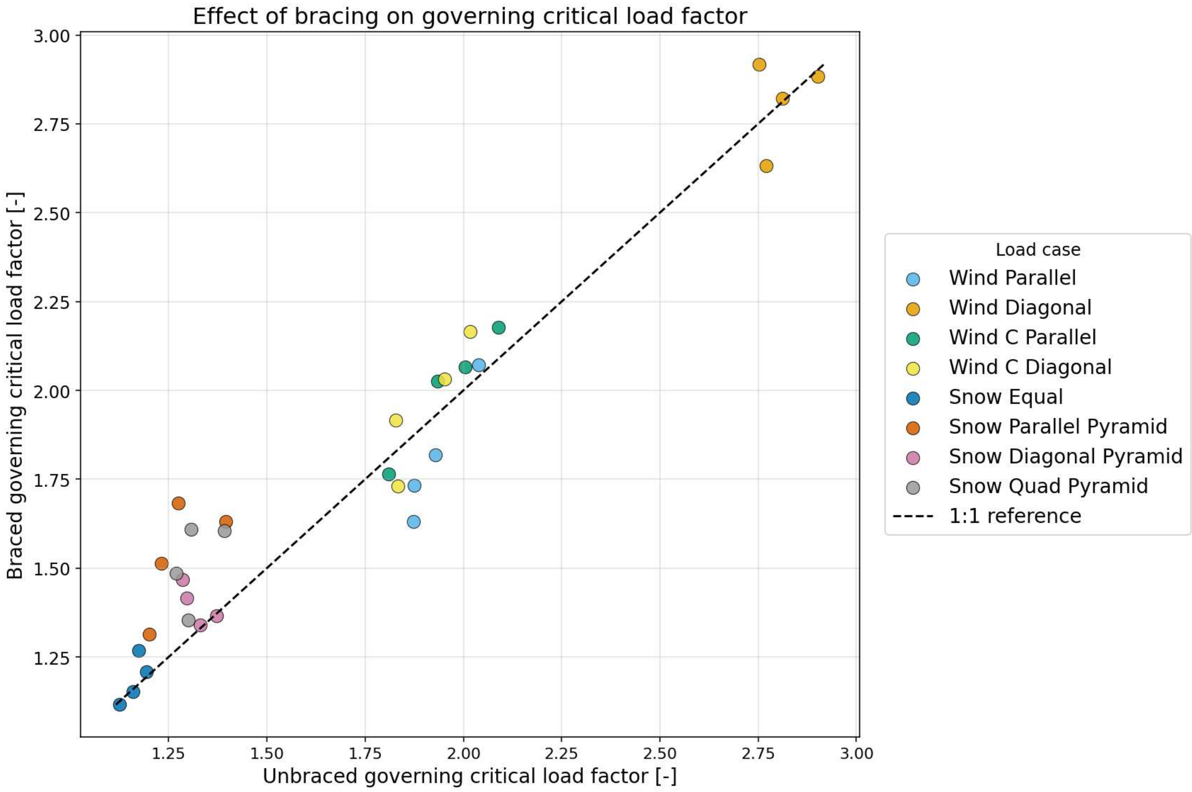
Effect of bracing on governing critical load factor
Braced governing critical load factor [-]
Unbraced governing critical load factor [-]
3.00
2.75
2.50
2.25
2.00
1.75
1.50
1.25
Load case
Wind Parallel
Wind Diagonal
Wind C Parallel
Wind C Diagonal
Snow Equal
Snow Parallel Pyramid
Snow Diagonal Pyramid
Snow Quad Pyramid
1:1 reference

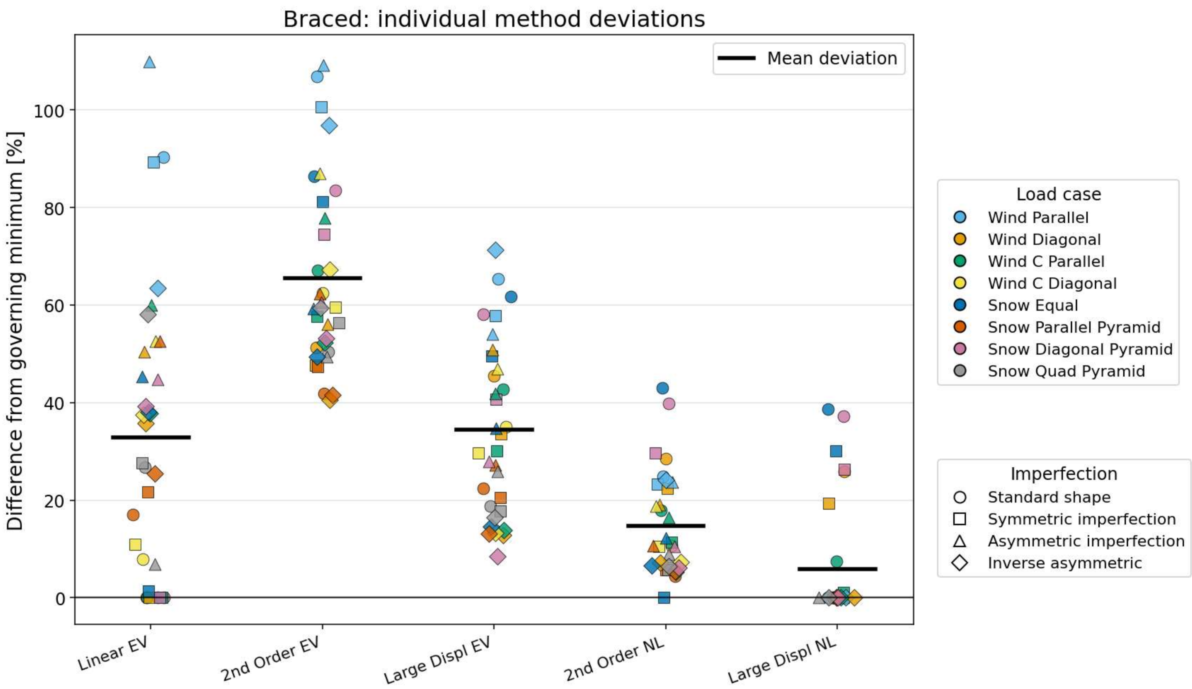
Braced: individual method deviations
Mean deviation
Difference from governing minimum [%]
100
80
60
40
20
0
Linear EV
2nd Order EV
Large Displ EV
2nd Order NL
Large Displ NL
Load case
Wind Parallel
Wind Diagonal
Wind C Parallel
Wind C Diagonal
Snow Equal
Snow Parallel Pyramid
Snow Diagonal Pyramid
Snow Quad Pyramid
Imperfection
Standard shape
Symmetric imperfection
Asymmetric imperfection
Inverse asymmetric

In plane stiffness effects for larger profile sizes second order analysis

Load Combination	Mode 1 Critical Load Factor	Mode 1 Non-linear Critical load factor
ULS Wind Parallel	2.516	1.830
ULS Wind Diagonal	3.161	2.760
ULS Wind C Parallel	2.174	1.830
ULS Wind C Diagonal	2.213	1.840
ULS Snow Equally	1.291	1.130
ULS Snow Parallel Pyramid	1.470	1.230
ULS Snow Diagonal Pyramid	1.523	1.310
ULS Snow Quad Pyramid	1.532	1.430

$320 \times 160, 3 \times 4\ 20\ mm, C_{yy} = 4165\ kNm/rad, C_{zz} = \infty, E_{0.05} = 7400$ Asymmetric Imperfection

Load Combination	Mode 1 Critical Load Factor	Mode 1 Non-linear Critical load factor
ULS Wind Parallel	2.476	1.840
ULS Wind Diagonal	3.109	2.750
ULS Wind C Parallel	2.131	1.820
ULS Wind C Diagonal	2.179	1.830
ULS Snow Equally	1.260	1.140
ULS Snow Parallel Pyramid	1.458	1.220
ULS Snow Diagonal Pyramid	1.495	1.300
ULS Snow Quad Pyramid	1.494	1.420

$320 \times 160, 3 \times 4\ 20\ mm, C_{yy} = 4165\ kNm/rad, C_{zz} = 2025\ kNm/rad, E_{0.05} = 7400$ Asymmetric Imperfection

Load Combination	Mode 1 Critical Load Factor	Mode 1 Non-linear Critical load factor
ULS Wind Parallel	2.481	1.860
ULS Wind Diagonal	3.044	2.750
ULS Wind C Parallel	2.058	1.800
ULS Wind C Diagonal	2.097	1.820
ULS Snow Equally	1.297	1.200
ULS Snow Parallel Pyramid	1.412	1.210
ULS Snow Diagonal Pyramid	1.442	1.290
ULS Snow Quad Pyramid	1.506	1.470

$320 \times 160, 3 \times 4\ 20\ mm, C_{yy} = 4165\ kNm/rad, C_{zz} = 1\ kNm/rad, E_{0.05} = 7400$ Asymmetric Imperfection

Load Combination	Mode 1 Critical Load Factor	Mode 1 Non-linear Critical load factor
ULS Wind Parallel	3.479	2.010
ULS Wind Diagonal	4.146	3.130
ULS Wind C Parallel	3.160	2.050
ULS Wind C Diagonal	3.282	2.050
ULS Snow Equally	1.950	1.350
ULS Snow Parallel Pyramid	2.163	1.450
ULS Snow Diagonal Pyramid	2.289	1.560
ULS Snow Quad Pyramid	2.440	1.740

$320 \times 160, 3 \times 4\ 20\ mm, C_{yy} = 4165\ kNm/rad, C_{zz} = 1\ kNm/rad(bracing), E_{0.05} = 7400$ Asymmetric Imperfection

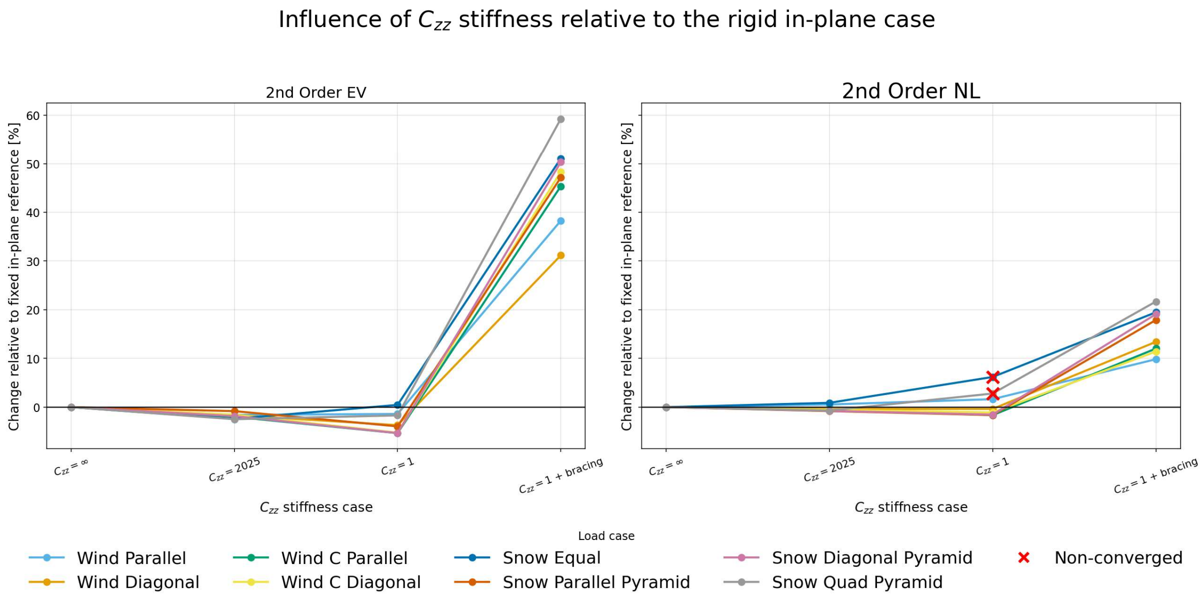

Estimation of required in plane stiffness based on the fixity factor

$$\frac{C_r l}{2EI + C_r l} = \alpha$$

$$\frac{4165 \cdot 2.475 \cdot 10^9}{2 \cdot 7400 \cdot \frac{1}{12} \cdot 160 \cdot 320^3 + 4165 \cdot 2.45 \cdot 10^9} = 0.615 = \alpha_{yy}$$

$$\frac{2025 \cdot 2.45 \cdot 10^9}{2 \cdot 7400 \cdot \frac{1}{12} \cdot 320 \cdot 160^3 + 2025 \cdot 2.475 \cdot 10^9} = 0.756 = \alpha_{zz}$$

$320 \times 160, 3 \times 4\ 20\ mm, C_{yy} = 4165\ kNm/rad\ , C_{zz} = 2025\ kNm/rad, E_{0.05} = 7400$ Asymmetric Imperfection

$$\frac{3919 \cdot 2.475 \cdot 10^9}{2 \cdot 7400 \cdot \frac{1}{12} \cdot 160 \cdot 320^3 + 3919 \cdot 2.45 \cdot 10^9} = 0.6 = \alpha_{yy}$$

$$\frac{1725 \cdot 2.45 \cdot 10^9}{2 \cdot 7400 \cdot \frac{1}{12} \cdot 320 \cdot 160^3 + 1725 \cdot 2.475 \cdot 10^9} = 0.725 = \alpha_{zz}$$

$320 \times 160, 3 \times 4\ 20\ mm, C_{yy} = 3919 \frac{kNm}{rad}, C_{zz} = 1725\ kNm/rad, E_{0.05} = 7400$ Asymmetric Imperfection

$$\frac{9351 \cdot 2.475 \cdot 10^9}{2 \cdot 7400 \cdot \frac{1}{12} \cdot 200 \cdot 400^3 + 9351 \cdot 2.475 \cdot 10^9} = 0.594 = \alpha_{yy}$$

$$\frac{2325 \cdot 2.475 \cdot 10^9}{2 \cdot 7400 \cdot \frac{1}{12} \cdot 400 \cdot 200^3 + 2325 \cdot 2.475 \cdot 10^9} = 0.593 = \alpha_{zz}$$

$400 \times 200, 4 \times 5\ 20\ mm, C_{yy} = 9351\ kNm/rad\ , C_{zz} = 2325\ kNm/rad, E_{0.05} = 7400$ Asymmetric Imperfection

$$\frac{9567 \cdot 2.475 \cdot 10^9}{2 \cdot 7400 \cdot \frac{1}{12} \cdot 200 \cdot 400^3 + 9567 \cdot 2.475 \cdot 10^9} = 0.6 = \alpha_{yy}$$

$$\frac{3100 \cdot 2.475 \cdot 10^9}{2 \cdot 7400 \cdot \frac{1}{12} \cdot 400 \cdot 200^3 + 3100 \cdot 2.475 \cdot 10^9} = 0.660 = \alpha_{zz}$$

$400 \times 200, 4 \times 5\ 20\ mm, C_{yy} = 9351\ kNm/rad, C_{zz} = 2325\ kNm/rad, E_{0.05} = 7400$ Asymmetric Imperfection

$$\frac{19850 \cdot 2.475 \cdot 10^9}{2 \cdot 7400 \cdot \frac{1}{12} \cdot 240 \cdot 480^3 + 19850 \cdot 2.475 \cdot 10^9} = 0.6 = \alpha_{yy}$$

$$\frac{6025 \cdot 2.475 \cdot 10^9}{2 \cdot 7400 \cdot \frac{1}{12} \cdot 480 \cdot 240^3 + 6025 \cdot 2.475 \cdot 10^9} = 0.646 = \alpha_{zz}$$

$480 \times 240, C_{yy} = 19850\ kNm/rad, C_{zz} = 6025\ kNm/rad, E_{0.05} = 7400$ Asymmetric Imperfection

b	h	Iyy	Izz	Out of plane Stiffness	Out of plane fixity	In-plane stiffness	In-plane fixity
160	320	4.37E+08	1.09E+08	3918.92	0.6	1725	0.725352704
200	400	1.07E+09	2.67E+08	9567.68	0.6	3100	0.660331349
240	480	2.21E+09	5.53E+08	19839.53	0.6	6025	0.645656377
280	560	4.10E+09	1.02E+09	36755.19	0.6	10500	0.631546107

Load Combination	Mode 1 Critical Load Factor	Mode 1 Non-linear Critical load factor
ULS Wind Parallel	2.476	1.840
ULS Wind Diagonal	3.109	2.750
ULS Wind C Parallel	2.131	1.820
ULS Wind C Diagonal	2.179	1.830
ULS Snow Equally	1.260	1.140
ULS Snow Parallel Pyramid	1.458	1.220
ULS Snow Diagonal Pyramid	1.495	1.300
ULS Snow Quad Pyramid	1.494	1.420

$320 \times 160, 3 \times 4\ 20\ mm, C_{yy} = 4165\ kNm/rad, C_{zz} = 2025\ kNm/rad, E_{0.05} = 7400$ Asymmetric Imperfection

Load Combination	Mode 1 Critical Load Factor	Mode 1 Non-linear Critical load factor
ULS Wind Parallel	4.199	3.170
ULS Wind Diagonal	5.039	4.520
ULS Wind C Parallel	3.620	3.120
ULS Wind C Diagonal	3.662	3.150
ULS Snow Equally	2.222	2.060
ULS Snow Parallel Pyramid	2.549	2.150
ULS Snow Diagonal Pyramid	2.587	2.290
ULS Snow Quad Pyramid	2.601	2.490

$400 \times 200, 4 \times 5\ 20\ mm, C_{yy} = 9351\ kNm/rad, C_{zz} = 2325\ kNm/rad, E_{0.05} = 7400$ Asymmetric Imperfection

Load Combination	Mode 1 Critical Load Factor	Mode 1 Non-linear Critical load factor
ULS Wind Parallel	4.199	3.170
ULS Wind Diagonal	5.039	4.520
ULS Wind C Parallel	3.620	3.120
ULS Wind C Diagonal	3.662	3.150
ULS Snow Equally	2.222	2.060
ULS Snow Parallel Pyramid	2.549	2.150
ULS Snow Diagonal Pyramid	2.587	2.290
ULS Snow Quad Pyramid	2.601	2.490

480×240 $C_{yy} = 19850\ kNm/rad$, $C_{zz} = 6025\ kNm/rad$, $E_{0.05} = 7400$ Asymmetric Imperfection

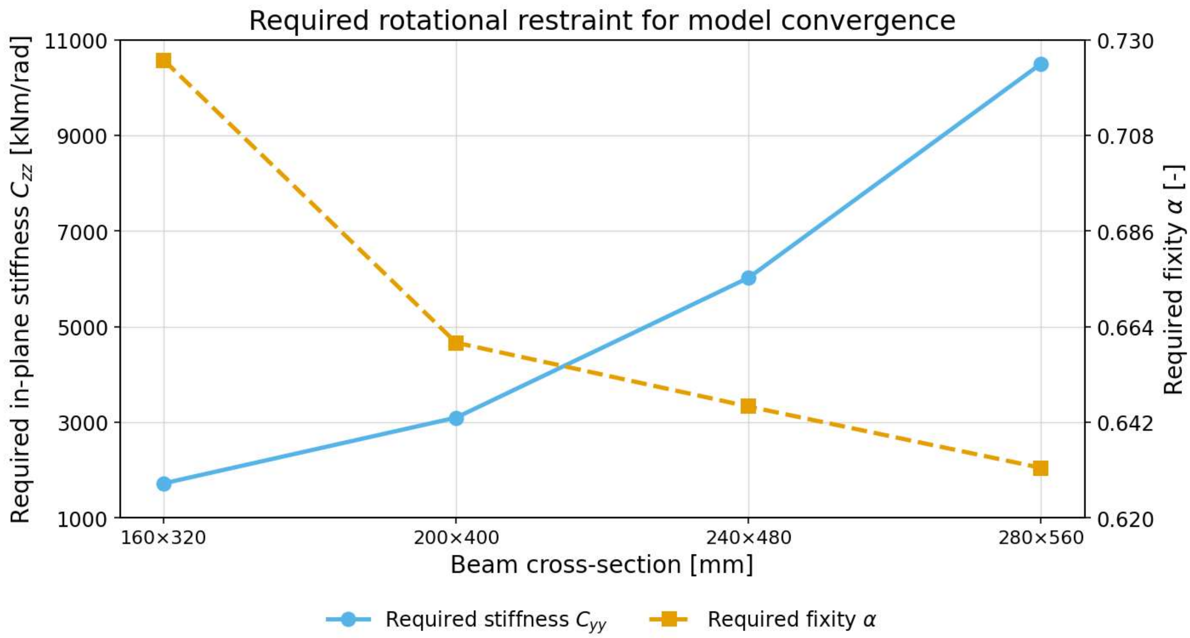

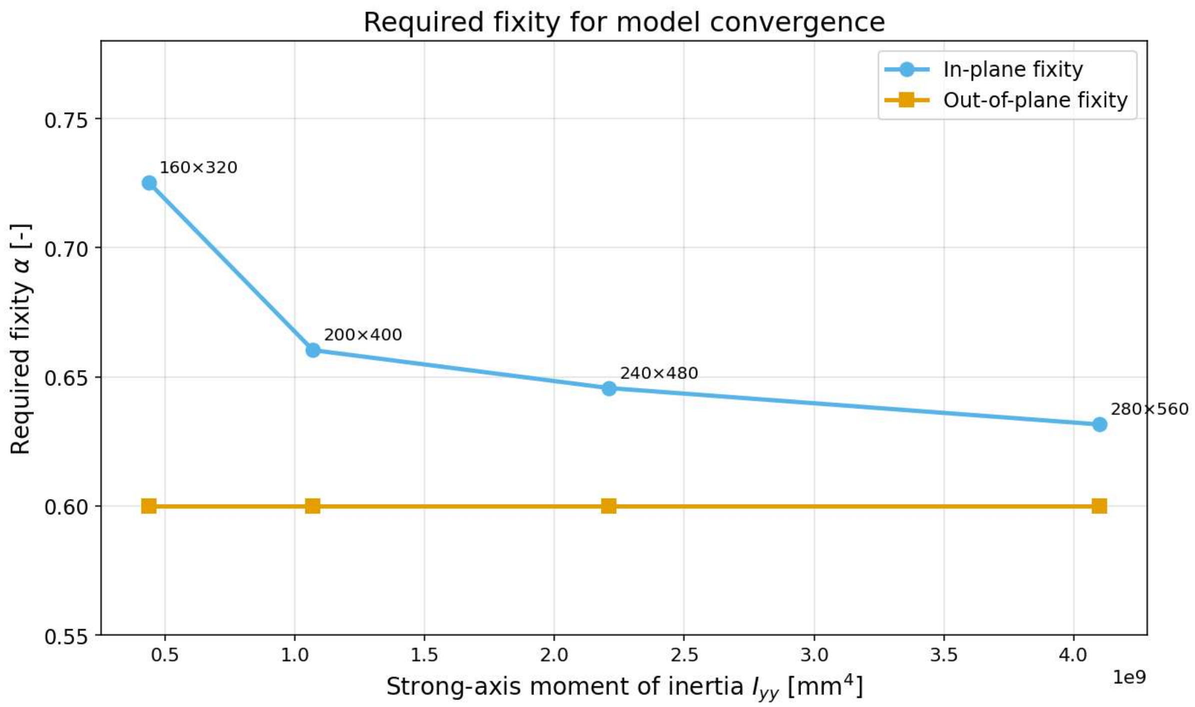

Final Design unbraced 400x200 2ND ORDER ANALYSIS

Load Combination	Mode 1 Eigenvalue Critical Load Factor	Mode 1 Non-linear Critical load factor
ULS Wind Parallel	3.959	2.322
ULS Wind Diagonal	4.764	4.763
ULS Wind C Parallel	3.491	3.450
ULS Wind C Diagonal	3.497	3.469
ULS Snow Equally	2.071	2.070
ULS Snow Parallel Pyramid	2.390	2.265
ULS Snow Diagonal Pyramid	2.429	2.427
ULS Snow Quad Pyramid	2.430	2.322

$400 \times 200, 3 \times 4\ 16\ mm, C_{yy} =\ 5964\ kNm/rad\ , C_{zz}\ = 14\ kNm/rad, E_{0.05} = 7400$ 2nd Order Incremental method with eigenvalue and nonlinear stability analysis

Load Combination	Mode 1 Eigenvalue Critical Load Factor	Mode 1 Non-linear Critical load factor
ULS Wind Parallel	3.805	3.212
ULS Wind Diagonal	4.580	4.579
ULS Wind C Parallel	3.355	3.303
ULS Wind C Diagonal	3.361	3.328
ULS Snow Equally	1.993	1.993
ULS Snow Parallel Pyramid	2.294	2.175
ULS Snow Diagonal Pyramid	2.337	2.334
ULS Snow Quad Pyramid	2.337	2.236

$400 \times 200, 3 \times 4\ 16\ mm, C_{yy} =\ 5964\ kNm/rad\ , C_{zz}\ = 14\ kNm/rad, E_{0.05} = 7400$ Symmetric Imperfection 7400 Incremental method with eigenvalue and nonlinear stability analysis (Lanczos) 2nd Order

Load Combination	Mode 1 Eigenvalue Critical Load Factor	Mode 1 Non-linear Critical load factor
ULS Wind Parallel	4.141	3.224
ULS Wind Diagonal	5.016	4.564
ULS Wind C Parallel	3.544	3.123
ULS Wind C Diagonal	3.597	3.162
ULS Snow Equally	2.297	2.120
ULS Snow Parallel Pyramid	2.503	2.158
ULS Snow Diagonal Pyramid	2.551	2.293
ULS Snow Quad Pyramid	2.686	2.600

$400 \times 200, 3 \times 4\ 16\ mm, C_{yy} =\ 5964\ kNm/rad\ , C_{zz}\ = 14\ kNm/rad, E_{0.05} = 7400$ Asymmetric Imperfection 7400 Incremental method with eigenvalue and nonlinear stability analysis (Lanczos) 2nd Order

Load Combination	Mode 1 Eigenvalue Critical Load Factor	Mode 1 Non-linear Critical load factor
ULS Wind Parallel	3.901	2.328
ULS Wind Diagonal	4.998	4.535
ULS Wind C Parallel	3.883	3.560
ULS Wind C Diagonal	3.591	3.152
ULS Snow Equally	2.274	2.087
ULS Snow Parallel Pyramid	2.617	2.510
ULS Snow Diagonal Pyramid	2.538	2.273
ULS Snow Quad Pyramid	2.662	2.328

$400 \times 200, 3 \times 4\ 16\ mm, C_{yy} =\ 5964\ kNm/rad\ , C_{zz}\ = 14\ kNm/rad, E_{0.05} = 7400$ Inverse Asymmetric Imperfection 7400 Incremental method with eigenvalue and nonlinear stability analysis (Lanczos) 2nd Order

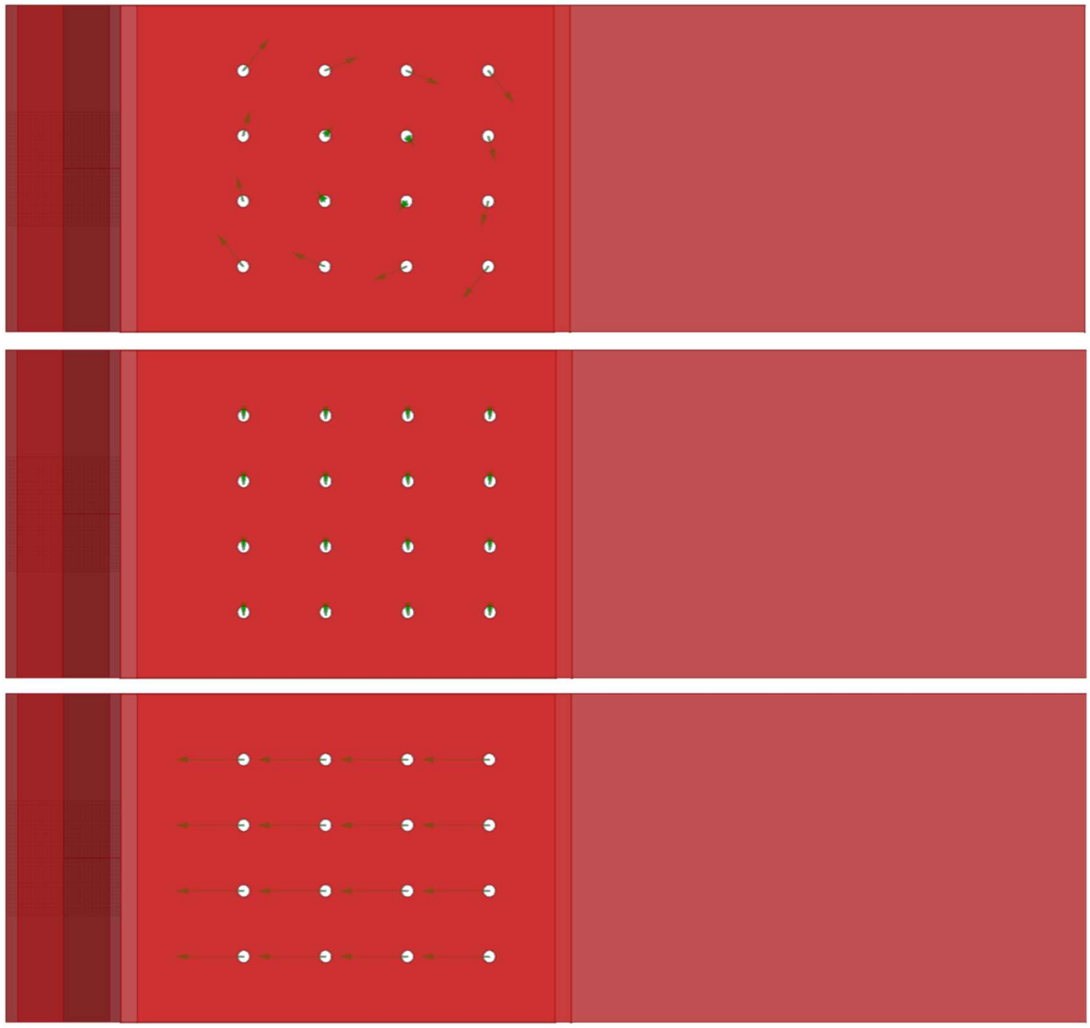

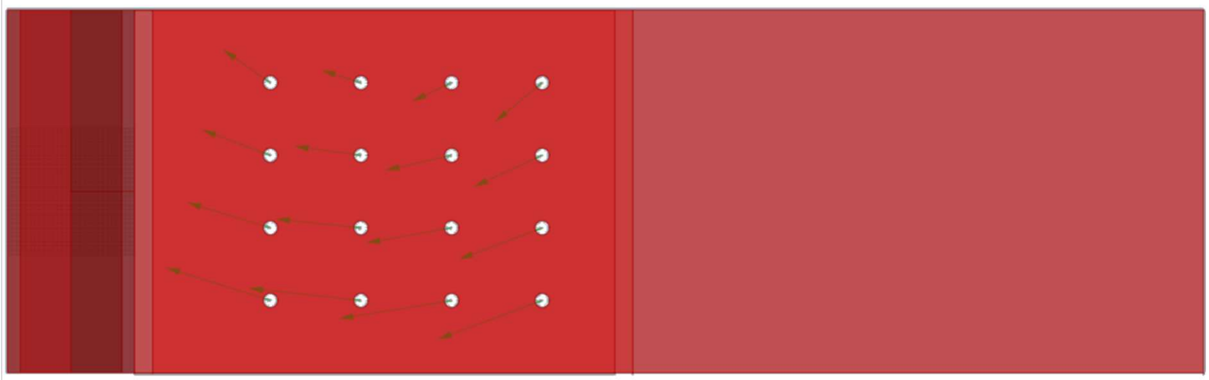

8. Case Study: C30 Connection Verification

Check	Governing Load combination	Internal Hinge Force	Unity Check
N	ULS Snow Equally	$-165.47\ kN$	$0.37 \leq 1.0$
V_y	ULS Snow Diagonal Pyramid	$1.09\ kN$	$0.01 \leq 1.0$
V_z	ULS Wind Parallel	$6.17\ kN$	$0.02 \leq 1.0$
M_{yy}	ULS Wind Parallel	$11.44\ kNm$	$0.37 \leq 1.0$
M_{zz}	ULS Wind Parallel	$0.04\ kNm$	$0.00 \leq 1.0$
T	ULS Snow Diagonal Pyramid	$-0.36\ kNm$	$-$

Bolt	Angle relative to grain direction [○]	Force per shear plane 11.44 kNm [kN]
1	51.34	5.041
2	75.07	3.226
3	75.07	3.226
4	51.34	5.041
5	22.62	4.369
6	51.34	1.680
7	51.34	1.680
8	22.62	4.369
9	22.62	4.369
10	51.34	1.680
11	51.34	1.680
12	22.62	4.369
13	51.34	5.041
14	75.07	3.226
15	75.07	3.226
16	51.34	5.041

$$F_v, Rk = min \begin{cases} f_{h,1,k} t_1 d \ (a) \\ f_{h1} t_1 d \left(\sqrt{2 + \frac{4M_{y,Rk}}{f_{h,1,k} t_1^2 d}} - 1 \right) (b) \\ 2.3 \sqrt{M_{y,Rk} f_{h,1,k} d} \ (c) \end{cases}$$

$$f_{h,k} = \ characteristic\ bearing\ strength\ of\ the\ timber$$

$$t_1 = the\ embedment\ length\ of\ the\ timber$$

$$d = dowel\ diameter$$

$$M_{y,Rk} = characterisitc\ yield\ moment\ of\ the\ dowel$$

Load Combination	Highest Unity Check per bolt
ULS Wind Parallel	$0.58 \leq 1.0$
ULS Wind Diagonal	$0.32 \leq 1.0$
ULS Wind C Parallel	$0.40 \leq 1.0$
ULS Wind C Diagonal	$0.45 \leq 1.0$
ULS Snow Equally	$0.48 \leq 1.0$
ULS Snow Parallel Pyramid	$0.49 \leq 1.0$
ULS Snow Diagonal Pyramid	$0.42 \leq 1.0$
ULS Snow Quad Pyramid	$0.55 \leq 1.0$

Timber bearing

Load Combination	Highest Unity Check per bolt
ULS Wind Parallel	$0.19 \leq 1.0$
ULS Wind Diagonal	$0.11 \leq 1.0$
ULS Wind C Parallel	$0.13 \leq 1.0$
ULS Wind C Diagonal	$0.15 \leq 1.0$
ULS Snow Equally	$0.16 \leq 1.0$
ULS Snow Parallel Pyramid	$0.17 \leq 1.0$
ULS Snow Diagonal Pyramid	$0.15 \leq 1.0$
ULS Snow Quad Pyramid	$0.19 \leq 1.0$

Von misses

Load Combination	Highest Unity Check per bolt
ULS Wind Parallel	$0.38 \leq 1.0$
ULS Wind Diagonal	$0.21 \leq 1.0$
ULS Wind C Parallel	$0.26 \leq 1.0$
ULS Wind C Diagonal	$0.30 \leq 1.0$
ULS Snow Equally	$0.32 \leq 1.0$
ULS Snow Parallel Pyramid	$0.32 \leq 1.0$
ULS Snow Diagonal Pyramid	$0.27 \leq 1.0$
ULS Snow Quad Pyramid	$0.36 \leq 1.0$

Bolt capacity

$$F_{b,Rd} = \frac{k_1 \alpha_b f_u d t}{\gamma_{M2}}$$

Load Combination	Highest Unity Check per bolt
ULS Wind Parallel	$0.07 \leq 1.0$
ULS Wind Diagonal	$0.04 \leq 1.0$
ULS Wind C Parallel	$0.05 \leq 1.0$
ULS Wind C Diagonal	$0.06 \leq 1.0$
ULS Snow Equally	$0.06 \leq 1.0$
ULS Snow Parallel Pyramid	$0.06 \leq 1.0$
ULS Snow Diagonal Pyramid	$0.05 \leq 1.0$
ULS Snow Quad Pyramid	$0.07 \leq 1.0$

Steel bearing

$$F_v, Rk = min \begin{cases} f_{h,1,k} t_1 d \\ f_{h1} t_1 d \left(\sqrt{2 + \frac{4M_{y,Rk}}{f_{h,1,k} t_1^2 d}} - 1 \right) \\ 2.3 \sqrt{M_{y,Rk} f_{h,1,k} d} \end{cases}$$

$$f_{h,k} = \ characteristic\ bearing\ strength\ of\ the\ timber$$

$$t_1 = the\ embedment\ length\ of\ the\ timber$$

$$d = dowel\ diameter$$

$$M_{y,Rk} = characterisitc\ yield\ moment\ of\ the\ dowel$$

$$M_{y,Rk} = 0.3 \cdot f_{u,k} \cdot d^{2.6}$$

$$M_{y,Rk} = 0.3 \cdot 800 \cdot 16^{2.6} = 3.24 \cdot 10^5\ Nmm$$

$$f_{h,1,k} = \frac{f_{h,0,k}}{k_{90} \sin^2 \alpha + \cos^2 \alpha}$$

$$f_{h,0,k} = 0.082(1 - 0.01d)p_k$$

$$f_{h,0,k} = 0.082(1 - 0.01 \cdot 16) \cdot 350 = 24.108$$

$$k_{90} = 1.35 + 0.015d$$

$$k_{90} = 1.35 + 0.015 \cdot 16 = 1.59$$

$$F_v, Rk = min \begin{cases} f_{h,1,k} t_1 d \\ f_{h1} t_1 d \left(\sqrt{2 + \frac{4M_{y,Rk}}{f_{h,1,k} t_1^2 d}} - 1 \right) \\ 2.3\sqrt{M_{y,Rk} f_{h,1,k} d} \end{cases}$$

Blok of schijf afschuiving

$$L_{net,v} = \sum_i l_{v,i}$$

$$L_{net,v} = 140 + 100 \cdot 3 = 440\ mm$$

$$L_{net,v} = \sum_i l_{t,i}$$

$$L_{net,v} = 3 \cdot 80 = 240\ mm$$

$$A_{net,t} = L_{net,t} t_1$$

$$A_{net,t} = 240 \cdot 90 = 21600$$

$$A_{net,v} = \frac{L_{net,v}}{2}(L_{net,t} + 2t_{ef})$$

$$F_{bs,Rk} = \begin{cases} 1.5 A_{net,t} f_{t,0,k} \\ 0.7 A_{net,v} f_{v,k} \end{cases}$$

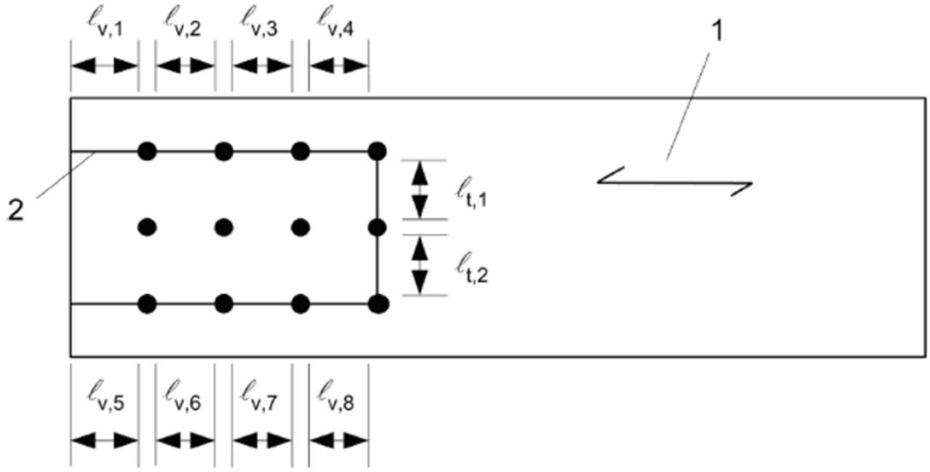

Verklaring

1 vezelrichting
2 breuklijn

Figuur A.1 — Voorbeeld van blokafschuiving

$$F_{ax,k,Rk} = \frac{n_{ef} f_{ax,k} d l_{ef} k_d}{1.2\cos^2\alpha + \sin^2\alpha}$$

$$f_{ax,k} = 0.52 d^{-0.5} l_{ef}^{-0.1} p_k^{0.8}$$

$$k_d = min\begin{cases}\frac{d}{8}\\ 1\end{cases}$$

$$n_{ef} = n^{0.9}$$

$$\sqrt[0.9]{\frac{\frac{F_{ax,k,Rk}}{k_{mod}} \cdot \gamma_m (1.2\cos^2\alpha + \sin^2\alpha)}{f_{ax,k} d l_{ef} k_d}} = n$$

$$k_d = min\begin{cases}\frac{8}{8}\\ 1\end{cases} = 1$$

$$f_{ax,k} = 0.52 \cdot 8^{-0.5} \cdot 120^{-0.1} \cdot 350^{0.8} = 12.35\ N/mm^2$$

$$\sqrt[0.9]{\frac{6.3 \cdot \frac{1.3}{0.9} \cdot (1.2\cos^2 90 + \sin^2 90)}{12.4 \cdot 8\ \cdot 120 \cdot 1}} = 0.74$$

Load Combination	Check	Unity Check
ULS Wind Parallel	Timber bearing	$0.58 \leq 1.0$
ULS Wind Parallel	Timber Beam First Order	$0.19 \leq 1.0$
ULS Snow Equally	Timber Beam Second Order	$0.80 \leq 1.0$
ULS Wind Parallel	Plate von Misses	$0.19 \leq 1.0$
ULS Wind Parallel	Plate bearing	$0.07 \leq 1.0$
ULS Wind Parallel	Dowel shearing	$0.38 \leq 1.0$
ULS Wind Parallel	Splitting	$22.0 < 27.6kN$